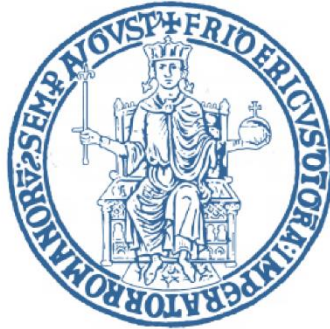


Università degli Studi di Napoli Federico II

Istituto Italiano di Tecnologia



# Out-of-plane graphene materials for enhanced cell-chip coupling

Ph.D. Program in Industrial product and process engineering  
XXXIII - cycle

Laura Matino, M. Sc.

**Supervisor:** Dr. Francesca Santoro

**Coordinator:** Prof. Andrea D'Anna

## Table of the content

List of Figures .....	5
List of Tables.....	8
Abstract.....	9
List of Abbreviations .....	10
<b>Chapter 1: Introduction.</b> .....	<b>12</b>
1.1 Bioelectronics. ....	12
1.1.1 Principles of bioelectronics.....	12
1.1.2 In vitro platforms for electrophysiology. ....	13
1.2 Cell-material crosstalk: the use of 2.5 and 3D topography.....	18
1.2.1 Engineering cell instructive materials.....	19
1.3 Characterization of cell-material interface. ....	25
1.3.1 Electron microscopy for nanometer resolution of the cell-material interface. ....	28
1.4 Graphene materials for bioelectronics application.....	32
1.4.1 Graphene-based in vitro applications.....	32
1.5 Our study .....	35
<b>Chapter 2: Materials and Methods.....</b>	<b>37</b>
2.1 Out-of-plane graphene synthesis and fabrication. ....	37
2.2 Substrate characterization.....	39
2.2.1 Scanning electron microscopy.....	39
2.2.2 Raman spectroscopy.....	39
2.2.3 Contact angle measurements.....	39
2.3 Substrate preparation for cell cultures.....	40
2.3.1 Cleaning and sterilization.....	40
2.3.2 Substrate functionalization.....	40
2.4 Cell Culture. ....	41
2.4.1 HL-1 cardiomyocytes -like cell line.....	41
2.4.2 Primary cortical neurons.....	42
2.5 Biocompatibility assay and cellular electrophysiological activity.....	45
2.5.1 Toxicity assay. ....	45
2.5.2 Calcium imaging.....	46
2.6 Immunohistochemistry.....	47
2.6.1 Cytoskeleton, focal adhesion proteins and nuclei labelling. ....	47

2.6.2	Endocytic proteins labelling.....	48
2.6.3	Dendrites, axons and nuclei labelling.....	49
2.6.4	Structural cytoskeleton of neural growth cone.....	50
2.6.5	Cell body and nuclear envelopes labelling.....	50
2.6.6	Analysis of plasma membrane integrity.....	51
2.7	Image acquisition.....	52
2.8	Image processing and analysis.....	53
2.8.1	Live/dead cell populations analysis.....	53
2.8.2	Ca <sup>2+</sup> wave imaging analysis.....	54
2.8.3	Cell shape descriptors analysis.....	55
2.8.4	Fluorescence intensity profile analysis across cells area.....	56
2.8.5	Fluorescence intensity profile along a linear region of interest.....	57
2.8.6	Axon length measurements and secondary neurites counting.....	58
2.8.7	3D optical reconstruction of cell body.....	59
2.9	Electron Microscopy for cell-material characterization.....	60
2.9.1	Ultrathin plasticization (UTP) method <sup>11,40</sup> .....	60
2.9.2	Whole-cell scanning electron microscopy.....	62
2.9.3	Focused ion beam sectioning/scanning electron microscopy of cross sections.....	63
<b>Chapter 3: Results and discussion.....</b>		<b>65</b>
3.1	Out-of-plane graphene substrates characterization: morphology and composition.....	65
3.2	Graphene-cell interface: general considerations.....	70
3.3	Biocompatibility of out-of-plane graphene materials.....	71
3.3.1	HL-1 cells viability.....	71
3.3.2	HL-1 Calcium Imaging.....	72
3.3.3	Primary cortical neuronal cells viability.....	76
3.4	Growth and adhesion modulation of cardiomyocytes-like by means of graphene topography.....	78
3.4.1	HL-1 cell area and height modulation by out-of-plane graphene materials.....	78
3.4.2	HL-1 cells polarization, actin and focal adhesion proteins organization.....	81
3.4.3	Investigation of endocytic processes at the cell-material interface.....	95
3.4.4	HL-1 – material interface characterized at the nanoscale by scanning electron microscopy/focused ion beam.....	99
3.5	Neuronal polarization outgrowth mediated by out-of-plane graphene materials.....	105
3.5.1	Neuronal polarity and growth cone morphology.....	105

3.5.2	Growth cone analysis of neurons cultured on planar Si/SiO <sub>2</sub> substrates.....	110
3.5.3	Growth cone analysis for neurons cultured on 2DG substrates. ....	112
3.5.4	Growth cone analysis for neurons cultured on 3DFG substrates. ....	114
3.5.5	Growth cone analysis for neurons cultured on wires templated graphene substrates. ....	116
3.5.6	Actin and tubulin arrangement at the growth cone. ....	121
3.5.7	Axon elongation, neuronal branching.....	129
3.5.8	Neuron-graphene material coupling investigated by SEM/FIB. ....	136
<b>Chapter 4: Conclusions. ....</b>		<b>140</b>
<b>References .....</b>		<b>143</b>
<b>List of Publications.....</b>		<b>154</b>
<b>Annex A.....</b>		<b>155</b>
1.	Optical cross section of HL-1 cytoskeleton.....	155
2.	FIB/SEM cross sectioning parameters. ....	158
3.	Optical cross section of CME pathways of HL-1 cells.....	159
4.	PM integrity through analysis of possible calcein internalization.....	160
<b>Annex B.....</b>		<b>161</b>

## List of Figures

**Figure 1.1.** Overview of the Bioelectronics field.

**Figure 1.2.** Electrical equivalent circuit of the cell-electrode interface.

**Figure 1.3.** Examples of *in vitro* 3D recording systems.

**Figure 1.4.** Dimension comparison between several biological entities, viruses, proteins, DNA and cells.

**Figure 1.5.** Topography effects on filamentous actin and FA organization.

**Figure 1.6.** Membrane curvature as topographical hub for actin reorganization.

**Figure 1.7.** Engineered protruding nanostructures to probe endocytic vesicle accumulation.

**Figure 1.8.** Characterization of the cell-material interface.

**Figure 1.9.** Cross section preparation for EM.

**Figure 1.10.** Cell-material interactions comparison depending on the feature-feature distance.

**Figure 1.11.** Graphene-based bioelectronics for extracellular measurement.

**Figure 2.1.** HL-1 cell culture.

**Figure 2.2.** Egg content visualization.

**Figure 2.3.** Schematic of a fertilized egg content after 9 days from the incubation.

**Figure 2.4.** Chicken and brain dissection.

**Figure 2.5.** Cortical neurons morphogenesis from plating to 3 DIV.

**Figure 2.6.** Live/dead cells labelling.

**Figure 2.7.** Exemplary images of the  $\text{Ca}^{2+}$  wave propagation.

**Figure 2.8.** F-actin, FAs and nuclei staining.

**Figure 2.9.** Endocytic vesicles labelling.

**Figure 2.10.** Axons, dendrites, and nuclei staining.

**Figure 2.11.** Neuronal cytoskeleton.

**Figure 2.12.** Cell body and nuclear envelop staining.

**Figure 2.13.** Cell body staining and plasma membrane integrity investigation.

**Figure 2.14.** Live/dead image analysis.

**Figure 2.15.**  $\text{Ca}^{2+}$  wave imaging process.

**Figure 2.16.** Cell shape descriptors processing.

**Figure 2.17.** Cell fluorescence intensity quantification.

**Figure 2.18.** Cell fluorescence intensity along one pixel line.

**Figure 2.19.** Axon length measurement and neurite processes counting.

**Figure 2.20.** 3D cell reconstruction in ImageJ.

**Figure 2.21.** Ultra-thin plasticization method.

**Figure 2.22.** Resin layer embedding as a function of ethanol removal.

**Figure 2.23.** Whole-cell scanning electron micrograph.

**Figure 2.24.** FIB/SEM cross-sectioning and imaging procedure.

**Figure 3.1.** 3D schematics of the synthesized graphene-based material.

**Figure 3.2.** Scanning electron micrographs of the graphene materials.

**Figure 3.3.** Raman spectra of planar and out-of-plane graphene materials.

**Figure 3.4.** Contact angle measurements.

**Figure 3.5.** Schematics of possible mechanism at the cell out-of-plane material interface.

**Figure 3.6.** HL-1 biocompatibility assay.

**Figure 3.7.** Ca<sup>2+</sup> wave speed incidence.

**Figure 3.8.** Kymographs of Ca<sup>2+</sup> ions flow.

**Figure 3.9.** Neuronal cells viability on graphene materials.

**Figure 3.10.** Average area of HL-1 cells cultured on the graphene substrates.

**Figure 3.11.** 3D HL-1 cell membrane reconstruction by confocal microscopy and cell height analysis.

**Figure 3.12.** Optical cross sections.

**Figure 3.13.** Cell morphology analysis.

**Figure 3.14.** Actin organization in HL-1 cell cultures on the different graphene substrates.

**Figure 3.15.** Average actin-associated fluorescence intensity quantification at 95 % confidence interval.

**Figure 3.16.** HL-1 paxillin distribution and its association with actin fibers on Si/SiO<sub>2</sub>.

**Figure 3.17.** HL-1 paxillin distribution and its association with actin fibers on 2DG.

**Figure 3.18.** HL-1 paxillin distribution and its association with actin fibers on 3DFG.

**Figure 3.19.** HL-1 paxillin distribution and its association with actin fibers on NT-3DFGc.

**Figure 3.20.** HL-1 paxillin distribution and its association with actin fibers on NT-3DFGnc.

**Figure 3.21.** Paxillin fluorescence intensity quantification at 95 % confidence interval.

**Figure 3.22.** Endocytic pathways in HL-1 cultured on Si/SiO<sub>2</sub> and 2DG.

**Figure 3.23.** Endocytic pathways in HL-1 cultured on out-of-plane graphene materials.

**Figure 3.24.** Fluorescence intensity quantification of clathrin and cav-1 protein.

- Figure 3.25.** Scanning electron micrographs of HL-1 cells culture on planar materials.
- Figure 3.26.** Scanning electron micrographs of HL-1 cells cultured on out-of-plane graphene.
- Figure 3.27.** FIB/SEM cross section of HL-1 cells cultured on planar materials.
- Figure 3.28.** FIB/SEM cross section of HL-1 cells cultured on out-of-plane graphene materials.
- Figure 3.29.** Neural development and neurite initiation.
- Figure 3.30.** Growth cone morphology classification.
- Figure 3.31.** Definition of peculiar growth cone regions.
- Figure 3.32.** Growth cone characterization on Si/SiO<sub>2</sub>.
- Figure 3.33.** Growth cone characterization in 2DG cultures.
- Figure 3.34.** Growth cone characterization in 3DFG cultures.
- Figure 3.35.** Growth cone characterization on NT-3DFGc.
- Figure 3.36.** Growth cone characterization on NT-3DFGnc.
- Figure 3.37.** Fluorescence intensity quantification of actin and  $\beta$ III-tubulin in neuronal cells.
- Figure 3.38.** Fluorescence intensity quantification across GC domains on Si/SiO<sub>2</sub>.
- Figure 3.39.** Fluorescence intensity quantification across GC domains on 2DG.
- Figure 3.40.** Fluorescence intensity quantification across GC domains on 3DFG.
- Figure 3.41.** Fluorescence intensity quantification across GC domains on NT-3DFGc.
- Figure 3.42.** Fluorescence intensity quantification across GC domains on NT-3DFGnc.
- Figure 3.43.** Axon elongation through the graphene topographies.
- Figure 3.44.** Secondary neurites investigation along the axon shaft.
- Figure 3.45.** Neuron-Si/SiO<sub>2</sub> adhesion.
- Figure 3.46.** Neuron-2DG adhesion.
- Figure 3.47.** Neuron-3DFG adhesion.
- Figure 3.48.** Neuron-NT-3DFGc adhesion.
- Figure 3.49.** Neuron-NT-3DFGnc adhesion.
- Figure A1.1.** xz and yz vies of HL-1 cells cultured on 2DG.
- Figure A1.2.** xz and yz vies of HL-1 cells cultured on 3DFG.
- Figure A1.3** xz and yz vies of HL-1 cells cultured on NT-3DFGc.
- Figure A1.4.** xz and yz vies of HL-1 cells cultured on NT-3DFGnc.
- Figure A3.1.** Clathrin-mediated protein spatial distribution.

**Figure A4.1** HL-1 membrane integrity from interaction with out-of-plane structures.

## List of Tables

**Table 2.1.** Contact angle classification.

**Table 3.1.** Calcium wave speed quantification of HL-1 cells culture on the different graphene materials.

**Table 3.2.** Significant differences of cell area at 95% confidence interval performing a OneWay ANOVA analysis.

**Table 3.3.** Significant differences of HL-1 cells height at 95 % confidence interval by one-way ANOVA analysis.

**Table 3.4.** Significant difference of polarization ratio at 95 % confidence interval.

**Table 3.5.** Significant difference of F-actin fluorescent signals at 95 % confidence interval.

**Table 3.6.** Significant difference of paxillin proteins fluorescence at 95 % confidence interval.

**Table 3.7.** Significant difference of clathrin proteins fluorescence at 95 % confidence interval.

**Table 3.8.** Significant difference of cav-1 proteins fluorescence at 95 % confidence interval.

**Table 3.9.** Percentage increase of axonal length compared to planar graphene culture.

**Table A2.1.** Milling operational setting.

**Table A2.2.** Polishing operational setting.

## Abstract

Bioelectronic devices interact directly with biological systems to monitor cellular electrical activity and promote cell reaction to electrical stimulation. The capabilities of such devices, in terms of recording and stimulation, are affected by the effective cell-platform coupling. Therefore, during the last years, the development of engineered 2.5-3D micro and nanostructures has improved the effectiveness of biosensors using protruding structures to achieve a more intimate contact between cells and substrates. The vertical structures, due to their surface curvature, can actively modulate the cell-material interaction and the coupling conditions by regulating peculiar cellular processes at the interface such as membrane bending, ruffling, which ultimately reduce the distance between the electroactive materials and the biological components.

In parallel, the rising of carbon-based materials (*i.e.*, graphene) for bioelectronics has gained attention during the last years because of their outstanding chemical properties which allow improved cell-device interfacing. Given this scenario, 3D out-of-the-plane graphene structures has been designed and grown on planar platforms, exploiting the electrical, mechanical and optical features of this promising material. 3D fuzzy graphene (3DFG) and two nanowire-templated arrangements (NT-3DFG collapsed and non-collapsed) were realized to ultimately increase the dimensionality at the interface with cells through nanoscale features and wire-based architectures.

Here we report a comprehensive study of the electrogenic cells-material interface by using fluorescence and electron microscopy for characterizing cell-graphene materials interactions at micro and nanoscale. First, we investigated the biocompatibility and the adhesion effect (cell stretching and outgrowth) of the diverse graphene-based pseudo-3D surfaces coupled to cardiomyocytes-like cells and primary cortical neuronal cells. Then, we examined the membrane deformation and the actual cell-device coupling *via* scanning electron microscopy/focused ion beam sectioning. We found out an enhanced cells adhesion on the substrates, suggesting that out-of-the-plane platform could improve the coupling between cells and sensors not only for electrophysiology application but also to modulate cellular functionalities and outgrowth.

## List of Abbreviations

- 2D** two-dimensional
- 2DG** planar graphene
- 3D** three-dimensional
- 3DFG** three-dimensional fuzzy graphene
- Ab I** primary antibody
- Ab II** secondary antibody
- ANOVA** Analysis Of Variance
- BSA** Bovine Serum Albumin
- [Ca<sup>2+</sup>]** Calcium ions concentration
- C<sub>f</sub>** final concentration
- CIRC** Ca<sup>2+</sup>-induced Ca<sup>2+</sup> release
- CME** clathrin-mediated endocytosis
- CPD** critical point drying
- CPV** Ca<sup>2+</sup> wave propagation velocity
- CVD** chemical vapor deposition
- DI water** deionized water
- DIV** day/s in vitro
- ECM** extracellular matrix
- FA** focal adhesion
- F-actin** filamentous actin
- FEG** field emission gun
- FET** field-effect transistor
- FIB** focused ion beam
- FLIC** fluorescence interference contrast
- FWHM** Full width at half maximum
- GC** Growth cone
- LPCVD** low pressure chemical vapor deposition
- LTCC** voltage-gated L-type Ca<sup>2+</sup> channels
- MEA** Multi-electrode array
- MT** Microtubules

**NP** Nanoparticles

**NT-3DFGc** Collapsed nanowire-mesh template covered with fuzzy graphene

**NT-3DFGnc** Non-collapsed nanowire-mesh template covered with fuzzy graphene

**NW** Nanowires

**PBS** Phosphate buffer saline

**PECVD** Plasma-enhanced chemical vapor deposition

**PDF** probability density function

**PFA** Paraformaldehyde

**PLL** Poly-L-lysine

**PM** Plasma membrane

**PMMA** Polymethylmethacrylate

**RF** Radiofrequency

**ROI** Region of Interest

**Rpm** rotation per minute

**SEM** Scanning electron microscopy

**Si/SiO<sub>2</sub>** Silicon / Silicon Oxide

**SPRi** Surface plasma resonance imaging

**SR** sarcoplasmatic reticulum

**sscm** standard cubic centimetre per minute

**T<sub>A</sub>** acquisition time

**TEM** transmission electron microscopy

**UTP** ultra-thin plasticization

**VGA** video contact angle system

**VLS** vapor-liquid-solid

**λ<sub>EX/EM</sub>** excitation/emission wavelength

## Chapter 1: Introduction.

### 1.1 Bioelectronics.

#### 1.1.1 Principles of bioelectronics.

Bioelectronics is an interdisciplinary field where electronic platforms directly interact with biological systems to monitor physiological processes or modulate certain functions by the application of electrical fields (**Figure 1.1**). Bioelectronic devices have found major applications in interfacing the brain or the heart as the functionalities of these organs are mainly governed by the generation and propagation of electrical signals. Thus, motor or visual prosthesis, cochlear implants, deep brain stimulation systems for brain applications<sup>1</sup>, as well as soft electronics with marked abilities in recording depolarization and repolarization cardiac cycles, and in registering heart sound analysis as a phonocardiography<sup>2</sup>, promise to pave the way for new real-time diagnosis of critical disorders, but most importantly delivering personalized therapies and support to suffering individuals.

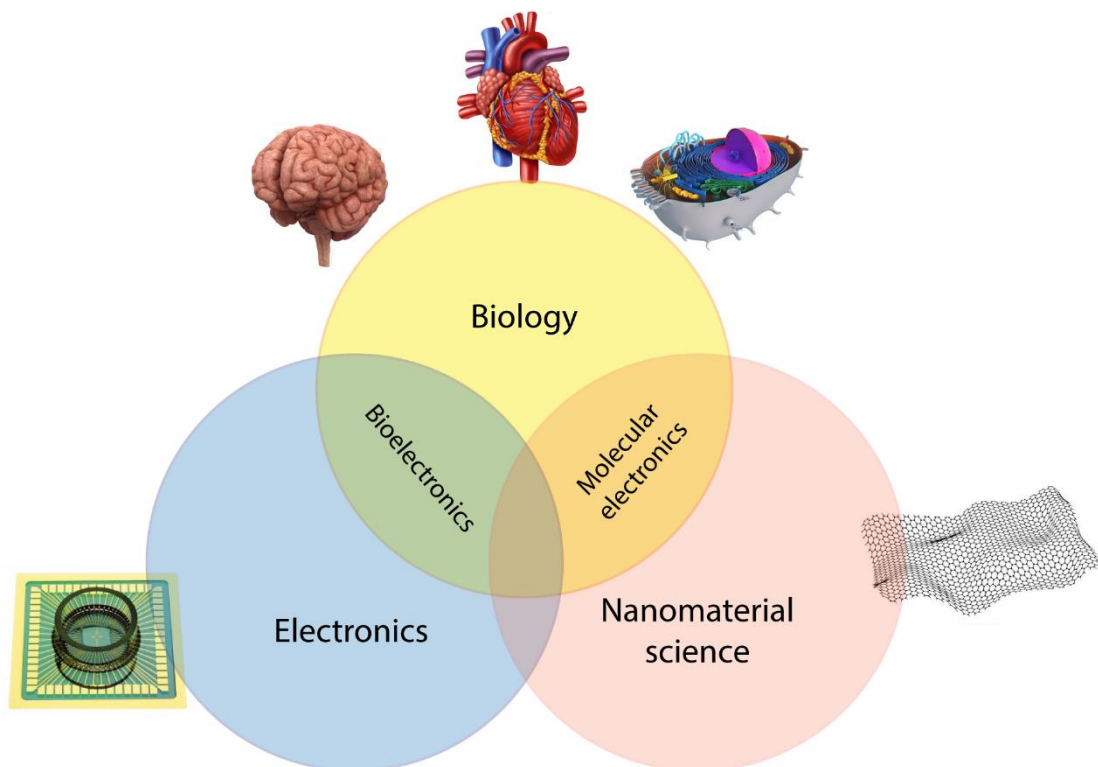


**Figure 1.1. Overview of the Bioelectronics field.** Bioelectronics is the branch of science concerned with the application of engineered materials or electronics to interface with living systems.

As a matter of fact, excitable cells, present in the brain and the heart, such as neurons and cardiomyocytes, send information and interact with their neighboring cells through the modulation of action potentials

which are transient electrical signals crossing the cellular body and plasma membrane (PM) through ion-specific channels and pumps opening<sup>3</sup>. The resulting changes of voltage are due to the flow of certain ions, whose difference in concentrations provide gradient driving forces (*i.e.*, electrochemical gradient) for them to move across the PM. Thus, ionic movements push cells from their resting state to the excited one, from which action potential event potentially propagates to adjacent cells<sup>3</sup>. Therefore, understanding the electrical activities of electrogenic cells not only might characterize the metabolism of a single cell, but also its network connection. Moreover, a comprehensive study of the cellular electric state might further elucidate pathological conditions which comprises impaired electrical activity at cellular and/or cellular network level.

Considering the above, numerous methods of investigation have been developed to study biological electrical activities which include non-invasive approaches as electrography<sup>4</sup>, functional magnetic resonance imaging<sup>5</sup> or even positron emission tomography, or invasive procedure which directly and intimately interface the electronics with the brain tissues or beating heart<sup>2</sup> (implantable devices).

### ***1.1.2 In vitro platforms for electrophysiology.***

Bioelectronic devices might be also directly coupled with single cells. In order to investigate their electrical activity, *in vitro* platforms provide recording and stimulation at single cell as well as network level through micro and nanofabricated electroactive elements.

These platforms for cellular electrical activity investigation include, for instance, the exploitation of microelectrode arrays (MEAs), substrate-integrated of microscopic electrode arrays, and field-effect-transistors (FETs), three-terminal devices (source, drain and gate) whose operation is based on the current modulation between two terminals through the application of voltage at the third terminal. Both these classes of devices have recently gained attention for their ability to facilitate long-term and multi-site recordings with sub-millisecond temporal resolution<sup>6,7</sup>, as well as stimulation with high spatial resolution<sup>8</sup> (single-to-few cells)<sup>9</sup>. However, the efficiency of these bioelectronic probes is contingent on how good the measuring electrode is electrically coupled with cells, the extension of the exposed surface area and the impedance value of the electrode<sup>6,10</sup>. Tuning these parameters might steer toward improved device performance.

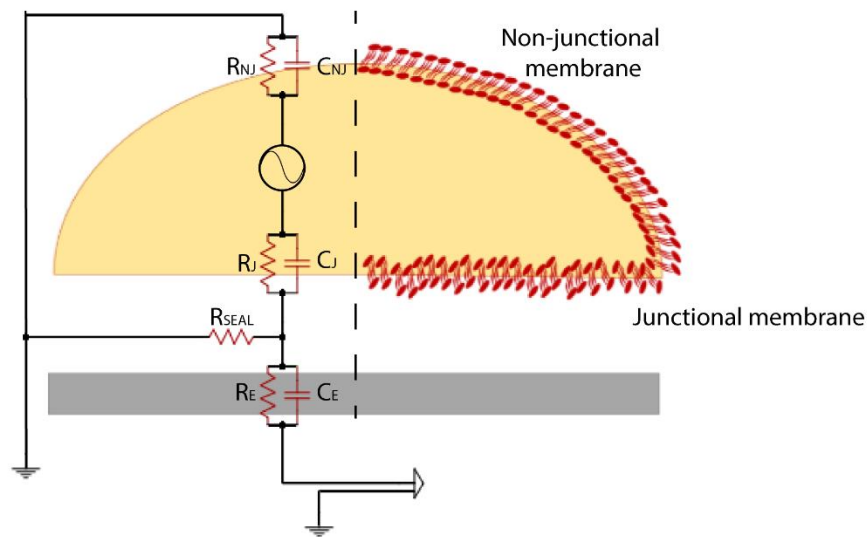


**Figure 1.2. Electrical equivalent circuit of the cell-electrode interface.**

Schematics depicts the spatial relationship between a cell and a sensing electrode with the analogue passive electric circuit.

From an electrical point of view, the structural relationship between the components of this hybrid system (cell, sensing electrode and the gap which separates them) might be modelled with the element of a passive electronic circuit, as shown in **Figure 1.2**. Each cell in contact with an electrode has two different PM domains, the *junctional membrane* and *non-junctional membrane*, depending on whether the cell membrane faces the sensing area or towards the electrolyte solution, respectively. Regardless the specific domain, the PM is generally represented by a parallel of the capacitance (C) and the resistance (R), where C models the accumulation of charges at the cell-electrolyte solution interface, in contrast R describes the opposition to the flow of ions across the electrical charge layer (in **Figure 1.2** junctional and non-junctional membranes are pointed with the subscripts *j* and *n<sub>j</sub>*, respectively). The intracellular ionic flow is expressed as an alternating current power source. Similar modelling was ascribed to the sensing pad, which holds an impedance  $Z_e$  (resulting from the parallel of  $R_e$  and  $C_e$ , where the resistance depends on the material properties of the electrodes and the capacitance models the charge accumulation at electrolyte solution-electrode interface). As depicted in **Figure 1.2**, the cell and the sensing electrode are decoupled by a spatial gap (cleft) filled by the ionic solution. The electrical description of this cleft is given by the seal resistance  $R_{SEAL}$ , which directly modulates the amplitude of the recorded signal based on its width and the portion of electrode surface actually in contact with the cell. Moreover, it is a key actuator of the effective capacitive coupling.

Hence, in conventional planar bioelectronics, studies revealed a typical gap width ranging 40-100 nm<sup>11-13</sup>, which could reduce the sensitivity of the device to more subtle and critical events, such as subthreshold excitatory and inhibitory postsynaptic potentials or subthreshold potential oscillations travelling across the membrane<sup>6,14</sup>. Indeed, theoretically and experimentally, amplitude and shape of the recording signal are assessed by the multiplication of  $R_{SEAL}$  value and the ion flow that crosses it.  $R_{SEAL}$  was estimated to follow the ensuing equation, which includes a geometric contribution:

$$R_{SEAL} = \frac{\delta}{d} \rho_s \quad [ 1 ]$$

where:  $\rho_s$  is the resistivity of the electrolyte solution,  $d$  is the average cleft distance and  $\delta$  represents electrode surface fraction in contact with the cell above it cultured<sup>10</sup>. Bearing in mind that the better readout signal results from system configuration which provides higher  $R_{SEAL}$  values<sup>6,10</sup>, recent efforts have been made in order to increase  $R_{SEAL}$  by acting on both  $d$  and  $\delta$  parameters, which ultimately arise with closer approach between sensing platform and the biological part. In this direction, bioelectronic devices, which rely on two-dimensional (2D) architectures, show their shortcoming effects due to the poor interactions with interfaced cells and tissues and the limited exposed surface area<sup>6,9,14</sup>. Therefore, these 2D architectures, have been gradually complemented by non-planar sensing probes<sup>14-16</sup>. Extending the dimensionality with the introduction of three-dimensional (3D) topography at the electrode surface, has effectively addressed the issues of the 2D configurations by increasing the exposed electronic surface area at the interface with the cells, enhancing cell-device coupling and lowering the total electrode impedance<sup>6,10</sup>. Moreover, these topographical features might enable single-cell sensing which provides not only precise cell-to-electrode registration, but also large signal-to-noise ratio typically reserved to patch clamp recordings<sup>6,16</sup>. Indeed, the use of sharp electrodes has the striking effect to recreate the concept of the patch clamp technique at the nanoscale. Here, the electrical measurements (*i.e.*, voltage or current across the cell membrane) are determined by accessing cell interior with an electrode<sup>17</sup> and tearing the cell membrane. The resulting physical contact ensures excellent electrical coupling, direct cell stimulation, as well as faithful accurate readout of the biological signals with a resolution down to the single membrane ion channel. However, these high-fidelity measurements are extremely time-consuming and thereby, the procedure is not scalable. In addition, the invasive nature of the method limits both the recording time and the observation to only few cells in parallel<sup>18</sup>.

Therefore, the rise of 3D bioelectronics has tackled these limitations, and significantly improved the device performance in numerous ways. Compared to the patch clamp technique, extracellular 3D electrodes prevent mechanical damages to the cell, yet ensuring thigh contact with the biological components<sup>6,14,19,20</sup>. Pillars, mushroom, wires, tubes, or general protruding structures have been designed as means to increase

the accessible surface area for the cell that contributes to the double-layer capacitance, as well as increment the portion of electrode actually in contact with cells<sup>6,14,19,21</sup>. Indeed, with out-of-plane electrode configurations,  $R_{SEAL}$  values account for either the contribution of the cellular adhesion area of the pillar stalk and the top area or the enlarged surface area exposed to the cell<sup>10</sup>, depending on the electrode geometry. As a consequence, in comparison to planar electrodes, the gap between micro and nanostructured electrodes and cells is drastically reduced from  $\sim 50 - 200$  nm to 5 - 30 nm, as measured by microscopy techniques or predicted by numerical simulations<sup>10,12,13</sup>. Thereby, according to the equation [1],  $R_{SEAL}$  results to have higher value<sup>6,10,11,14,18,22</sup>.

Furthermore, these nano and micro-textured electrodes might be seamlessly integrated into MEA and FET circuitry using complementary metal oxide semiconductor (CMOS) process<sup>6,19,21</sup>.

Multiple microelectrodes (from ten up to thousands), contained in a single MEA, have been exploited as transducer of biological ionic currents across the cellular PM into electronic signals, during the recording activities<sup>18,22</sup>, and as ionic current injector when used in stimulation mode. In parallel, electrochemical biosensor based on FET offers high sensitivity, selectivity, and short time response, for extracellular and intracellular recording, as well as stimulation<sup>18,22</sup>. The potential for large-scale multiplexing of signals from individual cells or network, offered by both these two electronic architectures, has been even more upgraded with the integration of 3D electrodes<sup>15,22</sup>. Successful examples of 3D integrated topographies into MEA was given by Spira and coworkers, who fabricated mushroom-shaped electrodes that protrude from the flat surface<sup>6,7</sup>. With this electrode configuration, resembling the shape of dendritic spines in the neuronal tissue, they achieved a 50-fold higher coupling compared to the planar configuration, enough to record both action potential and subthreshold synaptic potentials<sup>6,7</sup> (**Figure 1.3 A**). Similarly, Cui's research group developed a nanopillared MEA which used to electroporate and then record cardiomyocytes, above them cultured. The resulting transient increase of cell membrane permeability, through the application of a local electrical field, enables to capture intracellular electrical activity with a typical positive footprint<sup>23</sup> (**Figure 1.3 B**). Promising results were achieved with the use of silicon nanowire FET by Patalosky *et al.*. Here, the high-aspect-ratio structures (nanowires) were leveraged as local and non-invasive probes for neuronal projections, enabling electrical signals recording, stimulation of the action potential (AP) propagation and back-propagation, as well as AP inhibition with a blocking threshold voltage<sup>24</sup> (**Figure 1.3 C**). Similarly, other different vertical topographies, which comprise, nanowires<sup>20,25</sup>, tubes or cones<sup>19</sup>, have proven to efficiently record both extracellular and intracellular electrical activities, thanks to the closer contact provided by the PM engulfment of the protruding structures or by external poration (electroporation<sup>19</sup> or optoporation<sup>169</sup>). The great potential to design and fabricate protruding electrodes

with feature size smaller than the cellular dimension could be further exploited for cellular stimulation<sup>16</sup>. Miniaturizing electrodes, enough to be interface and engulfed by a single cell, might prevent accidental haphazard activation of cell, not in direct contact with the stimulating electrode. 3D electrodes ultimately improve cell-to-electrode registry and the spatial accuracy of stimulation<sup>16</sup>.

Taken together, the advancement in 3D bioelectronics has further pushed the investigation to the cellular regimes, hence, achieving the detection of cellular sub-threshold electrical events<sup>6</sup>, without inflicting mechanical damage to the cell's PM<sup>6,14,26</sup>.

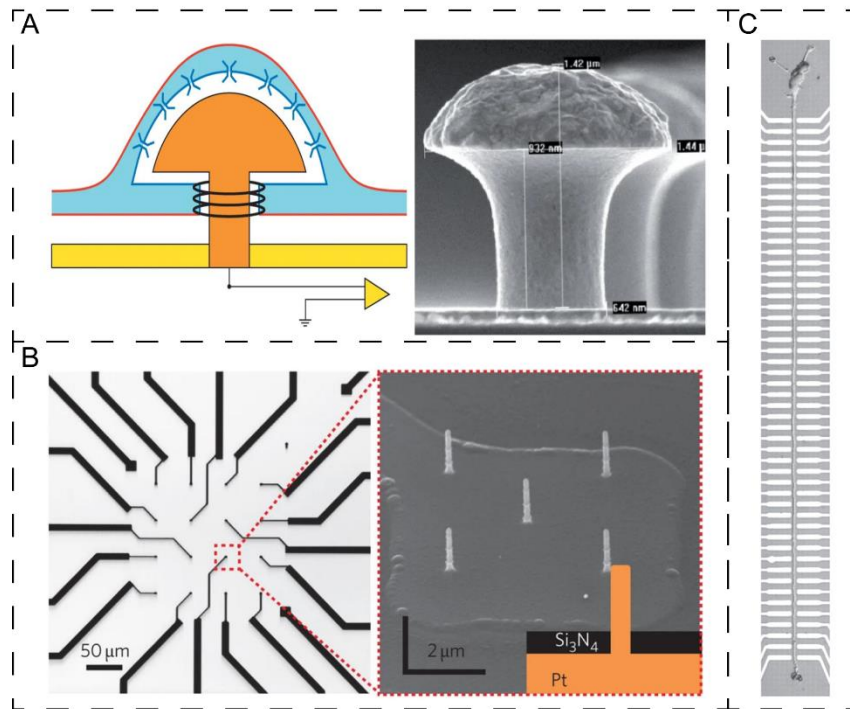


**Figure 1.3. Examples of *in vitro* 3D recording systems.** (A) On the left: schematics of a neuron engulfing a mushroom-shaped microelectrode, the interaction between the two is stabilized by actin structures, indicated by the black circles. On the right: scanning electron micrograph of a gold mushroom-shaped protruding microelectrode. Adapted from [6]. (B) On the left: optical image of a nanopillar MEA. On the right: scanning electron micrograph of a five vertical nanopillar electrode, with inset of the nanopillar composition. Adapted from [23]. (C) Optical image of aligned axon crossing an array of nanowire device. Adapted from [24].

## 1.2 Cell-material crosstalk: the use of 2.5 and 3D topography.

Giving this scenario, 2.5 – 3D patterned materials might be optimal candidates to encourage a tighter cellular attachment to the exogenous bioelectrical counterpart. Moreover, these out-of-plane materials have been shown to modulate certain cellular processes and regulate cell fate. For instance, *in vitro* studies indicated that precise engineering of 2D nanopatterns and 3D nanostructures, with well-defined features to interface with cells, has provided structural frameworks on which cellular adhesion may initiate<sup>15,27</sup>. As a matter of fact, cells are able to sense micro and nanofeatures, notably respond to these mechanical cues as readily as they do in their original environment<sup>15,27</sup>. The rationale behind these tenets relies on two basic and connected conditions. Firstly, features triggering biological responses have a range size from the nano up to the microscale, which makes them in comparable scale to the intracellular machinery, protein complexes, or even cell membrane processes (*i.e.*, filopodia, microspikes or rafts), yet far from bulk material behavior or simple planar systems<sup>15,27,28</sup> (**Figure 1.4**). As a consequence, a straightforward cellular response, in ways specific to the order, shape and scale of the features, directly induces protein activation. Secondly, the gimmick of using protruding structures, to interface with biological counterparts, aims to replicate part of topography, cells generally come into direct contact in their original environment. Indeed, under *in vivo* conditions, the modulation of cellular behavior and ultimately its life is supported by the dynamic continuous and reciprocal crosstalk with the extracellular environment<sup>29–31</sup>. Thereby, extrinsic cellular signals, as engaging with adjacent cells (namely membranes with micro and nano-sized features), or interacting with geometrically different biomolecules (*i.e.*, pores, fibers or crystals) embedded into the extra-cellular matrix (ECM) eventually determine cell fate as equal as the intrinsic cell cues (*i.e.*, information from the genetic code)<sup>29</sup>.

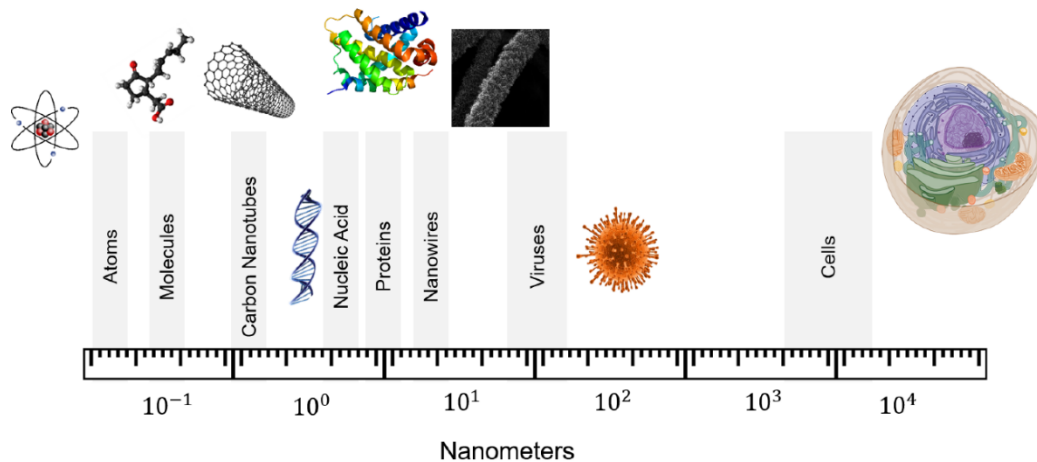
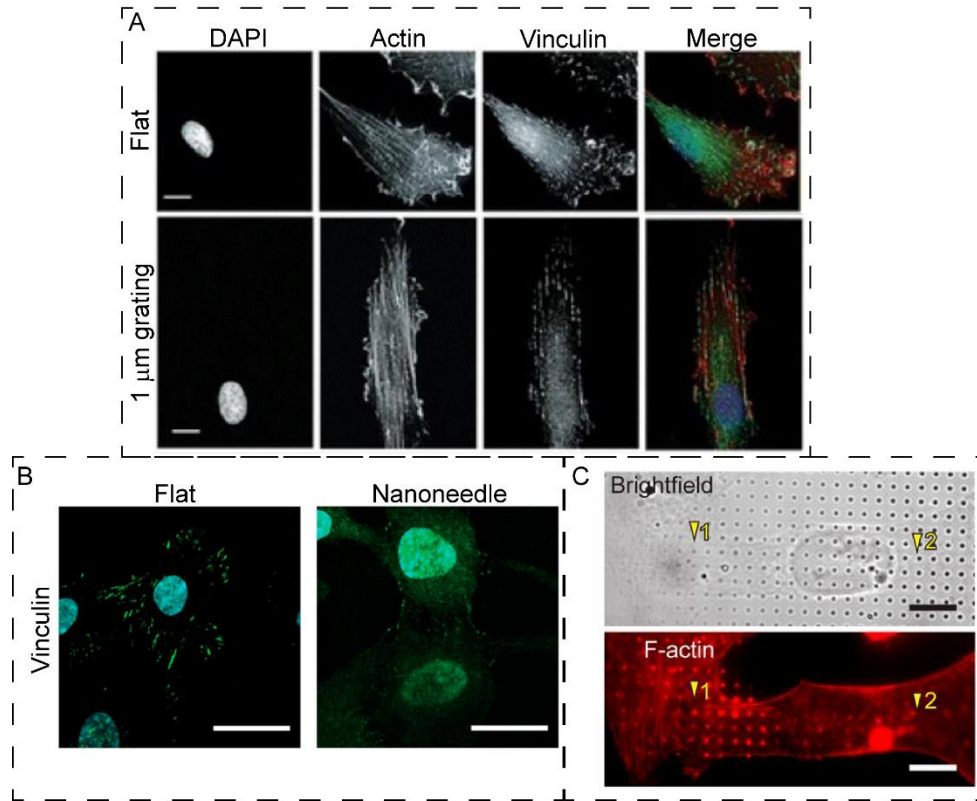


Figure 1.4. Dimension comparison between several biological entities, viruses, proteins, DNA and cells.

### **1.2.1 Engineering cell instructive materials.**

Therefore, the possibility to affect and influence cell functions by externally activating specific molecular events at the cell-material interface, as well as the advancement in material sciences and micro/nano fabrications<sup>15,22,29</sup>, paves the way to the generation of new materials – referred to as *cell instructive materials* – purposely envisioned to impart commands and instructions to the cells above them cultured<sup>30,31</sup>. Among them, patterned surfaces encourage to study the role of topography in cell-material interaction by focusing on single cell machineries. Hereby, careful design of the structures' parameters, considering as influencing the final target system properties *e.g.*, geometry (height, tip-width, and base-width), the spacing between the structures (uniform or uneven) and the composition (*i.e.*, the bulk material), has led to a smorgasbord of different topographies<sup>15</sup>. However, the most studied topographies comprise grooves and ridge<sup>32–35</sup>, grids<sup>36</sup>, upright protrusions and cavities arrays<sup>15,37–40</sup>. Regardless topography-driven response might be cell-specific, as well as depending on feature size and geometry, from the emerging literature, we can extrapolate general trends in cell responses<sup>41</sup>. The immediate consequence of the crosstalk with the underneath patterns leads cells to reshape their **morphology**. Indeed, it is called contact guidance the process by which cells start to polarize and then migrate<sup>34</sup> or hire a ball-like spheroid form<sup>37</sup>. Cellular reshaping process depends on the local topography of the growth surface and sees the succession of mature protein adhesive structures patterning, better-known as focal adhesion (FA), and actin polymerization. Thus, groove/ridge configuration provides a longitudinal direction for FA and actin fibers to co-align, eventually leading to a cell alignment<sup>30,32</sup> (**Figure 1.5 A**). Instead, reduced growth surface provided by pattern with vertical protruding structures is generally accompanied by weak FA formation (**Figure 1.5 B**) and a less organized cytoskeleton<sup>30,37,42</sup>, with actin architectures similar to a ring at the interface with the upright features (**Figure 1.5 C**)<sup>43,44</sup>.



**Figure 1.5. Topography effects on filamentous actin and FA organization.**

(A) Actin cytoskeleton and vinculin spatial organization of human retinal pigment epithelial cells cultured on fibronectin coated substrates (flat and 1  $\mu\text{m} \times 1 \mu\text{m}$  gratings, above and bottom, respectively). Scale bar 10  $\mu\text{m}$ . Adapted from [45]. (B) Discrepancies of FA generation and architecture of HUVEC cells: dense vinculin structures and diffuse fluorescence signal on flat and nanoneedle-structured growth substrates, respectively. Scale bar 25  $\mu\text{m}$ . Adapted from [42]. (C) U2OS cells, cultured on gradient nanopillar array, shows strong filamentous actin accumulation on small diameter nanopillars than large ones. Adapted from [43].

Bearing in mind that actin is an essential component to establish cell shape and cell crosstalk with the nanostructures, numerous works reported the reduction of the total long actin fibers in favor of its accumulation, when the protruding topography relies on the presence of vertical features<sup>42,44,46</sup>. This was the case of vertical hollow oxide nanotubes connected to subsurface microchannels<sup>44</sup>, designed by *Persson et al.* to increase the throughput of the biomolecules injection inside cells. Here, fibroblasts interaction with nanotubes was supported by clustered actin within 24 hours from plating. Similarly, *Hansel et al.* employed vertically oriented porous silicon nanoneedles as powerful tool to target intracellular organelles for studying both molecular and functional consequences of the topography interaction<sup>42</sup>. Here, dense actin rings were localized at the nanostructure's engagement sites. Consisted with the results of the reported

papers, the distribution of actin stress filaments of CHO cells cultured over a silicon nanosponge structures, generated to partially resemble *in vivo* environment, was clustered in a punctuate manner at the contact sites of cell-extracellular topography<sup>46</sup>. Therefore, these examples support the hypotheses that the actin cytoskeleton is significantly affected by surface topography. In this direction, the comprehensive study, conducted by Lou *et al.* shed the light on the molecular origin of the actin machinery and reorganization<sup>43</sup>. Here, the change in the cell PM curvature, due to the interaction effect with geometrically structured surfaces (*i.e.*, arrays of SiO<sub>2</sub> nanopillars and nanobars) was found as precursor of an intracellular signaling cascade that firstly activated the recruitment curvature-sensing proteins (BAR proteins recruiting and accumulation at pillars tips and around nanobar profiles) and then regulated actin polymerization. Where the topography was able to induce a high membrane curvature, actin cytoskeleton appeared preferentially as dot on small-diameter pillars and at the nanobar end, and as ring on large-diameter ones. In addition, the colocalization of FBP17 curvature-sensing BAR protein and Arp2/3 actin nucleators, involved into the formation of branched F-actin, substantiates that resulting PM bending from the interaction with nanostructured surfaces ultimately activates actin polymerization and accumulation through Arp2/3 action (Figure 1.6)<sup>43</sup>.

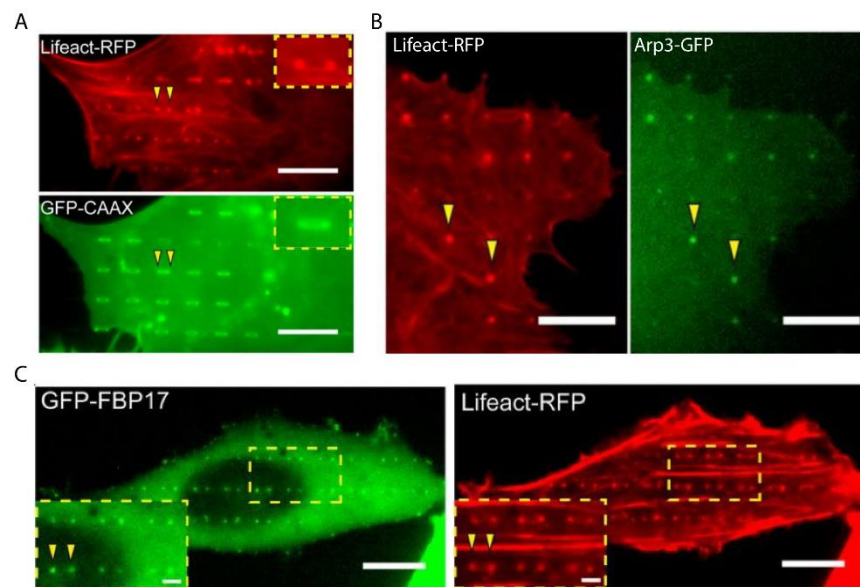


**Figure 1.6. Membrane curvature as topographical hub for actin reorganization.**

(A) U2OS cells co-transfected with Life-RFP and GFP-CAAX (F-actin and PM markers, respectively) show Lifeact-RFP accumulation at the nanobar ends, even distribution of GFP-CAAX along the length of the same nanobar. Scale bar 10  $\mu\text{m}$ . (B) Colocalized actin and Arp3 signals in U2OS cells co-transfected cell with Life-RFP and GFP-Arp3. Scale bar 10  $\mu\text{m}$ . (C) Colocalized actin and FBP17 signals in U2OS co-transfected cell with Life-RFP and GFP-FBP17. Scale bar 10  $\mu\text{m}$  and insets 2  $\mu\text{m}$ . Adapted from [43].

In the light of these results, cell ability to accommodate vertically-aligned structures within its area *via* engulfment events is guaranteed either by PM asymmetry (*i.e.*, curvature) or by filamentous actin (F-actin) reorganization. F-actin might act as stabilizer mean of cellular seal with protruding endogenous materials<sup>6,43</sup>. Simultaneously, the intracellular spatial arrangement of actin, which is supplemented by other cytoskeleton components (microtubules, microfilaments, intermediate filaments and spectrin), might work as barrier to cell access. Synergically with PM, these actin accumulations, on the top and around the stalk of the surface features secure intracellular environment from an easy entrance<sup>47</sup>.

However, considering the active actin network reorganization to the different topography, if these structures are comparable to the cellular scale (*i.e.*, large patterns with tens of micrometres dimensions) it results in a physical confinement of the single cell body. Alternatively, as soon as topographic features size becomes commensurate to sensorial organelles (*i.e.*, filopodia and lamellipodia, as well as protein clustered structured resulting in FA) relevant effects on the processes of surface recognition and adhesion are clearly visible.

Another aspect to consider is the enhanced cell-material coupling, ensuing from the direct interaction with structured surfaces. Single vertical structure locally pushes inward the PM, thus modulating lipid bilayer curvature in a fashion depending on the geometry and size of topographic feature and eventually heightening cellular **attachment**<sup>11,19,28,40,43,47</sup>. As a matter of the fact, the first approach, cells have with the protruding structures embedded in the cell growth substrate is PM-mediated. Far from being a passive component of the cell, not only PM defines the cell boundaries from the extracellular environment, but most importantly it participates to a large variety of essential biological processes, including cell division, migration, morphogenesis, vesicle trafficking<sup>11,28,40,47,48</sup>. Most of these physiologic dynamics cause transients change in membrane bending. However, structured device might induce stable and controlled PM curvature<sup>28,40</sup>. Thanks to the chemical properties of the different lipid components and the intrinsic high flexibility own by the lipid acyl<sup>49</sup>, the PM is able to achieve distinct topologies through the local regulation of its curvature. In these curvature-gymnastics processes, two main configurations might be obtained<sup>11,15,28,48</sup>. Membranous extensions outwards the cell body are classical examples of PM *negative-curvatures* and a hallmark of filopodia or microvilli cases. On the contrary, inward bending of the PM, generally dubbed *positive-curvature*, is the distinctive shaping of the endocytic vesicle budding. If these conformational changes frequently occur *in vivo* conditions to withstand specific cellular needs, the interfacing with *in vitro* structured platforms might ultimately promote those membrane deformations in a controlled fashion<sup>48,50</sup>. Hence, the external membrane protrusion might be considered cellular attempt

to grasp to the substrate features, whilst cells strong affinity to wrap and engulf the protruding nanostructures resembles an attempt to internalize them and adopt a macrophage-like process<sup>11,15,22</sup>. In both configurations, an improvement of the membrane anchorage to the substrate, as well as a reduction of the distance from the material surface of tens of nanometres are achieved. These effects were considered beneficial, and thereby exploitable, both for electrophysiology<sup>6</sup> and drug delivery applications<sup>51,52</sup>. Indeed, topographic structures enables single cell sampling, sub-threshold electrical signals recording and efficient cargoes materials injection<sup>6,39,51,52</sup>.

Loss in the PM symmetry is a result of a coordinated biological machinery between lipids and proteins. Indeed, both proteins harbouring within the PM and extrinsic ones, acting outside the lipid bilayer itself and inside the cytoplasm, contribute to the membrane asymmetry and curvature stabilization<sup>48</sup>. In this scenario, curvature sensitive proteins (*i.e.*, Bin-amphiphysin-Rvs, BAR) and coat proteins, such as clathrin and caveolin-1, are readily recruited during the membrane bending, bound to the internal membrane surface to fulfil a scaffolding role and manipulate PM shape up to micrometre scale<sup>48,53</sup>. Significantly, protein assistance to the membrane curvature becomes increasingly enhanced with monomers oligomerization<sup>53</sup>. According to this protein machineries, nano and microstructures strive to advance our understanding on the possibility to modulate endocytosis rate through the extracellular microenvironment<sup>15,39,47,54</sup>. Local inward pushing forces applied by these structures on cell membrane might directly stimulate vesicle budding and activate the uptake of molecules surrounding the cells, as shown in **Figure 1.7**, by the spatial accumulation of clathrin and dynamin2 proteins which mediate internalization pathways<sup>47</sup>.

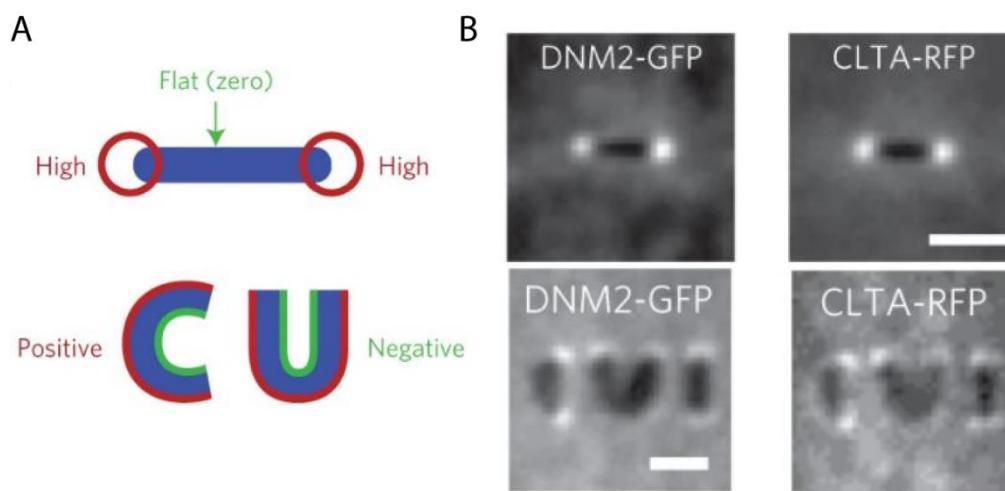


**Figure 1.7. Engineered protruding nanostructures to probe endocytic vesicle accumulation.**

(A) Protruding nanobar and nanoletter design for inducing PM high curvature. (B) Emitted fluorescence signals

from SK-MEL-2 cells cultured on nanobar and nanoletter arrays. Spatial distribution of Dynamin2 and Clathrin proteins with strong preference for high curved regions. Scale bar 2  $\mu\text{m}$ . Adapted from [47].

The best-studied itinerary for the intracellular intake comprises clathrin lattice which surrounds the newly formed vesicle during the whole rearrangement till its final detachment from the PM<sup>53</sup>. This clathrin-mediated-endocytosis (CME) shows a spatial preference on highly positive curved surface over flat<sup>47,54</sup>. Moreover, lifetime monitoring of CME appears to decrease significantly on nanostructures. Conceivably, this finding suggests that topography-induced pre-curved PM might either reduce energy barrier for membrane bending and promote a boost CME turnover<sup>47</sup>. However, alongside the CME, alternative endocytic pathways still work to ensure the uptake of membrane proteins, lipids, extracellular ligands, and soluble molecules. One of these biological motors involves the endocytosis through caveolae, curved PM invaginations of 50 – 80 nm in diameter or with flask shape<sup>55-57</sup>. Although different from CME, caveolae biogenesis occurs as consequence of increased cell surface stress. Moreover, being ligand-triggered, internalization *via* caveolae is an intrinsically selective sorting process related to membrane components that enrich PM rafts<sup>55,56</sup>. Indeed, it was shown that caveolae work as additional reservoirs of bulk PM, that readily release during high mechanical tension to provide membrane protection and minimize potential damages<sup>57,58</sup>.

Beside cell morphology and adhesion, micro and nanomodified surfaces have also been shown to affect **proliferation** profiles of cells cultured on top. Although, from the growing body of the literature, no general tendency might be surmised for cell proliferative states<sup>15,39,59,60</sup>, depending on the topographical scale it might be inferred that microscale surface modification are less profitable to induce high rate of proliferation since the resulting cells physical confinement, large cytoplasmic penetrations, as well as decreased cellular mobility might verify<sup>29</sup>.

Lastly, topographic features are active hubs for determining cell lineage bias and thus inducing the **differentiation** of stem cells tightly engaged on them<sup>15,22,27,30,61,62</sup>. As a matter of the fact, the spatial arrangement, foisted by the topography firstly interferes with the cell adhesion formation, and then directly regulates magnitude and direction of cytoskeleton-generated traction forces to be exerted on nucleus. Under this outside-inside mechanism called *mechanotransduction*, these forces are reasonably broadcasted to the chromosomes, thus altering gene expression (especially the accessibility of the genetic code)<sup>30</sup>.

To sum up, nano and micro-modified surface materials hold a great potential to regulate cell fate by acting on different length scale: at molecular level through the spatial distribution of the adhesive domains,

whereas at macromolecular one by interfering on the cytoskeleton assembly (micrometer scale). Hence, either the FA formation or the cytoskeleton organization are the starting points of a chain of signaling events that ultimately condition most of the aspects of cell life. In this scenario, the regulation of cell fate appears to be highly profitable in different tissue engineering areas. As well as, understanding the mechanisms behind the interplay between surface topography and cellular response represents a pivotal step toward the development of next generation of smart surfaces in regenerative medical devices and implants.

Hitherto, this was particularly true for breast implants, widely used for cosmetic augmentation or post-mastectomy breast reconstruction<sup>63</sup>, for all the different endo-osseous systems<sup>64</sup>, and even for bioelectronic neural interfaces<sup>65</sup>. As result, tissue ingrowth into textured surfaces increased compared with smooth surface implants cases.

### **1.3 Characterization of cell-material interface.**

As mentioned earlier, the interest in designing active platforms that better interact and perform *in situ* with biological host, has become a challenge in several fields, including tissue engineering, bioelectronics, regenerative medicine. The interplay occurring at the interface between living cells or tissue and artificial materials is decisive to determine both device performance and ultimately biological response<sup>66</sup>. In this context, the characterization and the analysis of the interfaces between cell and endogenous materials have become of foremost importance<sup>22</sup>. As already discussed, this was especially true in bioelectronics field, where the distance established between sensing electrode and biological entities drastically affects the overall performance of the electric devices<sup>6,10,14,22</sup>. Hence, several techniques for the observation of the interface have been set to directly measure and quantify the cell/substrate distance, spacing in either optical or electronic microscopy. However, equally important, in the study of the interaction between bioelectronics device and cells, are the evaluations of the biological processes occurring at the interface between the two. Therefore, preferential contact points, PM ruffling, high positive membrane curvature and engulfment events, might give information of modulated adhesion cells established with the growth substrate underneath.

For instance, surface Plasmon Resonance imaging (SPRi) has emerged as a label-free optical technique for single entities detection with size ranging from micrometers down to nanometers. SPRi relies on the interaction of an incident p-polarized monochromatic light beam at a metal-dielectric interface and the resulting generation of an oscillating free electrons wave, following the optic laws. Any subtle refractive index differences, at this interface, cause a gradual decrease of the reflective light intensity, which is

promptly recorded by a camera<sup>67</sup>. The reflected light profile is then analyzed to reconstruct the 3D structure of the interface with high sensitivity. In live cell imaging, SPRi has been harnessed to quantify cell-substrate distance in migrating cells, during cell adhesion or dynamic cellular processes<sup>12,13,67</sup>. Depending on the surface functionalization of the materials, cells can adhere with different contact types, thus varying substrate distance from 30 nm in lamellipodium state, down to 10-15 nm in focal contact<sup>68</sup>, respectively. Thereby, SPRi might measure the cleft gap distance by mapping point by point cellular basal PM in contact with the growth substrate or the sitting patterns (**Figure 1.8 A**)<sup>67</sup>. Moreover, cellular adhesion intensity might be gauged through SPRi due to the heterogeneous force distribution around the cell membrane. A promising study was conducted by Toma *et al.* to quantify the distance between human embryonic kidney 293 (HEK293) cells on Au films, functionalized with different coatings (poly-L-lysine, fibronectin, laminin) compared to bare case<sup>12</sup>. Larger distance from the substrates corresponds to weakly adherent cells, which arise when cells were cultured on bare Au or laminin-functionalized substrate. On the contrary, poly-L-lysine and fibronectin coatings show significantly reduced gap distance (~37 nm and ~70 nm, respectively), thereby cells adhere tighter to the substrate<sup>12</sup>. Thereafter, the same research group carried a cell-substrate distance investigation *via* SPRi to dynamically follow the gap thickness variation during the contraction-relaxation cycle of iPSC derived cardiomyocytes<sup>13</sup>. By scanning the cell region during the contraction-relaxation period, the maximal distance from the substrate was ascribed to the relaxed state, instead minimal gap thickness was achieved during contraction<sup>13</sup>.

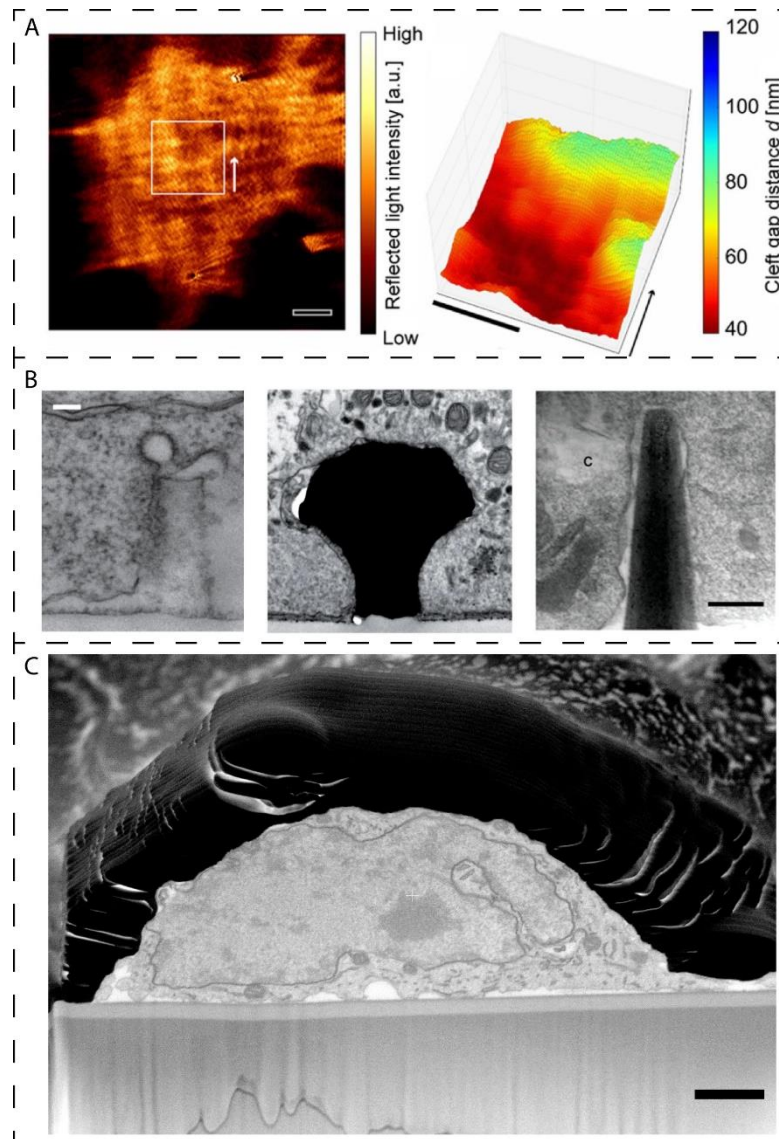


**Figure 1.8. Characterization of the cell-material interface.** (A) Distance measurement between HEK293 cells and poly-l-lysine (PLL) coated substrate gathered with lens imaging type surface plasmon microscope on the left and scanning localized surface plasmon microscope. Scale bar 5  $\mu\text{m}$ . Adapted from [12]. (B) TEM images of cell material interaction. On the left: SK-MEL-2 plasma membrane wrapping around a nanopillar captures a clathrin-coated pit. Scale bar 100 nm. Adapted from [47]. In the middle: gold mushroom-shaped microelectrodes engulfed by Aplysia neurons. Adapted from [6]. On the right: micrograph of thin section achieved *via* focused ion beam lift-out (see below). Scale bar 200 nm. Adapted from [39]. (C) Scanning electron micrograph of exposed interaction between cortical neuron and growth substrate achieved *via* SEM/FIB (see below). Scale bar 1  $\mu\text{m}$ .

Other optical methods to study the vertical distance between lipid membrane and reflective substrates is *via* fluorescence interference-contrast (FLIC) microscopy<sup>69,70</sup>, which requires biological cells to be fluorescently labelled. Here, fluorescent cells cultured on reflective substrate are stimulated by an incident light which interfere with its reflective contribution. Change in intensity contribution from the fluorescent cells are function of the distance from the reflective layer. Any small changes in PM-material distance might be identified with a high precision ( $\sim$  few Å)<sup>22</sup>.

If SPRi and FLIC strictly condition the material choice of the supporting platforms to reflective one, altogether the application of these optical techniques is hindered by the presence of micro-structures embedded onto the surface or in 3D complex systems case. Therefore, alternative powerful characterization techniques are needed to offer efficient screening at nanometer resolution of cell–material interactions.

### ***1.3.1 Electron microscopy for nanometer resolution of the cell-material interface.***

Promising results were achieved by using electron microscopy which provides the most unambiguous visualization of the cell–nanostructure interface<sup>15,22</sup>. Transmission electron microscopy (TEM) has been the first leading methodology to study the structures and functions of cells and tissue at new different levels of resolution: micrometers for the biological architecture (conventional TEM), nanometer for cellular organelles and molecular architectures (cryo-TEM) and near atomic resolution for single molecules (electron crystallography)<sup>71</sup>. Thereby, TEM enables to unravel the cell-material crosstalk with a vertical and lateral resolution down to 2.2 nm (**Figure 1.8 B**)<sup>72</sup>. However, samples must deal with a cogent requirement: they have to be thin enough to allow electrons to cross its fine volume. Therefore, prior to EM imaging, specimens are chemically fixed using aldehydes, stained with heavy metals to enhance the contrast of the intracellular structures, dehydrated and embedded in resin<sup>73</sup>. Once embedded in a bulky polymerized volume, samples are then mechanically trimmed in slices, named lamellae with thickness below 100 nm. Nevertheless, this physical sectioning is incompatible with hard substrates, as metals and semiconductors, often chose as constituent materials in bioelectronics. Thereby, such hard platforms must be removed by chemical (hydrofluoric acid) or physical means (liquid N<sub>2</sub> freeze fracture and sonication) and replaced with fresh resin filler, prior the serial slicing with mechanical knives<sup>22,71–73</sup>. Notwithstanding convincing attempts to characterize cell-material interface have been carried out on planar or structures devices<sup>6,72,73</sup>, the substrate removal might introduce artefacts at the interface, thus invalidating TEM imaging fidelity. One proposal of retaining representative interfacial interaction with minimal artefacts was given by Aslanoglou *et al.* with the introduction of an ultrathin octafluorocyclobutane (C<sub>4</sub>F<sub>8</sub>) film to cover silicon structured

platforms before cell seeding<sup>74</sup>. The non-stick C<sub>4</sub>F<sub>8</sub>-coating nature prevents strong adhesion to the epoxy resin and allows for detachment of Si-based substrates from the resin blocks upon polymerization. However, this operation still stresses the cell-material interface, potentially introducing artefacts. Therefore, a high-energetic ion beam (focused ion beam, FIB) has been explored as alternative sectioning tool to create lamellae for TEM visualization. The FIB enables to selectively etch a large area of interest through a large variety of materials, simultaneously preventing physical separation between cell and substrates and preserving their interaction<sup>11,14,22,40</sup>. The resulting lamellae generated *via* FIB milling is then directly transferred on customized TEM grids thanks to a micromanipulator present in FIB equipment<sup>39</sup>. As shown in **Figure 1.9 A**, to easily withdraw the lamellae from the bulk sample, it is required to excavate forward and backward the region of interest (ROI), thus giving only partial information of the interaction between a single cell interfaced with structured surface. Moreover, the localization of the region of interest (ROI) is very difficult because of the presence of a thick resin embedding layer. Thereby, scanning electron microscopy (SEM) coupled in-chamber with FIB turns out to be more successful than FIB-TEM combination. Indeed, any blind sectioning, usually performed for TEM lamellae generation, or loss of cellular context occur<sup>11,40</sup>.

Dual beam microscopy (with both ion and electron beams) is a promising technique to facilitate the production and investigation of cell-material cross-sections (**Figure 1.8 C**). The high-energy ion beam selectively etches ROI, through a large variety of materials without losing cell position of the support material. At the milling site, the interface is imaged by scanning the surface with the electron beam in backscattered mode. Moreover, by alternating sequential milling phase to electron beam assisted imaging of the exposed slice, three-dimensional rendering of the volume of interest might be represented and reconstructed with automated software<sup>11,22,40</sup>. As powerful tool for complete characterization of cell-material interplay, FIB-SEM requires an accurate preparation of the sample. The preparation of the hybrid systems, namely composed by cells and structured material might be carried out in two ways.

Critical point drying (CPD) was traditionally used for SEM visualization of cellular morphology<sup>22,75</sup>. Here, cell liquid components are gradually exchanged by ethanol to perform a complete dehydration of the cellular structures. Afterwards, the effective transition from wet samples (in ethanol) to completely dry ones is ensured by a hard drying step by which ethanol is gradually replaced with liquid carbon dioxide (CO<sub>2</sub>). CO<sub>2</sub> was inserted in the cells at specific temperature and pressure at which there is a continuity of state between liquid and gaseous phases. In particular, fixing 35° as temperature and 1,200 psi as pressure, CO<sub>2</sub> critical point might be achieved. At this conditions, complete dehydration of the biological structure occurs. Comparing to the bulk resin block produced for either TEM<sup>73</sup> or FIB/SEM sample preparation, here a direct

localization of whole cells on the support material might easily occur. However, the initial cellular volume is not completely preserved since the drying procedure introduces volume shrinkage artefacts. Moreover, cells are structurally weak compared to the one reinforced by resin embedding since the hard drying procedure leaves cavities into cytoplasm, which might cause cell structure collapse (**Figure 1.9 B**).

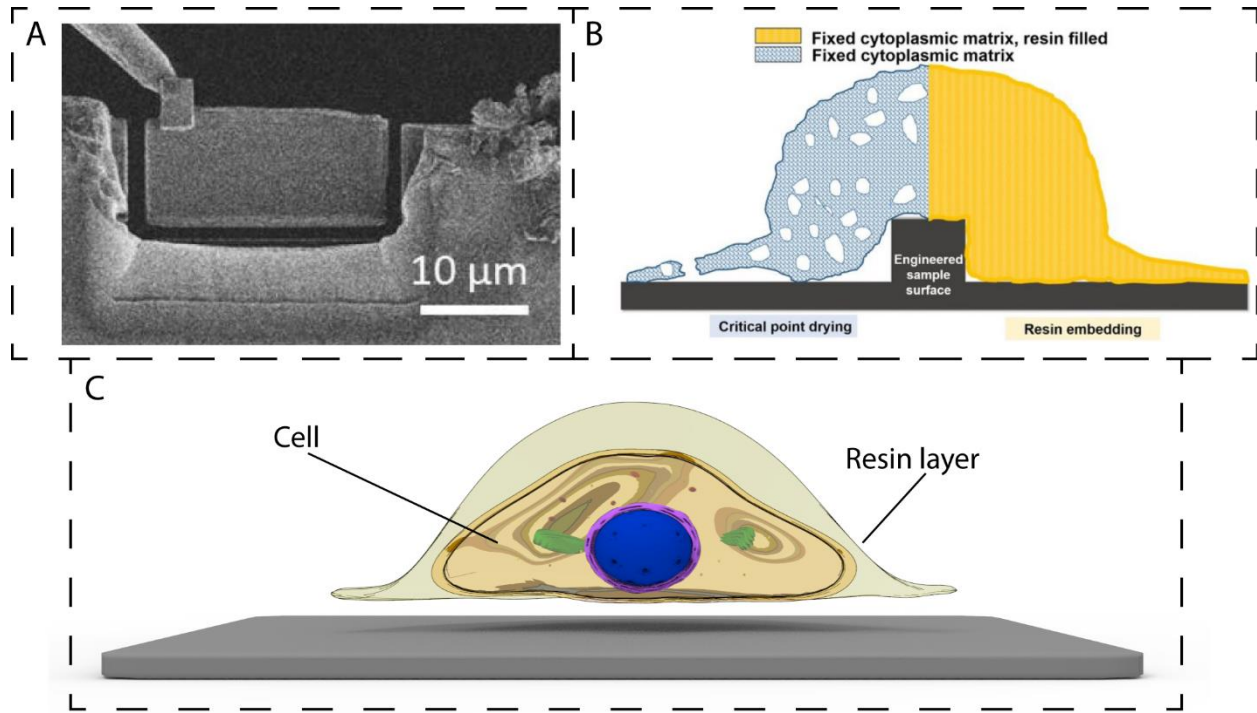


**Figure 1.9. Cross section preparation for EM.** (A) FIB-generated lamellae for TEM imaging. Adapted from [76] (B) Schematic comparison of CPD preparations versus thin-layer resin embedding preparation for scanning electron microscopy. Adapted from [75]. (C) UTP procedure for SEM/FIB image acquisition.

Therefore, by combining CPD sample preparation to FIB-assisted cross-sectioning, no intact cellular ultrastructures might be distinguished. Therefore, to overcome this limitation, a new method named ultra-thin plasticization (UTP), has been developed and optimized to combine the structural support role of the resin with the easy clear visualization of cell morphology, and cell-material crosstalk. As it will be widely explained in the next chapter step by step, the UTP procedure enables to obtain contrasted biological samples thanks to the staining performed with heavy metals, to preserve cellular structure and ultrastructures by the resin embedding, as well as to finely recognize cellular shape through the removal of the resin excess before the polymerization. Therefore, while cells are internally imbued with resin, only a micrometric resin layer covers them, as shown in **Figure 1.9 C**<sup>11,14,40,77</sup>. The winning points of combining UTP

preparation method with FIB/SEM acquisition tool rely on its suitability for every possible hybrid system, which include different cell lines, but more importantly different materials (*i.e.*, from soft up to hardest materials, as well as planar or structured one)<sup>14,40</sup>.

The UTP procedure and SEM/FIB imaging ensured clear characterization of the interaction between cells and electroactive materials, which is essential for the design of new bioelectronics platforms. However, biological processes which occur at the contact points with the structured materials depend on the specific platform pattern, as already explained in **Paragraph 1.2**. Spacing, diameter and height of nano and microfeatures have control on cellular adaption process. Different studies share common results: closely spaced features with large diameter (>300 nm) are not engulfed by the single cell but rather, the cell rests atop the nanopillar array (**Figure 1.10 A**). Therefore, cellular somas are suspended between the adhesive posts. The transition from suspension to engulfment might occur by decreasing feature diameters on equal pitch. Cells adopt a macrophage-like morphology in attempt to internalize the structures. However, any internalization might occur as long as the structures are firmly fixed on the substrate. With more spaced features, PM readily deforms and conformably wrap around protruding architecture (both smaller and larger diameter vertical features), thus touching either the top feature area or the bottom surface between the vertical structures, as shown in **Figure 1.10 B**.

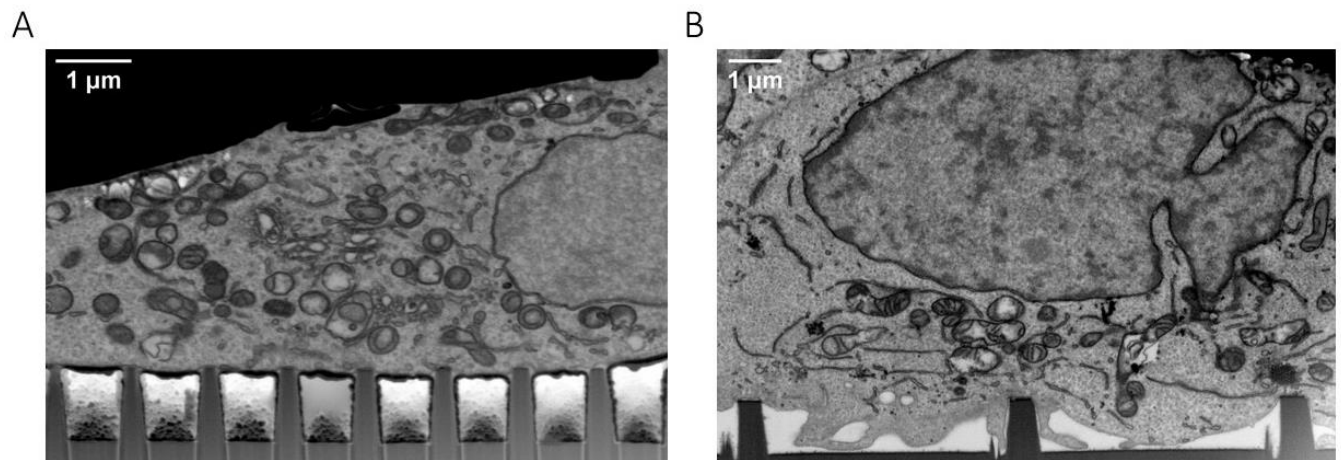


**Figure 1.10. Cell-material interactions comparison depending on the feature-feature distance.**

(A) Smaller pitch corresponds to cellular suspension on the topography. (B) Less dense structures correspond to cellular assumption of macrophage-like morphology.

#### **1.4 Graphene materials for bioelectronics application.**

Among the diverse materials exploited in bioelectronics, graphene was discovered in 2004, as the thinnest possible configuration of carbon molecules. Since that, a long list of graphene applications have been spreading over a wide range of technologies, including future flexible and transparent electronics, barrier materials, printable inks, energy and hydrogen storage<sup>78,79</sup>. All this tremendous interest has been due to its chemical structure, which comprises a flat monolayer of carbon atoms packed into a 2D honeycomb lattice<sup>78,79</sup>. The strong covalent bonds between the carbon atoms (C – C) makes graphene one of the hardest materials ( $\sim 1$  TPa)<sup>80</sup>, and thus appealing as reinforcing filler or as additive to improve mechanical properties of many soft polymers<sup>81</sup>. Alongside the mechanical properties, the  $\pi - \pi$  bonds nature renders graphene an enticing candidate material for miniaturized and high-performance electronic circuit<sup>26</sup>. In this direction, intrinsic high thermal<sup>82</sup> and electrical conductivities (5000 W/mK and, respectively)<sup>79</sup>, as well as ultra-high charge carrier mobility (up to  $200,000 \text{ cm}^2 \text{ V}^{-1} \text{ s}^{-1}$ ) are harnessed<sup>83</sup>. Moreover, thanks to its transparency over the 95% of an incident light or optically adsorption near-infrared range, graphene materials are becoming gradually spotlighted as versatile imaging tools<sup>79</sup>. Finally, several bottom-up and top-down synthesis approaches, such as chemical-vapor deposition (CVD), pyrolysis, chemical exfoliation and laser-induced graphene synthesis, have been developed, even still presenting challenges for controlling resultant microstructures and defect populations.

##### **1.4.1 Graphene-based *in vitro* applications.**

Notwithstanding its excellent properties, graphene-based material has been involved in encouraging *in vitro* biomedical applications only at later stage. As novel promising materials, grave concern on its possible toxic effects, as well as from its derivatives, in physiological environment has risen<sup>84</sup>. Indeed, several studies reported graphene detrimental effects when exposed to adherent or suspended cells, as in the cases of neural PC12 or erythrocytes, respectively<sup>84–86</sup>. In contrast, additional investigations highlight the potential support, graphene might offer to cells under *in vitro* conditions<sup>85</sup>, by providing anchorage spot for a better cellular adhesion, sustaining high cell proliferation<sup>86</sup>, driving differentiation into specific lineage<sup>86,87</sup>, or promoting neural network development<sup>88</sup>, also thanks to its carbon-based nature. Although from the emerging literature mixed findings might be extrapolated, it is worthwhile to note that, final device biocompatibility might be ascribed to the potential presence or absence of impurity or contaminants, arising from the fabrication procedure, on the graphene materials, beside the cell line-specific response. As a matter of the fact, this contamination might have a detrimental effect on cell-material interaction. However, there are procedures for graphene synthesis and transfer able to reduce any possible impurity

and contaminants on the graphene materials. In tandem, stably functionalized graphene-based materials are much less toxic than the unfunctionalized counterparts. Surface functionalization might help in pacifying the strong graphene hydrophobic reaction with cells, as well as in reducing the production of reactive oxygen species which mediates cellular apoptosis<sup>89</sup>. With this in mind, graphene-family materials have been attempted to be used in a variety of biomedical applications, including drug or gene carrier due to the high loading efficiency, in bioimaging, as scaffold component in tissue engineering approach, in bioelectronic devices, or even photothermal therapy for tumour<sup>26,79,89</sup>.

As passive element to be integrated in MEA circuitry, as well as transistor's active layer, graphene material shows its promising properties in bioelectronic applications. MEA devices, fabricated by *Kireev et al.*, were able to record independently network activity of two different electrogenic cell lines, cardiomyocytes HL-1 and rat cortical neurons with a good signal-to-noise-ratio as well as their functionality was validated pharmacologically (**Figure 1.11**)<sup>90</sup>. Complementing to the electrical recording, graphene-based MEA also ensures optical access to the cell culture enabling simultaneous recording of electrical activity and high spatial resolution of Ca<sup>2+</sup> imaging, as reported by *Rastogi et al.*. Similarly, high carrier mobility, graphene materials own, makes them appealing as active layer in FET technology<sup>91</sup>.

Specifically, graphene-based ion sensitive FET were designed, fabricated and produced by Li et al., for direct detection of K<sup>+</sup> ion emitted by U21-MG cells. The sensing performance gathered during the measurements was as promising as the one commercial ion sensitive FET based on silicon<sup>92</sup>.

Recently, different strategies to develop 3D graphene structures have been implemented, aiming to create cell cultures closely resembling *in vivo* counterpart. Synthesis of reduced graphene oxide suspension followed by its organization in 3D structures, for instance, supports first osteogenic differentiation and then bone matrix formation in long-term adipose derived stem cells cultures<sup>93</sup>. 3D graphene-based microenvironments were also obtained by growing graphene on nickel foam, as catalytic substrate, *via* chemical vapor deposition (CVD) process. These structures find appealing applications in therapeutic techniques for treating neurodevelopmental disorder studies or as candidate to support neuronal regeneration<sup>86,94</sup>. Moreover, graphene hydrogels represent also valuable examples of 3D systems which promote osteoinductive effects without the addition of external inducers on cells therein cultured<sup>95</sup>.

All these forms fulfill the general demands of high surface area in bioelectronics, as well as recreate more closely resembling biological structures. However, in all these cases, the graphene flakes or films are lying flat, exposing a 2D surface topology. In this direction, new approaches open up possibilities to leverage the extremely advantageous surface area-to-volume ratio of graphene, by exposing both sides of graphene. These out-of-plane graphene flakes configurations include synthesis of vertically aligned graphene sheet<sup>96</sup>,

produced by thermal decomposition of silicon carbide, as well as vertical carbon nanowalls *via* plasma-enhanced chemical vapor deposition (PECVD). Both these carbon-based arrangements, which generally consist of few-to-dozen graphene layers tethering and standing vertically on planar (2D) substrates, present significantly higher specific surface area compared to flat graphene. Promising applications of carbon nanowalls see them involved in encouraging cell proliferation<sup>97</sup>, as well as improving the performance of microelectrode for neuronal recording and stimulation<sup>98</sup>.

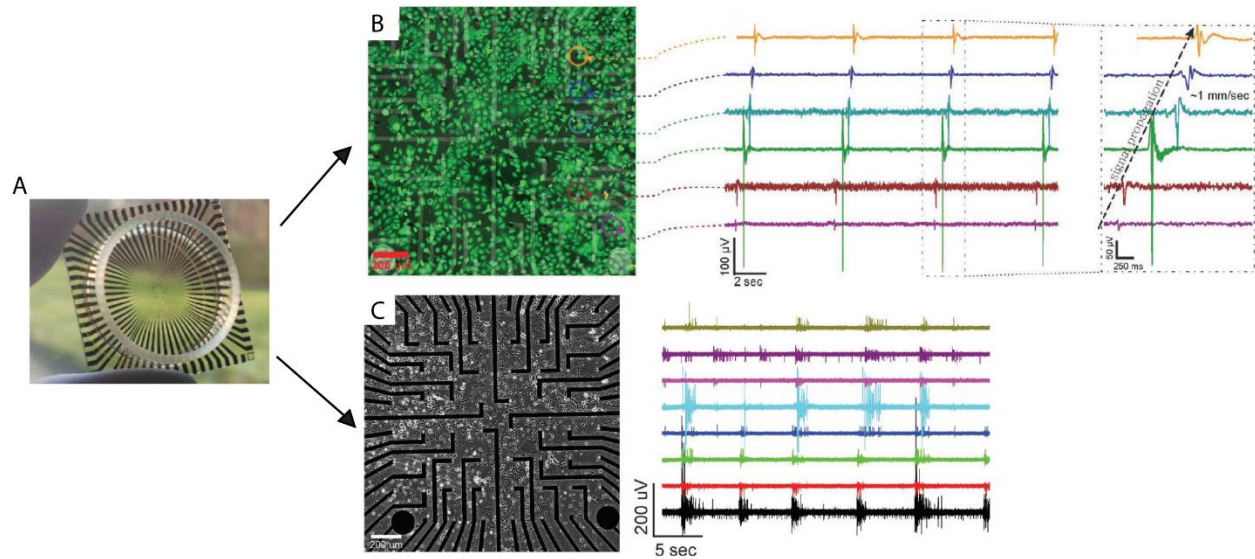


**Figure 1.11. Graphene-based bioelectronics for extracellular measurement.**

- (A) Optical image of graphene-based MEA used as tool for extracellular measurements from HL-1 cells and cortical neurons cultures.
- (B) Electrical recording of HL-1 cell culture from different channels.
- (C) Spiking-bursting activity recording of neuronal culture on graphene-based MEA. Adapted from [90].

## **1.5 Our study**

In this thesis, three different graphene-based topographies, with out-of-plane nature, have been realized as electrode patterns for a new class of *in vitro* MEA. The gimmick of using pseudo 3D structures has come to play a major role in bioelectronic applications, since it aims to increase exposed electronic surface area at the interface with the cells, enhance cell-device coupling and lower the total electrode impedance<sup>6,10</sup>. However, the morphology modification approach to shift from planar to pseudo-3D electroactive surface also matches with need to recreate patterns already present in *in vivo* context for a seamless integration of the artificial device<sup>30</sup>. Thus, inspired by the shapes and geometries present in the native ECM, cells were “tricked” to recognize the graphene-based materials as part of their original environment<sup>30,31</sup>.

The out-of-plane patterns under study were named:

- Three-dimensional fuzzy graphene, **3DFG**, with a nanoscale roughness, aims to mirror ending parts of proteoglycans present in ECM environment or soluble bioactive aggregates (*i.e.*, signalling molecules or protein receptors) released in ECM solution upon proteolysis;
- Collapsed nanowire-mesh template, **NT-3DFGc**, covered with nanoscale fuzzy graphene strives to replicate fibrils-like structures as unfolded/folded collagen filaments that encircle cells *in vivo*;
- Non-collapsed free-standing nanowire-mesh template, **NT-3DFGnc**, covered with nanoscale fuzzy graphene mimics the natural porosity of the tissue ECM where cavities alternate to fibres.

The different graphene topographies were singularly coupled with two different electrogenic cell lines: immortalized HL-1 cardiomyocytes-like cells and chicken embryonic cortical neurons (primary cell line) to study pattern-driven molecular dynamics which might occur after cell-material interaction. Biological responses to local changes in topography were here studied and compared to two planar topographies: one made of single to few-layer of graphene and named **2DG**, whereas the second planar growth substrate is a graphene negative control, made of silicon oxide layer and named of **Si/SiO<sub>2</sub>**.

This thesis strives to advance our understanding of the interaction between electrogenic cells and these specific produced graphene patterns. Following a biomimicry strategy, recapitulating ECM molecular motives through topography is here exploited to improve cell-chip communication. Therefore, biomolecular processes occurring at the interface with electroactive materials were here studied to prove cellular tethering to the substrate.

However, in the first part of the thesis, the different graphene materials were thoroughly characterized by means of Raman spectroscopy, SEM and contact angle analysis, to reveal composition, arrangement and surface properties of the out-of-plane structures, respectively. Physical adsorption of cell-adhesive components on the different materials was used as straightforward biofunctionalization approach to

maximize cellular interaction at the interface. Afterwards, either HL-1 or cortical neurons vitality were systematically investigated at specific days in vitro (DIV), to ensure the biocompatibility of the graphene materials. Cellular responses, as cytoskeleton assembly, FA complexes shaping, activation of endocytic pathways, which all results from membrane curvature deformation at the interface, were comprehensively and independently examined.

If gathered findings from the HL-1 interaction with graphene materials validate the resulting increased in cellular adhesion and its stabilization through actin accumulated structures, cortical neuron adaptation and adhesive processes to the out-of-plane structures underlie an additional effect of enhanced axonal elongation. Therefore, the convincing results will ultimately lead to graphene topographies utilization as electrode topographies, as well as in regenerative medicine since the instructive role exerted on neuronal cells.

## Chapter 2: Materials and Methods.

### 2.1 Out-of-plane graphene synthesis and fabrication.

Graphene materials were synthesized, in collaboration with the Cohen-Karni Lab at the Department of Materials Science and Engineering of Carnegie Mellon University (USA), to achieve three different out-of-plane topographies along with planar graphene, as previously described<sup>99,100</sup>. Therefore, four graphene materials have been employed: planar graphene (**2DG**), three-dimensional fuzzy graphene (**3DFG**), 3D silicon nanowire-template in collapsed configuration (**NT-3DFGc**), and 3D silicon nanowire-template in a non-collapsed configuration (**NT-3DFGnc**).

2DG was synthesized using a copper Cu-catalyzed low-pressure chemical vapor deposition (LPCVD) process. Copper (Cu) foils were chosen as growth catalyst. Before the graphene synthesis, Cu foils were cut into 2 cm x 6 cm and thoroughly cleaned in an ultrasonic bath for 5 minutes followed by an isopropyl alcohol rinse to remove all organic impurities from the surface. Cu foils were dried with nitrogen (N<sub>2</sub>), pre-treated with 5.4 % w/w nitric acid (HNO<sub>3</sub>) solution for 30 seconds, rinsed twice with deionized (DI) water and N<sub>2</sub> blow-dried. The synthesis process was carried out at 1050 °C and 0.5 Torr. The temperature was ramped up to 1050 °C in 15 minutes, followed by a stabilization step at 1050 °C for 5 minutes under argon (Ar) flow of 100 standard cubic centimetres per minute (sccm). The foil was annealed for 1 hour under hydrogen (H<sub>2</sub>) flow at 100 sccm, followed by the synthesis step of 8 minutes under the flow at 50 sccm methane (CH<sub>4</sub>, 5% in Ar) and 100 sccm H<sub>2</sub>. The synthesis process occurs under either the CH<sub>4</sub> or H<sub>2</sub> flows, where CH<sub>4</sub> is a carbon precursor gas, whereas H<sub>2</sub> acts as co-catalyzer and helps during the formation of bound carbon (C) species<sup>101</sup>. Afterwards, samples were rapidly cooled from growth temperature down to 100°C in 30 minutes while flowing 100 sccm Ar. Considering that graphene layer would grow on both Cu foil sides, only one layer was saved from the transfer procedure, which occurs *via* a wet etching process. Therefore, one layer of graphene was coated with 200 nm of polymethylmethacrylate (PMMA) to mechanically support the newly synthesized graphene and protect it from the subsequent steps. Instead, the other layer was etched for 15 minutes at 150°C using UV-ozone cleaner. The remaining exposed Cu-foil was wet-etched in a solution containing 25% w/w ferric chloride hexahydrate (FeCl<sub>3</sub>.6H<sub>2</sub>O), 4% w/w hydrochloric acid (HCl) acid and 71% w/w deionized (DI) water. At the end of the etching process, the PMMA supported graphene film was cleaned with DI water and rinsed for 3 times. Afterwards, graphene-PMMA stack was transferred to a Si/SiO<sub>2</sub> sample. The Si/SiO<sub>2</sub> substrate consists of a silicon (Si) substrate with a 285 nm wet thermal oxide (p-type, 0.001-0.005 Ω-cm), that before the graphene deposition were cleaned with acetone in an ultrasonic bath for 5 minutes, subsequently washed in isopropyl alcohol and finally N<sub>2</sub> blow-dried. The PMMA-

graphene-substrate stack sample was air-dried overnight and then baked in the oven at 150 °C for 30 minutes. Afterwards, the PMMA support was dissolved in acetone at 60 °C for 30 minutes. Finally, the samples were annealed at 300 °C for 1 hour under 10 sccm H<sub>2</sub> at ambient pressure to remove polymer impurities from the graphene surface.

3DFG was synthesized using plasma enhanced chemical vapor deposition (PECVD) process. An induction coil was added to the quartz tube in the CVD system to generate inductively coupled plasma using a 13.56 MHz radiofrequency (RF) power supply (AG 0313 Generator and AIT-600 RF, power supply and auto tuner, respectively, T&C Power Conversion). A 1.5 cm x 1.5 cm Si/SiO<sub>2</sub>, namely, Si substrate with a 600 nm wet thermal oxide (p-type,  $\leq 0.005 \Omega \text{ cm}$ ) sample was cleaned with acetone and isopropyl alcohol in an ultrasonic bath for 5 minutes each, and then N<sub>2</sub> blow-dried. The temperature was ramped up to 800 °C in 13 minutes, followed by a stabilization step at 800°C for 5 minutes, under a flow of 100 sccm Ar. The synthesis process was carried out for 30 minutes at 800°C and 0.5 Torr under the flow of CH<sub>4</sub> with partial pressure of 25 mTorr. The plasma power was kept constant at 50 W. Finally, the plasma was shut down after the synthesis step and the sample was rapidly cooled from growth temperature to 100°C in 30 minutes under 100 sccm Ar flow.

Collapsed and non-collapsed nanowire-templated 3D fuzzy graphene (NT-3DFG c and nc, respectively) were fabricated starting from Si nanowires (SiNWs) growth process, as previously reported<sup>99</sup>. Here, gold nanoparticles (AuNP) were exploited as catalyst of the vapor-liquid-solid (VLS) growth process. A 1.5 cm x 1.5 cm Si/SiO<sub>2</sub> sample, namely, Si substrate with a 600 nm wet thermal oxide (p-type,  $\leq 0.005 \Omega \text{ cm}$ ) was cleaned with acetone and isopropyl alcohol in an ultrasonic bath for 5 minutes each, and then N<sub>2</sub> blow-dried. The substrate was placed in a UV-ozone system for 10 minutes at 150°C, then, functionalized with 400  $\mu\text{L}$  of 4:1 DI water : poly-L-lysine (PLL) (0.1% w/v) for 8 minutes. Following this step, the substrate was gently washed 3 times in DI water and N<sub>2</sub> blow-dried. An AuNP suspension, made of 450  $\mu\text{L}$  of 30 nm AuNP solution, was dispersed onto the PLL coated substrate for 8 minutes. The substrate was gently washed 3 times in DI water, N<sub>2</sub> blow-dried and introduced into a custom-built CVD setup. Once the baseline pressure of  $1 \cdot 10^{-5}$  Torr was reached, the temperature was ramped up to 450°C in 8 minutes, followed by a stabilization step of 5 minutes. Nucleation was conducted at 450°C for 15 minutes with 80 sccm H<sub>2</sub> and 20 sccm SiH<sub>4</sub> (10% in H<sub>2</sub>) at 40 Torr. This was followed by a growth step under 60 sccm H<sub>2</sub>, 20 sccm SiH<sub>4</sub> and 20 sccm PH<sub>3</sub> (1000 ppm in H<sub>2</sub>) at 40 Torr for either 100 minutes (for NT-3DFG c samples) or 5 minutes (for NT-3DFG nc samples). The sample was then rapidly cooled down to room temperature at base pressure. Afterwards, collapsed wires in NT-3DFGc materials were kneeled over by flowing liquid N<sub>2</sub> into the CVD quartz tube under 200 sccm Ar flow to form a NW mesh. The system was then evacuated to base pressure

followed by mesh annealing step at 800°C under 200 sccm H<sub>2</sub> flow at 1.6 Torr for 10 minutes and finally rapidly cooled to room temperature. The annealed samples with collapsed wires were then introduced in the PECVD system followed by 3DFG synthesis that provided a fuzzy graphene coating on the collapsed NW mesh.

On the contrary, NT-3DFGnc samples were directly introduced in the PECVD system for the 3DFG coating synthesis, without performing other steps. Therefore, NWs in NT-3DFGnc remain freestanding.

## **2.2 Substrate characterization.**

### **2.2.1 Scanning electron microscopy.**

SEM imaging of the graphene materials was carried out using a ULTRAPLUSS ZEISS field emission gun (FEG) microscope equipped with secondary and backscattered electrons detectors. The samples were imaged fixing the acceleration voltages in the range 5-20 kV and a working distance of 8-30 mm. The samples were not coated with a conductive coating prior to imaging.

### **2.2.2 Raman spectroscopy.**

Raman spectroscopy was performed by NT-MDT NTEGRA Spectra (100X objective) using 532 nm excitation. Laser power of 2.38 mW was used, and the spectra were recorded with an acquisition time of 30 seconds. For G dispersion (Disp(G)) calculations, Raman spectra of each point were acquired using dual lasers- 532 nm and 633 nm (2.38 mW for both wavelengths).

### **2.2.3 Contact angle measurements.**

A wettability assay was performed to evaluate the hydrophobicity/hydrophilicity behaviors of the different graphene materials, as well as modifications in their wetting state after surface functionalization. Therefore, contact angle static measurements were performed with a video contact angle system (VCA). In particular, surfaces treated with cell-adhesive solutions were rinsed in phosphate-buffered saline (PBS) and allow to dry before the analysis. A 1.5 µL-DI water droplet was dropped onto the sample and the images were taken 5 seconds after the water droplet landing onto the sample surface. Contact angle values were determined with the use of AutoFAST Imaging Software (AST Products). Contact angle classifications are summarized in **Table 2.1**.

**Contact angles**

Value [°]	Nature	Effect
$\theta_c = 0$	Superhydrophilic	Droplets spread becoming as surface film
$0 < \theta_c < 90$	Hydrophilic	Droplets spread out on the surface
$90 < \theta_c < 120$	Hydrophobic	Droplets bead-up
$\theta_c > 120$	Superhydrophobic	Droplets highly bead

**Table 2.1. Contact angle classification.**

## 2.3 Substrate preparation for cell cultures.

### 2.3.1 Cleaning and sterilization.

Graphene-based and Si/SiO<sub>2</sub> substrates were first immersed in water for at least 3 minutes, and subsequently washed with 70% ethanol for at least 10 minutes. The solution was then gradually replaced with DI water to ensure that ethanol solution was completely removed. Samples were dried under a laminar flow of a biological sterile hood and further exposed to UV light for 1 hour.

### 2.3.2 Substrate functionalization.

Samples surfaces were functionalized prior to cells' plating *via* cell-adhesive solutions casting which are:

- Fibronectin/gelatin solution: used for cardiomyocytes-like HL-1 cells culture. The solution is made of 1 mL of sterilized water, 100  $\mu$ L of 0.2% porcine gelatin and 10  $\mu$ L of 0.1% fibronectin (fibronectin final concentration ( $C_f$ ) is 0.01%). The protein coating was then removed and washed with PBS. The type of interaction between cells and coated platforms relies on the cellular recognition of fibronectin domains, since it is a protein present in the original ECM environment<sup>102–104</sup>.
- Poly-L-lysine (PLL, molecular weight 30000-70000): used at 0.1% w/v in water for primary neural culture. After the incubation, the cell-adhesive coating was then removed and washed with PBS. The type of interaction between cells and platforms relies on electrostatic attraction. Polycationic molecules present in poly-lysine were adsorbed on the surfaces and combined with the anionic sites on cell membrane.

## 2.4 Cell Culture.

### 2.4.1 HL-1 cardiomyocytes-like cell line.

HL-1 cell culture was carried out following the conditions reported by Claycomb *et al.*<sup>105</sup>, to preserve longer cell phenotype and their contractile activity.

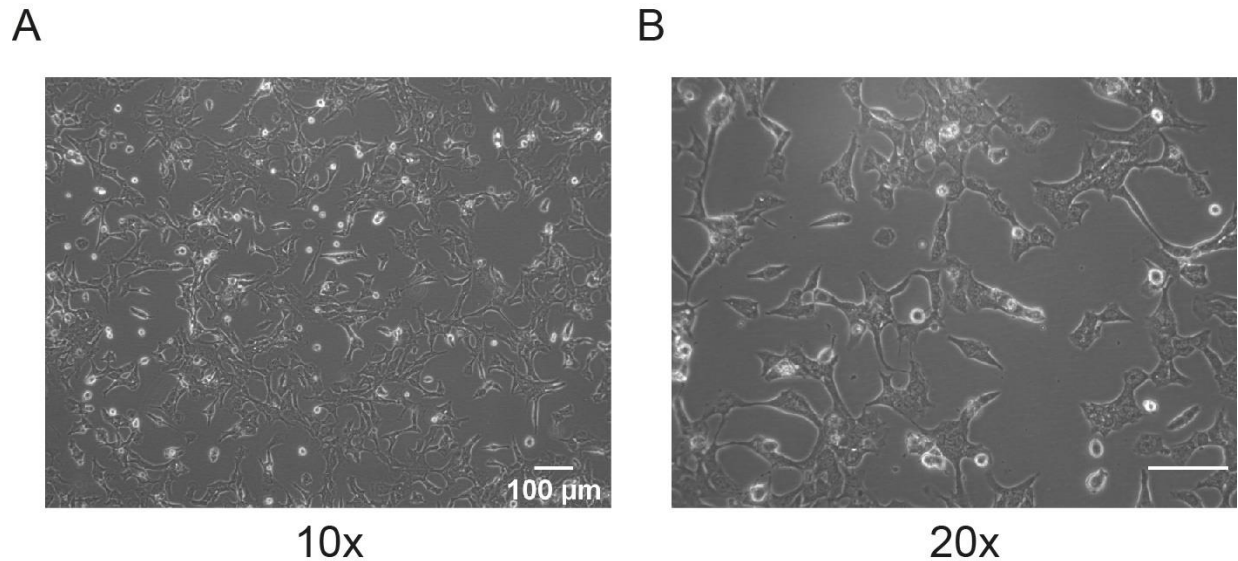


**Figure 2.1. HL-1 cell culture.**

Brightfield micrograph of cells after 1 DIV at 10x (A) and 20x (B) magnification.

Frozen cells were thawed and plated on fibronectin/gelatin coated T25 flask/substrate (see **Paragraph 2.3.2**). Cells were maintained in supplemented media containing Claycomb medium, 10% of fetal bovine serum, 1% penicillin-streptomycin ( $C_F = 100$  units penicillin/mL and  $100 \mu\text{g}$  streptomycin/mL), 1% L-glutamine ( $C_F = 2\text{mM}$ ) and 1% norepinephrine solution ( $C_F = 0.1 \text{mM}$ ). The norepinephrine solution, used to induce cells contraction, was obtained by mixing 30 mM acid ascorbic aqueous solution (0.59 mg of acid ascorbic in 100 mL of DI water) and 160 mg of norepinephrine powder. The mixture ( $C_F = 10 \text{mM}$ ) was then filtered with a  $0.22 \mu\text{m}$  syringe filter. The supplemented media was prepared and stored under light-shielding conditions. During cell culture, the medium was changed approximatively every 2-3 days and cells were grown in the incubator at  $37^\circ\text{C}$ , 5%  $\text{CO}_2$  and 95% humidity.

**Figure 2.1** depicts a brightfield micrograph of HL-1 cells on functionalized glass after 1 *day in vitro* (DIV) at two magnifications 10x (in **Figure 2.1 A**) and 20x (in **Figure 2.1 B**). When cells reached 80% confluency, they were gently detached using 0.25% Trypsin-EDTA with an incubation of 5 minutes at  $37^\circ\text{C}$ , 5%  $\text{CO}_2$  and 95% humidity. Cells were observed under a microscope to ensure their detachment from the substrate. Pre-warmed complete growth media was added to the cell suspension in Trypsin with two-fold higher volumes

to inactivate the enzymatic action and the whole cell suspension was then transferred into a tube for centrifugation with 1200 rotation per minute for 5 minutes. The supernatant was then removed, and the cell pellet was resuspended in pre-warmed complete growth medium. Cell density of viable cells was determined by using Countess™ II Automated Cell Counter for the plating. According to their growth rate, HL-1 cells were maintained and split at 80-85% confluency every 3-5 days.

Final cell density was established according to the specific experiment. Therefore, for single cell analysis, as in the case of cytoskeleton/adhesion or endocytosis investigation, cells were cultured with 60 % density (~21,000 cells/cm<sup>2</sup>). For cellular network investigation, as in the case of Ca<sup>2+</sup> investigation, HL-1 were plated with 85 % density (~ 100'000 cells/cm<sup>2</sup>).

#### **2.4.2 Primary cortical neurons.**

Primary cortical neurons were obtained from excised chicken embryo brain. Therefore, fertilized eggs were purchased from Charles Rivers company and incubated for 9 days at 37°C. The egg content was verified by illuminating it with a candler, prior to the dissection. Typically, when a chicken embryo is developed, the eggs look darker and blood vessel are visible as depicted in **Figure 2.2 A** and **B**. The egg content was then poured into a Petri dish after a mild cracking. A schematic image of the egg content is shown in **Figure 2.3**. The embryo was first washed in Hibernate™-A buffer to remove additional yolk and amniotic fluids. With the help of fine and sharp tweezers, the chicken was placed under a stereomicroscope keeping the tissue always on ice (**Figure 2.4**).

The chicken head was firstly teared with tweezers. Albeit the brain is enclosed by skin, skull and meninges are clearly visible. The entire brain was then isolated, and the cortex hemispheres were collected considering their anatomical localization from previous study, (**Figure 2.4**)<sup>106</sup>. The cortex is carefully inspected to remove possible cloaked blood, which might later contaminate the neuronal culture. Cortices were collected in a 15 mL tube with fresh Hibernate buffer solution and left on ice until the digestion step. Tissues were then digested in 1 mL of 0.25% Trypsin-EDTA at 37°C, 5% CO<sub>2</sub> and 95% humidity for 20 minutes. Afterwards, digested tissues in trypsin solution were transferred in a 2 mL microtube and the tissue was let settle down. The supernatant was discarded and replaced with 1 mL of pre-warmed Neurobasal™ medium supplemented with 1% B-27™ supplement, 1% L-glutamine (C<sub>F</sub> = 2mM) and 0.2% penicillin-streptomycin (C<sub>F</sub> = 20 units penicillin/mL and 20 µg streptomycin/mL). The tube was manually swirled for 10 times and then the tissue was let settle down. The supernatant was discarded, replaced with pre-warmed supplemented Neurobasal media and the procedure was repeated 3-4 times to completely remove trypsin from the tissue solution. The tissue was then mechanical triturated by a gentle pipetting

(with either 1000  $\mu\text{L}$  and 200  $\mu\text{L}$  plastic pipettes). The number of viable cells was determined by using Countess™ II Automated Cell Counter for the automatic counting and the desired cell density was plated on 0.01% Poly-L-Lysin coated substrates. Considering that each investigation was focused on the single neuron, cells were cultured with a low density (20'000 cells/cm<sup>2</sup>).

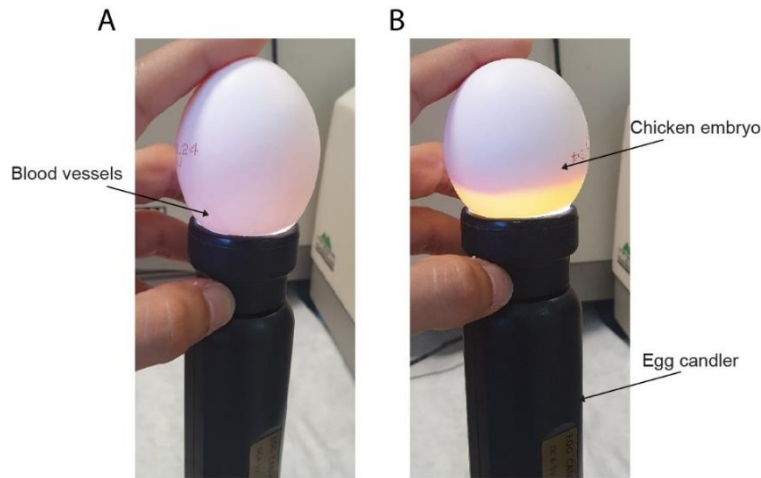


**Figure 2.2. Egg content visualization.** Egg candler is used to check whether the chicken embryo is going to develop. If the egg is yellow, the egg does not have any embryo inside. Darker tissues and visible blood vessels indicate a developed embryo.

Cells were let adhering for 3 hours and then cell media was completely exchanged. Every 3 days, Neurobasal medium was refreshed by exchanging half of the volume with fresh media to remove cellular metabolites and provide fresh nutrients. **Figure 2.5** shows the outgrowth of neuronal cells in the first 3 DIV. After 3 hours from plating (stage 1: initial attachment), neurons mainly have a spherical shape with several lamellipodia and thin filopodia, as shown in **Figure 2.5 A**<sup>107,108</sup>. After 1 DIV (stage 2: neuritogenesis), lamellipodia protrude forward and immature neurites start to extend: here, one neurite would spin off to form the axon (**Figure 2.5 B**). After 3 DIV, neurons become polarized since the axon developing and the remaining neurites arborize into morphologically distinct processes (**Figure 2.5 C**).

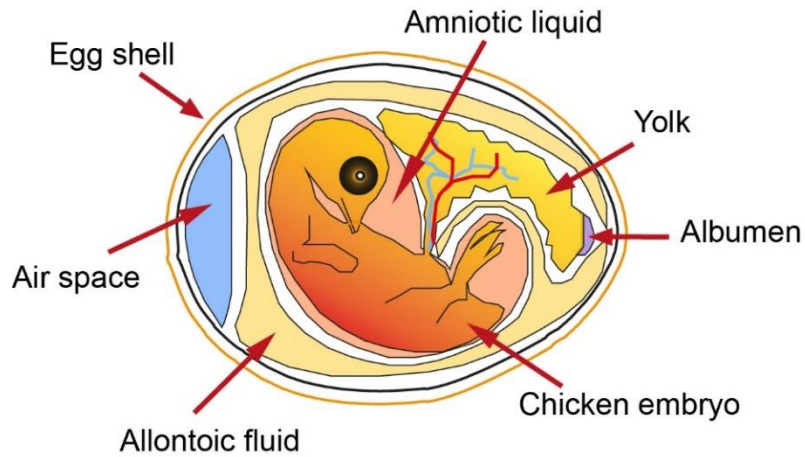


Figure 2.3. Schematic of a fertilized egg content after 9 days from the incubation.

The yolk sac supplies food materials for the embryo body. The thin membrane of amnion surrounds the embryo and provides for protection. The albumen is the main source of protein for tissue synthesis<sup>109</sup>. The allantoic fluid works as reservoir for waste and is engaged in the oxygenation of the embryo. The air cell serves for the pulmonary respiration once the chick is ready to inhale (at day 20).

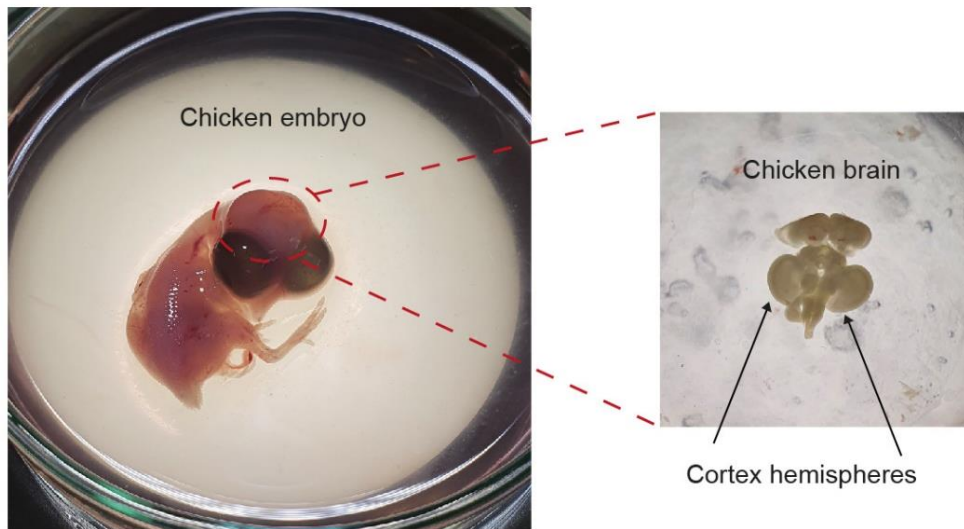
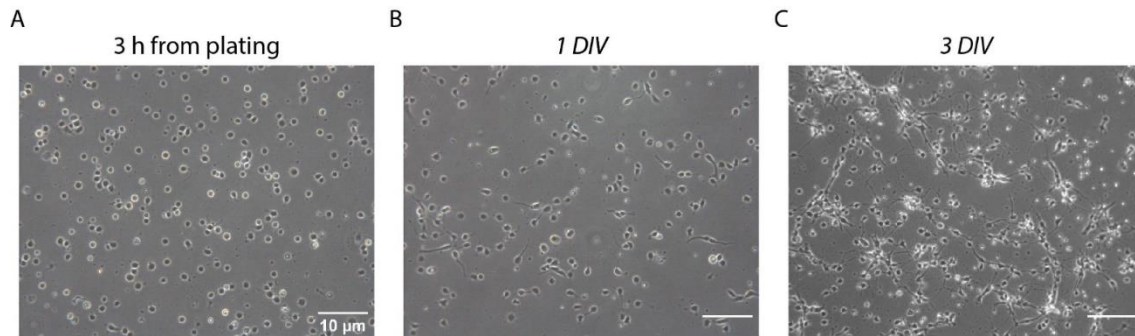


Figure 2.4. Chicken and brain dissection. After 9 days of incubation, chicken embryo was dissected and its brain removed from the skull.



**Figure 2.5. Cortical neurons morphogenesis from plating to 3 DIV.**

(A) Cortical neurons after 3 hours *in vitro* with spherical shape. (B) After 1 DIV, cortical neurons start to lose the spherical symmetry. (C) At 3 DIV, neurons mature with extended axon, and arborized dendrites.

## 2.5 Biocompatibility assay and cellular electrophysiological activity.

### 2.5.1 *Toxicity assay.*

Substrates cytotoxicity and cells viability were evaluated by a live/dead assay using Calcein acetoxymethyl (Calcein-AM) and Ethidium Homodimer dyes after 1 DIV for HL-1 cell culture and after 3 and 5 DIV for cortical neurons culture. Calcein-AM is a non-fluorescent cell-permanent dye that selectively labels living cells. Here, once incubated in cell culture, the calcein-AM is converted in green-fluorescent calcein after the hydrolysis of acetoxymethyl ester by intracellular esterases. Calcein is well-retained in the cell cytoplasm and once excited at  $\lambda_{EX}$  488 nm, it fluorescently emits in  $\lambda_{EM}$  495/515 nm wavelength range. On the contrary, ethidium homodimer is a cell-impermeable dye used to detect dead or apoptotic cells through DNA-binding,  $\lambda_{EX/EM} = 528/617$  nm. After removing the culture media and wash the cells with PBS, the staining solution ( $C_F = 1 \mu\text{g}/\text{mL}$  for Calcein AM and  $1 \mu\text{g}/\text{mL}$  for Ethidium Homodimer) was added to the cell culture and incubated for 15 minutes at 37°C, 5% CO<sub>2</sub> and 95% humidity. Afterwards, cells were rinsed in PBS for de-esterification of the intracellular AM esters and images were acquired at microscope.

Exemplary frames of live and dead cells are shown in **Figure 2.6, A and B**, respectively.

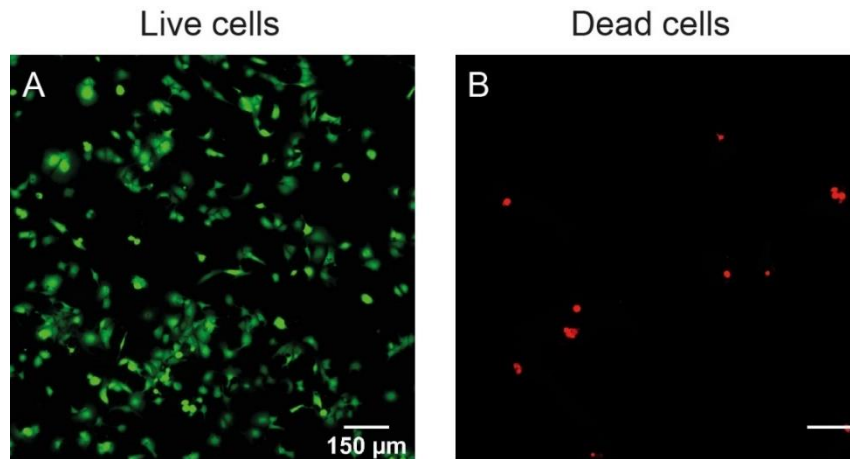


**Figure 2.6. Live/dead cells labelling.** Exemplary micrographs of HL-1 cells labelled with (A) Calcein-AM and (B) Ethidium Homodimer.

### 2.5.2 Calcium imaging.

HL-1 cells electrical activity was studied by monitoring intracellular calcium ions dynamics. Therefore, HL-1 cells at 85% confluency were washed with PBS and then loaded with 2  $\mu\text{M}$  Fluo-4 AM as final concentration in PBS for 30 minutes at cell culture conditions. Fluo-4 AM is a membrane-permeable dye, exhibits a large fluorescence intensity increase on binding free  $\text{Ca}^{2+}$ . After the incubation time, cells were washed in PBS for de-esterification of the intracellular AM esters and incubated again for 30 minutes with standard culture media prior to image acquisition. Exemplary time-sequential images of cells labelled with Fluo-4 AM are shown in **Figure 2.7**. Here, the  $\text{Ca}^{2+}$  wave propagates from the upper part of the objective field of view to the bottom part, as it indicates by the red arrows.

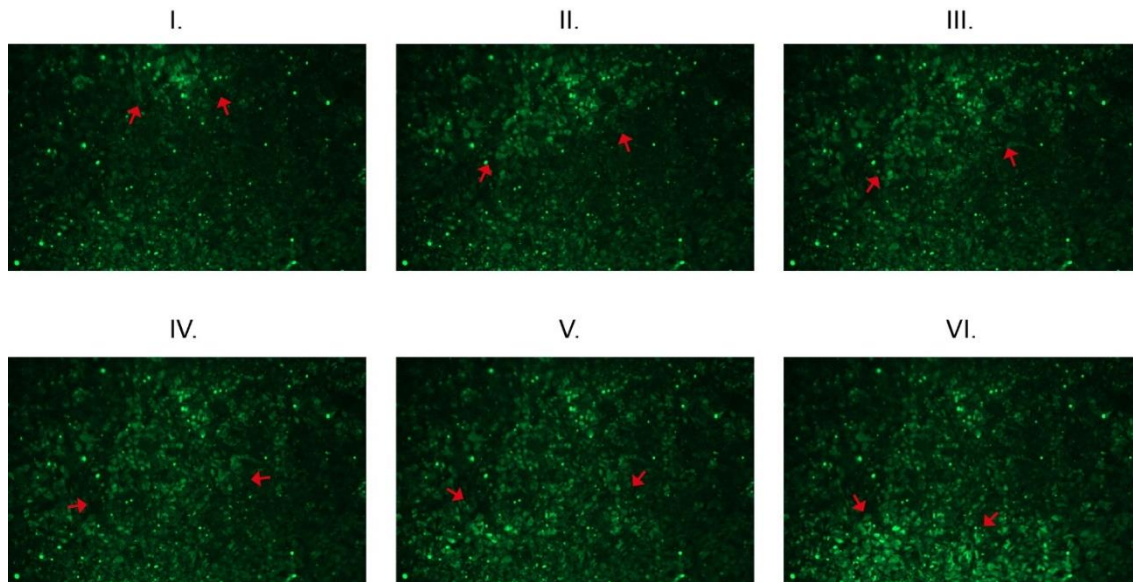


**Figure 2.7. Exemplary images of the  $\text{Ca}^{2+}$  wave propagation.** Wave propagation through a confluent layer of HL-1 cells. Each frame was acquired after 0.10 s.

## **2.6 Immunohistochemistry.**

The immunolabelling procedure provides the detection and spatial localization of a protein of interest within a cell. It is generally performed by using antibodies which bind cellular targets with high specificity and, simultaneously, may be conjugated with fluorescent tags for optical tracing.

At the desired time point for the investigation, the cell culture media was removed and washed once with warm PBS, to remove dead cells or debris in suspension. Then, cells were fixed with pre-warmed 4% paraformaldehyde (PFA) in PBS (pH 7.2) for 10 minutes and then gently washed 2 times with PBS at room temperature. Cell membranes were permeabilized to provide antibody access to targets into the nucleus or other organelles with 0.1% Triton-X 100 in PBS for 5 minutes at room temperature and then washed 2 times with PBS. To prevent any non-specific binding of the antibody, specimens were incubated in 2% bovine serum albumin (BSA) in PBS for at least 45 minutes at room temperature. To detect antigens of a protein, the following step requires the insertion of fluorescent probes which label the target protein with high specificity. This targeting might occur using (1) primary and secondary antibodies (Ab I and Ab II, respectively) or (2) conjugated dyes.

### **2.6.1 Cytoskeleton, focal adhesion proteins and nuclei labelling.**

Cells were immunolabelled against paxillin primary antibody (mouse) (with  $C_F = 0.2 \mu\text{g}/\text{mL}$  in 2% BSA in PBS) to detect focal adhesion structures, for 1-1.5 hours at room temperature or overnight at  $4^\circ\text{C}$ . Then, samples were washed 3 times for 5 minutes in 2% BSA (diluted in PBS). Cells were incubated with Alexa Fluor 488

Ab II (1:1000 dilution to have a  $C_F = 0.2 \mu\text{g/mL}$ , anti-mouse,  $\lambda_{EX/EM} = 490/525 \text{ nm}$ ) in 2% BSA for 1 hour at room temperature. Cells were washed 3 times in 2% BSA solution. Afterwards, actin filaments labelling was performed by incubating phalloidin-X 555 conjugated dyes (1:1000 dilution to have a  $1x$  as  $C_F$ ,  $\lambda_{EX/EM} = 556/574 \text{ nm}$ ) in 2% BSA for 1 hour at room temperature, following 2 washes for 5 minutes in 2% BSA. Cell nuclei were then stained with nuclear marker Hoechst (1:1000 dilution in PBS,  $C_F = 10 \mu\text{g/mL}$ ,  $\lambda_{EX/EM} = 350/461 \text{ nm}$ ) for 5-10 minutes at room temperature. Samples were shielded from light until imaging. **Figure 2.7** depicts representative images of FAs structures, F-actin and nuclear immunohistochemistry labelling.

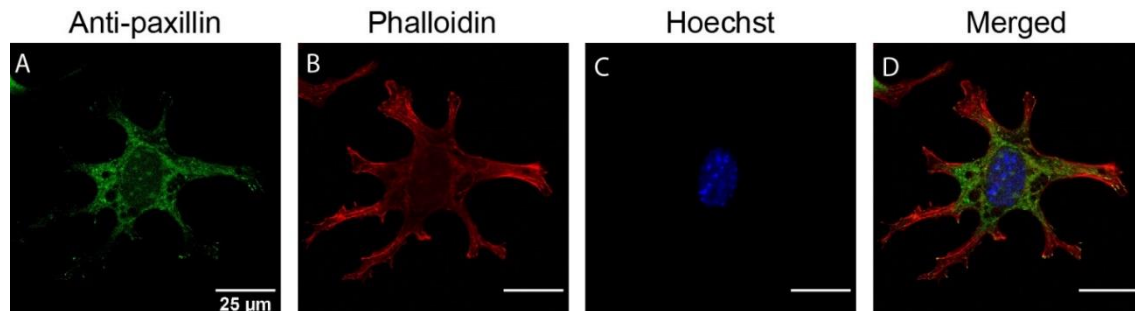


**Figure 2.8. F-actin, FAs and nuclei staining.** Exemplary confocal micrographs of HL-1 cells that underwent immunohistochemistry labelling of (A) focal adhesion patches (paxillin protein in green), (B) cytoskeleton (F-actin filaments in red) and (C) nuclei (in blue). (D) Merged micrograph.

### **2.6.2 Endocytic proteins labelling.**

Anti-clathrin and anti-cav-1 Ab I (rabbit and mouse, respectively) were used to label clathrin and caveolin-mediated endocytic pathways.

Cells were incubated with the Ab I solution for at least 40 minutes at room temperature or overnight at 4°C (1:1000 and 1:100 dilution in PBS respectively for anti-clathrin and anti-cav-1,  $C_F = 1 \mu\text{g/mL}$  in 2% BSA). Afterwards, samples were washed 3 times for 5 minutes in 2% BSA to remove untied antibodies. Alexa Fluor 546 (anti-mouse,  $\lambda_{EX/EM} = 561/572 \text{ nm}$ ) was used to bind anti-clathrin Ab I and Alexa Fluor 488 (anti-rabbit,  $\lambda_{EX/EM} = 490/525 \text{ nm}$ ) for anti-cav-1 Ab I (1:1000 dilution  $C_F = 2 \mu\text{g/mL}$  in 2% BSA) for at least 1 hour at room temperature. Cell nuclei were then labelled with Hoechst die (1:1000 dilution in PBS,  $C_F = 10 \mu\text{g/mL}$ ,  $\lambda_{EX/EM} = 350/461 \text{ nm}$ ) for 5-10 minutes at room temperature. Samples were shielded from light until imaging. Exemplary micrographs of endocytosis immunolabelling are depicted in **Figure 2.9**.

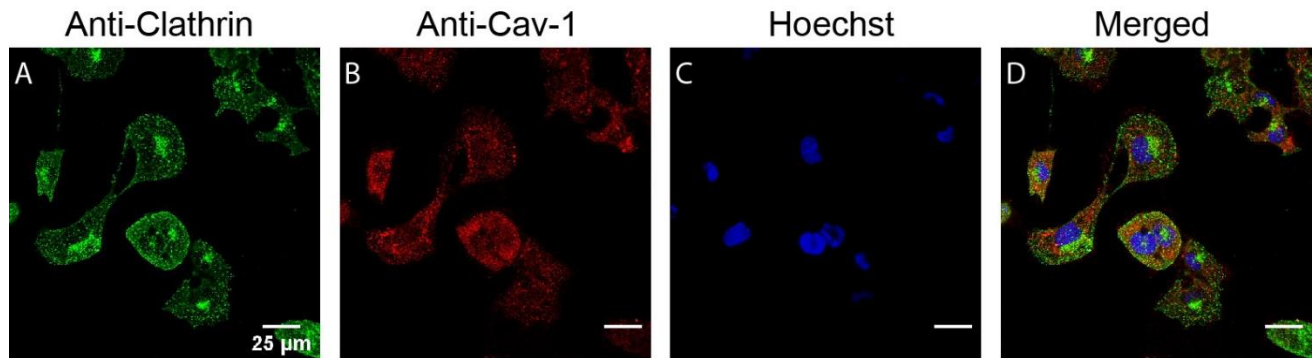


**Figure 2.9. Endocytic vesicles labelling.** Exemplary confocal micrographs of HL-1 cells that underwent immunohistochemistry labelling for endocytic pathways mediated by (A) clathrin (green), (B) cav-1 (red). (C) depicts nuclei labelled with Hoechst blue) and (D) is the merged micrograph.

### 2.6.3 Dendrites, axons and nuclei labelling.

Neuronal processes, *i.e.* axons and dendrites, were selectively labelled with anti-Tau (mouse) and anti-MAP2 (rabbit) Ab I, respectively. The Ab I solution was incubated considering a  $C_F = 2 \mu\text{g/mL}$  for both anti-Tau and anti-MAP2 antibodies and added to the samples for at least 1 hour at room temperature or overnight at 4°C. Samples were then washed 3 times for 5 minutes in 2% BSA. Alexa Fluor 546 (anti-mouse  $\lambda_{\text{EX/EM}} = 561/572 \text{ nm}$ ) was used to bind anti-Tau and Alexa Fluor 488 (anti-rabbit,  $\lambda_{\text{EX/EM}} = 490/525 \text{ nm}$ ) for anti-MAP2 (both at 1:1000 dilution,  $C_F = 2 \mu\text{g/mL}$  in 2% BSA) and let incubate for 1 hour at room temperature. Afterwards, cells were washed 3 times in 1% BSA and cell nuclei were labelled with Hoechst (1:1000 dilution ratio in PBS,  $\lambda_{\text{EX/EM}} = 361/497 \text{ nm}$ ) for 5-10 minutes at room temperature. Samples were shielded from light until imaging. **Figure 2.10** depicts exemplary micrographs of cells labelled with anti-Tau, anti-MAP2 and, Hoechst.

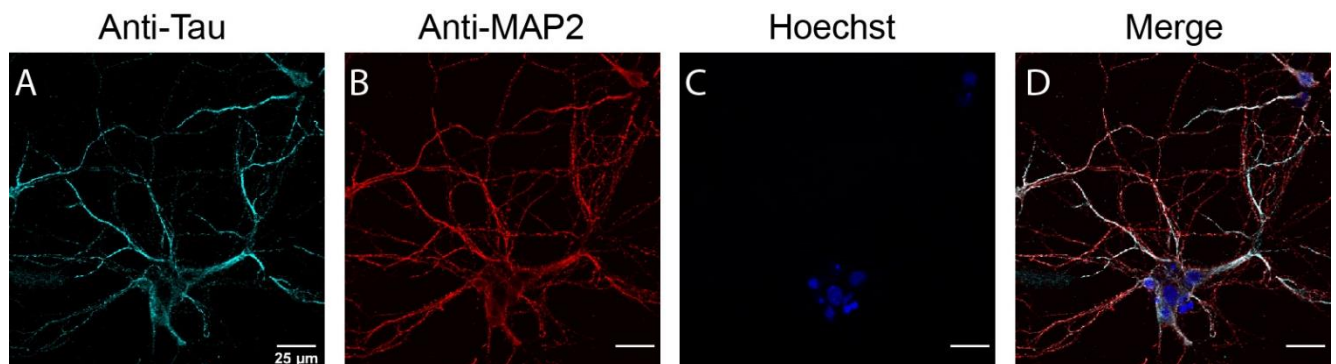


**Figure 2.10. Axons, dendrites, and nuclei staining.** Primary cortical neuronal cells were labelled to identify (A) axons (cyan), (B) dendrites (red) and (C) nuclei (blue). (D) depicts the merged micrograph.

#### **2.6.4 Structural cytoskeleton of neural growth cone.**

The architecture of the neural cytoskeleton was labelled with anti- $\beta$ III-tubulin (mouse) and phalloidin (conjugated dye). The anti- $\beta$ III-tubulin Ab I solution was incubated considering a  $C_F = 5 \mu\text{g/mL}$  in 2% BSA for at least 1 hour at room temperature or overnight at  $4^\circ\text{C}$ . Samples were then washed 3 times for 5 minutes to remove unbound antibodies. To label actin filaments, samples were incubated with phalloidin-X 555 conjugated dyes (1:1000 dilution in PBS,  $C_F = 1\text{x}$ ,  $\lambda_{\text{EX/EM}} = 556/574 \text{ nm}$ ) in 2% BSA for 1 hour at room temperature, following 2 washes for 5 minutes in 2% BSA. Alexa Fluor 488 (anti-mouse,  $\lambda_{\text{EX/EM}} = 490/525 \text{ nm}$ ) Ab II for anti- $\beta$ III-tubulin was diluted (1:1000 dilution,  $C_F = 2 \mu\text{g/mL}$  in 2% BSA) and let incubate for 1 hour at room temperature. Cell nuclei were then labelled by incubating a nuclear marker Hoechst (1:1000 dilution,  $C_F = 10 \mu\text{g/mL}$  in PBS,  $\lambda_{\text{EX/EM}} = 350/461 \text{ nm}$ ) for 5-10 minutes at room temperature. Samples were shielded from light until imaging. **Figure 2.11** shows exemplary micrographs of cells immunolabelled for light microscopy against  $\beta$ III-tubulin, actin and nuclei.

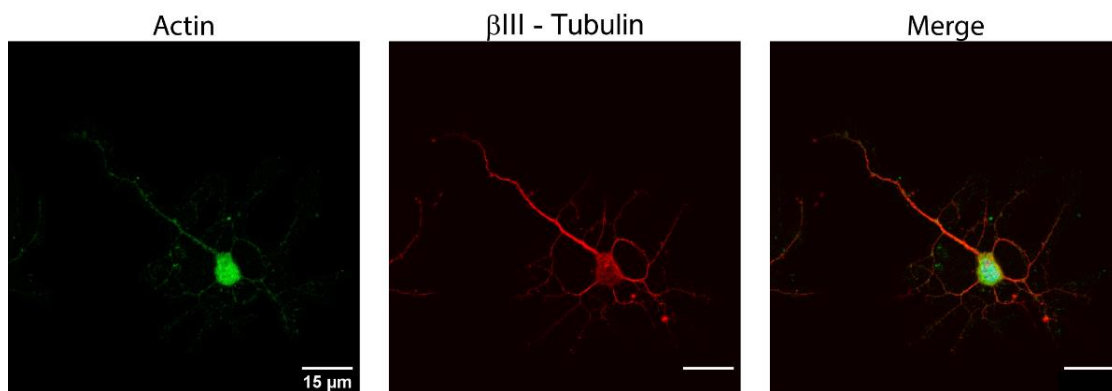


**Figure 2.11. Neuronal cytoskeleton.** The cytoskeleton of primary cortical neurons was labelled to identify actin (green Phalloidin, A) microtubules (in red  $\beta$ III-tubulin, B) and nuclei (in blue Hoechst, merge image in C).

#### **2.6.5 Cell body and nuclear envelopes labelling.**

Cellular envelope was labelled with Wheat Germ Agglutinin (WGA) conjugated dye with  $C_F = 5 \mu\text{g/mL}$  in 2% BSA for at least 1 hour at room temperature or overnight at  $4^\circ\text{C}$  ( $\lambda_{\text{EX/EM}} = 632/647 \text{ nm}$ ). Cell nuclei were then labelled by incubating the nuclear marker Hoechst (1:1000 dilution,  $C_F = 10 \mu\text{g/mL}$  in PBS,  $\lambda_{\text{EX/EM}} = 350/461 \text{ nm}$ ) for 5-10 minutes at room temperature. Samples were shielded from light until imaging. **Figure 2.12** shows exemplary micrographs of cells immunolabelled for light microscopy against WGA and nuclei. Since

the staining was performed for a 3D reconstruction of the cell structure, the optical cross sections were here provided, in **Figure 2.12 C and D**.

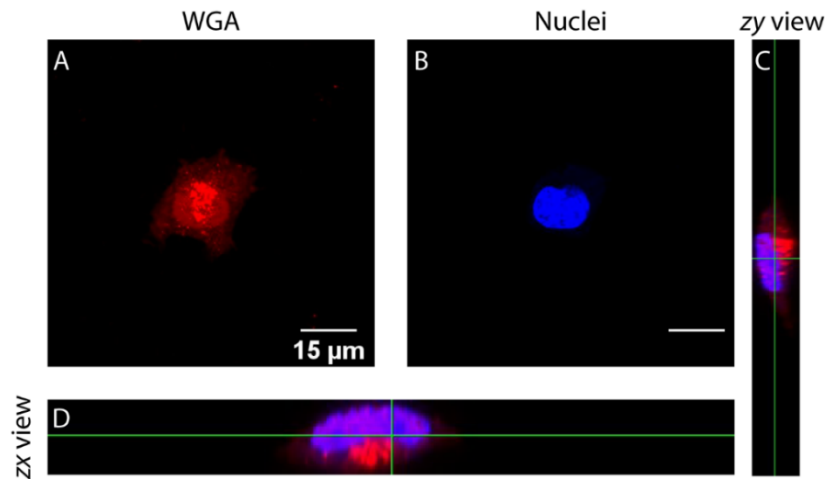


**Figure 2.12. Cell body and nuclear envelop staining.** PM and nuclear envelope were singularly labelled with WGA (A) and Hoechst (B). Optical cross sections (zy and zx views) were provided beside the xy acquisition, (C and D, respectively).

### 2.6.6 Analysis of plasma membrane integrity

PM integrity of cells growing on out-of-plane graphene materials was estimated by monitoring possible internalization of membrane-impermeable fluorescence dye, Calcein. Therefore, Calcein was incubated for 10 minutes at cell culture conditions ( $C_F = 1 \mu\text{M}$  in PBS, wavelengths excitation/emission  $\lambda_{EX/EM} = 490/525$  nm). Afterwards, cells were rinsed in warm PBS and CellMask™ Plasma membrane marker was incubated for 5 minutes ( $C_F = 1x$  in PBS,  $\lambda_{EX/EM} = 554/567$  nm). Samples were shielded from light until imaging. **Figure 2.13** depicts representative images of cells labelled with Cell Mask and Calcein to visualize possible spontaneous penetration event which would lead Calcein to be internalized by cells.

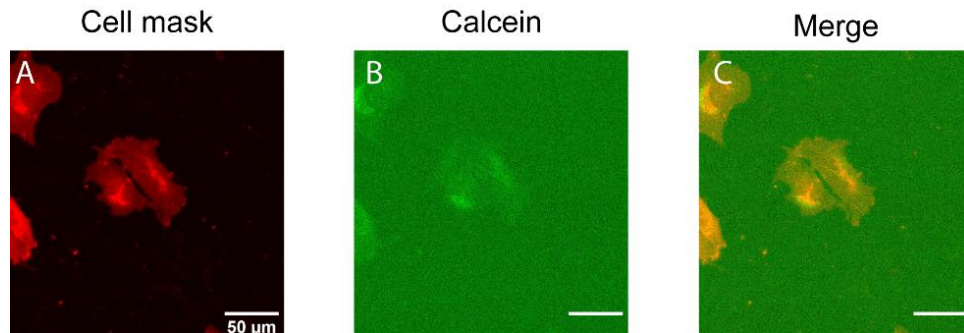


**Figure 2.13. Cell body staining and plasma membrane integrity investigation.** (A) HL-1 cells labelled with cell mask and (B) calcein loading. (C) merged micrographs.

## **2.7 Image acquisition.**

Image acquisition was performed with different optical microscopes, depending on the resolution needed for the imaging and whether cells were retained in live or fixed conditions. All labelled cells were shielded from light until image acquisition.

- a. Widefield fluorescence microscope (Axio Observer Z1, Zeiss) operated through epifluorescence and was used for live/dead imaging with 10x or Planar Apocromat 20x 0.8 dry;
- b. Inverted microscope (Axio Vario, Zeiss) operates through epifluorescence and was used to track the  $\text{Ca}^{2+}$  flow variation across a confluent layer of live cells. Images were collected using an EC Plan-Neofluar 10 x/0.3 numerical aperture (NA) objective;
- c. Laser scanning confocal microscope (LSM 700, Zeiss) was used for cells labelled by immunohistochemistry mainly using a 63x /1,4 NA oil immersion objective. HL-1 cell morphology and endocytic pathways data, as well as neuronal polarization images by means of this microscope;
- d. Laser scanning confocal microscope (STED-SP5) was used to acquire images of the growth cones of neuronal processes with 100x / 1,4 NA oil immersion objective.

## 2.8 Image processing and analysis.

### 2.8.1 Live/dead cell populations analysis.

Acquired images were processed with Image J software (NIH, USA) to perform cell counting of live and dead cells populations. The analysis was performed on each frame derived by the Calcein-AM and Ethidium Homodimer labelling (as described in Paragraph 2.5.1).

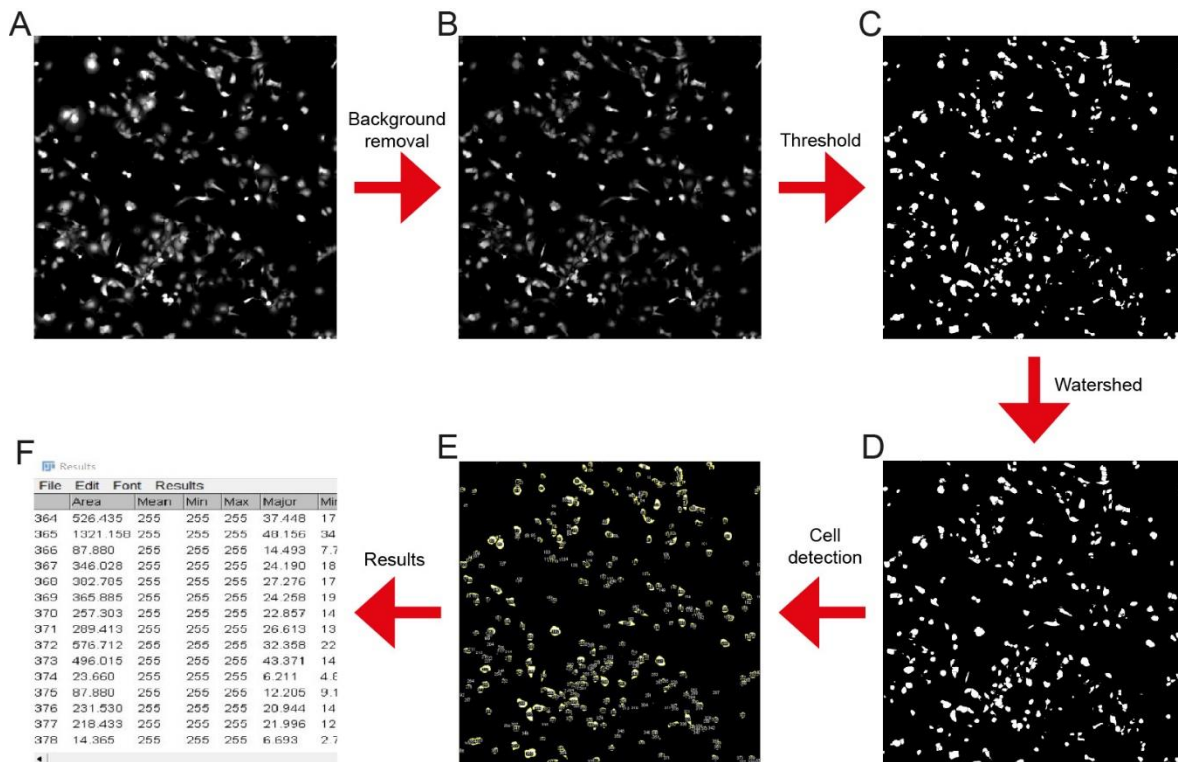


**Figure 2.14. Live/dead image analysis.** Schematic of the semi-automatic cell counts for viability quantification.

- (A) Live and dead cells frames were individually opened, (B) image background removed, (C) a size-dependent threshold applied to identify single cells. (D) Bulkier particles were divided with watershed plugin, (F) cells were automatically counted (E-F).

The main analysis steps are described in **Figure 2.14**. In details, uneven background was removed from the fluorescence microscopy images (**Figure 2.14 B**). Afterwards, an intensity threshold was applied to highlight all cells to count. This creates a binary version of the image with only two-pixels intensity (**Figure 2.14 C**): black = 0 (ascribed to the background) and white = 255 (assigned to the cells). Adjacent cells might be merged after the threshold filter application, so the watershed function was usually used to separate cell clusters by adding 1-pixel line between them (**Figure 2.14 D**). Through the ImageJ particles analysis plugin, each cell was considered as a particle and automatically counted (**Figure 2.14 E**). However, cellular debris,

often present in the cell culture, might be excluded from the automatic counting by adjusting the size particles or their circularity values. Viability was determined by acquiring 10 frames per experiment from 3 independent cell preparations (thereby  $p = 10$  is the population amount,  $N = 3$  the statistical sample) collected randomly over the material surface. Each experimental condition was studied in triplicate ( $n = 3$ ). Therefore, the amount of both live and dead cells was discerned from a total of 90 frames.

% viability quantification was evaluated using the following formula:

$$\% \text{ Viability} = \frac{(\text{Live cells})}{(\text{Live cells} + \text{Dead cells})} \times 100 \quad [2]$$

Data are analyzed by one-way ANOVA with a Tukey- post-hoc test (GraphPad Prism 8.4.3) for 95% as confidence interval.

### **2.8.2 $\text{Ca}^{2+}$ wave imaging analysis.**

$\text{Ca}^{2+}$  wave imaging analysis was performed with MATLAB software.

Images were re-scaled using bicubic interpolation, going from 1216x1920 pixels to 60x96 pixels (**Figure 2.15 A**). From the scaling, each pixel acquires a new size of 19 x 19  $\mu\text{m}$ , which increasingly aids the tractability of the data. In this way, each pixel might cover an area corresponding to a single cell. The average fluorescence intensity of each frame was calculated over time (among all **Figure 2.15 B**). Each  $\text{Ca}^{2+}$  wave appeared as a large positive spike in the frame-wide average intensity time-series (**Figure 2.15 C**). The 16 frames before and after the positive peak were extracted and considered representative and belonging to a single  $\text{Ca}^{2+}$  wave event. On individual events, the frame number of maximum intensity was identified for each pixel, yielding a single image of the event that depicts the displacement of the calcium wave across the field of view of the microscope (**Figure 2.15 D**). A 3x3 pixels filter was applied to this image to detect edges which represent the wave fronts at different times. The filtered edges were thresholded and used as a binary filter on the image with the intensity maxima for the given event. The resulting image shows the position of the wave front at each time point or frame of the detected event (**Figure 2.15 E**). The distance travelled by the calcium wave between consecutive frames was estimated as the minimum distance between wave front positions observed at consecutive time points. The propagation speed was obtained by dividing the estimated travelled distance for the acquisition period (the time between frames in the image series, 0.056 s). A schematic that summarized the main calcium imaging analysis steps is shown in **Figure 2.15**.

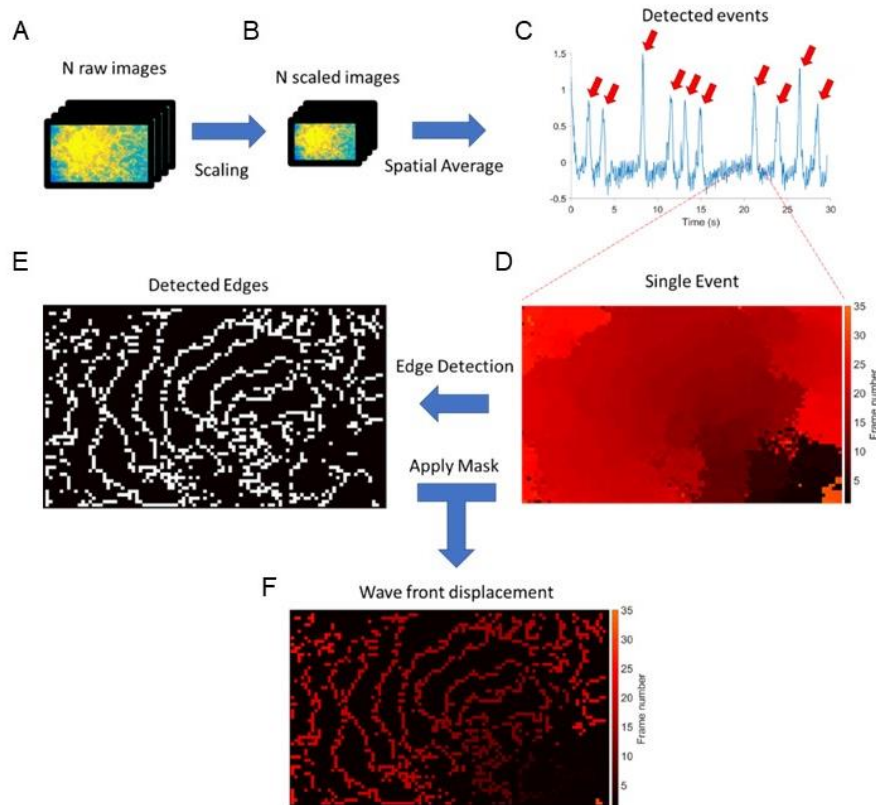


**Figure 2.15.  $\text{Ca}^{2+}$  wave imaging process.** Schematic of the main steps adopted for the analysis including (A) time-series size rescaling, (B) fluorescence intensity averaging, (C-D)  $\text{Ca}^{2+}$  wave detection as positive peak, (E) application of edge detection filter, (F) until the wave front displacement.

### 2.8.3 Cell shape descriptors analysis.

The morphological analysis of the HL-1 shape was carried out with the ImageJ software, by considering images acquired after immunolabelling of actin fibers by means of Phalloidin-X conjugated dye, explained in Paragraph 2.6.1. As shown in the schematic of Figure 2.16, the cells shape was identified after removing the background and applying the threshold plugin of Image J. The intensity threshold highlights the fluorescence region to analyze (basically the cell), thus creating a binary version of the image with only two-pixel intensity: black = 0 ascribed to the background and white = 255 to the cells. The highlighted region was then measured with ImageJ automatic measure plugin leading to a detailed analysis of the cell shape descriptor: area, cell elongation, minor and major cell axis lengths (also considered as cellular width and length, respectively), and cell circularity. Cellular shape was described by acquiring 10 cells per experimental condition from 3 independent cell preparations (thereby  $p = 10$  is the statistical population and the statistical sample is  $N = 3$ ). Each experimental condition was studied in triplicate ( $n = 3$ ). The One-

way Analysis of Variance test (ANOVA test) was carried out with the GraphPad Prism 8.4.3 to statistically characterize the cell behavior, and the Tukey test was run to confirm where the differences occurred between groups. A p-value lower than 0.5 was considered significant.

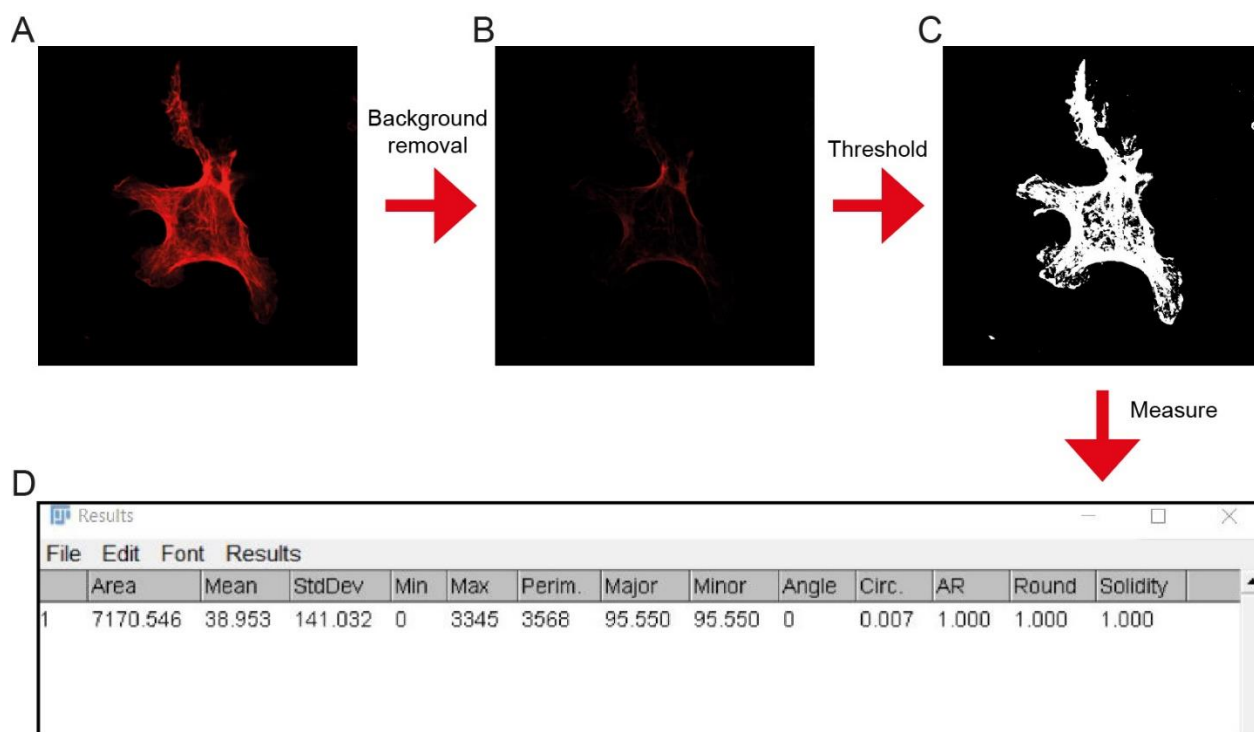


**Figure 2.16. Cell shape descriptors processing.** Schematic of the main steps adopted for the analysis of the shape descriptor, including (A) the acquisition of fluorescence micrographs, (B) the background removal, (C) the intensity threshold filter application and (D) descriptors measurement.

#### 2.8.4 Fluorescence intensity profile analysis across cells area.

Fluorescence intensity was quantified through the ImageJ software. This procedure was applied for the evaluating the expression of actin, focal adhesion and endocytic protein for HL-1 cells, and actin and microtubules structures for neurons. Each investigation was performed in triplicate with 3 independent cell preparations and the image acquisition parameters (*i.e.*, exposure time, laser power and detectors gain) were fixed throughout the experiments. Each cell in the frame was selected independently and the intensity quantification was carried on by considering the mean grey value (*i.e.*, the mean fluorescence intensity for all pixels within the selected area) as shown in **Figure 2.17 A**. Mean grey values, associated to the background, were measured from regions devoid of cells (**Figure 2.17 B**) and subtracted from the fluorescence intensity values of the investigated samples by following the ensuing formula:

$$\text{Fluorescence intensity} = \text{Cell fluorescence} - \text{Background fluorescence} \quad [3]$$

where: cell fluorescence is the cell mean grey value and background fluorescence is the background mean grey value. The One-way ANOVA was carried out with the GraphPad Prism 8.4.3 and the Tukey test was run to confirm where the differences occurred between groups. A p-value lower than 0.5 was considered significant.

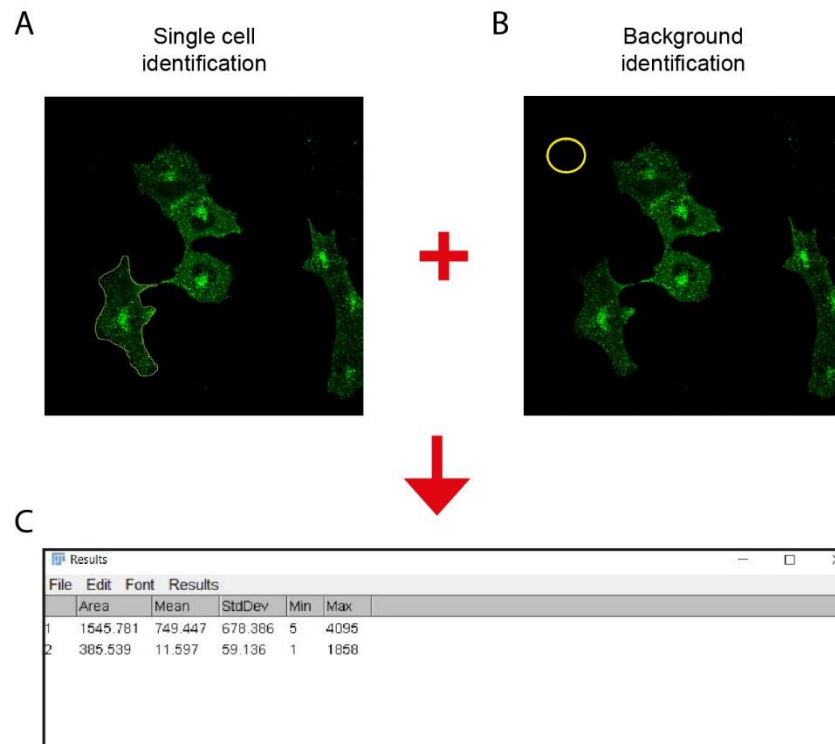


**Figure 2.17. Cell fluorescence intensity quantification.** Fluorescence intensity was quantified by measuring (A) first the mean grey value and (B) the background value from the control sample. (C) Fluorescence value resulting from the application of equation [3].

### 2.8.5 Fluorescence intensity profile along a linear region of interest.

The spatial localization of the fluorescence signals emitted from HL-1 cells labelled with anti-clathrin and anti-cav-1 probes, as well as from cortical neurons GC labelled against actin and microtubules was studied. Therefore, one pixel line, cutting HL-1 cells and cortical neuron GC shape in two, was drawn and the fluorescence intensities from the labelled proteins were plotted in function of the segment length (**Figure 2.18 A**). To reduce noise, seen as random jumps in the fluorescence intensity profile, a smoothing filter was applied in ImageJ (**Figure 2.18 B**). After the application of this filter, each new pixel depends upon the

average of the values in a  $3 \times 3$  pixel region. This operation averages out much of the noisy variation, giving a result that is considerably smoother. The intensity values found along the line were then plotted by using Graph Pad Prism 8.4.3.

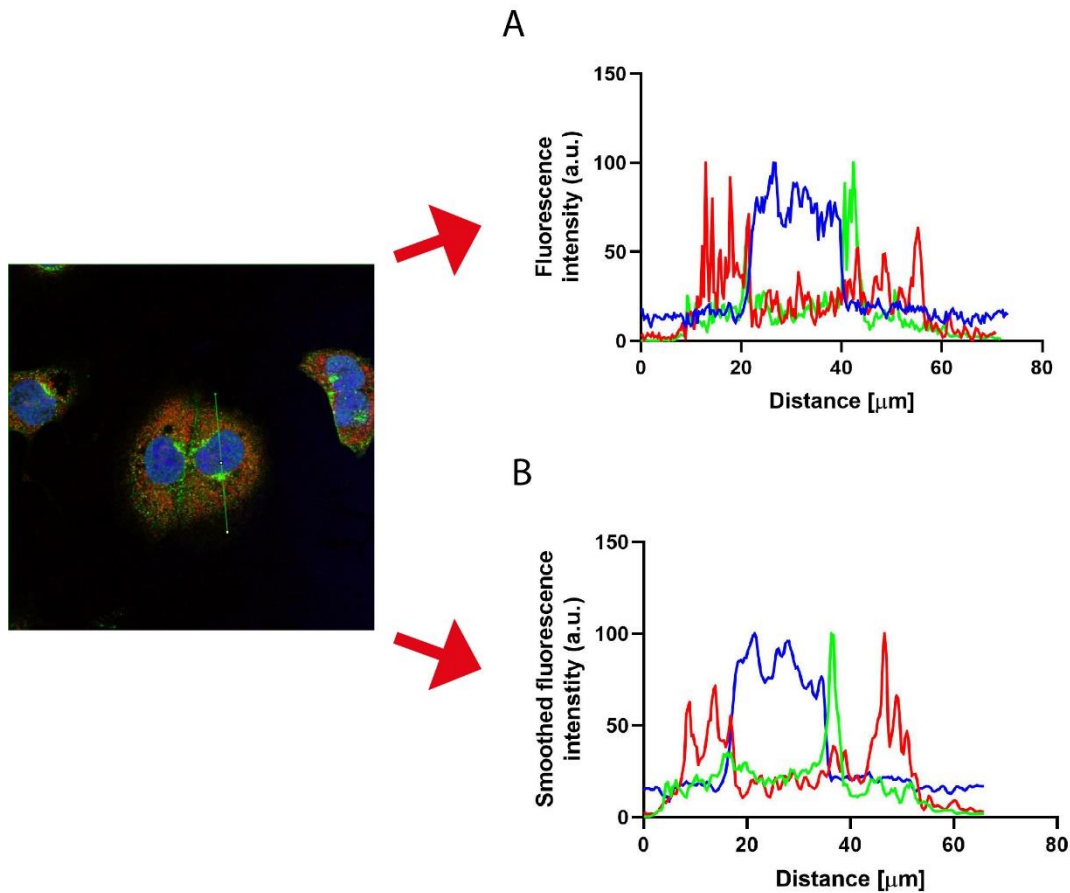


**Figure 2.18. Cell fluorescence intensity along one-pixel line.** The intensity of fluorescence signals emitted by HL-1 was plotted along a line, (A) without applying or (B) by exploiting a smooth filter.

### 2.8.6 Axon length measurements and secondary neurites counting.

Axon lengths and the number of secondary neurites emerging from the axons were quantified from cortical neural cell cultures labelled against MAP2 and Tau proteins (see **Paragraph 2.6.3**). Analysis was performed on solitary or almost solitary neurons within the field of view 63x/1,4 NA oil immersion objective. NeuronJ plugin in the ImageJ software was used to measure in semi-automated fashion the axonal length and the secondary neurites. Each neuron process was first outlined from its starting point to the terminal end and then identified as axon, secondary, tertiary processes or even dendrites with a color code, as shown in **Figure 2.19 B**. Afterwards, lengths measurements of the processes, as well as their counting, was performed in an automated way by measurements ImageJ plugin (**Figure 2.19 C**).

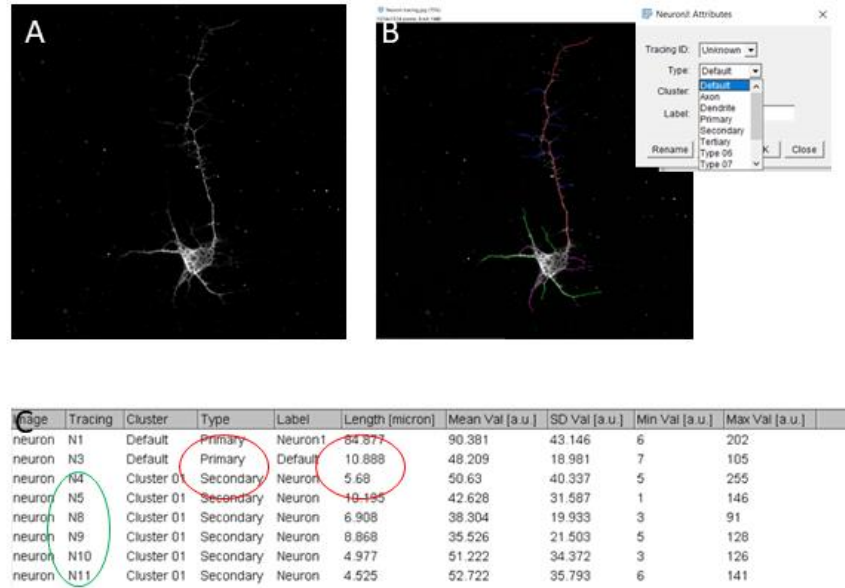


**Figure 2.19. Axon length measurement and neurite processes counting.** (A) MAP2 and TAU labelled cortical neurons, (B) whose processes were identified as axon, secondary, tertiary and dendrites processes with a color code. (C) Afterwards, length measurements and counting were performed in automated way.

### 2.8.7 3D optical reconstruction of cell body.

3D rendering of the cell body was performed by using ImageJ software (plugin 3D viewer). Therefore, z-stack acquisition of the cell body was performed fixing the slice thickness ( $\Delta h$ ) equal to  $0.25 \mu\text{m}$ . The plugin 3D viewer was set to volume (**Figure 2.20 B**) and the background to white color (red, green and blue channels fixed at 255 as pixel value). In order to gather a lateral visualization of the 3D reconstructed cell, the view was set to +yz plane (the basal PM is localized at the bottom) as shown in **Figure 2.20 C**.

The cell volume is calculated as the sum of the slice surface areas multiplied by the slice height:

$$\text{Cell volume} = \sum_n A_n \Delta h \quad [4]$$

where  $A_n$  is the surface area of each acquired slice, measured *via* the ImageJ software algorithm (as described in **Paragraph 2.8.3**) and  $h$  is the slice height.

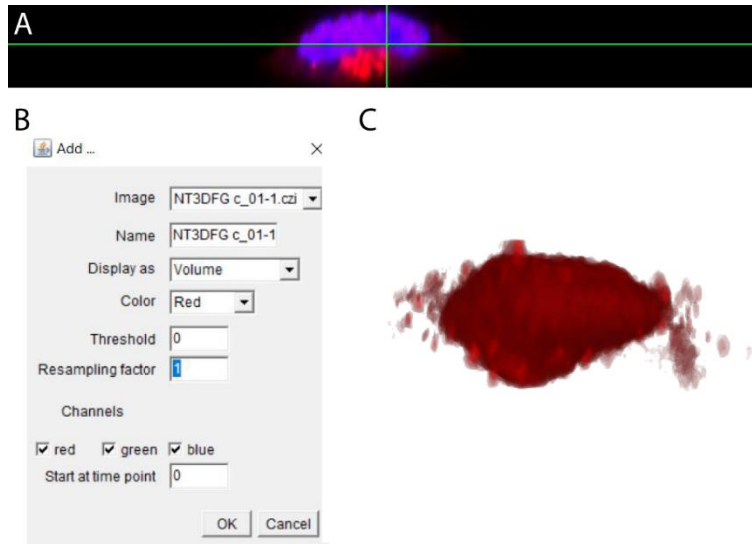


**Figure 2.20. 3D cell reconstruction in ImageJ.** 3D rendering of a cell from an acquired optical z-stack (A) processed with the 3D viewer plugin in ImageJ environment fixing volume as final displaying (B). (C) Cell 3D view.

## 2.9 Electron Microscopy for cell-material characterization.

### 2.9.1 Ultrathin plasticization (UTP) method<sup>11,40</sup>.

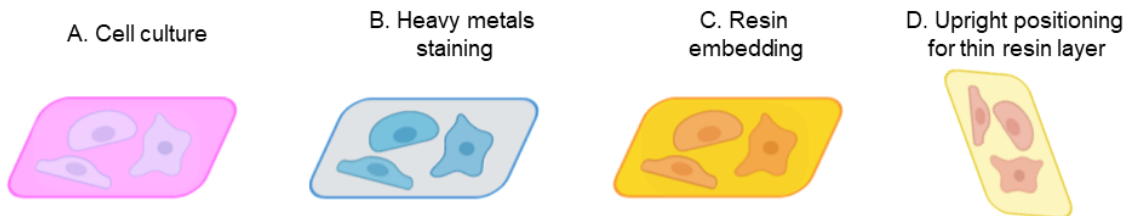


**Figure 2.21. Ultra-thin plasticization method.** In this schematic the procedure of biological sample preparation for EM is shown. (A) figures the cell culture, which is firstly (B) stained with heavy metals to add density and contrast to the cells and then (C) embedded in resin. (D) Ultra-thin resin removal.

Cells were firstly rinsed with PBS and then washed in 0.1 M sodium cacodylate buffer ( $C_2H_6AsNaO_2$ ) at physiological pH for 5 minutes before being fixed in in 2.5% glutaraldehyde diluted in the same buffer at room temperature. Fixation is performed to block any cellular degeneration processes and preserve morphological shape from shrinkage and swelling (osmotic damages). Therefore, glutaraldehyde stabilizes cellular ultrastrcutures *via* permanent cross-linking which occurs between its -CHO groups and any protein

nitrogen<sup>110</sup>. However, this strong and irreversible fixative effect only involves protein structures. Lipidic structures must undergo a secondary fixation to retain their structures during the entire method. After the fixative incubation, samples were transferred on ice (4° C) and washed 3 times for 5 minutes with buffer. Unreacted aldehyde groups, not bound to anything, were quenched with 20 mM glycine solution in 0.1 M buffer solution for 20 minutes at 4°C. Specimens were then washed 3 times with buffer (5 minutes each) at 4°C. To preserve lipidic membranes and fix glycogen, a second fixative step is performed by incubating cells with 2% osmium tetroxide and 2% potassium ferrocyanide for 1 hour at 4°C. This post-fixative adds density and contrast to the cell as staining solution<sup>111</sup>. Samples were then washed 3 times with buffer solution at 4° C. Prior thiocarbohydrazide (TCH) step, cells were gently washed with DI water at room temperature (to prevent TCH salt precipitation). Afterwards, samples were immersed in 1% filtered thiocarbohydrazide (TCH) in DI water for 20 minutes at room temperature. TCH solution profoundly enhanced the contrast of the osmiophilic cell components.

Specimens were washed 3 times with DI water for 5 minutes and subsequently immersed in 2% tetroxide osmium solution for 30 minutes at room temperature. This entire procedure of staining, **Figure 2.21 B**, is also known as *RO-T-O* because it includes solutions of potassium ferrocyanide-reduced osmium (RO step), TCH (T step) and osmium (O step). Afterwards, specimens were washed with DI water 3 times for 5 minutes and incubated overnight in 4% filtered uranyl acetate at 4°C. Uranyl acetate reacts with phosphate and amino groups (*i.e.*, nucleic acid, proteins, mitochondria). Then, samples were washed 3 times with DI water and incubated with 0.15% tannic acid for 3 minutes at 4°C and then washed 2 times with DI water. Dehydration was carried out with a series of ethanol dilutions (30, 50, 75, 95, 100% v/v ethanol in water) for 10 minutes each at 4°C. 100% ethanol was exchanged 2 times at room temperature. Specimens were then gradually embedded in resin (25 mL of NSA, 8 mL D.E.R. 736, 10 mL of ERL 4221, 301 µL of DMAE) with an ethanol : resin ratio (1:3 for 3 hours, 1:1 overnight, absolute resin for at least other 8 hours (**Figure 2.21 C**). Minimal resin covering on the cells was achieved by upright positioning the samples and let the resin drain by gravity for 2 hours (**Figure 2.21 D**). In addition, to significantly reduce the final resin layer, samples were quickly rinsed with 100% ethanol for less than 2 minutes prior to polymerization. Therefore, the whole procedure to prepare biological samples for EM imaging is known as ultrathin plasticization method (UTP)<sup>11,40</sup>. However, absolute ethanol flushing step might introduce some artefacts. Indeed, longer washes cause complete exposition and potential dehydration of cellular bodies and processes. **Figure 2.22** shows resin layer reduction as function of the ethanol washing time. Finally, resin was polymerized in the oven at 70°C for 12-24 hours. Samples were mounted onto aluminum pin stubs (diameter 3.2 mm) using silver conductive paste and sputtered with 5 nm-thick gold layer prior to imaging.

### 2.9.2 Whole-cell scanning electron microscopy.

Specimens were loaded in a dual-beam microscope which supports both an electron beam column (e-beam) and a Ga<sup>+</sup> ions focused beam column (FIB or i-beam). Cell morphology, polarization and development of cellular processes (*i.e.*, filopodia, axons and dendrites) were visualized by whole-cell imaging. Once a ROI was located and, whole-cell micrographs in top and tilted view were acquired by scanning the surface point by point with the e-beam. Moreover, high magnification micrographs of cellular processes were acquired to further characterize cellular spreading and polarization. Here, the e-beam applied voltage and current were in the range 5 - 10 kV and 0.34 – 2.7 nA, respectively. Micrographs were acquired in secondary electrons mode, which well resolves characteristic topographic and volumetric features of the material and by fixing time the dwell time to 45  $\mu$ s., Low magnified micrographs (from 1000x up to 3500x) were taken for visualizing the biological culture or cell morphology and spreading. High magnified micrographs (from 5000x to 8000x) were acquired to visualize cell processes like filopodia or dendrites. Exemplary whole-cell scanning electron micrographs are shown in **Figure 2.23**.

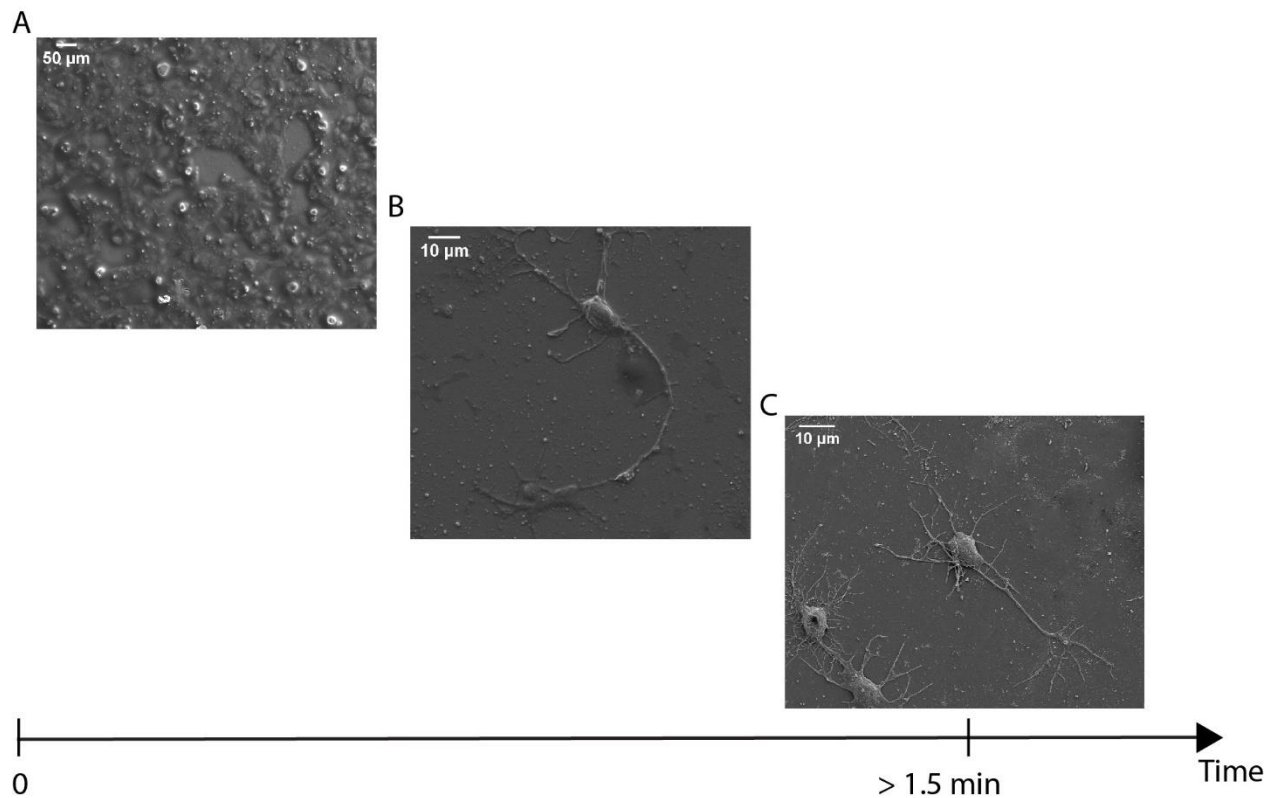


**Figure 2.22. Resin layer embedding as a function of ethanol removal.** (A) Thick resin embedding layer allows only to identify cell on the substrate. (B) Cellular features might be visible with slightly longer ethanol

washes. (C) However, extended ethanol rinses bring cells to a complete resin removal and dehydration.

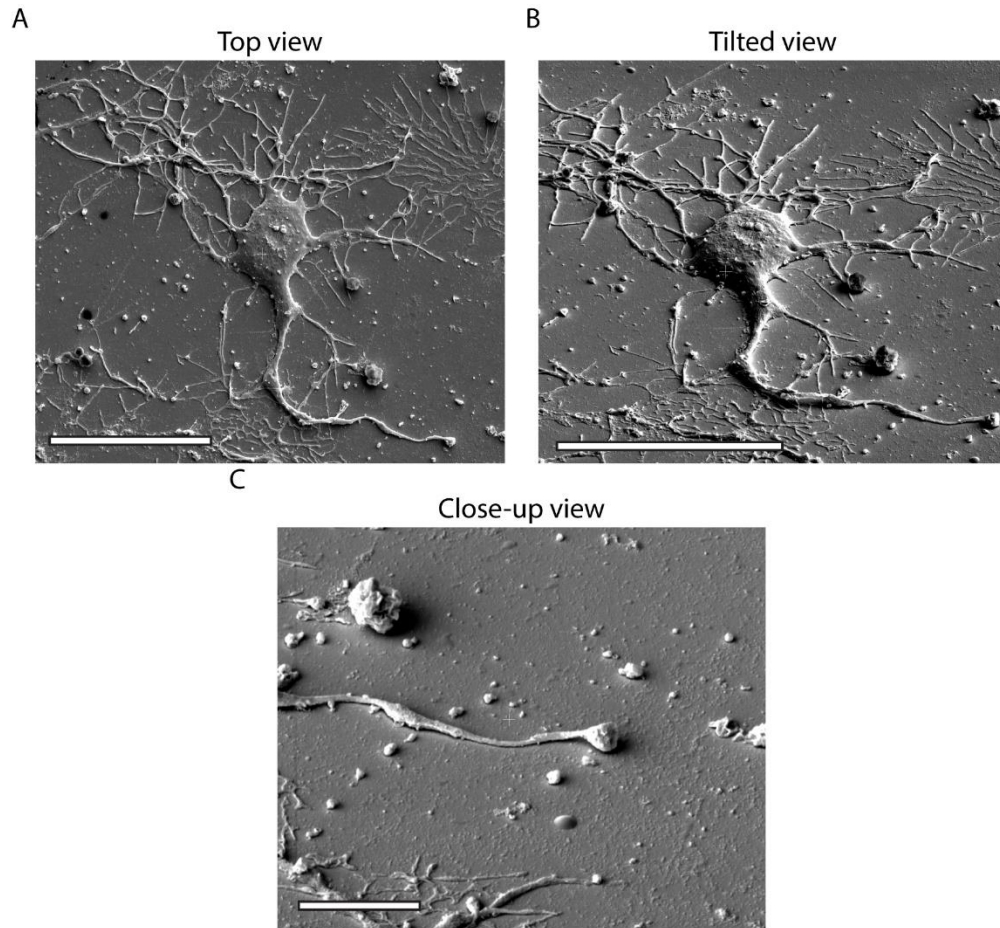


**Figure 2.23. Whole-cell scanning electron micrograph.**

SEM micrograph of cell in top (A), tilted (B) and close-up view (C). Scale bar 20  $\mu\text{m}$  (A, B), 5  $\mu\text{m}$  (C).

### ***2.9.3 Focused ion beam sectioning/scanning electron microscopy of cross sections.***

The cell-material contact area was exposed through FIB milling and imaging was then performed with SEM. Here, a ROI was identified (**Figure 2.24 A**), a double platinum (Pt) layer was deposited to preserve the sample structures from the ensuing destructive cross-sectioning steps. First a 0.5  $\mu\text{m}$ -thick Pt layer was deposited by e-beam assisted deposition by fixing the voltage of the electron beam at 3 kV and the current at 0.69 – 2.7 nA. Then a second layer ( $\sim 1 \mu\text{m}$  nominal thickness) was deposited by ion beam-assisted deposition (**Figure 2.24 B,C**), fixing at 30.0 kV and 0.79 nA the ion beam voltage and current, respectively. Afterwards, by fixing the ion beam voltage and current at 30 kV and 0.25 – 9.3 nA, respectively, a large amount of material can be removed by milling, allowing precise exposition of cell-material interface (**Figure**

2.24 D). Notably, the nominal depth (as for silicon) was set to  $\sim 5 \mu\text{m}$  and the milling profile used was the ramp. The resulting surface was then further polished avoiding curtaining effects with the ion beam voltage and current at 30.0 kV and 80 pA-0.23 nA, respectively<sup>112</sup>. Further details on FIB/SEM cutting and polishing operations are reported in **Annex A.2**.

The SEM cross-section imaging was performed using the backscattered detector (backscattered electrons, BSE). In this configuration, grey levels belonging to the reconstructed images detect contrast between areas with different chemical compositions since the number of emitted BSEs is proportional to sample atomic number (**Figure 2.24 D**). Therefore, osmophilic membranes which are highly dense regions compare to the cytoplasm appear darker in the micrograph.

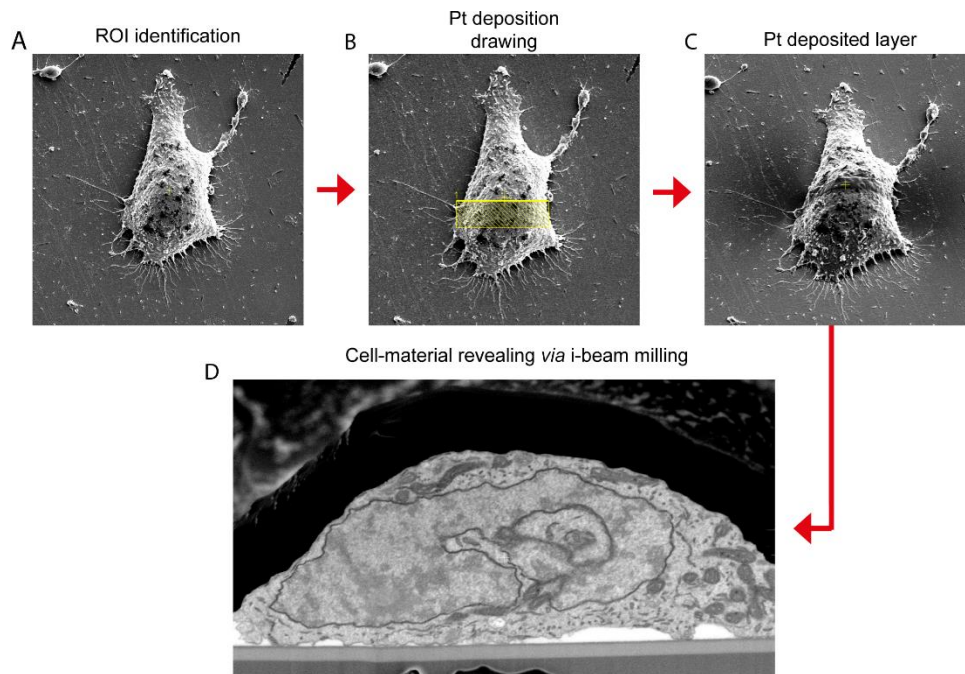


**Figure 2.24. FIB/SEM cross-sectioning and imaging procedure.** Cell-material contact area imaging was achieved by following these sequential steps: (A) ROI identification, (B-C) Pt layer deposition with e-beam and i-beam to preserve cellular structures, (D) i-beam assisted milling to expose the cross section, and backscattered imaging.

## Chapter 3: Results and discussion.

### 3.1 Out-of-plane graphene substrates characterization: morphology and composition.

**Figure 3.1** shows 3D schematics of the fabricated graphene-based materials. In particular, graphene was deposited to achieve a planar configuration (**Figure 3.1 A**), while all the other topographies exhibit a 2.5 – 3D morphology. Indeed, 3DFG presents a nanoscale roughness where two sides of the graphene flakes are exposed (**Figure 3.1 B**). The arrangement of collapsed NWs in NT-3DFGc offers interspersed micrometric cavities and wires located at different heights (**Figure 3.1 C**) and finally, NT-3DFGnc (**Figure 3.1 D**) was synthesized to obtain a mesh of free-standing NWs. The morphology of each graphene-based substrate was examined by scanning electron microscopy (SEM, **Figure 3.2**).

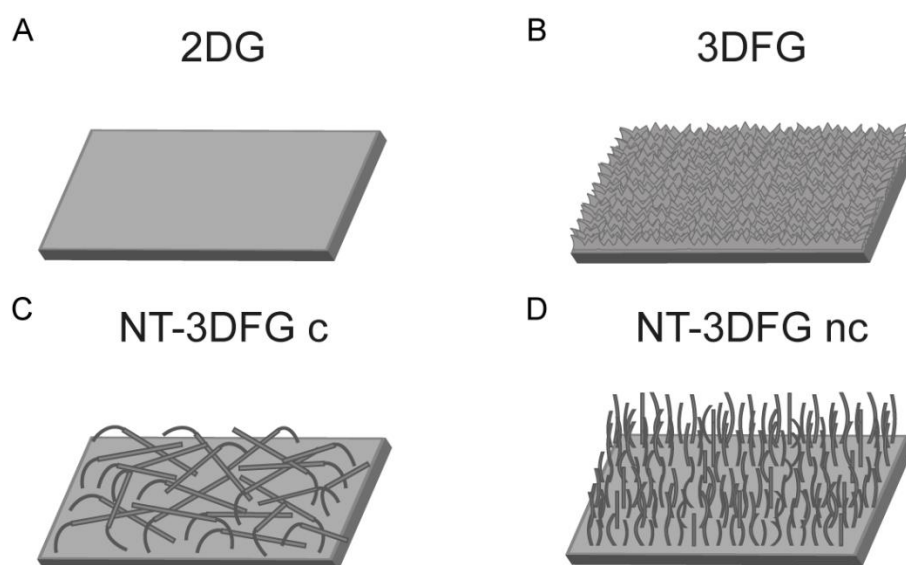


**Figure 3.1.** 3D schematics of the synthesized graphene-based material. (A) planar graphene; (B) 3D fuzzy-graphene; (C) collapsed nanowire-templated covered with 3D fuzzy graphene; (D) non-collapsed nanowire-templated covered with 3D fuzzy graphene.

**Figure 3.2 A** depicts the planar graphene (2DG) surface morphology. The white arrow highlights the grain boundary of the graphene layer obtained during the LPCVD deposition process (**Materials and methods 2.1**). Instead, the fuzzy morphology of 3DFG material (**Figure 3.2 B**) is achieved by specific deposition parameters: the graphene flakes were oriented perpendicularly out from the substrate, and their density was adjusted during the synthesis which was carried for 30 min at 800°C and 25 mTorr as CH<sub>4</sub> partial pressure. Compared to the planar film, the submicrometric roughness of the final surface topography leads

to a larger surface area, as also reported earlier<sup>99</sup>. The hybrid composition of the NT-3DFG meshes, either in collapsed and non-collapsed arrangements, consist of Si NWs catalyzed by a VLS process and coated with few layers of graphene flakes which extend from the surface of the wires (insets in **Figure 3.2 C, D**). On the one hand, NT-3DFGc material (**Figure 3.2 C**) exhibits a tangled collapsed wires mesh network, where microcavities, indicated with yellow arrows, are formed between collapsed wires, giving an overall micrometric topography to the material (mesh thickness is  $7.2 \pm 1.9 \mu\text{m}$ ). On the other hand, the NT-3DFGnc template, instead, has thick bundles of free-standing NWs which are unevenly distributed across the substrate (**Figure 3.2 D**). Here, the average NW length is in the order of few tens of microns. From the SEM observations, wire tips are easily recognizable, however a large number of wires appear to be tilted from the vertical position. Therefore, alongside wires end parts, portion of sidewalls, belonged to kinked wires, can be recognized.

Due to the presence of the fuzzy graphene coating deposited on each Si wire, the average diameter of the single structure hovers  $163 \pm 22 \text{ nm}$ <sup>99</sup>. Therefore, for both NT-3DFGc and nc substrates, the deposited fuzzy graphene provides a local nanometric roughness, alongside the topographic effect in the micrometric scale fulfilled by each Si wire (core size).

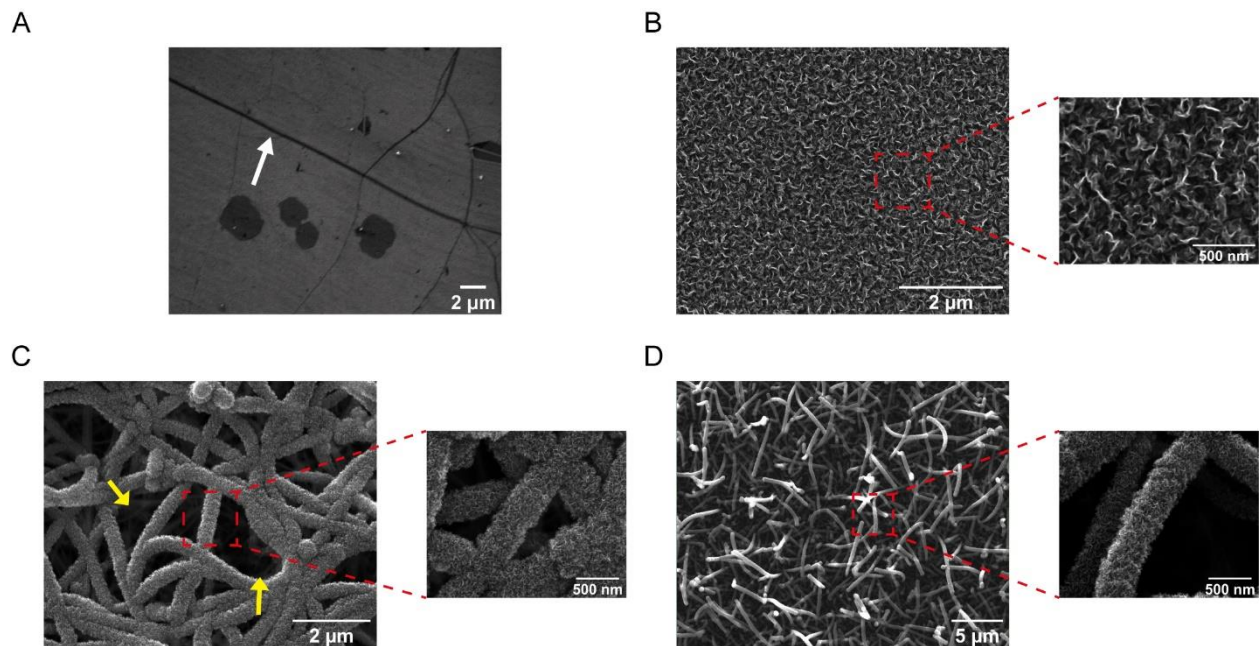


**Figure 3.2. Scanning electron micrographs of the graphene materials.** (A) 2DG planar material: white arrow points to the grain boundary; (B) 3DFG material with highly magnified micrograph of the exposed graphene flakes; (C-D) NT-3DFGc and NT-3DFGnc out-of-plane materials with highly magnified micrograph given of the wires mesh and the fuzzy graphene coating. Yellow arrows in (C) indicate the presence of interspersed microcavities.

Then, the graphene-based materials were characterized through the Raman spectroscopy technique (**Materials and methods 2.2.2**). Raman measurements provide information on the molecular composition of the material through Raman scattering. Therefore, the effects of edges, the presence of defects, and number of graphene layers can be inferred from the characteristic peaks analysis (*i.e.*, shape, intensity and position)<sup>113</sup>. These measurements were performed in the Biomedical Engineering Department of Carnegie Mellon University, USA.

In **Figure 3.3**, the purple curve refers to the spectra of the planar graphene. Here, the presence of a sharp G peak at ca. 1580  $\text{cm}^{-1}$  and a symmetric 2D peak at ca. 2700  $\text{cm}^{-1}$  with full width at half-maximum (FWHM) of ca. 40  $\text{cm}^{-1}$ , corroborate the monolayer graphene nature. As reported in previous works<sup>113,114</sup>, single layer or few-layers of graphene can be easily distinguished from bulk graphite thanks to the evolution of both G and 2D peak at ca. 2700  $\text{cm}^{-1}$ . Indeed, if bulk graphite shows a wider peak with two components, 2D<sub>1</sub> and 2D<sub>2</sub> (roughly 0.25 % and 0.5 % of the height of G peak, respectively<sup>114</sup>), graphene has a sharp 2D peak (with four-time higher intensity than the G peak), as depicted in **Figure 3.3**. Moreover, the absence of a significant D peak at ca. 1340  $\text{cm}^{-1}$  indicates that the synthesized graphene has very limited structural defects. On the contrary, the presence of D peak, and D' peaks, as a shoulder to the G peak in the spectra of 3DFG (blue curve), NT-3DFGc (green curve) and NT-3DFGnc (red curve in **Figure 3.3**) materials is attributed to the peculiar graphene edges. The breaking in the translational symmetry due to the presence of the graphene flakes edges has direct effect in the activation of D and D' peaks<sup>115</sup>. Moreover, a careful study of the 2D band shape, width and, number of Lorentzian peaks (which can be fitted in the single 2D peak) might provide information about the stacking of the graphene layers and the number of the additive graphene sheets<sup>113–115</sup>. Therefore, for the 3DFG and NT-3DFG templates the broad and symmetric 2D peak, fitted in a single Lorentzian, suggests the presence of juxtaposed single- to few-layer of graphene flakes in the high density 3DFG, as already reported by *Garg et al.*<sup>99</sup>.

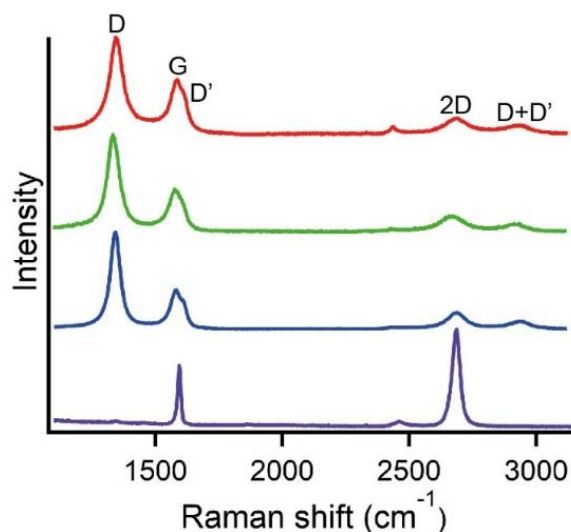
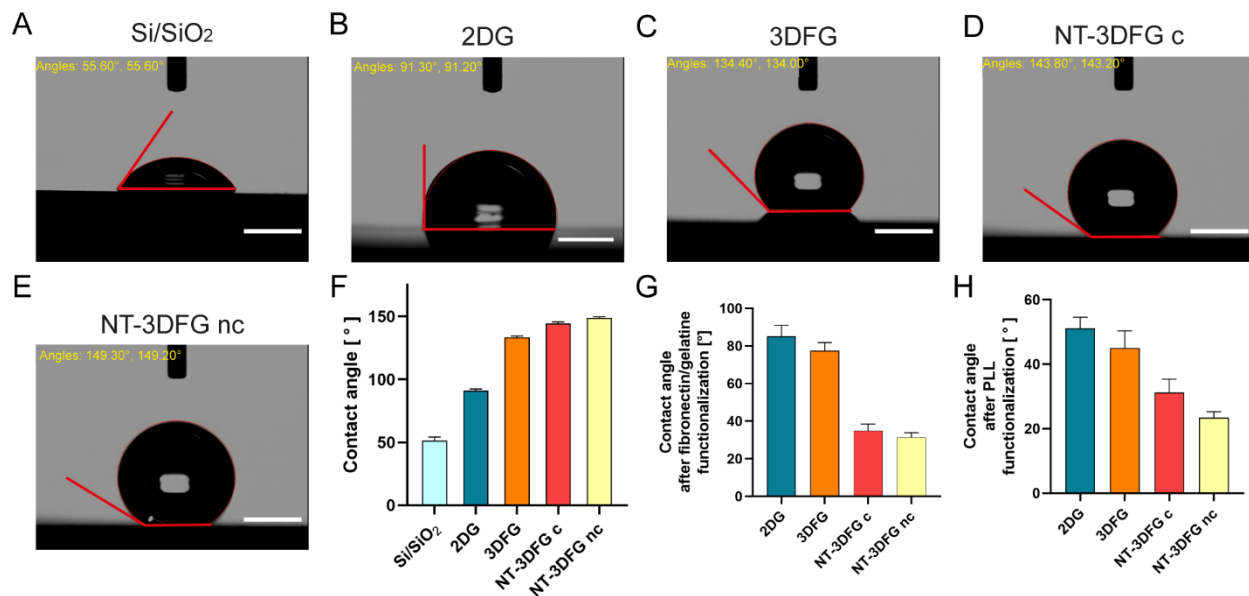


Figure 3.3. Raman spectra of planar and out-of-plane graphene materials.

Exemplary spectra of 2DG (violet), 3DFG (blue), NT-3DFGc (green) and NT-3DFGnc (red).

In addition, the roughness at the material surface might affect the physical and chemical properties of the different graphene materials. Here, considering that hydrophobicity/hydrophilicity influences the coupling with biological cells, we investigated the surface wettability through contact angle measurements (**Materials and methods 2.2.3**). Planar graphene shows a slight hydrophobicity (**Figure 3.4 B, F**, average angle  $\theta \sim 91 \pm 1.3^\circ$ ,  $N=3$ ), compared to the hydrophilicity of the control sample, Si/SiO<sub>2</sub> ( $\theta \sim 51.5 \pm 2.7^\circ$ , **Figure 3.4 A, F**). When contact angle measurements were performed in the case of out-of-plane graphene materials, the angles were  $\theta \sim 133 \pm 1.1^\circ$ ,  $\theta \sim 144.5 \pm 1.6^\circ$ ,  $\theta \sim 148.8 \pm 0.9^\circ$  for 3DFG, NT-3DFGc and NT-3DFGnc, respectively (**Figure 3.4 F**), which ultimately correspond to a superhydrophobic behaviour. Although in the 2DG configuration graphene owns a hydrophobic nature, the nanoscale roughness of 3DFG, as well as the complex architectures of NT-3DFGc and nc templates further enhance this condition. Indeed, possibly the presence of air pockets trapped between the micro- and nano-scaled asperities in the out-of-plane materials, as explained by the Cassie–Baxter model in the case of porous surface wettability<sup>116</sup>, attributes water-repellent properties. In this model, a water droplet is suspended above the structures rather than follow the rough profile of the surface, typical of Wenzel wetting state<sup>117</sup> and hence, the solid/water interface is minimized as similarly induced by the increase of micro-pores in the topographies, as in the cases of NT-3DFGc and NT-3DFGnc<sup>118</sup>.

The hydrophobic nature of the graphene materials could preclude their use for biological purposes. Thereby, graphene surfaces were functionalized prior to cell culture with PLL and fibronectin/gelatine solutions (**Materials and methods 2.2.3**) based on the cultured cell type.



**Figure 3.4. Contact angle measurements.** Images of a 1.5  $\mu\text{L}$  of DI water droplet injected on (A) Si/SiO<sub>2</sub>, (B) 2DG, (C) 3DFG, (D) NT-3DFGc and (E) NT-3DFGnc. Scale bars, 1 mm. (F) Average contact angles measurements of the materials without functionalization, (G) fibronectin/gelatine and (H) PLL functionalizations (N = 3).

Here, the wettability properties of graphene materials were evaluated with a VCA system, after overnight incubation of cell-adhesive solutions, as shown in **Figure 3.4 G** and **H** for fibronectin/gelatine and PLL functionalization, respectively. The transition from Cassie-Baxter to Wenzel wetting state was observed as well as a drastic hydrophilic inversion estimated over the graphene materials, especially in presence of NWs meshes. Indeed, measured contact angles of PLL-treated graphene substrates highlight an increase in hydrophilicity of  $\sim 43.9\%$ ,  $66.3\%$ ,  $78.4\%$  and  $84.3\%$ , in 2DG, 3DFG, NT-3DFGc and NT-3DFGnc materials, respectively.

Hydrophilicity increased also after the absorption of fibronectin/gelatine solution, whilst the effect was only distinctly noticeable in the case of out-of-plane topographies. Indeed, hydrophilic improvement was estimated to be nearly equal  $\sim 6.5\%$ ,  $41.9\%$ ,  $75.9\%$  and  $78.9\%$ , in 2DG, 3DFG, NT-3DFGc and NT-3DFGnc materials, respectively.

The overnight adsorption of either high positive charges for PLL solutions or protein components in the fibronectin/gelatine coating modifies the wetting behaviour of graphene materials by providing the chemical links to maximize the solid/water interface and, in turn, increase the hydrophilicity of the materials' surface. Moreover, compared to the planar graphene, the presence of air pockets between the protruding nano and micro graphene structures, in NT-3DFGc and nc materials, favours the liquid to flow through the cavities and across the surface.

### 3.2 Graphene-cell interface: general considerations.

Here, the different graphene materials have been characterized to primarily enable an optimal contact to cells and also modulate peculiar cellular processes at the interface such as polarization and outgrowth which ultimately regulate the cell-chip coupling on the long term. First, possible toxicity effects of the materials were evaluated through specific assays and investigation of physiological electrical activity of the cells.

HL-1 cells were used as cardiac cell model as they own morphological and electrophysiologic characteristics of adult cardiac monocytes; in addition, primary cortical neurons were employed for the investigation of the neuron-graphene materials coupling and its implications in the early development stage of neuronal outgrowth. Therefore, considering these peculiar cells properties, either nanoscale and microscale topography features were leveraged to study the possible effects they exerted on the cellular cytoskeleton reorganization and polarity, the attachment to the surface, possible initiation of endocytosis events, and ultimately on cellular metabolism.

However, it is important to highlight the key role of the cellular PM in the dynamics of interaction occurring at the interface between nanostructured materials and biological cells<sup>28</sup>. Indeed, the PM and its curvature-dependent arrangement govern the cell-material physical coupling through topography sensing and stabilization phases<sup>28,30</sup>. From the interaction with the underlying substrate, different scenarios might ensue (**Figure 3.5**): i) wrapping of cell membrane around the structures, ii) initiation of endocytosis events, iii) structure penetration through the cell membrane.

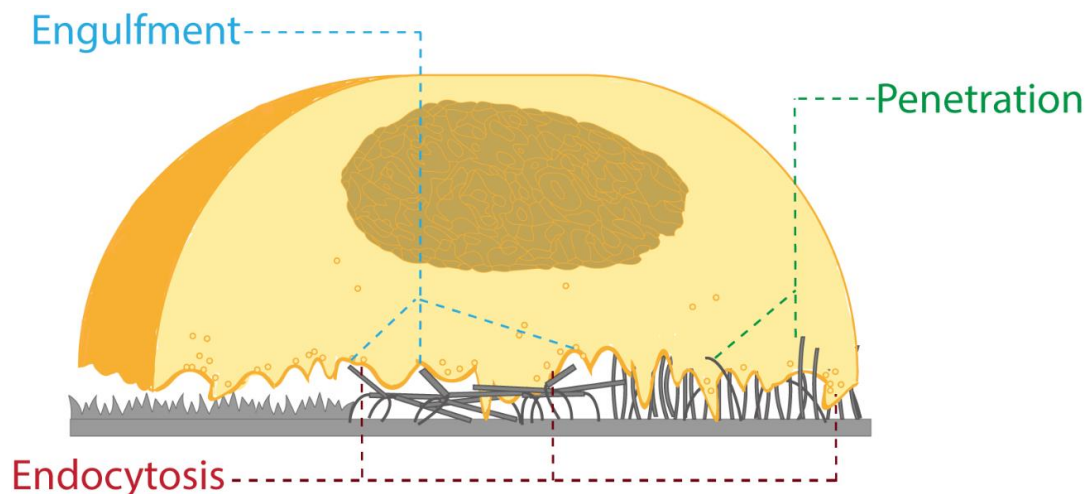
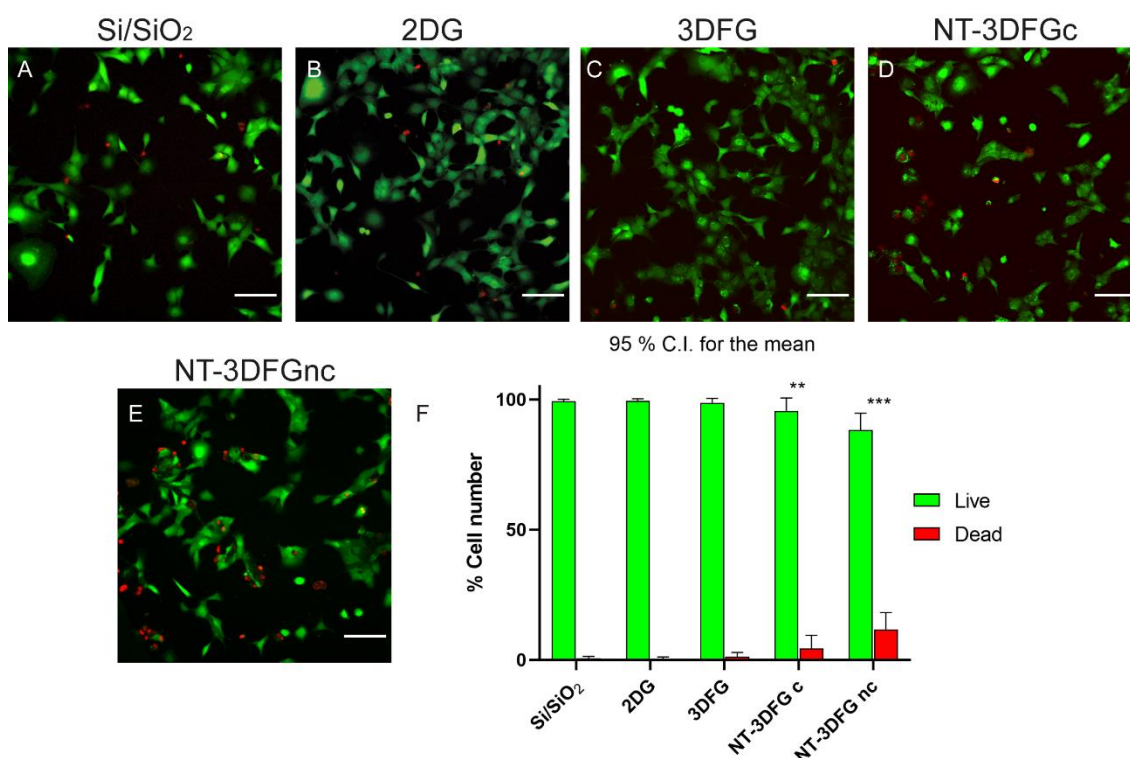


Figure 3.5. Schematics of possible mechanism at the cell out-of-plane material interface.

### 3.3 Biocompatibility of out-of-plane graphene materials.

#### 3.3.1 HL-1 cells viability.

Cytotoxic effects of out-of-plane materials were evaluated through a biocompatibility assay performed at 1 DIV. Therefore, live and dead cells populations were labelled with green and red fluorescence markers in Figure 3.6, respectively (Materials and methods 2.5.1 and 2.81). The statistics on the two populations is summarized in Figure 3.6 F. HL-1 cells showed higher viability on planar graphene than the control (Si/SiO<sub>2</sub>), while the percentage of live cells slightly decreased by increasing the dimensionality of the topography. In particular, besides the NT-3DFGnc culture, the overall percentage of living cells is in average larger than 90%. When cells were cultures on free-standing NWs meshes, cell viability was estimated to be nearly 88%.



**Figure 3.6. HL-1 biocompatibility assay.** Optical micrographs of HL-1 cultured on (A) Si/SiO<sub>2</sub>; (B) 2DG; (C) 3DFG; (D) NT-3DFGc; (E) NT-3DFGnc. Green fluorescence signal refers to live cells, red fluorescence signal refers to dead cells. Scale bar: 100 μm. (F) Quantification and statistical analysis of cell viability. Data are analyzed by one-way ANOVA with a Tukey- post-hoc test (GraphPad Prism 8.4.3) for 95% as confidence interval.

This might be due to the specific topography of the material and the possible piercing effect which might occur when individual cells are in contact at the NW tip. As a result, cell cytosol damage and homeostasis could be induced. However, previous studies showed the NWs effect to facilitate movement across cellular

and intracellular barrier, as well as loss in cellular stability owing to the high surface-to-volume ratio influencing cell viability<sup>119–121</sup>.

### **3.3.2 HL-1 Calcium Imaging.**

As a consequence of the adaptive process which drives cells to adhere onto protruding structures, internal relocation of cytoskeleton and organelles, including the sarcoplasmic reticulum (SR), and ultimately perturbation of metabolic processes might occur. Therefore, we investigated the metabolic activity associated to calcium ions ( $\text{Ca}^{2+}$ ), their diffusion across a highly confluent HL-1 cells monolayer. Remarkably, in cardiac monocyte, the rhythmic changes in the  $\text{Ca}^{2+}$  concentration are not only correlated to the occurrence of action potentials across cells but also support the contractile function of the cardiac tissue<sup>122–124</sup>. Therefore, the calcium ion flow was evaluated through live fluorescence imaging (**Materials and Methods 2.5.2 and 2.8.2**).

A  $\text{Ca}^{2+}$  wave is a complex spatio-temporal biological event that consists of a rhythmic increase and decrease in cytoplasmic  $\text{Ca}^{2+}$  concentration ( $[\text{Ca}^{2+}]$ )<sup>122,125,126</sup>. The dynamics of this biological event encompasses an early  $\text{Ca}^{2+}$  ions influx within the cellular body through voltage-gated L-type  $\text{Ca}^{2+}$  channels (LTCC) activation during membrane depolarization. The resulting increase of  $\text{Ca}^{2+}$  concentration triggers a second  $[\text{Ca}^{2+}]_i$  amplification by  $\text{Ca}^{2+}$  release from the SR  $\text{Ca}^{2+}$  store through a mechanism called  $\text{Ca}^{2+}$ -induced  $\text{Ca}^{2+}$  release (CICR). The ensuing availability of free  $\text{Ca}^{2+}$  ions throughout the cytoplasm volume allows to activate the myofilaments contractile machinery<sup>122,127</sup>. However, changes in  $[\text{Ca}^{2+}]_i$  usually assumes a rhythmic pace where contraction phases are always balanced by relaxation ones, which require  $[\text{Ca}^{2+}]_i$  decline and free  $\text{Ca}^{2+}$  ions transport out of the cytosol. Moreover, these  $\text{Ca}^{2+}$  dynamics spatially expands from a localized  $\text{Ca}^{2+}$  puff within the single cell body to a large-scale propagating movement of ions from one cell to the next adjacent ones<sup>125,126</sup>.

Here, studying the signal propagation might either give insights about single cell metabolism or network interaction (cell-cell communication). However, a homogeneous  $\text{Ca}^{2+}$  wave within the entire cell volume or among a cell layer relies on the mutual interaction of LTCCs and SR during both contraction and relaxation period, as well as on an elaborate network of tubules which brings in close proximity the two entities.

Here, HL-1 cells were cultured on the different substrates to reach 90% of confluency after 1 DIV. Then, after labelling with Fluo-AM (**Materials and Methods 2.5.2**), live fluorescence microscopy acquisition was performed to record movies of the  $\text{Ca}^{2+}$  flow for 30 s at  $\sim 17$  frame/s (**Materials and Methods 2.8.2**). The pre-set acquisition rate enables to follow the transient increasing and decreasing of  $[\text{Ca}^{2+}]$  and propagating phenomena across the single cell body or cell layer. Here, the intercellular  $\text{Ca}^{2+}$  wave propagation speed

(or  $\text{Ca}^{2+}$  wave propagation velocity, CPV), frequency and wave fronts provide information on the effect that the graphene materials might have on the cell electrical activity. The average propagation velocities are reported in **Table 3.1**. Slightly faster propagation was recorded when HL-1 cells were in contact with the nanoscale features of 3DFG materials, compared to the planar case and the control. Possibly, the presence of protruding graphene flakes locally pushes the cell membrane inwards, facilitating a close apposition of the SR and the plasma membrane that hosts LTCCs. On the contrary, in the case of the NT-3DFGc cultures, characterized by microcavities and collapsed wires, the wave velocity was significantly slowed down. Finally, in the case of the NT-3DFGnc cultures, the detected intracellular  $\text{Ca}^{2+}$  transients fail to propagate across the confluent layer of cells. Probably, this results from the presence of vertical wires that pin the plasma membrane in several points, by restraining and hamper a proper cell-cell communication. Significantly, this prevents the  $\text{Ca}^{2+}$  wave development and propagation.

<b><math>\text{Ca}^{2+}</math> wave propagation speed [mm/s]</b>		
	Velocity	Standard deviation
Si/SiO <sub>2</sub>	0.87	0.010
2DG	1.22	0.013
3DFG	1.27	0.0250
NT-3DFG c	0.76	0.013
NT-3DFG nc	-	-

**Table 3.1. Calcium wave speed quantification of HL-1 cells culture on the different graphene materials.**

In addition to the speed analysis, **Figure 3.7** reports the probability of a specific  $\text{Ca}^{2+}$  wave speed, estimated for each culture type, to occur. Therefore, larger probability density function (PDF) values correspond to more recurrent velocity. The average propagation speed in both Si/SiO<sub>2</sub> and NT-3DFG was about 0.8 mm/s while in the case of 2DG and 3DFG cultures was 1.2 mm/s. However, the overall speed values result to be in average lower than previously reported<sup>123</sup>. This decrease in CPV was attributable to the effective temperature (25°C) maintained during the experiment which it is known to affect the cell activity<sup>128,129</sup>, rather than to a possible negative effect that out-of-plane topographies could have on the final velocities.

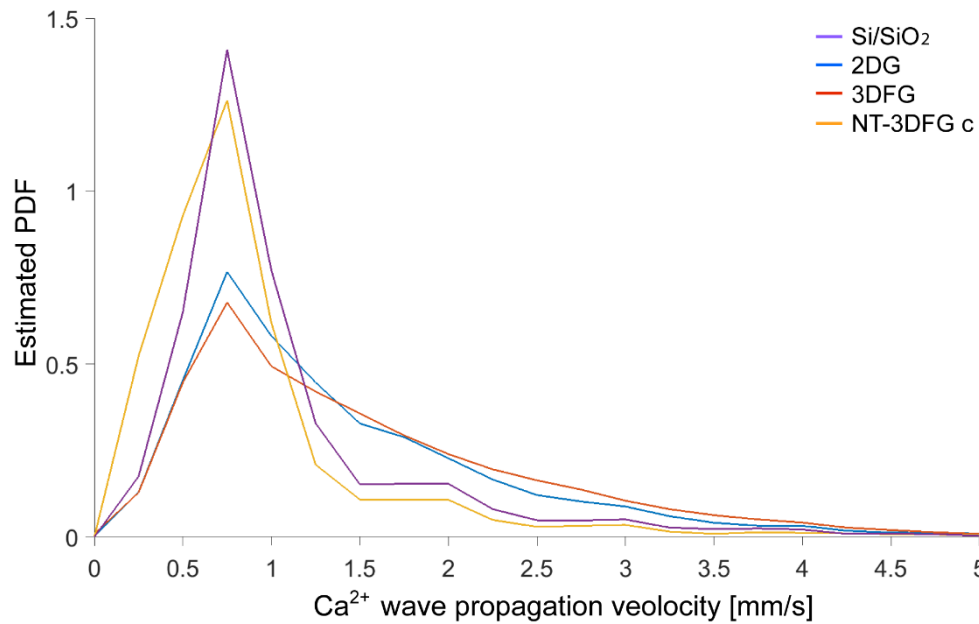


**Figure 3.7.  $\text{Ca}^{2+}$  wave speed incidence.**  $\text{Ca}^{2+}$  wave incidence plotted as function of its velocity (mm/s).

Therefore, the *x-axis* of the graph represents the propagation velocity of the waves, whereas, on the *y-axis* there are the normalized observation frequencies (essentially the number of observations for each value of wave propagation velocity, on *x*, divided by the total number of observation).

To further investigate the spontaneous  $\text{Ca}^{2+}$  activity across a confluent layer of cells cultured on the graphene materials, the fluorescence intensity profiles, identified by rising (increase in  $[\text{Ca}^{2+}]_i$ ) and decay phases (consecutive decrease in  $[\text{Ca}^{2+}]_i$ ), were represented for each substrate as function of the acquisition time ( $T_A$ ). In the case of HL-1 cells culture on Si/SiO<sub>2</sub> (**Figure 3.8 A**), distinct  $\text{Ca}^{2+}$  peaks were recognized. **Figure 3.8 B** shows the  $\text{Ca}^{2+}$  ions propagation in cells cultured on planar graphene material. Here, due to the presence of a sequential  $\text{Ca}^{2+}$  spikes, the trailing edge of each wave fails to reach the minimum intensity value, typical of a  $[\text{Ca}^{2+}]$  decay phase. Therefore, in this condition, abortive waves (which do not achieve the minimum fluorescence value) were succeeded by regenerative  $\text{Ca}^{2+}$  waves. Conversely, as shown in the propagation profile originating by HL-1 cultured on 3DFG (**Figure 3.8 C**), each  $\text{Ca}^{2+}$  sparks looked confined in time and space, with sharp and distinct peaks. Thereby, when cultured on nanoscale topography, cells retain a constant frequency of oscillation during the  $T_A$ , where each wave sparks and fades its fluorescence independently from the other waves.

The  $\text{Ca}^{2+}$  fluorescence signal generated by HL-1 cells cultured on the NT-3DFGc template, was significantly lower compared to the other cases, as shown in **Figure 3.8 D**.

Each fluorescence peak, representative of a single  $\text{Ca}^{2+}$  wave, looked broader (as a matter of fact, higher fluorescent values were retained for longer) and often showed more than one apex (higher fluorescent value). This additive or regenerative  $\text{Ca}^{2+}$  waves event was due to secondary waves originated by other cell pacemaker, which appeared in different areas and originated from the initial triggering region (within the analyzed field of view). Arguably, NT-3DFGc geometry-derived cellular dislocation often allows the creation of cellular independent pacing areas.

Finally, **Figure 3.8 E** depicts the fluorescence signal originated in the intracellular domain. Short consecutive spikes, representing rising and decay phases of  $[\text{Ca}^{2+}]_i$ , fail to become propagating intercellular wave due to the restricted cell-cell communication, which is hampered by the microscale protruding features of the NT-3DFGnc topography. The discrepancies in  $\text{Ca}^{2+}$  wave propagations highlight the great influence the topographical cues might have in singularly cueing cells, promoting their architecture remodelling and influencing their metabolism.

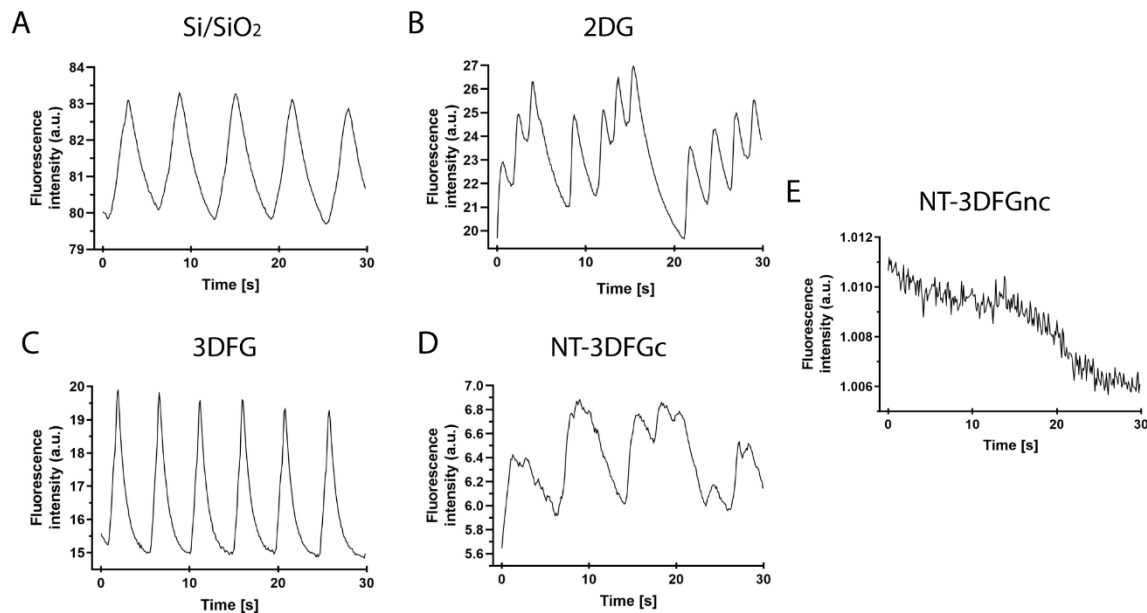


**Figure 3.8. Kymographs of  $\text{Ca}^{2+}$  ions flow.** Fluorescence intensity profiles of  $\text{Ca}^{2+}$  wave events, across (A) Si/SiO<sub>2</sub>, (B) 2DG, (C) 3DFG, (D) NT-3DFGc and (E) NT-3DFGnc cultures, were plotted as function of  $T_A$  (N=10).

Previous studies already highlighted the potential contribution cardiac tissue architecture has in dictating its electrophysiological activities<sup>170-172</sup>. Indeed, as pathological remodelling of cardiac tissue occurring after myocardial infarction or hypertrophy, directly affects the generation of path and velocity propagation of electric signals and  $\text{Ca}^{2+}$  ions flow, similarly *in vitro*, topography-driven cardiac architecture changes,

contribute to different electrical signalling dynamics. Notably, this is due to the ensuing distribution of gap junctions' structures which provide low-resistance channels for action potential and  $\text{Ca}^{2+}$  wave to flow through<sup>171</sup>. The presence of resistive discontinuities profoundly affects electrical impulse initiation and propagation. Thus, elongated and aligned cardiac engineered cell cultures, which better replicate the cardiac striated architecture, present faster electrical activity along the axis of the cardiac fibres<sup>170,172</sup>. Instead, the discontinuous nature of propagation, which are encountered in isotropic cell architectures and produced by the discrete nature of cardiomyocytes, might markedly alter the action potential and  $\text{Ca}^{2+}$  wave propagations which result to be slower<sup>170</sup>.

Equally, the physical presence of graphene protruding NWs, in NT-3DFGc and nc, might limit resistive continuum through the HL-1 cell layer, by influencing the propagation and initiation of  $\text{Ca}^{2+}$  waves. On the contrary, the nanoscale nature of 3DFG does not prevent cells to be separated but rather supports a continuous cells monolayer, which results in faster electrical dynamics.

### ***3.3.3 Primary cortical neuronal cells viability.***

Cytotoxicity assays were also carried out in the case of primary neuronal cultures on the diverse graphene materials. Viability experiments were performed at 3 and 5 DIV by labelling live and dead cell populations with Calcein AM and Ethidium Homodimer, respectively (**Materials and methods 2.5.1**) as depicted in **Figure 3.9 A – E**. Similarly to HL-1 cell culture, the higher percentage of dead cells was found in correspondence of wired meshes (**Figure 3.9 F**).

Moreover, the mortality rate between 3 and 5 DIV was evaluated. As shown in the **Figure 3.9 F**, in the case of planar cultures (both Si/SiO<sub>2</sub> and 2DG), the incremental rate of mortality, resulting from the angular coefficients, was almost similar and hovered around  $\sim 6.9 \pm 0.3 \%$ , while the mortality rate was among  $\sim 9.1 \pm 0.1 \%$ ,  $7.4 \pm 0.3 \%$ ,  $3.9 \pm 0.2 \%$ , in the case of 3DFG, NT-3DFGc and NT-3DFGnc cultures.

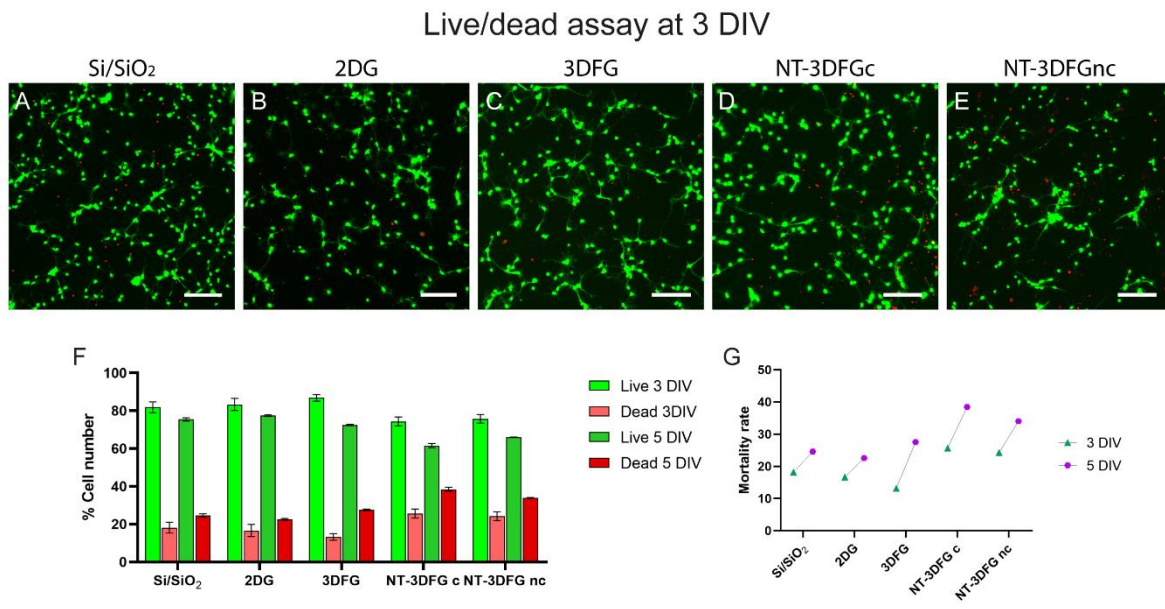


**Figure 3.9. Neuronal cells viability on graphene materials.** Exemplary fluorescence micrographs at 3 DIV of cells cultured on (A) Si/SiO<sub>2</sub>, (B) 2DG, (C) 3DFG, (D) NT-3DFGc and (E) NT-3DFGnc. Green refers to live cells, instead, red signal to dead cells. Scale bars 100 μm. (F) Percentage of live and dead cell populations at 3 and 5 DIV, (N = 3). (G) Mortality rate between 3 to 5 DIV, (N = 3).

### 3.4 Growth and adhesion modulation of cardiomyocytes-like by means of graphene topography.

#### 3.4.1 HL-1 cell area and height modulation by out-of-plane graphene materials.

To evaluate the effect of the different graphene-based materials on the cell adhesion and spreading, the cells' morphology was first investigated through the analysis of the spreading area.

The spreading area was quantified by tracing the cell perimeter (**Materials and Methods 2.8.3**), measuring the average area values and then performing an ANOVA statistical analysis (**Figure 3.10 and Table 3.2**).

In the case of planar materials and 3DFG, HL-1 cells exhibit a significant spreading without a preferential direction, as effectively no relevant topographical features might physically confine the cells. However, in presence of NW-templated graphene materials (both collapsed and non-collapsed NWs arrangements), cells have a smaller spreading area suggesting that the discontinuous adhesive surface, due to the alternating presence of exposed tips, microcavities and NWs sidewalls (in NT-3DFGc), or the presence of separate free-standing and kinked wires (in NT-3DFGnc material) hinders cells to spread.

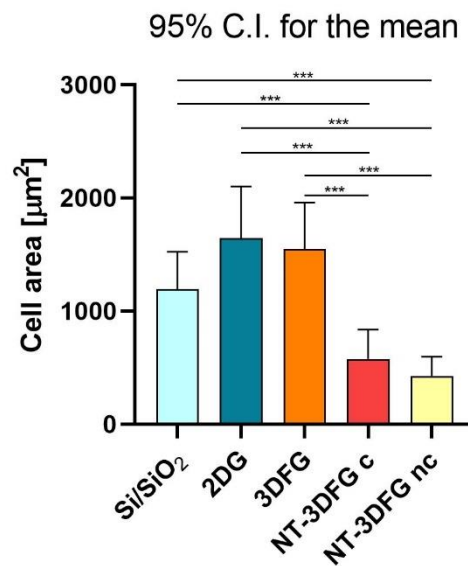


Figure 3.10. Average area of HL-1 cells cultured on the graphene substrates. Data are analyzed by OneWay ANOVA with Tukey- post-hoc test for at least 95% confidence interval.

Significant difference of cell area [μm<sup>2</sup>]

		p-value	Significant difference for $\alpha = 0.05$
Si/SiO <sub>2</sub>	2DG	0.167	-
Si/SiO <sub>2</sub>	3DFG	0.141	-
Si/SiO <sub>2</sub>	NT-3DFGc	< 0.001	✓

Si/SiO <sub>2</sub>	NT-3DFGnc	< 0.001	✓
2DG	3DFG	0.579	-
2DG	NT-3DFGc	0.002	✓
2DG	NT-3DFGnc	0.001	✓
3DFG	NT-3DFGc	< 0.001	✓
3DFG	NT-3DFGnc	< 0.001	✓
NT-3DFGc	NT-3DFGnc	0.691	-

**Table 3.2. Significant differences of cell area at 95% confidence interval performing a OneWay ANOVA analysis.**

OneWay Anova analysis further confirm the impact the physical features of the topographies have on cell morphology. Considering the significant level equal to 5 % (it means  $\alpha = 0.05$ ), if:

- $p > \alpha \rightarrow$  the difference of the two means is not significant; [ 5 ]
- $p < \alpha \rightarrow$  the difference of the two means is significant.

If nanoscale structures given by exposed graphene flakes in 3DFG do not confine cells to occupy large regions, both collapsed and non-collapsed wires rather impose physical constraints to cells. These results confirm that cells are able to sense differences in surface roughness, as well as discriminate between differently sized surface structures as previously shown<sup>37,41,130,131</sup>. The informative cues exchanged at the interface between cells and material might produce a robust morphological cellular response as previously demonstrated in the case of cells cultured on ordered straws or microfabricated grooves where cell polarization was effectively driven by the directionality imposed by the material topography<sup>35</sup>. Moreover, vertical structures as pillars or wires, have been shown to also restrict cellular spreading to ultimately induce a spheroidal cell morphology<sup>37,46,132</sup>.

Here, we further analyzed the cellular morphology and volume by fluorescence labelling the plasma membrane with wheat germ agglutinin (WGA, **Materials and Methods 2.6.5**) and acquiring confocal z-stack micrographs fixing a slice thickness ( $\Delta h$ ) of 0.25  $\mu\text{m}$ . 3D reconstructions of sequential micrographs (**Materials and methods 2.8.7, Figure 3.11 A-E**) revealed that the overall cell volume was in average 1200-1600  $\mu\text{m}^3$  independent of the culture substrate, while the cell height was significantly different (**Figure 3.11 F, Table 3.3**). In both NT-3DFG configurations, with collapsed and free-standing NWs, the reduced area for cellular growth, provided by few anchoring sites, induced a cell reshaping (*i.e.*, pinning – yellow arrow in **Figure 3.11 E**) which results in a more complex cellular arrangement than the flattening occurring on planar

substrates or in the case of 3DFG. Indeed, in the attempt to find new adhesion points to grasp, cells on NWs meshes were able to grow in depth along the vertical structures.

Comparable topography to NWs templates was reported by *Lee et al.* where Zinc oxide (ZnO) vertical nanorods were interfaced with three different cell lines (NIH 3T3, HUVEC and BCE) to study their viability and adhesion dynamics<sup>173</sup>. With reference to the ZnO flat configuration, cell spreading processes were markedly altered by the presence of protruding structures which reduced greatly cellular extension area. Equally, *Formentín et al.* found out less elongated and more compact and rounded human aortic endothelial cells after 2 DIV when interfaced human aortic endothelial cells with SiO<sub>2</sub> micropillars in ordered and random distributions, compared to flat control surface<sup>174</sup>.

Taken together, cell spreading processes were considerably affected by the topographies, especially when the material features sizes were comparable to the cellular dimensions. Indeed, NWs arrangements, in NT-3DFGc and nc, physically confine cells to freely spread in xy direction, however HL-1 cells adapt and spread on the top and in between the protruding microstructures, which ultimately results in larger cellular height. Differently, topographic features commensurate in size to sensorial organelles, as in the case of fuzzy graphene, promote cell adhesion and flattening on the xy plane, which results larger coverage area and smaller height, as also it occurs in planar cultures.

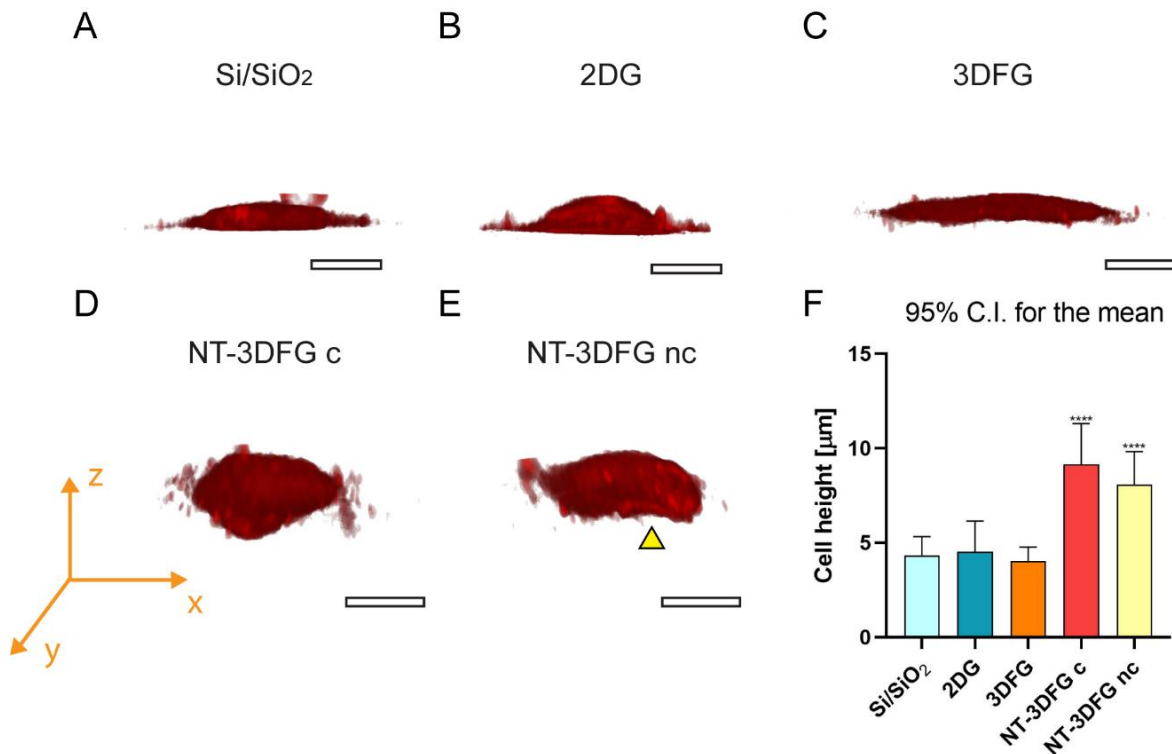


**Figure 3.11. 3D HL-1 cell membrane reconstruction by confocal microscopy and cell height analysis.**

Z-Stack of WGA-labelled HL-1 cells were acquired at 1 DIV by fixing the slice thickness at 0.25  $\mu\text{m}$ . 3D reconstruction of cell body was provided for HL-1 cultured on (A) Si/SiO<sub>2</sub>, (B) 2DG, (C) 3DFG, (D) NT-3DFGc and (E) NT-3DFGnc. Scale bar 10  $\mu\text{m}$ . (F) Cell height measurement by one-way ANOVA with a Tukey- post-hoc test for at least 95% confidence.

**Significant differences between HL-1 cells heights [ $\mu\text{m}$ ]**

		p-value	Significant difference for $\alpha = 0.05$
Si/SiO <sub>2</sub>	2DG	0.993	-
Si/SiO <sub>2</sub>	3DFG	0.971	-
Si/SiO <sub>2</sub>	NT-3DFGc	< 0.0001	✓
Si/SiO <sub>2</sub>	NT-3DFGnc	< 0.0001	✓
2DG	3DFG	0.713	-
2DG	NT-3DFGc	< 0.0001	✓
2DG	NT-3DFGnc	< 0.0001	✓
3DFG	NT-3DFGc	< 0.0001	✓
3DFG	NT-3DFGnc	< 0.0001	✓
NT-3DFGc	NT-3DFGnc	0.092	-

**Table 3.3. Significant differences of HL-1 cells height at 95 % confidence interval by one-way ANOVA analysis.**

### **3.4.2 HL-1 cells polarization, actin and focal adhesion proteins organization.**

As discussed in **Chapter 1**, micro and nanopatterned materials can modulate certain cellular processes such as polarization and eventually migration<sup>41</sup>. Here, contact guidance might determine cells' elongation, during the polarization progress, through the competing influence of intracellular and extracellular cues<sup>34,41</sup>. Cell elongation involves two basic internal mechanisms: actin polymerization and focal adhesion proteins organization.

Filamentous actin (F-actin), complemented microtubules, and intermediated filaments represents a component of the cell cytoskeleton. It provides internal mechanical support, aids movements of intracellular materials and sustains and strengthen the plasma membrane during the cellular elongation and motion<sup>133</sup>. F-actin represents only a part of the cytoskeleton that supports cell structures. Although, it

is one of the smallest filamentous components (with a diameter of about 10 nm), under physiological conditions the polymerization and assembly of actin filamentous into thicker stress fibres can occur. Those thicker structures suffice to change the shape of the cells, as well as produce membrane protrusions<sup>133</sup>. Equally, the shaping of adhesive structures, the FAs, is crucial in the modulation of the crosstalk between cells and substrate underneath. These supramolecular complexes are made of integrin proteins, direct mediators of the interaction with the extracellular environment, adapter proteins (*i.e.*, talin, vinculin and paxillin)<sup>134</sup> which are associated to the cytoplasmic domains of the integrin, cytoskeleton elements and signalling molecules. Altogether these constituents not only modulate cellular attachment, but also participate to the “outside-in” transmission of mechanical cues (physical and structural activities) as well as “inside-out” biological signals (signalling tasks)<sup>135,136</sup>.

Therefore, to study cellular polarization, cytoskeleton arrangement and FAs formation triggered by the presence of the different graphene materials, F-actin and paxillin proteins were first labelled through immunohistochemistry after 1 DIV (**Materials and Methods 2.6.1**) and then confocal fluorescence micrographs were acquired (**Materials and Methods 2.7**).

**Figure 3.12** shows the z-stack optical cross sections acquired by fixing the slice thickness ( $\Delta h$ ) of 0.125  $\mu\text{m}$ . Xz and zy views depict the actin spatial arrangement which on planar and nanoscale topography encircle the nucleus and populate the peripheral cortex (**Figure 3.12 A, B** and **Annex A.1**). In contact with NW-templated materials, the actin cytoskeleton acts either as an intracellular barrier to NW-tip penetration or as physical spacer together with the membrane to isolate the internal cytoplasm from the outer environment (**Figure 3.12 C, D**). Therefore, denser actin fluorescence signals were recognized solely at basal membrane when NWs were in collapsed arrangement, whereas both at the basal and apical membranes in non-collapsed configuration. In this case, the actin accumulation could indicate that possible engulfment events might have occurred when cells are interfaced with needle-like structures as the NW tips.

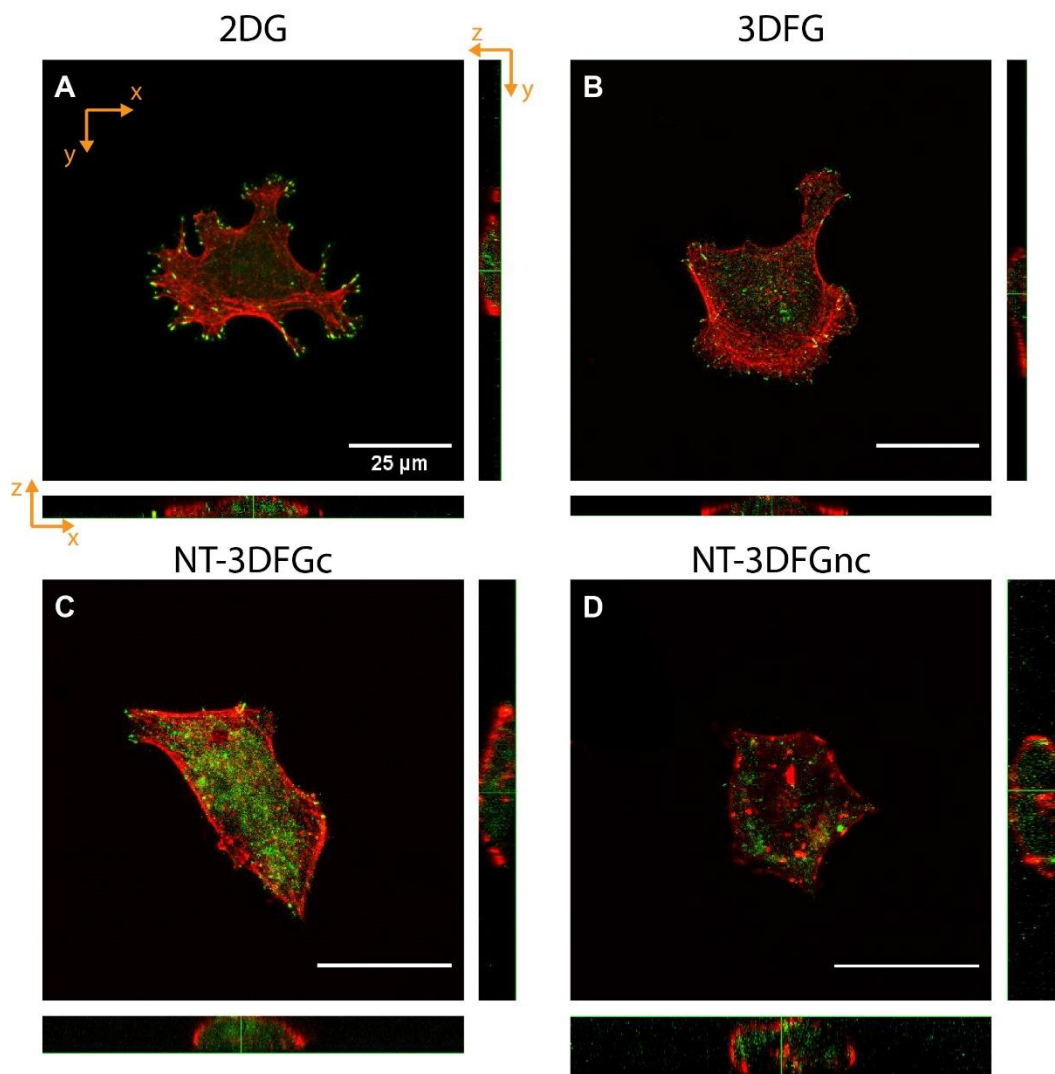


**Figure 3.12. Optical cross sections.** Z-stack fluorescence images ( $xy$  plane) and optical cross sections (bottom  $xz$  plane, right  $yz$  plane) of HL-1 on (A) 2DG, (B) 3DFG, (C) NT-3DFGc, (D) NT-3DFG nc labelled against actin filaments in red and paxillin proteins in green. Slice thickness was fixed at  $0.125\ \mu\text{m}$ ; scale bar  $25\ \mu\text{m}$ .

Moreover, the cell morphology was evaluated considering a classification in non-polar and polar configurations. Non-polar cells show no discernible front or rear regions, or prominent extensions from the central body while polar cells present two or more prominent extensions that protrude outside the main cell body as shown in **Figure 3.13 A, B**. The percentage of non-polar and polar cells (**Figure 3.13 C**) was determined considering the acquired optical images. HL-1 cells cultured on planar and 3D fuzzy graphene showed mainly a polar morphology while in the out-of-plane cultures, cells mostly arranged in a non-polar configuration.

Cell polarization was further evaluated through the analysis of the minimum and maximum axis average length (Materials and Methods 2.8.3, Figure 3.13 D) and their aspect ratio (Figure 3.13 E) defined as:

$$\text{Aspect ratio} = \frac{\text{minimum cell axis}}{\text{maximum cell axis}} \quad \left. \begin{array}{l} 1 \rightarrow \text{cell form a perfect circle.} \\ 0 \rightarrow \text{cell show a polarized shape.} \end{array} \right\} [6]$$

No significant differences in polarization were found comparing the morphological behaviours across the different topographies as supported by the OneWay Anova test (Table 3.4). Indeed, aspect ratios were in the range 0.6 - 0.7 (Figure 3.13 E). Despite of the measured values that could be interpreted as a similar cell polarization across the different graphene topographies, standard deviations have high values. These findings were fundamentally due to the presence of polarized cells along with the circular ones over the substrates, as illustrated in Figure 3.13 C.

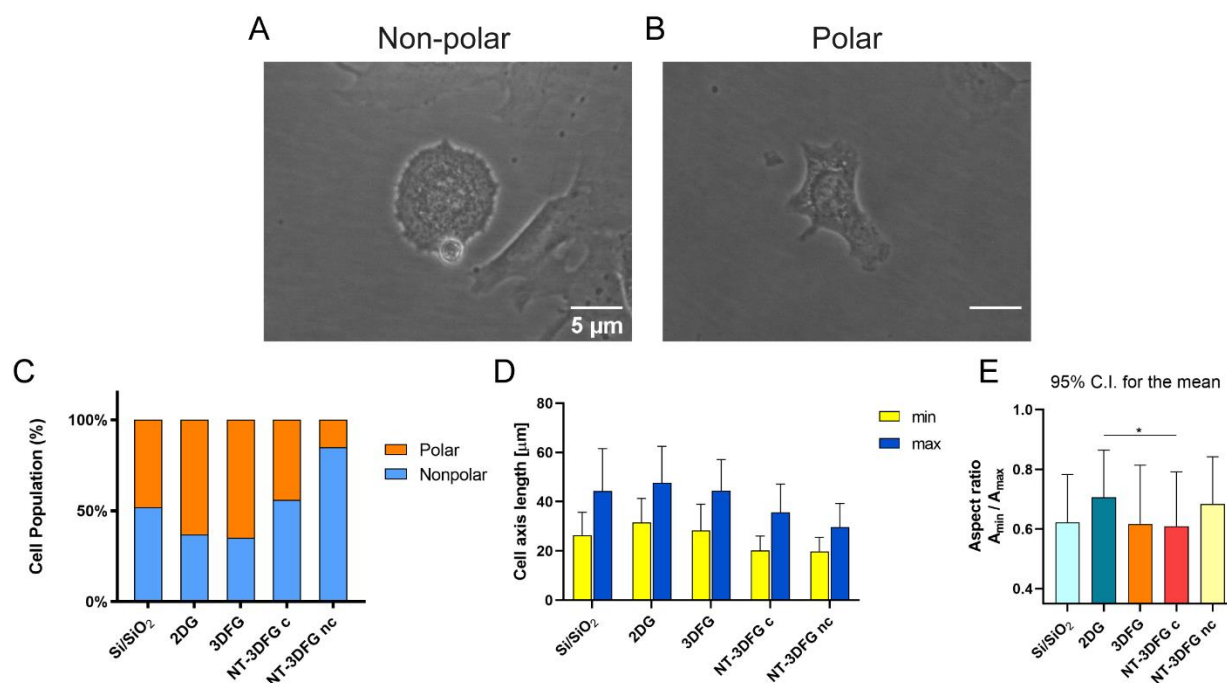


**Figure 3.13. Cell morphology analysis.** Brightfield images of a (A) non-polar and (B) polar HL-1 cells; (C) Percentage of non-polar and polar cell populations across all substrates; (D) Quantification of minimum and maximum cellular axes length. (E) Axis aspect ratio quantification and analysis with OneWay Anova with Tukey-post-hoc test at 95 % confidence interval.

Significant difference of polarization ratio

		p-value	Significant difference for $\alpha = 0.05$
Si/SiO <sub>2</sub>	2DG	0.106	-
Si/SiO <sub>2</sub>	3DFG	> 0.999	-
Si/SiO <sub>2</sub>	NT-3DFGc	0.996	-
Si/SiO <sub>2</sub>	NT-3DFGnc	0.373	-
2DG	3DFG	0.075	-
2DG	NT-3DFGc	0.042	✓
2DG	NT-3DFGnc	0.968	-
3DFG	NT-3DFGc	0.999	-
3DFG	NT-3DFGnc	0.294	-
NT-3DFGc	NT-3DFGnc	0.194	-

Table 3.4. Significant difference of polarization ratio at 95 % confidence interval.

In addition to the polar vs. non-polar classification, the F-actin arrangement and expression was further investigated. In fact, on planar substrates, HL-1 cells exhibit thick actin bundles which support internal scaffolding (**Figure 3.14 A-D**). Here, quasi-circular cells have a predominant presence of F-actin at the cell periphery while in the case of polarized cells, the actin network is homogeneously distributed at the cell body.

Similarly, HL-1 cells cultured on 3DFG develop long and thick fibres within the cell body, however in non-polar cells these fibres were mainly located at the cortical region (**Figure 3.14 E, F**).

HL-1 cells cultured NWs mesh templates (NT-3DFG materials), showed a different actin organization characterized by accumulation points. Indeed, in the case of collapsed NWs, over NT-3DFGc template, shorter and thinner actin filaments were complemented with clusters, sporadically recognized at the cell-substrate contact area (**Figure 3.14 G, H**). In addition, the free-standing NWs of NT-3DFGnc triggered actin accumulation as shown in **Figure 3.14 I, J**. Here, despite few NWs in kinked configuration, the majority of the wires expose their tips directly to be in contact with the basal membrane of cells, where the actin fluorescence signal exhibits accumulation points. Therefore, in both NT-3DFGc and nc cultures, actin assemblies into few thick and long fibres were completely reduced and accumulation points often developed when cells encounter NWs tips as contact sites. Possibly, the cytoskeleton distribution with actin accumulation sites might operate as intracellular scaffolding barrier to the single nanowire-tip

penetration<sup>137</sup> or eventually stabilizes the cell attachment over the protruding structures, which is highly beneficial with designed pseudo-3D electrodes in bioelectronics<sup>6</sup>.

As discussed in **Chapter 1**, the interaction between cells and out-of-plane materials modulates the spatial organization of cytoskeletal components, and in particular the actin architecture, whose arrangement resembles rings/caps or clusters at the contact points with the structured materials.

The limited available surface liable for cellular adhesion and the initial bending of the PM during the adaptative process to conform to the underneath structures dictate actin filament polymerizations as well as the dynamics of cell spreading, as already reported in literature<sup>30,43</sup>.

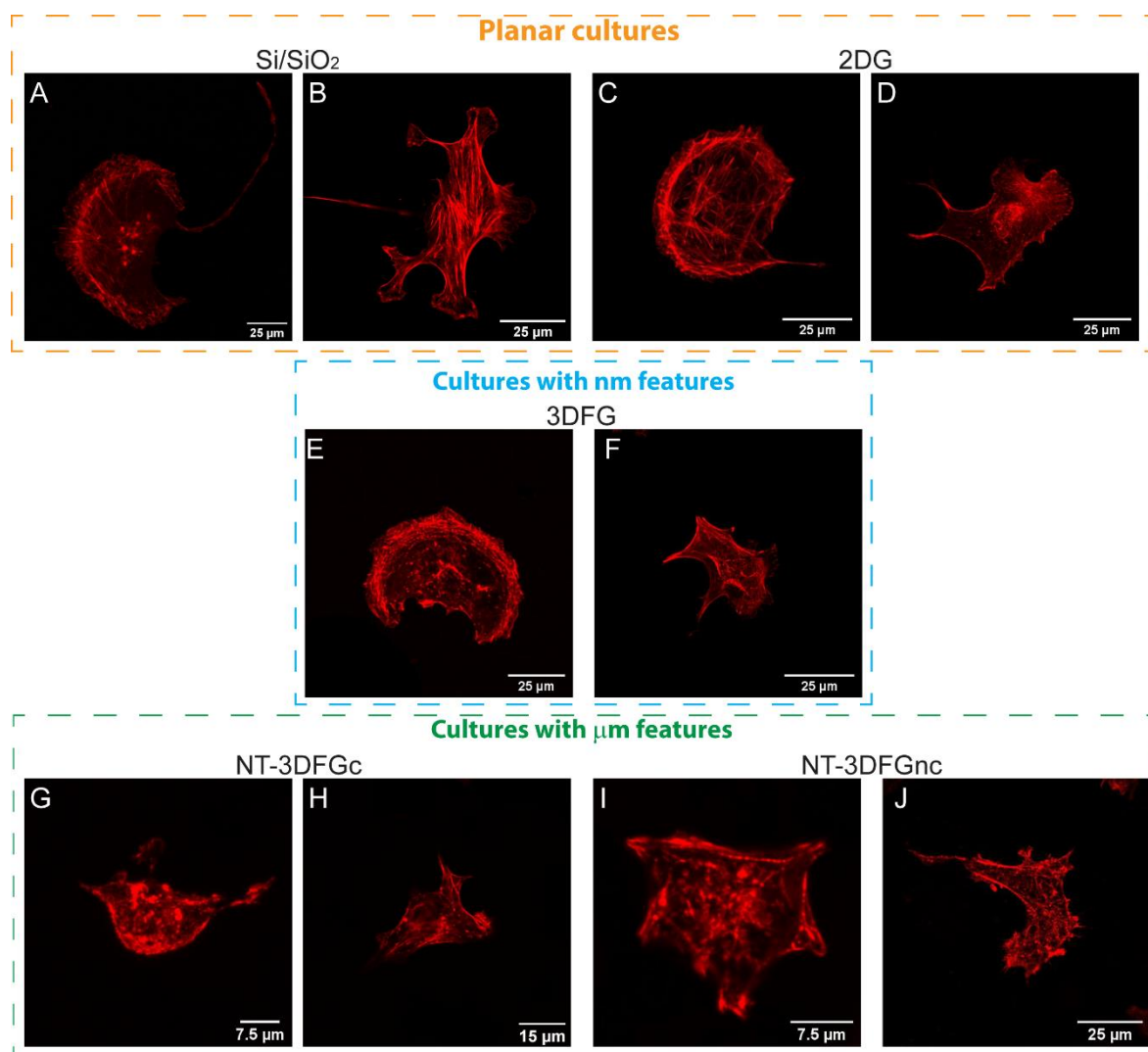


**Figure 3.14. Actin organization in HL-1 cell cultures on the different graphene substrates.** F-actin was fluorescently labelled with Phalloidin-555 in the case of Si/SiO<sub>2</sub> (non-polar and polar configurations in A, B, respectively), 2DG (non-polar and polar configurations in C,D, respectively), 3DFG (non-polar and polar

configurations in E, F, respectively), NT-3DFGc (non-polar and polar configurations in G, H, respectively) and NT-3DFGnc (non-polar and polar configurations in I, J, respectively).

Furthermore, to evaluate the F-actin protein expression, we analyzed the intensity profiles extracted from the fluorescence micrographs as previously described (**Materials and Methods 2.8.4**)<sup>139</sup>. The statistical analysis was carried out through a OneWay Anova test. As shown in **Figure 3.15**, the highest F-actin intensity was found when cells were cultured on the 3DFG material. Here, actin fibres were yet longer and thicker compared to the other materials. However, from the OneWay Anova analysis, no significant difference was found in comparison to the 2DG case (p-values are indicated in **Table 3.5**). HL-1 cells in contact either with planar or fuzzy graphene, were able to build longer actin bundles and ultimately an interlaced actin internal scaffold. Notwithstanding the presence of actin accumulation sites at the interface with NWs tips, the fluorescence signals collected from cells cultured on NT-3DFG templates were, instead, milder. Indeed, beside the actin accumulation spots, sparsely distributed within the HL-1 cell bodies, only few short actin filaments were recognized. In contrast, interwoven and long actin bundles formed in the whole cell body, with an increased density at the peripheral regions when cells assumed a non-polar configuration. Here, the average fluorescence intensity value was correlated to the protein expression level: lower fluorescence values correspond to reduced expression of the target proteins, which is in line with the overall decrease of the number of actin stress fibres formed in the case of cultures with protruding topographies<sup>43,46,140</sup>.

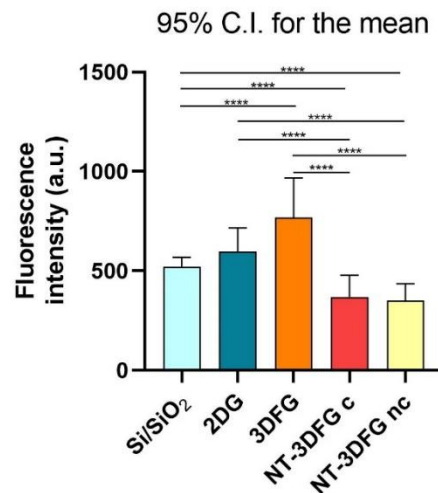


**Figure 3.15.** Average actin-associated fluorescence intensity quantification at 95 % confidence interval. Data were analyzed with OneWay Anova with Tukey- post-hoc test at 95 % confidence interval.

Significant difference of F-actin fluorescent signal [a.u.]			
		p-value	Significant difference for $\alpha = 0.05$
Si/SiO <sub>2</sub>	2DG	0.849	-
Si/SiO <sub>2</sub>	3DFG	0.012	✓
Si/SiO <sub>2</sub>	NT-3DFGc	0.054	✓
Si/SiO <sub>2</sub>	NT-3DFGnc	0.036	✓
2DG	3DFG	0.143	-
2DG	NT-3DFGc	0.004	✓
2DG	NT-3DFGnc	0.002	✓
3DFG	NT-3DFGc	< 0.001	✓
3DFG	NT-3DFGnc	< 0.001	✓
NT-3DFGc	NT-3DFGnc	0.999	-

**Table 3.5. Significant difference of F-actin fluorescent signals at 95 % confidence interval.**

Similarly, cellular adhesion was analyzed by labelling the integrin-associated protein paxillin which binds the cytoplasmic tail of the integrin. Thus, the distribution and expression of paxillin proteins were evaluated through confocal microscopy to characterize the assembly of FAs.

**Figure 3.16 A, B** and **Figure 3.17 A, B** show FAs localization when HL-1 were cultured on planar materials: here dense FAs plaques form at the extremity of actin fibres to link intracellular cytoskeleton to the outer space. In particular, beside elongated fibrillar adhesion at the actin extremities, numerous attachment locations were found over the entire cell ventral surface (**Figure 3.16 A, B**).

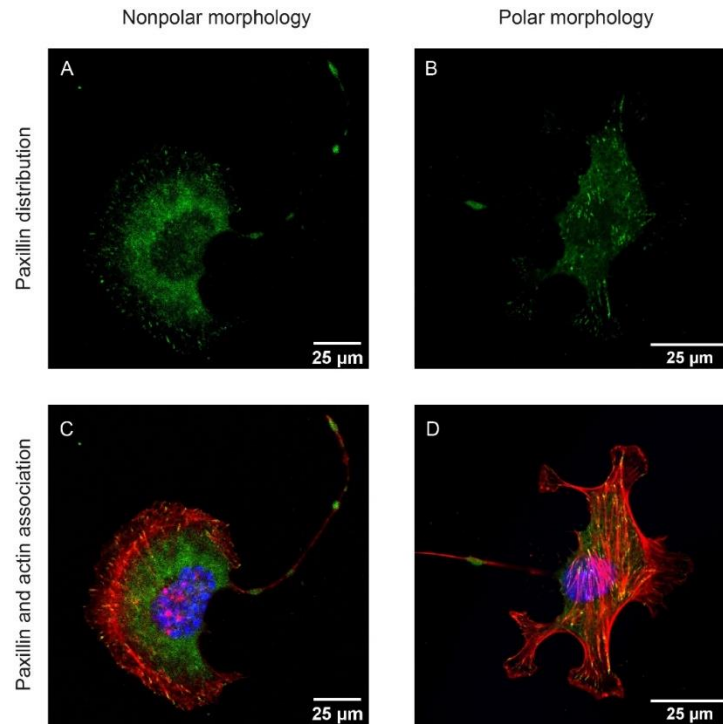


**Figure 3.16.** HL-1 paxillin distribution and its association with actin fibers on Si/SiO<sub>2</sub>.

(A, B) Paxillin distribution of non-polar and polar cells cultured on planar Si/SiO<sub>2</sub>.

(C, D) FAs association with actin fibres extremities in non-polar and polar configuration.

The transition from molecular to supramolecular adhesive complexes, typical of the protein clustering process, is characterized by an increase in FAs length and total area, as well as association with the terminal ends of actin stress fibres<sup>136</sup>. Therefore, in both Si/SiO<sub>2</sub> or 2DG cultures the continuous surface area available to cells, enables the formation of mature and stable adhesion patches. As a matter of fact, stable FA assemblies require close integrin ligand interspacing<sup>135,136</sup>, which in planar cultures is ensured.

However, considering that the distance between each exposed graphene flakes, comprised in the underlying 3DFG topography, is less than 100 nm (as shown **Figure 3.2 B**) similar results to the planar case were achieved: the adhesion proteins clustering enables the formation of mature adhesive complexes. In addition, besides the elongated patches at the cellular edge in correspondence of lamellipodia and filopodia protrusions, a diffused paxillin-associated fluorescence signal was observed in correspondence of the central region of the cell bodies (**Figure 3.18 A and B**).

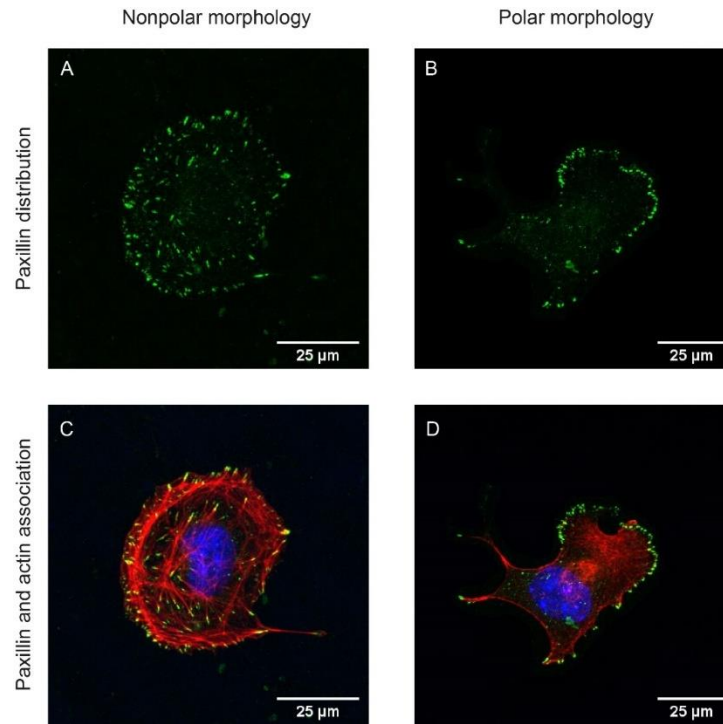


**Figure 3.17.** HL-1 paxillin distribution and its association with actin fibers on 2DG.

(A, B) Paxillin distribution of non-polar and polar cells cultured on planar 2DG.

(C, D) FAs association with actin fibres extremities in non-polar and polar configuration.

In the case of NT-3DFGc and NT-3DFGnc cultures, abnormal assembly of FAs arises due to integrin inability to cluster over contiguous lengths of micron scale. Therefore, within HL-1 bodies cultured on NWs mesh, the paxillin-associated fluorescence signal was significantly diffused (**Figure 3.19 A, B**). Sporadic paxillin spots were localized within and the edge of cell body in the case of NT-3DFG c (**Figure 3.19 A**), probably where cell finds larger anchoring points. Although a statistical analysis on the FAs plaque size is out of the scope of this thesis, fluorescence micrographs show FAs formed in correspondence of collapsed wires present a dot-like shape and smaller area (compared to the planar cultures), distinctive for nascent FAs<sup>136</sup>. However, because of NT-3DFGc topography characterized by interspersed micrometric cavities and NWs, as well as the presence of few exposed NWs tips, diffuse fluorescence was mostly recognized on these samples.

Finally, in the NT-3DFGnc templates, a diffused milder fluorescent signal was distributed within the cell bodies (**Figure 3.20 A, B**). Despite of the freestanding NWs being densely distributed and often in contact with the basal membrane, the interspacing between single nanostructures do not suffice to ensure the

minimal required distance for FAs plaques maturation<sup>135</sup>. Moreover, a clear link to the actin structures was not recognizable (Figure 3.20 C, D).

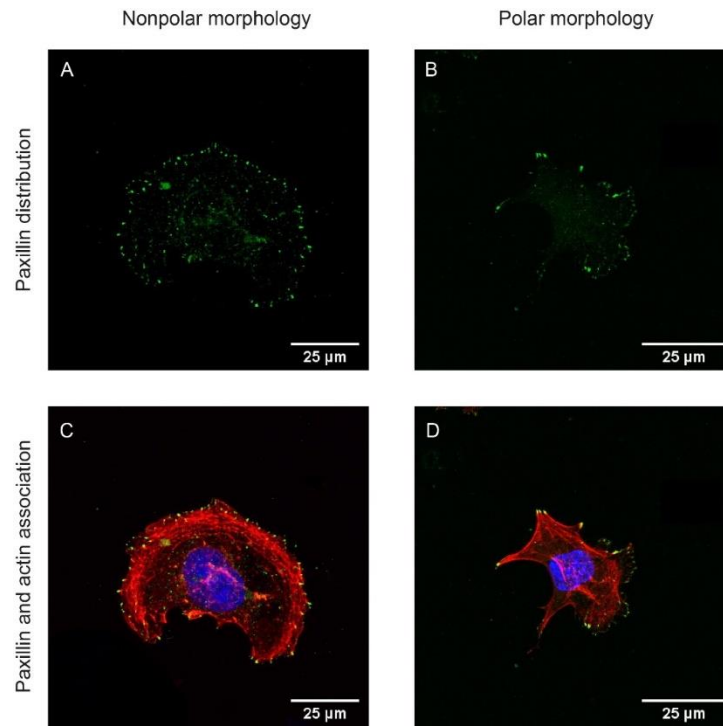


**Figure 3.18. HL-1 paxillin distribution and its association with actin fibers on 3DFG.**

(A,B) Paxillin distribution of non-polar and polar cells cultured on planar 3DFG.

(C,D) FAs association with actin fibres extremities in non-polar and polar configuration.

Furthermore, the intensity of the paxillin-associated fluorescence signal was measured and analyzed using OneWay Anova test (Figure 3.21, p-values are depicted in Table 3.6). Comparing the mean fluorescence values among the samples, the intensity related to the FAs organization was higher when cells were cultured on Si/SiO<sub>2</sub>, 2DG and 3DFG materials due to the presence of denser and larger adhesive structures. Less anchoring sites provided by the substrates with NWs lead to a reduced number of mature FAs and in turn lower fluorescent paxillin-associated intensity. Nevertheless, the presence of sporadic dot-like FAs at the cell body edge on NT-3DFGc leads to a slightly higher mean intensity value than in the NT-3DFGnc case. Therefore, based on the paxillin-associated fluorescence signal intensity and distribution across the cell body, stable and mature FAs were built in 2DG and 3DFG cultures. Beside the visualization of large adhesive plaques, solid cytoskeleton structures terminating with dense FAs further suggest that no physical impediments inhibit FAs maturation on planar and nanoscale topographies. On the contrary, NWs

interspacing exceed the maximum distance required for FAs formation, resulting in hindered FAs assembly and maturation.

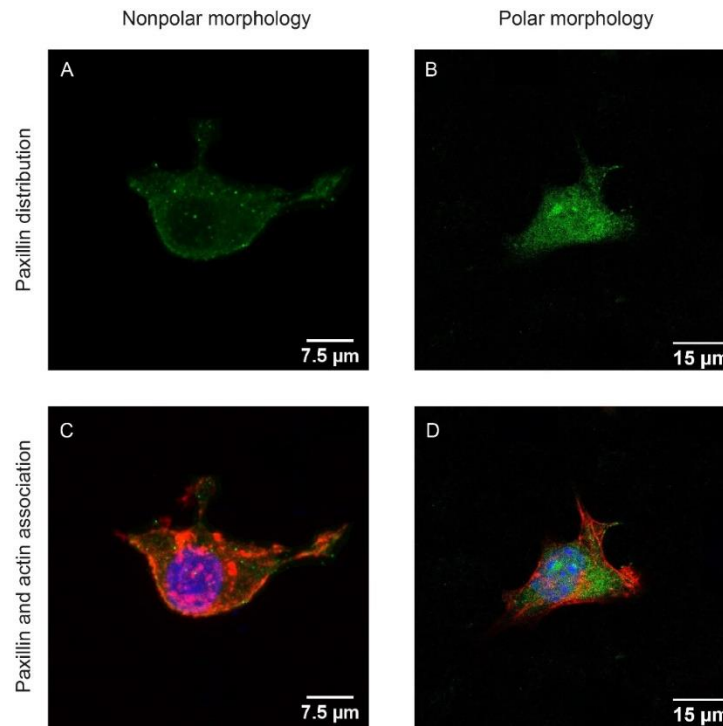


**Figure 3.19.** HL-1 paxillin distribution and its association with actin fibers on NT-3DFGc.

(A, B) Paxillin distribution of non-polar and polar cells cultured on planar NT-3DFGc.

(C, D) FAs association with actin fibres extremities in non-polar and polar configuration.

Consistent with our results, hampered FAs development was previously reported, for different cell lines in contact with protruding structures<sup>15,42,43,66</sup>.

For instance, nanoprotusions with edge-edge spacing below 60 nm do not perturb lateral spacing of integrin clustering yet increasing the number of available binding sites for FAs formation. Therefore, stable and larger adhesive structures were found in flat conditions or when features spacing within 60 nm, as it occurred in the 3DFG case study. On the contrary, in the case of surface patterning in the micrometer range and inter-structures period exceeding the critical ligand interspacing, local integrin aggregation might be disrupted<sup>66</sup>.

Taken together the results from the SEM characterization of the graphene materials, cellular spreading analysis as well as actin and FAs investigation, the variation in substrate topography from nano to microscale features (*i.e.*, from 3DFG to NWs templates) might modulate nanoscale integrin ligation and

clustering, resulting in changes in adhesion assembly. Since FAs are signaling structures responsible of intracellular pathways activation, topographic-driven changes in adhesion results in different regulation of cell behavior. Notably, inadequate FAs formation and maturation affects actin filaments polymerization, which in turn contributes to decreased cell spreading over microstructured graphene surfaces (both NT-3DFGc and nc).

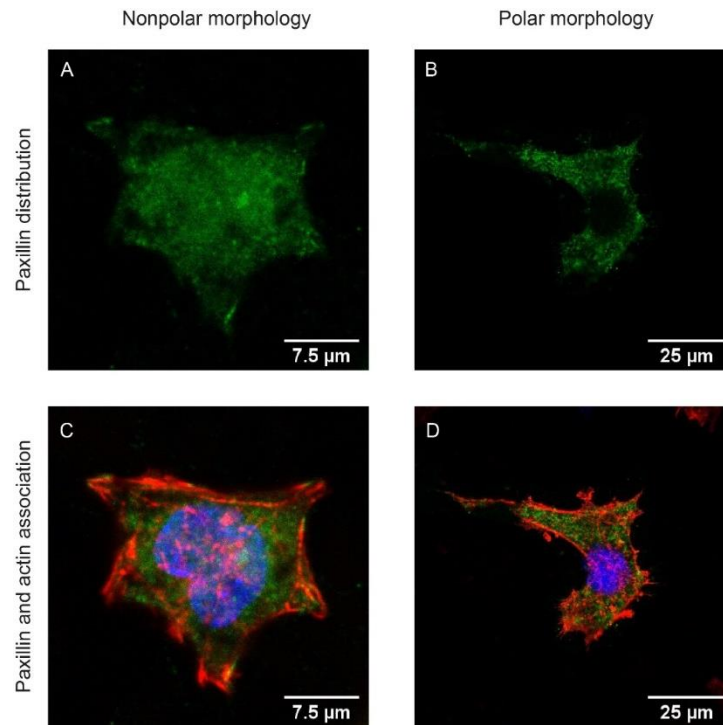


**Figure 3.20.** HL-1 paxillin distribution and its association with actin fibers on NT-3DFGnc.

(A, B) Paxillin distribution of non-polar and polar cells cultured on planar NT-3DFGnc.

(C, D) FAs association with actin fibres extremities in non-polar and polar configuration.

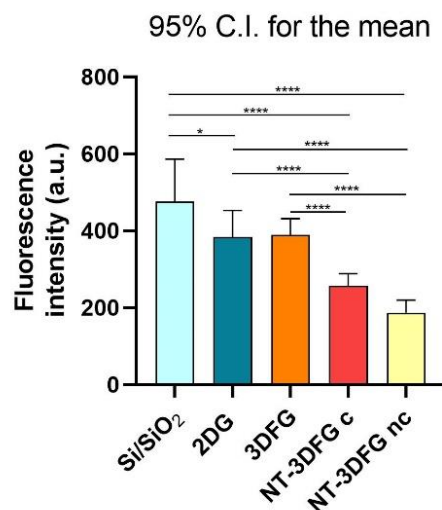


Figure 3.21. Paxillin fluorescence intensity quantification at 95 % confidence interval. Data were analyzed with OneWay Anova with Tukey- post-hoc test at 95 % confidence interval.

Significant difference of Paxillin protein fluorescence [a.u.]

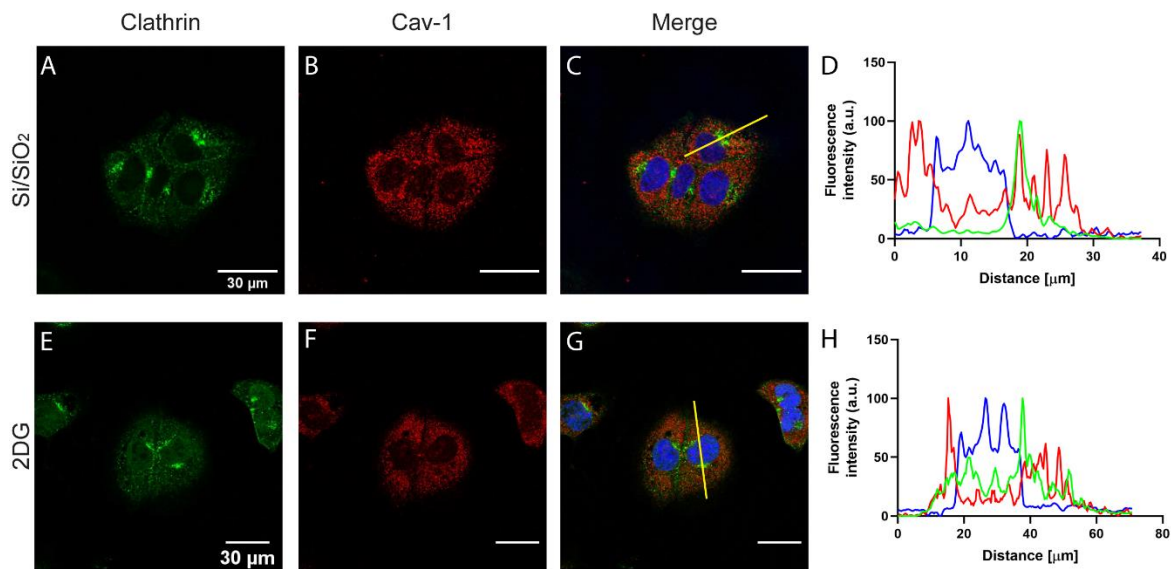
		p-value	Significant difference for $\alpha = 0.05$
Si/SiO <sub>2</sub>	2DG	0.012	-
Si/SiO <sub>2</sub>	3DFG	0.086	-
Si/SiO <sub>2</sub>	NT-3DFGc	< 0.0001	✓
Si/SiO <sub>2</sub>	NT-3DFGnc	< 0.0001	✓
2DG	3DFG	0.992	-
2DG	NT-3DFGc	< 0.0001	✓
2DG	NT-3DFGnc	< 0.0001	✓
3DFG	NT-3DFGc	< 0.0001	-
3DFG	NT-3DFGnc	< 0.0001	✓
NT-3DFGc	NT-3DFGnc	0.297	-

Table 3.6. Significant difference of paxillin proteins fluorescence at 95 % confidence interval.

### 3.4.3 Investigation of endocytic processes at the cell-material interface.

Actin organization is actively involved into the processes of approaching and stabilization of cell growth onto micro and nanopatterned materials. As demonstrated in previous reports<sup>43</sup>, actin spatial remodelling with the combined effects of membrane bending might be modulated by the interaction with vertical protruding materials.

Mechanisms occurring at the interface, as stable and controlled PM curvatures, locally recapitulate membrane geometries which cells encounter during their physiologic dynamics, as along vesicles trafficking<sup>39,47,54</sup>. Here, high positive curvature induced by the material topography might facilitate clathrin-coated pits and caveolae formation<sup>53,56,141,142</sup>. However, at the interface, this coupling might be governed also by the spontaneous rupture of the PM and penetration of the structured materials in the intracellular domain. If a penetration does not occur, the membrane bending triggered by the recruitment of endocytic vesicles might still enable a very tight contact at the cell-material interface.



**Figure 3.22. Endocytic pathways in HL-1 cultured on Si/SiO<sub>2</sub> and 2DG.** (A,B) and (E,F) Spatial distribution of clathrin and cav-1 mediated vesicles, when cells were interfaced with Si/SiO<sub>2</sub> and 2DG, respectively. (C,G) The yellow segments are the region of interest (ROI) along which fluorescence intensity signals were investigated to assess the spatial distribution of the endocytic structures. (D,H) Fluorescence intensity profiles along the yellow segment highlights the distribution of the vesicles within cellular body on Si/SiO<sub>2</sub> and 2DG, respectively. Green traces depict clathrin intensity profile, red indicates cav-1 signal, and finally blue traces show nuclei fluorescence profiles. Each trace was obtained by averaging among ten different cells.

In this scenario, endocytic proteins recruitment and vesicle budding formation, resulting from the local inward pushing forces applied by nano and microstructures of the graphene materials, were considered by labelling clathrin and caveolin-1 (cav-1) proteins by means of immunohistochemistry (**Materials and Methods 2.6.2**).

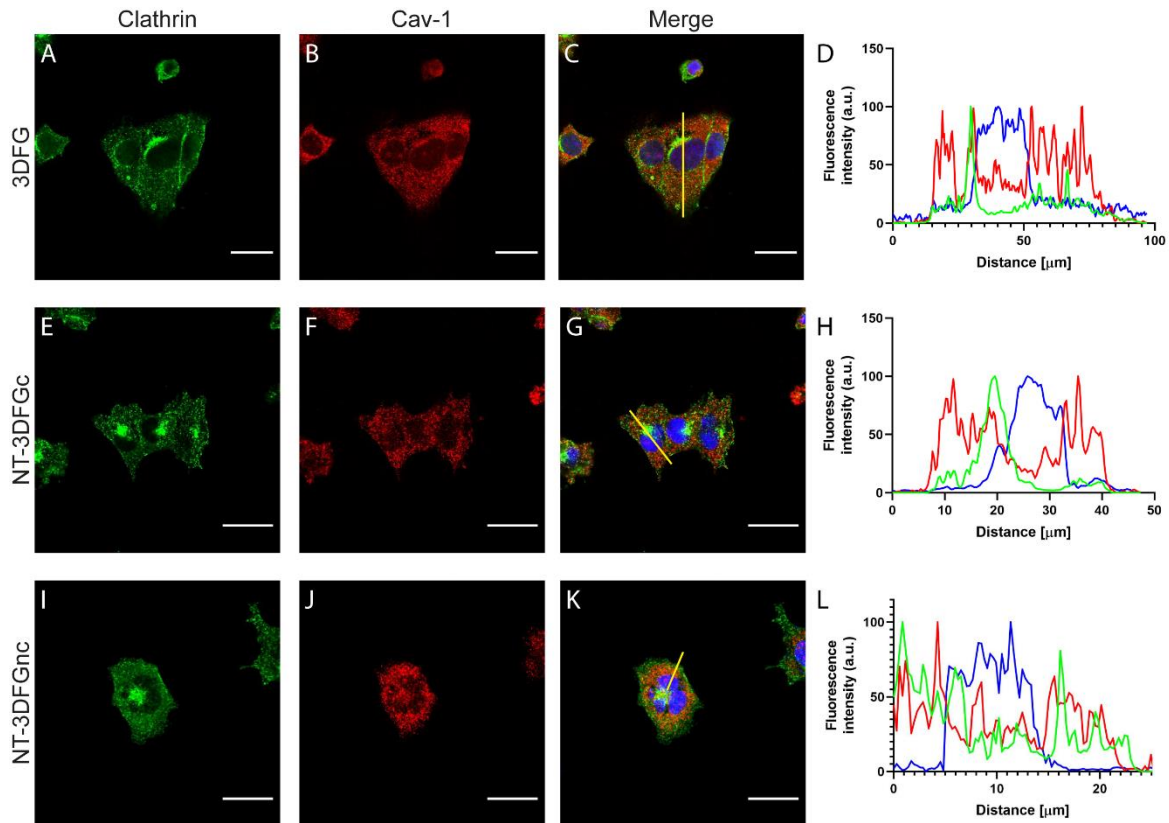


**Figure 3.23.** Endocytic pathways in HL-1 cultured on out-of-plane graphene materials.

(A, B), (E, F) and (I, J) spatial distribution of clathrin and cav-1 mediated vesicles on 3DFG, NT-3DFGc and NT-3DFGnc, respectively. (C, G, K) The yellow segments are the ROIs along which fluorescence intensity signals were investigated to assess the spatial distribution of the endocytic structures. (D H, L) Fluorescence intensity profiles along the yellow segment highlights the distribution of the vesicles, when cells were in contact with 3DFG, NT-3DFGc and NT-3DFGnc, respectively. Green traces depict clathrin intensity profiles, red indicates the cav-1 fluorescence signal, and finally blue traces show nuclei fluorescence intensity profiles. Each trace was obtained by averaging among ten different cells.

Notwithstanding, endocytic vesicles are difficult to resolve *via* optical microscope, the presence of punctuated fluorescence signals provides evidence about the accumulation of both clathrin-supported

structures and caveolae at the basal membrane as shown in **Figure 3.22** and **Figure 3.23** for cells cultured on planar substrates and out-of-plane graphene materials.

Here, newly formed vesicles (possibly detached from the membrane) or PM-invaginations and pits which are promptly coated by clathrin-proteins or cav-1 are visualized.

By analysing the relative position and intensity of the fluorescence signals (**Materials and Methods 2.6.2**), CME vesicles were consistently present at the basal membranes of HL-1 cells. In particular, independent of the culture substrate, clustered clathrin-associated structures were discernible at the proximity of the nuclear envelope (**Figure 3.22 A, E** and **Figure 3.23 A, E, I** for Si/SiO<sub>2</sub>, 2DG, and 3DFG, NT-3DFGc and NT-3DFGnc, respectively). This is also confirmed by single peaks of green traces in the proximity of the blue trace (that refers to the nuclear fluoresce signal in **Figure 3.22 D, H** and **Figure 3.23 D, H**).

However, in the case of NT-3DFGnc cultures, the clathrin intensity profiles show more than one peak along the segment that defines a ROI located for the analysis, as well as higher fluorescence values. Consistently, from the fluorescence intensity quantifications, performed *via* OneWay Anova test, the higher mean values achieved were found when cells were cultured on free-standing wires. However, comparable clathrin-associated fluorescence intensities were measured when cells were in contact with the out-of-plane features, probably because all pseudo-3D topographies, even in NT-3DFG templates, had the same superficial roughness, given by the exposed graphene flakes which trigger membrane invaginations in the average size of the clathrin-coated pits. In contrast, by comparing planar cultures, significant differences were found (**Figure 3.24 A**, p-values in **Table 3.7**).

Furthermore, the fluorescence micrographs also show that cav-1 protein has a uniformly punctuated distribution within the cell body apart from the nuclear areas (**Figure 3.22 B, F** and **Figure 3.23 B, F**), which was reliably mirrored by the fluorescence intensity traces along cell-dividing segments (**Figure 3.22 D, H** and **Figure 3.23 D, H, L**). In addition, cav-1-associate fluorescence intensity profiles analysis suggest a higher expression when cells were cultured on out-of-plane graphene materials than planar substrates (**Figure 3.24 B**, p-values in **Table 3.9**).

In agreement with previous studies<sup>15,27,39,47</sup>, the presence of out-of-plane structures might facilitate enhanced ruffling and bending of the PM. The acquired pre-curved membrane configurations, from the interaction with nano and microstructured materials, not only might facilitate the recruitment and accumulation of endocytic vesicles, but also reduce the energy consumption required for PM bending<sup>47,57</sup>.

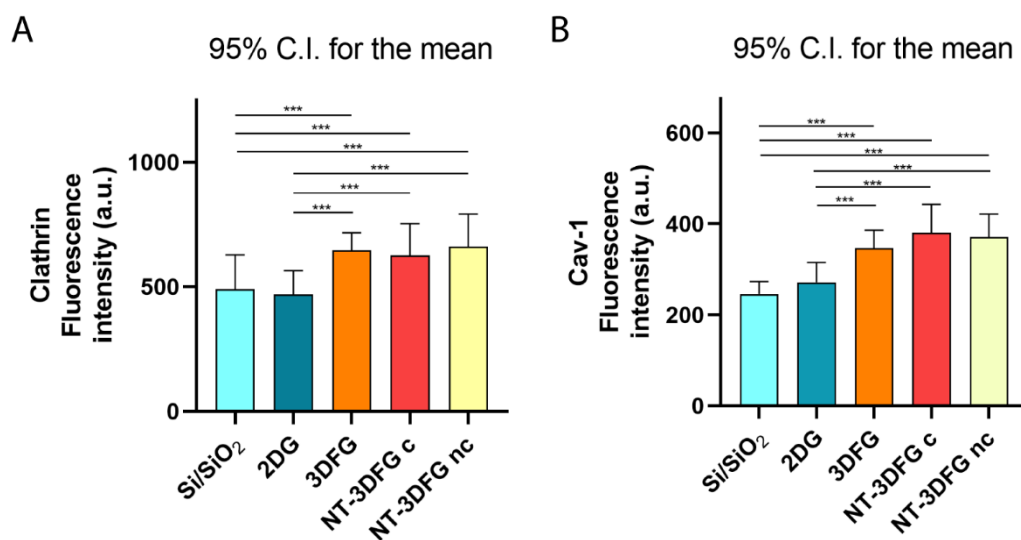


Figure 3.24. Fluorescence intensity quantification of clathrin and cav-1 protein.

(A) Mean values of intensity of clathrin- associated fluorescence signal; (B) Mean values of intensity of cav-1- associated fluorescence signal. Data were analyzed with OneWay Anova with Tukey- post-hoc test at 95 % confidence interval.

Significant difference of Clathrin protein fluorescence [a.u.]

		p-value	Significant difference for $\alpha = 0.05$
Si/SiO <sub>2</sub>	2DG	0.92	-
Si/SiO <sub>2</sub>	3DFG	< 0.001	✓
Si/SiO <sub>2</sub>	NT-3DFGc	< 0.001	✓
Si/SiO <sub>2</sub>	NT-3DFGnc	< 0.001	✓
2DG	3DFG	< 0.001	✓
2DG	NT-3DFGc	< 0.001	✓
2DG	NT-3DFGnc	< 0.001	✓
3DFG	NT-3DFGc	0.90	-
3DFG	NT-3DFGnc	0.97	-
NT-3DFGc	NT-3DFGnc	0.54	✓

Table 3.7. Significant difference of clathrin proteins fluorescence at 95 % confidence interval.

Significant difference of Cav-1 protein fluorescence [a.u.]			
		p-value	Significant difference for $\alpha = 0.05$
Si/SiO <sub>2</sub>	2DG	0.06	-
Si/SiO <sub>2</sub>	3DFG	< 0.001	✓
Si/SiO <sub>2</sub>	NT-3DFGc	< 0.001	✓
Si/SiO <sub>2</sub>	NT-3DFGnc	< 0.001	✓
2DG	3DFG	< 0.001	✓
2DG	NT-3DFGc	< 0.001	✓
2DG	NT-3DFGnc	< 0.001	✓
3DFG	NT-3DFGc	0.006	✓
3DFG	NT-3DFGnc	0.09	✓
NT-3DFGc	NT-3DFGnc	0.89	✓

Table 3.8. Significant difference of cav-1 proteins fluorescence at 95 % confidence interval.

#### 3.4.4 HL-1 – material interface characterized at the nanoscale by scanning electron microscopy/focused ion beam.

To further investigate the effect of the different materials on the membrane bending, the formation of membrane invagination to initiate endocytic processes and possible spontaneous internalization at the cell-material interface, we perform high resolution electron microscopy imaging of the contact area between the junctional domain of the PM and the surface of the diverse materials.

Here, whole-cell SEM provides an overview of the cell-material interaction through macroscopic visualization of cellular bodies and their spreading. We investigated the membrane elongated protrusions and local contact points to the material surface, and finally, performed cross sectioning through FIB in order to characterize the membrane curvature at cell-structures interface with nanoscale resolution.

As discussed in **Chapter 1**, TEM is one of the most used methods to resolve plasma membrane deformation and intracellular compartments with nanometer resolution resolution however, sample preparation might require the removal of the substrate *via* chemical or physical etching to create thin *lamellae*. This cell-material dissociation might induce artefacts at the interface and thus limit the investigation of the contact area and interaction between the membrane and material surface. Therefore, in the present study an

alternative method to the TEM process has been used both for specimen preparation and its imaging. The exploited procedure comprised of UTP for cell preparation and FIB/SEM for the sectioning and imaging<sup>40</sup>. Here, samples were fixed and stained with heavy metals after 1 DIV, as described in **Materials and methods 2.9.1** and the imaging was performed as described in **Materials and Methods 2.9.2**. The thin resin embedding provided by the UTP procedures ensures both biological samples and graphene features to be structurally preserved and distinguishable.

Top view images of HL-1 cultured on graphene materials reveal cell spreading and protrusions formation (**Figure 3.25** and **Figure 3.26**). Indeed, cell PM might form thin protrusive structures at the leading edge of cells called filopodia<sup>143,144</sup>. These hair-like extensions act as sensing “antennae” by which cells probe their neighbouring environment and gather spatial, topographical, and chemical information<sup>143,144</sup>. Indeed, there are several signalling receptors (*i.e.*, integrins) contained within filopodia tips and along their shaft. However, the interaction with the materials established by filopodia, differs according to the out-of-plane or planar natures of the materials. **Figure 3.25** depicts the interfacing of HL-1 cells in planar cultures, Si/SiO<sub>2</sub> and 2DG. In both cases cells appeared to spread across the growth substrate and established protrusive structures along the cellular perimeter. In particular, filopodia assemblies in short and long structures (**Figure 3.25 B, C, E, G**), as well as microspikes completely embedded into the cell cortex (**Figure 3.25 F**) were also identified.

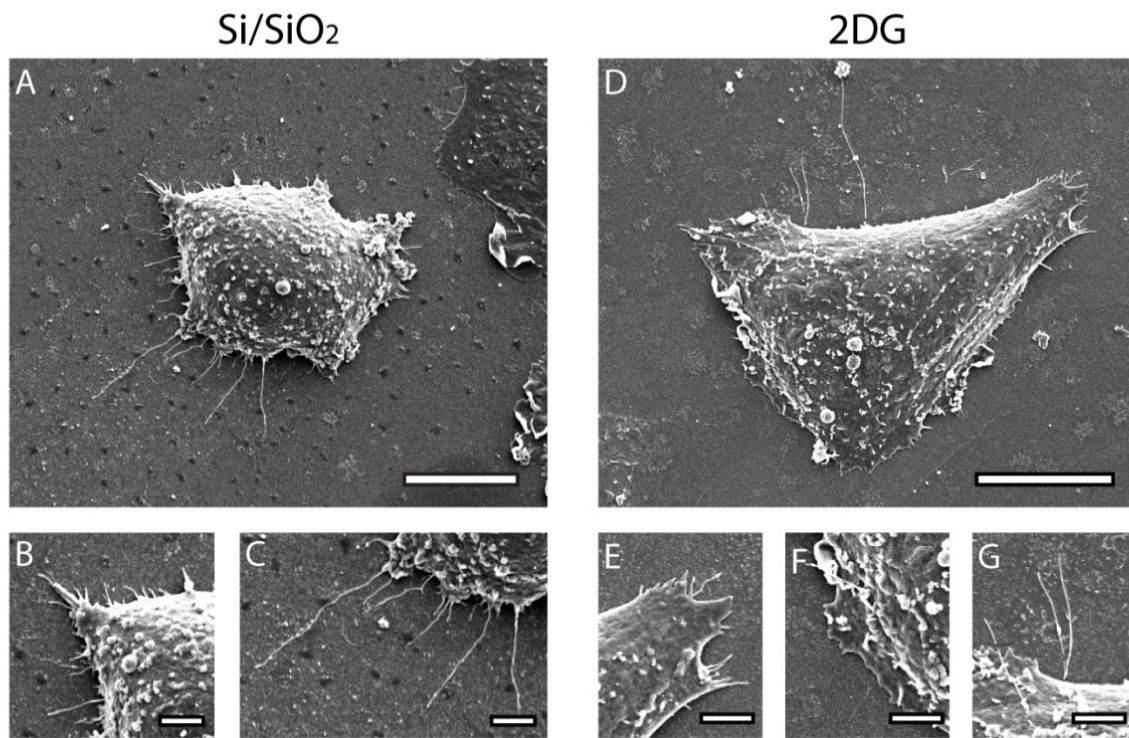


**Figure 3.25. Scanning electron micrographs of HL-1 cells culture on planar materials.**

(A) Lower magnified image of HL-1 cultured on Si/SiO<sub>2</sub>. (B, C) Higher magnified micrographs of membrane protrusions, short and long. (D) Lower magnified image of HL-1 cultured on 2DG. (E, F, G) Higher magnified micrographs of filopodia emerging from the cell body, in short, microspikes and long structures. Scale bars (A, D) 15 and 5  $\mu\text{m}$  (B, C, E, F, G).

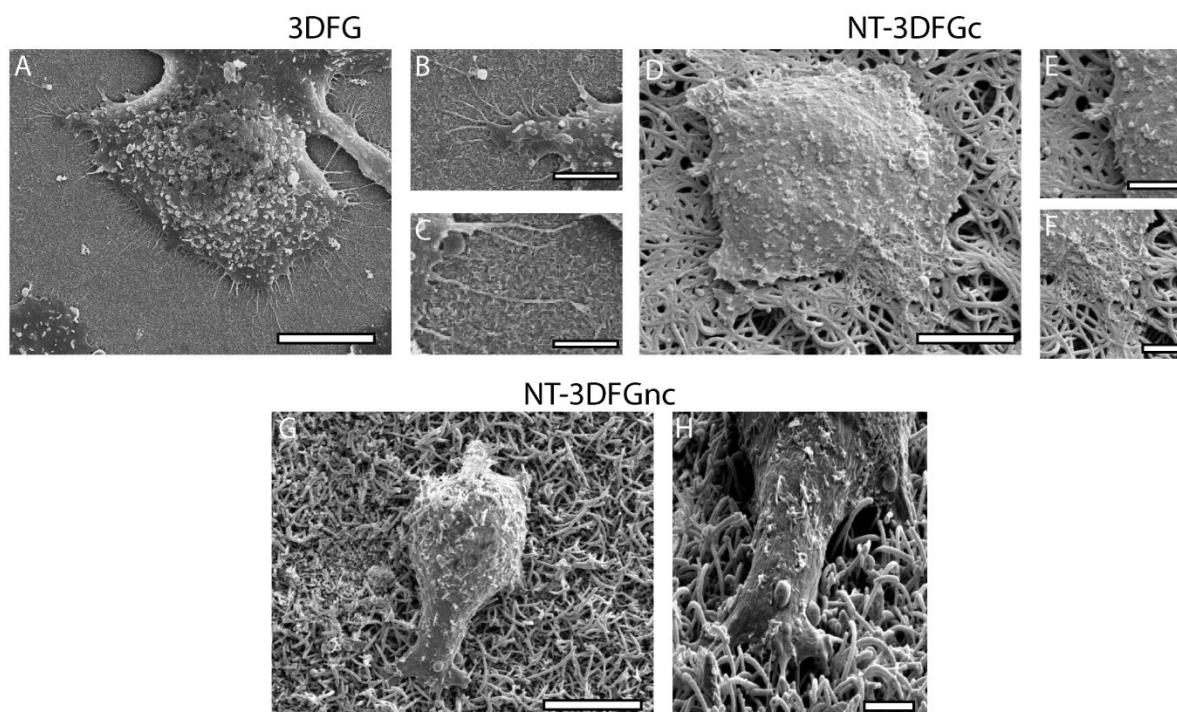


**Figure 3.26. Scanning electron micrographs of HL-1 cells cultured on out-of-plane graphene.**

(A) Lower magnified micrographs of HL-1 cultured on 3DFG. (B, C) Higher magnified micrographs of membrane protrusions. (D) Lower magnified micrograph of HL-1 cultured on NT-3DFGc. (E, F) Higher magnified micrograph of filopodia emerging from the cell body, in microspikes and thin structures, respectively. (G) Lower magnified micrograph of HL-1 cultured on NT-3DFGnc. (H) Higher magnified micrograph of filopodia which wraps the single NW. Scale bars 15 (A, D, G) and 5  $\mu\text{m}$  (B, C, E, F, H).

Here, vertical protruding graphene features emerging from the growth substrates offer anchoring sites to cells. Nanoscale features in 3DFG encourages the shaping of filopodia. Dense topography, as in the case of 3DFG with nanoscale features, appear like a continuous surface where cells can establish an adequate number of adhesions, which are supported by filopodia structures. These long-assembled projections further push the PM leading-edge forwards and supposedly promote additional cell extension, as shown in

**Figure 3.26 A, B, C.** In presence of interlaced NWs spaced with microcavities, HL-1 show either microspikes bulging from the membrane (**Figure 3.26 E**) or thin protrusions (**Figure 3.26 F**).

Finally, on vertical nanowires, cell-structures coupling was mediated by the formation of thick filaments able to wrap and grasp individually each free-standing nanowire (**Figure 3.26 G, H**).

To further valuate the interaction between cells and the single features embedded on the graphene material surface, direct visualization of the PM contact points is of critical importance, and therefore, here provided by exposing the cell-material cross section. As described in **Chapter 1.3.1**, FIB/SEM represents a powerful method for an *in situ* visualization of peculiar cellular processes at the interface (*i.e.*, membrane ruffling and budding vesicles) as well as the quantification of the physical distance (cleft) between the plasma membrane and the materials surface<sup>22,40,145</sup>.

When HL-1 cells were cultured on planar materials their PM mostly follow the surface, by flattening its shape and maximizing the contact with the materials (average distance was quantified to be  $\sim 80$  nm, **Figure 3.27 A, C**). However sporadic PM microdomains that bud inwards the intracellular environment were pointed by the red arrows in **Figure 3.27 B, D**. Deeper PM points distance from the planar surface of  $\sim 134.2 \pm 4.2$  nm, which is the characteristic size of endocytic vesicles<sup>47,141</sup>.

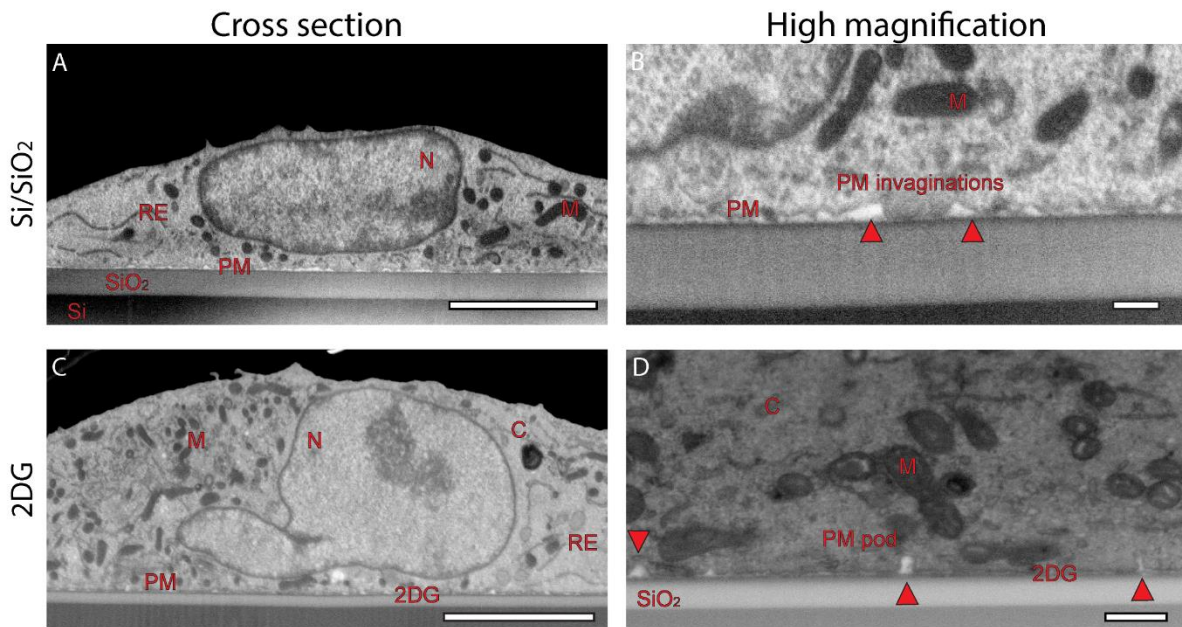


**Figure 3.27.** FIB/SEM cross section of HL-1 cells cultured on planar materials.

Cell-material cross-sections acquired in backscattered mode show HL-1 intracellular environment (nucleus, N, mitochondrion, M, cytoplasm, endoplasmic reticulum, RE) and the interaction with planar substrates, Si/SiO<sub>2</sub>

and 2DG. (A, C) Low magnified micrograph of cell-planar interface on Si/SiO<sub>2</sub> and 2DG, respectively. Scale bars 5 μm. (B, D) High magnified micrographs of PM processes occurring at the interface. Scale bar 500 nm.

However, when in contact with out-of-plane structures, cells deform the membrane curvature by assuming different shapes depending on either structures size or design<sup>15,22,28</sup>. As a consequence of cellular membrane flexibility, cells might promote engulfment events with the protruding features of the coupled materials, thus drastically decreasing cleft distance to few nanometres. In details, in the case of 3DFG substrates, HL-1 cells were able to locally pin their basal membrane as shown in **Figure 3.28 A, B**. Peculiar bending points were identified when cells were in contact with the exposed graphene flakes (whose thickness is  $\sim 464 \pm 25$  nm). In addition, at these locations, the plasma membrane seems to be in physical contact with the upper regions of the flakes, as indicated by the red arrows in **Figure 3.28 B**.

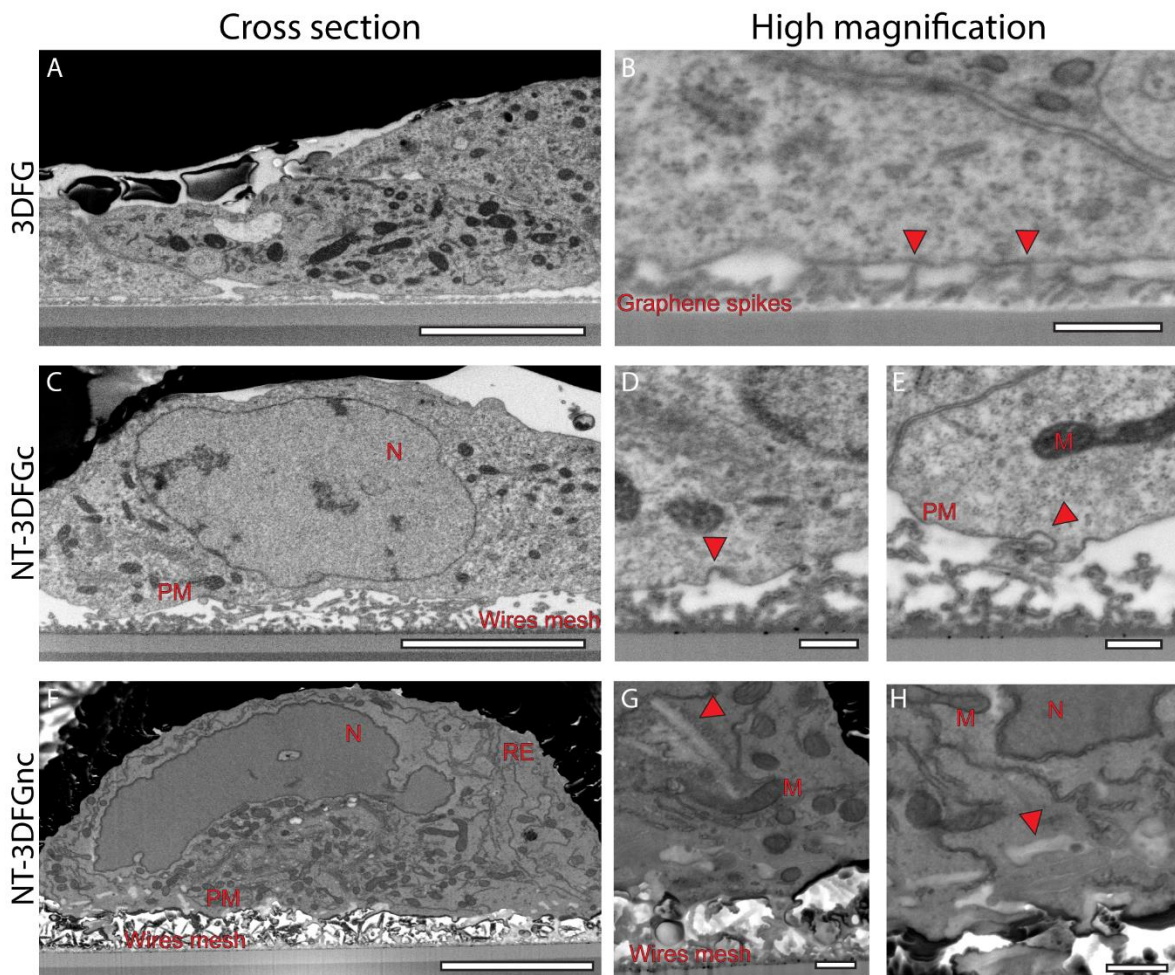


**Figure 3.28. FIB/SEM cross sections of HL-1 cells cultured on out-of-plane graphene materials.**

Cell-material cross-sections acquired in backscattered mode show HL-1 intracellular environment (nucleus, N, mitochondrion, M, cytoplasm, endoplasmic reticulum, RE) and the interaction with planar substrates, 3DFG, NT-3DFGc and nc. (A, C, F) Low magnified micrographs of cell-material interface on 3DFG, NT-3DFGc and nc, respectively. Scale bars 5  $\mu\text{m}$ . (B, D, E, G, H) High magnified micrographs of PM processes occurring at the interface. Scale bar 500 nm.

Instead, **Figures 3.28 C, D, E** show how cells remarkably deform their PM following the topography architecture of NT-3DFGc. In presence of alternating microcavities and collapsed wires, PM bends outwards to sink cell body into the cave regions and simultaneously cell body grows on the intertwined collapsed NWs. Therefore, in line with the 3D reconstruction in **Figure 3.11 D**, cell height results to be larger, since cell potentially grows at different depths. The peculiar topography, however, enables cells to gain an intimate contact with the substrates underneath. Moreover, in the fibers-like architectures clear membrane wrapping event might develop around the single NW as shown in **Figure 3.28 E** (red arrow). Finally, NT-3DFGnc architecture with high-aspect-ratio features might noticeably perturb the cell membrane profile. Indeed, it was reported that sharper nanostructures tend to favour great membrane deformation<sup>19,39</sup>, and their strong engulfment at the basal membrane of the cell body. Thereby, vertical or slight skewed wires, present in NT-3DFGnc, might facilitate more prominent PM bending, since membrane wrapping occurs around the single wires, as visible in **Figure 3.28 G, H** (red arrows). Cell turgidity in **Figure 3.28 F**, as well as darker grey signal around the wire in **Figure 3.26 G**, suggest that nanostructures does not gain direct access to cellular cytoplasm but rather promote a tight sealing. Moreover, **Annex 4** shows the results of additional experiments to ensure the PM integrity. From one side, cells accommodate into the cavities between adjacent wires when in contact with collapsed NWs mesh. However, in presence of free-standing or slightly tilted wires, despite the high density, complete structures engulfment occurs. In the light of this, the increase in dimensionality of the culture substrates not only enables to reduce the cleft, but also enlarges the superficial area of the structured material which is in direct contact with cells.

### **3.5 Neuronal polarization outgrowth mediated by out-of-plane graphene materials.**

#### **3.5.1 *Neuronal polarity and growth cone morphology.***

As discussed in **Chapter 1**, out-of-plane graphene materials might emulate structures already present in the ECM or even geometries similar to the finest neuronal processes of axons and dendrites, effectively providing unprecedented control in the interaction between neuronal membranes and the material surface. Thereby, to understand how size and arrangement of the graphene structures might affect the neuronal outgrowth and adhesion, primary chicken cortical neurons were cultured on the different graphene materials to characterize:

- architecture and cytoskeleton composition of the terminal ends of the axons;
- mean and maximum axon length;
- presence of secondary neurites emerging from the axon (hence, the mean number);
- attachment to the out-of-plane structures.

In *in vitro* cultures, neuronal cells undergo a sequence of developmental events which ultimately lead to the acquisition of the arborized shape and the establishment of a mature cell culture<sup>107,108,146,147</sup>. As shown in **Figure 3.29**, shortly after the initial attachment, neurons present a spheroidal shape (stage 0). However, the spherical symmetry breaks with the extension of circumferential lamellipodia around the cellular periphery (stage 1: formation of lamellipodia). This highly motile veil-like structure might coalesce into few discrete patches along the cellular periphery, thus starting the transition from lamellipodia to the emerging of first minor neurite processes (stage 2: outgrowth of minor processes). Multiple minor neurites are essentially indistinguishable, as any of them could potentially become axon. However, only one neurite begins to grow at much more rapid rate and then sprouts as axon (stage 3: neuronal polarization). Successively, the remaining neurites grow and arborize into morphologically distinct dendrites (stage 4: dendritic outgrowth), whose development proceeds with the dendritic spines enrichment. At this stage (stage 5: maturation), neurons form synaptic contacts through dendritic spines and axon terminals of different cells, thus establishing a mature neural network.

For the purpose of this thesis, the characterization of the interaction between cortical neurons and graphene materials has been carried out only in the early phase of the neuronal development (stage 3), where axons are fully established<sup>107,108,146</sup>.

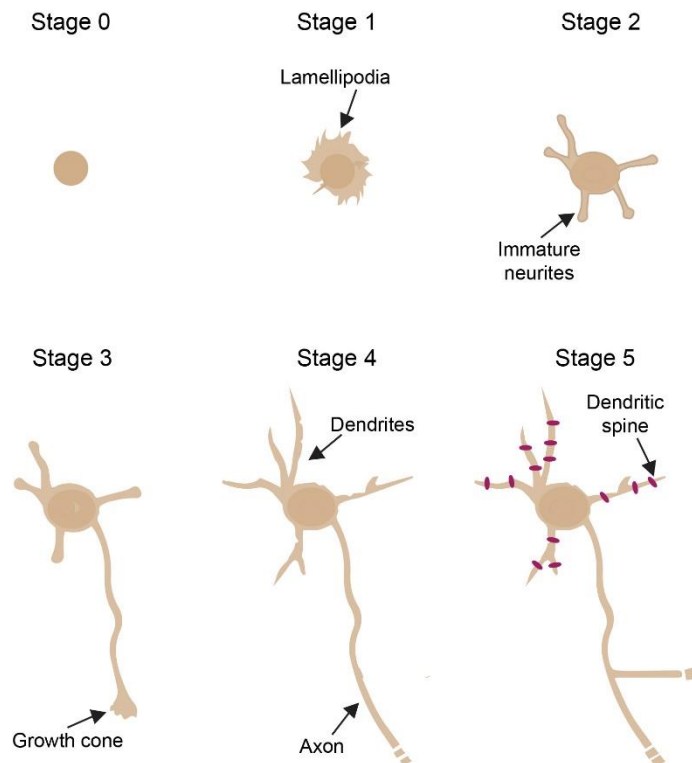


**Figure 3.29. Neural development and neurite initiation.** Neural morphogenesis might be divided in five different phases from the initial attachment in culture (stage 0): formation of lamellipodia (stage 1), outgrowth of minor processes (stage 2), neural polarization (stage 3), dendritic outgrowth (stage 4), and neural maturation (stage 5).

Although extracellular polarity-regulating cues might influence the overall process of the neural morphogenesis, cell-autonomous signalling cascade run in harmony to promote spontaneous neural polarization. Indeed, new PM is recruited and delivered by vesicles at the leading edge to extend; signalling molecules such as PI 3-kinase, Rho GTPase and receptors accumulate to mediate polarity development, as well as actin and microtubules (MTs) synergically are activated to stabilize neurite architecture<sup>108,147</sup>. These last two components enrich the neural cytoskeleton framework by holding essential roles. F-actin bear tensile forces and, either in the lamellipodia mesh or within the filopodia, drives the exploration and the motility across the environment<sup>108,148</sup>. In parallel, MTs resist compressive loads and act as principal railways along which the materials are transported from the cell body into the neurites<sup>108,148</sup>. Although separate entities, a bidirectional signalling between F-actin and MTs is existing, as previously shown<sup>149,150</sup>. Indeed, at the tissue level, F-actin and MTs synergically and actively participate to the brain development through the modulation of specified patterns of wiring between neurons. At the cellular level, their cooperation sustains not only changes in the cytoarchitecture and neural polarization<sup>106,147,149</sup>, but also the integration of

multiple stimuli from the extracellular environment<sup>151,152</sup>.

In these mechanisms, neuronal growth cones (GCs) play a key role: these highly dynamic and motile structures, located at the terminal ends of the axon, act as pathfinder during neuronal wiring dynamics to reach their axon synaptic partners<sup>106,149,151</sup>. GCs actively sense the neighbouring areas ahead of the neurites either for attractive or repulsive signals for neuron development.

In this context, an elaborate cue-receiving system, comprised of specific guidance signalling receptors at the GC region, deals with their transduction into adequate and coordinated cytoskeletal rearrangements. The adaptative process of the GC attachment to the growth surface initiate this signalling cascade<sup>151,153</sup>, where permissive surfaces support GC adhesion and neurites elongation. In contrast, repellent cues operate as physical boundaries by prohibiting axon advancement<sup>106,149,151</sup>, by causing axon steering movements or pauses. In response to the “go” and “stop” signals, GCs exhibit different morphologies.

In this scenario, out-of-plane graphene materials might provide alternating adhesive and repulsive growth surface for neurons polarization. Here, the terminal ends of the axons were ranked into four different classes based on their shapes. *Small GCs* present tapering shape, resembling either needles or bullets (**Figure 3.30 A**). This morphology is typically associated to active and rapidly extending axons<sup>150,154</sup>. The second class is identified as *large GCs*, which, occupy a rather wide area (often up to 50 µm in diameter, **Figure 3.30 B**). During prolonged pausing state from forward axon advance, cortical neurons develop large flat GC characterized by MT loops, extended lamellipodia and several spiky filopodia<sup>149,150,154</sup>. However, from stalling periods neurons might develop new extending GCs, thus the *re-extending axons* configuration is presented in **Figure 3.30 C**. Here, new protrusions emerge from the MT loops in the central region and unbundled short MTs are propelled away from the loop. Finally, the last considered GC shape is *the branching axon*, featured by numerous lateral filopodia, in the attempt to maximize the sensory exploration of the environment and extend the advancing edge (**Figure 3.30 D**).

Here, the occurrence of each GC shape was quantified through a direct visualization of the neuronal cultures at 3 DIV and shown in **Figure 3.30 E**.

In both Si/SiO<sub>2</sub> and 2DG cultures, the GC population was significantly heterogeneous. Indeed, the lack of any specific physical constrains and the large growth area available for the neuronal development enable the establishment of large as well as branching processes. However, even small GCs were found across the cell cultures, indicating the presence of rapidly growing axons.

Similarly, the high area to volume provided by the exposed graphene flakes in 3DFG cultures enables neurons to rapidly grow across the culture (**Figure 3.30 E**), as well as to sample larger area through several filopodia in the branching axon configuration. In the case of NT-3DFGc and nc cultures, where NWs were

covered with nanoscale fuzzy graphene, the dominant GC morphology was given by small GCs. Here, the NT-3DFGc material offers the lateral surfaces of the collapsed NWs as adhesive surface on which GCs might attach. Instead, the interspersed microcavities between the collapsed NWs might prohibit the axon advancement: these microcavities might be considered as a “stop” stimulus to further axonal advance, however, preventing the formation of large GCs (**Figure 3.30 E**). The repellent cues were thereby transduced as steering instructions during the GC routing and thus, in the axon direction.

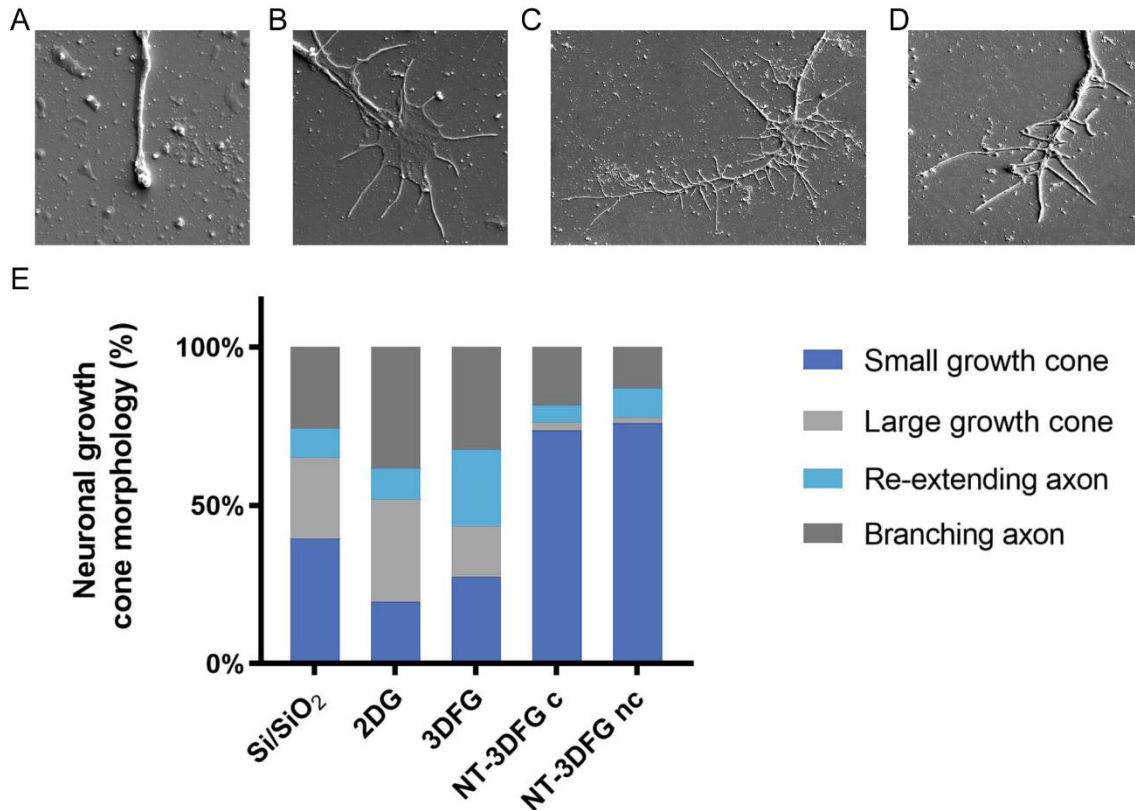


**Figure 3.30. Growth cone morphology classification.** Micrographs of GC shapes: (A) small, (B) large, (C) re-extending axon and (D) branching axon. (E) Occurrence of the GC shapes in the different cultures.

Similar results were achieved in the case of NT-3DFGnc cultures (**Figure 3.30 E**): here, the vertical NWs might prevent MTs to be bundled and looped and thus forming pausing shaped GCs. Thus, the predominant GC configuration established across NT-3DFGnc is the small, bullet-shaped GC. Therefore, the presence of bulkier structures embedded into the graphene materials, as in both NT-3DFG templates, entail lateral physical boundaries, hence preventing GC covering of large superficial area.

Considering the ability of neurons to polarize, the integration of topographical stimuli might ultimately dictate which GC morphology neurons is able to establish<sup>155–158</sup>. Thus, in the presence of pillar-like surfaces,

the need for a wide fan-shaped GC is drastically reduced in accordance with the available growth area<sup>105</sup>. Similarly, channels-based patterns enhance GCs confinement and consequently their dimension. Hence, wider channels tend to produce flatter GCs, enriched with more lamellipodia features, while neurons growing into narrower channels exhibit tube or bullet-like shaped GCs<sup>158</sup>.

Although a variety of regulating proteins is engaged in a spatial-temporal manner to form and drive the protrusion of the leading-edge membrane, we investigated actin and MTs structures which are largely involved in neuritogenesis and axogenesis. As a matter of fact, only their coordination can promote the neuronal development into a polarized cell<sup>106,151</sup>. This cooperative activity might support two fundamental mechanisms<sup>106,151</sup>:

- 1) New-advancing neurite assembles from the actin lamellipodia which surrounds cell body, afterwards polymerizing MTs bundle to stabilize the neurite shaft;
- 2) Emerging filopodia from the cell body become engorged with MTs, which penetrate into filopodium and colocalize with actin structures. The new-formed structure then becomes a neurite with a developed GC.

Therefore, here, the spatial distribution of either actin and MTs across the terminal end of the axon was thoroughly investigated by means of the immunofluorescence labelling and compared across the different growth substrates. Therefore, immunohistochemistry labelling with phalloidin and  $\beta$ III-tubulin antibody (Tuj-1) was performed as explained in **Materials and methods 2.6.4** at 3 DIV (stage 3 of neuronal development).

Moreover, depending on the mutual organization of the cytoskeletal components, GCs were generally subdivided into 3 regions<sup>106,149</sup>, as depicted in **Figure 3.31**. The central domain (C) directly outgoes from the neurite shaft, it contains some organelles (*i.e.*, mitochondria) and is mainly occupied by MTs. The green box in **Figure 3.31** displays the presence of bundled structures which are related to the neuronal MTs, that branches from the axonal shaft. Whereas peripheral domain (P) generally lies at about 0.5  $\mu$ m from the distal end of the GC and thereby it is defined as the leading edge. This region is devoid of organelles and defined by the actin network, as lamellipodia veil-like structures or bundled filopodia. The burgundy box in **Figure 3.31** depicts the actin-based structures, the quasi 2D mesh lamellipodia and the thicker filament which are associated to filopodia. Between the C and P domains, there is a transitional zone (T), where the actin network cohabits with MTs. In particular, actin structures should provide a physical obstacle for farther MTs invasion and extension towards the periphery, thereby actin elements lie perpendicular to both MTs from C and filopodia enclosed into the P zone (**Figure 3.31**). In the orange box in **Figure 3.31**, thicker structures are associated to MTs while smaller features underneath might also include actin fibres.

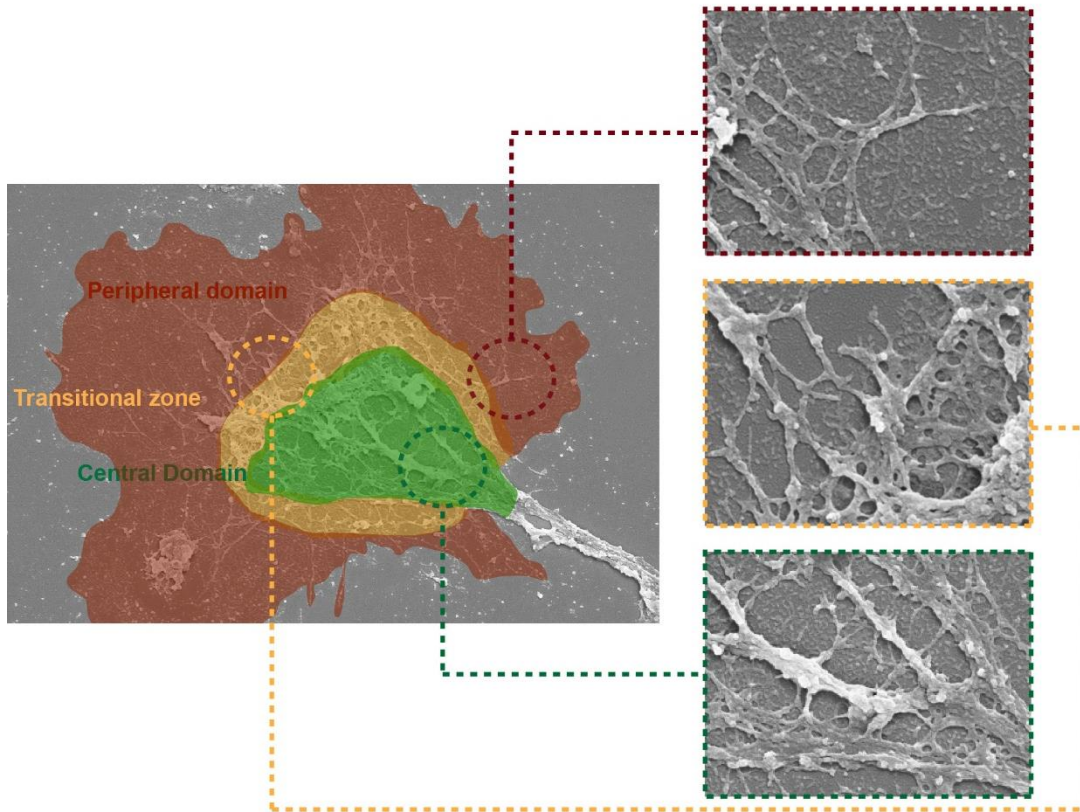


**Figure 3.31. Definition of peculiar growth cone regions.** A representative scanning electron micrograph of a large paused cortical neuron GC where PM was removed with a Triton-X100 treatment to expose the intracellular architecture. The central, transition and peripheral regions are indicated in green, orange, and red, respectively.

### 3.5.2 Growth cone analysis of neurons cultured on planar Si/SiO<sub>2</sub> substrates.

In Si/SiO<sub>2</sub> cultures, the continuous adhesive growth substrate and the lack of relevant topographic features which might address neurons towards a specific target or physically confine the final establishment of the GC shape, lead GC populations to be highly heterogeneous, as already shown in **Figure 3.30 E**. As a result, the chemotactic cellular endings navigate across the planar substrate and integrate the extracellular environment information by alternating advancement periods, pauses or regrowth phases. Considering the small GC shape, MTs initially grow along the actin fibres and then, exceed them to fix the new axonal direction (**Figure 3.32 E, I**). As mentioned earlier, the P domain, which lies in the very terminal part of neuronal ending, is typically occupied by actin structures<sup>150,151</sup>. However, during the neuronal stages of development, the initial actin remodelling becomes gradually supported by MTs which move from the C domain and invade the P area. This phase, called engorgement, aims at consolidating the new region of the axonal shaft<sup>151</sup>. Similarly, in the branching axon, the actin-based filopodia protrusions are supported by

dynamic pioneering MTs along their path, as shown by the colocalization of both actin and MTs fluorescence signals in **Figure 3.32 H, L**.

Moreover, in the case of large GCs, bundled MTs shaft first splay apart once approaching the cytoplasmatic C domain, then form prominent loops where their terminal ends fold towards the axonal shaft (**Figure 3.32 J**). Despite the MT looped-structure in the C domain, some pioneer MTs extend from the loop and engorge the emerging filopodia into the P zone. In addition, the C domain has weak actin structures which were instead found in the P domain (**Figure 3.32 F**).

Generally, the large GC configuration refers to prolonged pausing phase, during which axon stalls minutes up to hours without navigating the surrounding environment<sup>149,150,154</sup>. This is mainly achieved by MTs facing backwards.

During the transition from pausing to growth state, depicted in **Figure 3.32 C**, new short MTs sprout and invade the GC periphery from the loop-like arrangement to explore new possible directions of growth (**Figure 3.32 K**). Moreover, the fluorescence signal from the actin filaments is present in the T and P zones (**Figure 3.32 G**).

**Figure 3.32 M** depicts the growth cone area measurements of cells cultured on planar Si/SiO<sub>2</sub> substrates. Here, large GCs extend wider than the other three configurations onto the growth surface and the average area value hovered around 110-130  $\mu\text{m}^2$  (OneWay Anova analysis with p-value < 0.001, 95 % C.I. for the mean). Smaller area values were measured for the other configurations. In particular, small GCs and re-extending axons, which together represent the axon growth state, cover a similar area (no significant difference in the OneWay Anova analysis,  $\sim 23.5 \pm 9 \mu\text{m}^2$  and  $\sim 38.8 \pm 12.2 \mu\text{m}^2$  for small and re-extending shapes, respectively). In the branching axon configuration, the presence of several filopodia encircling the terminal end almost doubles the area underneath the single GC comparing to the small GC case (p-value < 0.001). By contrast, re-extending and branching axon configurations have similar coverage area (no significant difference, p-value < 0.87).

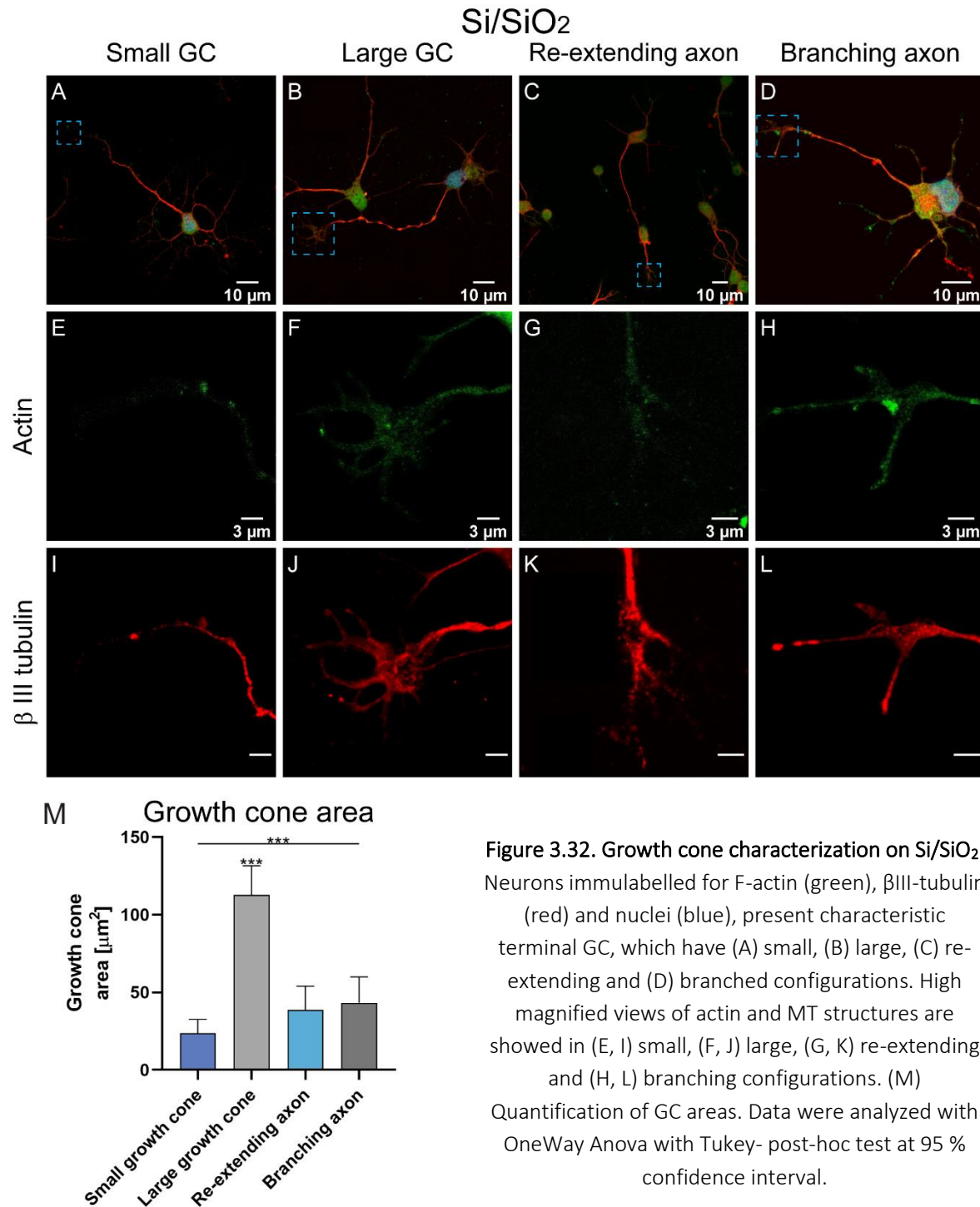


**Figure 3.32. Growth cone characterization on Si/SiO<sub>2</sub>.** Neurons immunolabelled for F-actin (green),  $\beta$ III-tubulin (red) and nuclei (blue), present characteristic terminal GC, which have (A) small, (B) large, (C) re-extending and (D) branched configurations. High magnified views of actin and MT structures are showed in (E, I) small, (F, J) large, (G, K) re-extending and (H, L) branching configurations. (M) Quantification of GC areas. Data were analyzed with OneWay Anova with Tukey- post-hoc test at 95 % confidence interval.

### 3.5.3 Growth cone analysis for neurons cultured on 2DG substrates.

Figure 3.33 A, E, I depict neurons on 2DG substrates with a small-shaped GC which occupies on the average an area of  $\sim 16 \pm 8.9 \mu\text{m}^2$  (Figure 3.33 M). Small GC establishment is supported either by actin structures or MTs in the sensing of the extracellular environment. Although the general consideration lies on the actin

filaments initiating the process of contact guidance<sup>150,151</sup>, different studies also show that MTs are capable of exploring the P domain and dictate axon orientation<sup>159</sup>, even in the low-extended structures where C and P domains are not distinguishable. The large GC configuration is shown in **Figure 3.33 B, F, J**: here, outgoing MTs from the axon shaft assume large loops in the C domain, which ultimately enlarge the overall occupied area. On the contrary, the actin-based fluorescence signal, colocalizes in the axon shaft, but gradually fades once approaching the P area. The re-extending axon (**Figure 3.33 C, G, K**) presents MTs fragments which break off from the loop configuration to create a new leading edge with both lamellipodia and MTs structures into the small-tipped end.

Finally, the branching axons present a typical bifurcation which is supported by MTs bundles in the C domain and actin in the farthest region from the cell body (**Figure 3.33 D, H, L**).

The average GC area measurements (**Figure 3.33 M**) show large GCs having the largest surface area and being statistically different from the other configuration (OneWay Anova analysis, p-value < 0.001). Indeed, in the large configurations GC were ~ 2-fold, ~ 4-fold and ~ 8-fold higher than the case of branching axon, re-extending axon and small growth cones, respectively.

Small and re-extending GCs, which both refer to the active state of the axonal terminal ends, share similar morphologies which only differ by the presence of broader regions in re-extending configuration (indicated by the white arrow in **Figure 3.31 G** and **K**). Thereby, from the parallel comparison performed by OneWay Anova, their means area values were found not statistically significant (p-value < 0.11).

On the contrary, by comparing small GCs and branching axons, membrane protrusions, typically enriching the neural terminal ends architecture in the last configuration, lead to a coverage area value almost 4-fold the extension area of small GCs (p-value < 0.001). The analysis of the area values of branching and re-extending axons shows a less pronounced difference, however, statistically significant for p-value = 0.003.

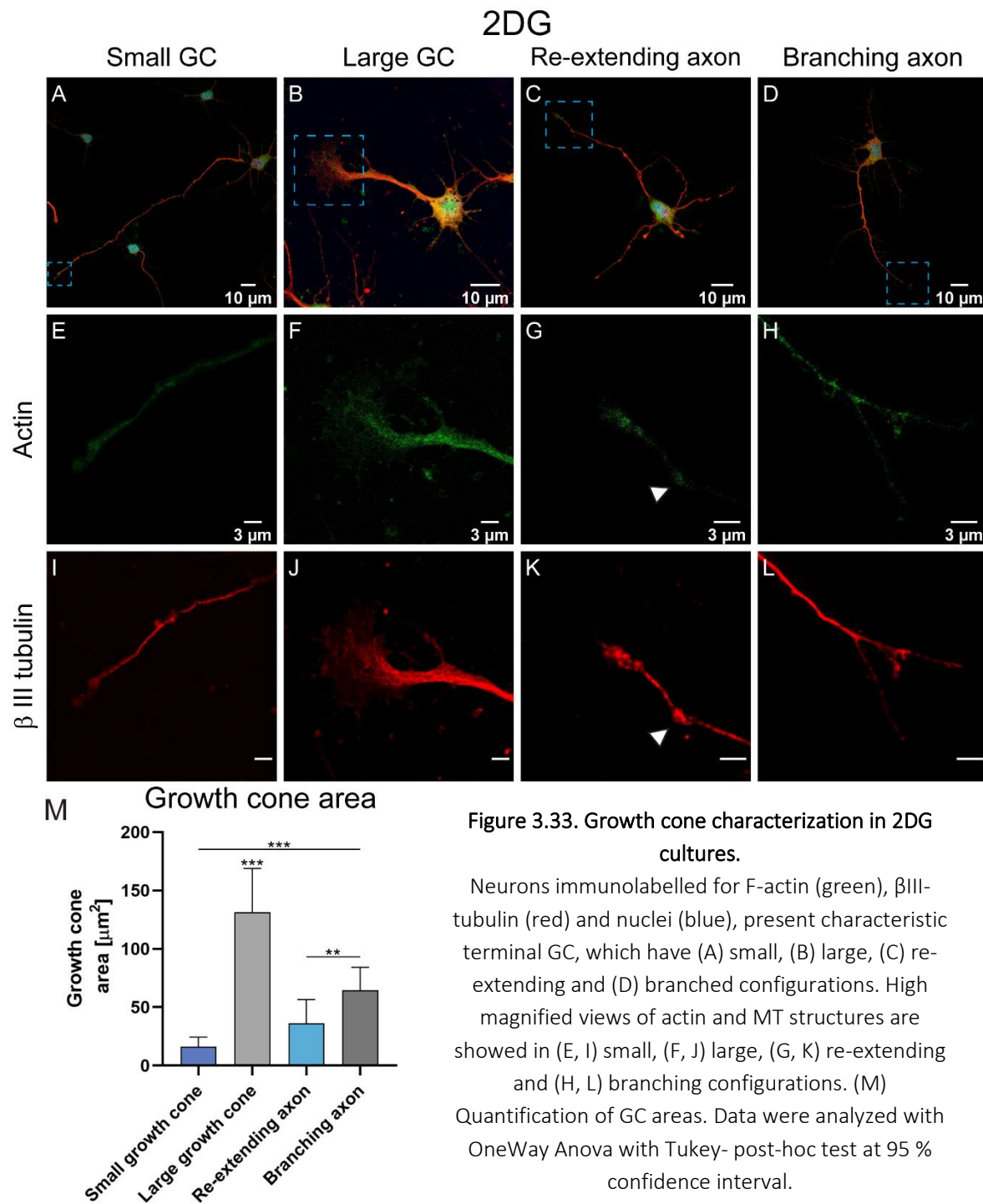


**Figure 3.33. Growth cone characterization in 2DG cultures.**

Neurons immunolabelled for F-actin (green),  $\beta$ III-tubulin (red) and nuclei (blue), present characteristic terminal GC, which have (A) small, (B) large, (C) re-extending and (D) branched configurations. High magnified views of actin and MT structures are showed in (E, I) small, (F, J) large, (G, K) re-extending and (H, L) branching configurations. (M) Quantification of GC areas. Data were analyzed with OneWay Anova with Tukey- post-hoc test at 95 % confidence interval.

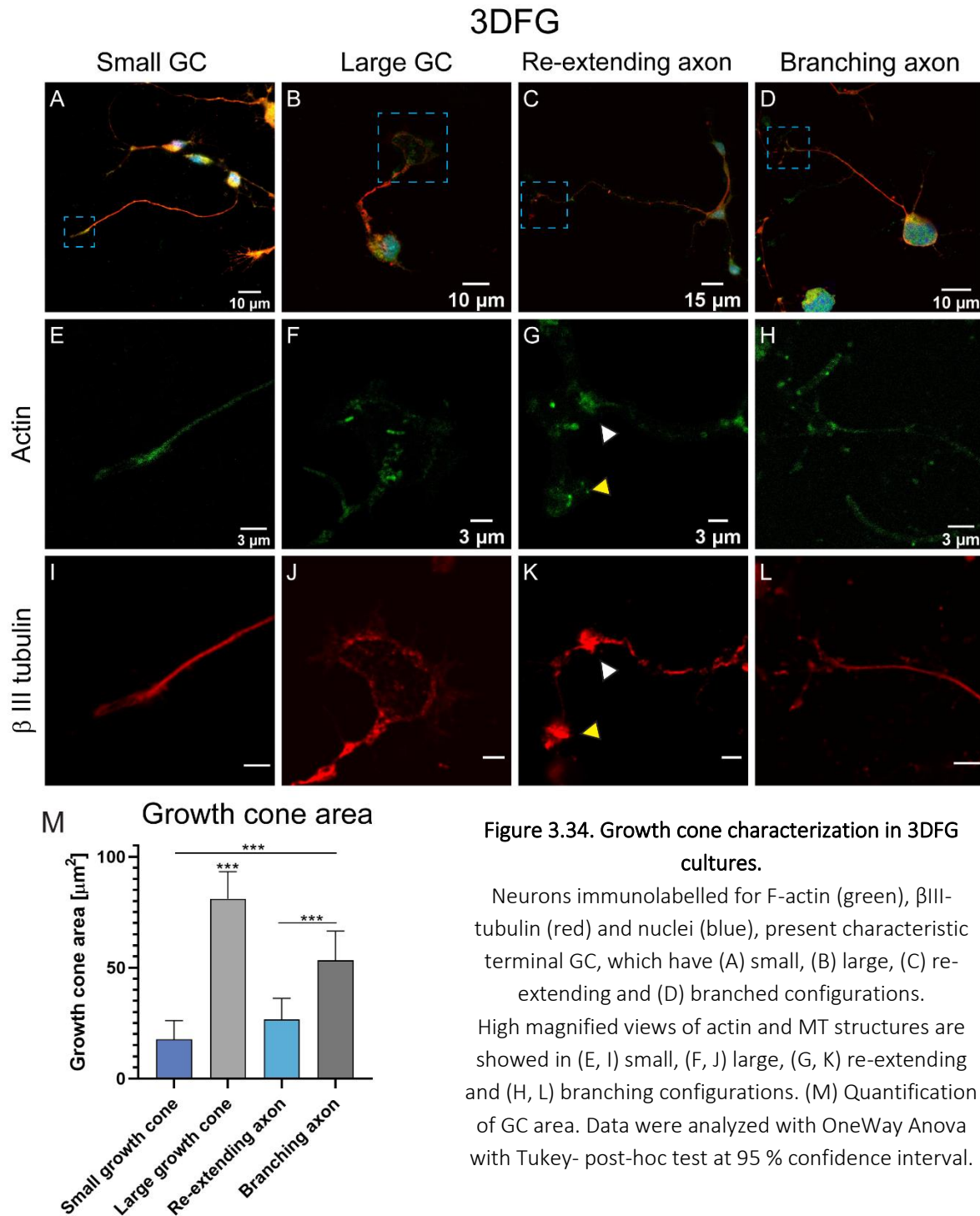
### 3.5.4 Growth cone analysis for neurons cultured on 3DFG substrates.

Figure 3.30 E shows high occurrence of branching axons which are specifically characterized by the outwards projected membrane in 3DFG cultures. This topography-driven effect might depend on the exposed graphene flakes which are comparable in size to the membrane receptors and could trigger their

activity<sup>153</sup>. However, small, large and re-extending GCs also populate the 3DFG cortical neurons culture. Small GCs (**Figure 3.34 A, E, I**), are supported either by the actin or MTs structures: the C domain has mainly MTs while both T and P zones present the colocalization of the two cytoskeleton components. The MT architecture of large GCs is characterized by a wide loop (MT filaments create a circular structure and face their terminal ends towards the axon shaft) in the C zone, wherein it is partially supported by actin structures. Instead in the T zone, ahead of the MT loop, the actin fluorescence signal is visible and associated to transversal actin arcs that limit the MTs advancement in the P domain.

The re-extending axons of cortical neurons in contact with 3DFG (**Figure 3.34 C, G, K**) present a small loop with a strong MT fluorescence signal (white arrow), from which a new-leading terminal appendage emerges. At the new forefront terminal (yellow arrow), a strong colocalization of both actin and MTs signals is visible, which indicates the axon active state in sampling the extracellular environment. This is mainly due to the axon motility that relies firstly on the dynamic properties of actin and MTs translocating into the P zone<sup>151,160</sup>. Similarly, branched neurons, which are the most recurring GC configuration in the 3DFG cell culture, present MTs aligned along the longitudinal axis of the filopodia as shown in **Figure 3.34 D, H, L**.

Finally, the average GC spreading area across the 3DFG was quantified by outlining the neuronal appendage (**Figure 3.34 M**). Significantly, large GCs exhibit the wider and larger morphologies compared to the other configurations found in the 3DFG culture ( $p$ -value  $< 0.001$ ). However, considering the average area measurements in the case of Si/SiO<sub>2</sub> and 2DG cultures (*i.e.*,  $112.9 \pm 18.7 \mu\text{m}^2$  and  $135.4 \pm 26.1 \mu\text{m}^2$ , respectively), the 3DFG topography supports smaller GCs. The presence of membrane protrusions in the branching axon configuration enables to cover an area significantly higher than the small GC ( $p$ -value  $< 0.001$ ), however, still limited than the large GC case ( $p < 0.001$ ). Instead, parallel analysis of small GC and re-extending ones reveal similarities between the two classes, which not only include small-tipped terminal but also reduced coverage area ( $p$ -value = 0.09).



### 3.5.5 Growth cone analysis for neurons cultured on wires templated graphene substrates.

Figures 3.35 A, E, I depict representative micrographs of bullet shape-tipped neurons in the case of NT-3DFGc cultures. In contrast to the previous results, large GCs fail to extend over  $30 \mu\text{m}^2$  wide areas as

probably their spreading is limited by the absence of a continuous adhesive growth support due to the succession of microcavities and finite collapsed graphene NWs. Here, MTs loops, previously found in the large GCs configuration, are not visible (**Figure 3.35 B**). Therefore, few neurons develop enlarged GCs that cover a very restricted area.

Consequently, the re-extending axons configuration which comes from the establishment of MT loops in the large GC, is not significantly present in the overall GCs' population. However, exemplary images of solitary neurons with re-extending tips are provided in **Figure 3.35 C, G, K**, where the white arrows point to the wider area from which new leading axons begin to venture across the growth substrate. Here, the development and axon guidance of the re-extending neuron are supported by either actin or MTs, especially in the terminal part. Finally, branching axons are shown in **Figure 3.35 D, H, L** whose occurrence within the GC population on NT-3DFGc has been appraised to be near the 18%. Here, the new extending filopodia, which surround the axonal terminal end, grasp sideways the collapsed wires as anchoring sites. In this guidance dynamics, MTs and actin fibres support altogether the cytoskeleton organization as visible in **Figure 3.35 H, L**.

From the GC area analysis, the highest GC coverage is attained by the branching configuration, whose means difference are statistically significant when compared to small and re-extending GCs ( $p$ -values  $< 0.001$ ). Instead, statistically mean difference was found by comparing branching axon and large GC configurations ( $p < 0.05$ , with 95 % C.I. for the mean). Coverage area values measured for small, re-extending and large GCs were almost comparable, indeed no significant differences were identified in the OneWay Anova analysis.

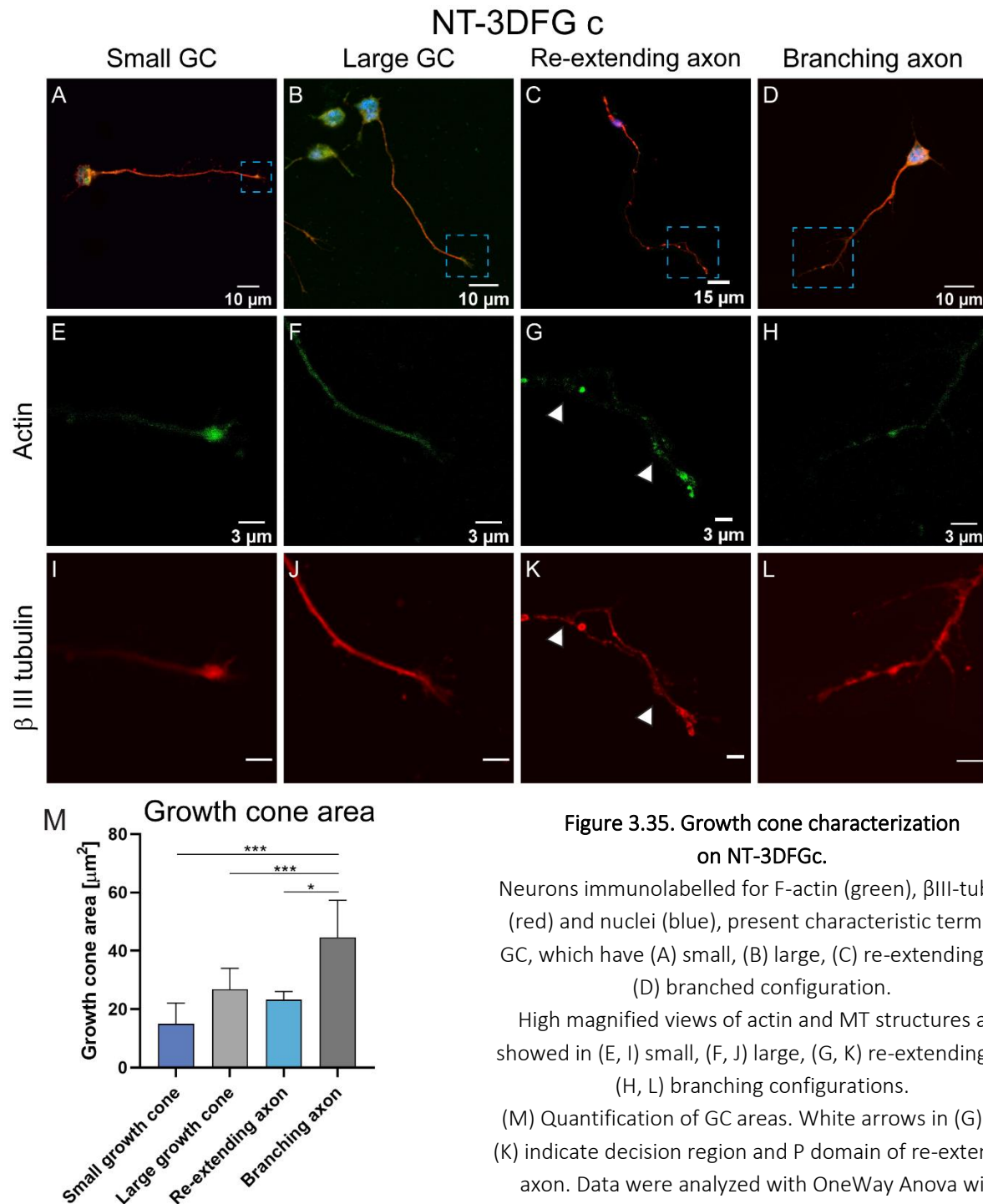


**Figure 3.35. Growth cone characterization on NT-3DFGc.**

Neurons immunolabelled for F-actin (green),  $\beta$ III-tubulin (red) and nuclei (blue), present characteristic terminal GC, which have (A) small, (B) large, (C) re-extending and (D) branched configuration.

High magnified views of actin and MT structures are showed in (E, I) small, (F, J) large, (G, K) re-extending and (H, L) branching configurations.

(M) Quantification of GC areas. White arrows in (G) and (K) indicate decision region and P domain of re-extending axon. Data were analyzed with OneWay Anova with Tukey- post-hoc test at 95 % confidence interval.

Finally, **Figure 3.36** shows the GC cytoskeleton analysis when cortical neurons were cultured on the NT-3DFGnc substrates. The available regions for cell growth and spreading are limited to the top extremities and portions of the lateral surface, in case of vertical or kinked NWs, respectively. Thus, the reduced contacting interface might compel the neuronal GCs cytoskeleton to have a smaller configuration, which is

the most predominant GC shape over the other neuronal terminal (**Figure 3.30 E**). **Figure 3.36 A, E, I** show exemplary images of a solitary cortical neuron with a small GC. The neuronal outgrowth across the wires template terminates with a bullet shape tip which is sustained either by actin structures or MTs. On the contrary, the very few GCs which might establish large appendage at the interface with the protruding graphene material, exhibit a rounded shape as shown in **Figure 3.36 B**. In this configuration, the terminal area presents the colocalization of both actin and MTs, without recognizing any specific spots where only one of the two cytoskeleton components is located (**Figure 3.36 F, J**), as it often occurs in the large GC configuration. **Figure 3.36 C, G, K** depicts re-extending with strong accumulation of actin and MTs in the distal end (yellow arrows) and the decision region (white arrows). In addition, branching axons, whose shape occurrence was identified to be  $\sim 13\%$  across the culture, have well-defined MTs structures. However, the actin presence is detectable by mild a fluorescence signal in the more peripheral region. Considering the GC extending area (**Figure 3.36 M**), small GCs occupy in average the most restricted area (almost  $\sim 11.5 \pm 5.3 \mu\text{m}^2$ , p-value  $< 0.001$ ). On the contrary, large GCs, re-extending and branching axons have comparable values (large GC vs. re-extending has  $p < 0.90$ , large GC vs. branching axon has  $p < 0.98$ , and finally re-extending and branching axon has  $p < 0.96$ ).

Similarly to the results discussed in the case of HL-1 cells interfaced with out-of-plane graphene materials, variations in substrate topography from simply fuzzy graphene to NWs templates directly modulate the available regions where cell adhesion might initiate. Thus, as in cardiomyocytes cultures, neuronal cell spreading, and axonal terminal reshaping was drastically influenced by the decreased adhesive surface. The analysis of neuronal GC extensions over the different graphene materials, revealed a reduction of GC extension for small GC, re-extending and branching axon configurations. However, the gradual decrease of GC extension was more prominent comparing the large GCs across the graphene materials; indeed, significant differences in mean area values were found comparing the planar graphene with 3DFG ( $p < 0.008$  with OneWay Anova at 95 % of confidence interval), NT-3DFGc and nc (both have p-value  $< 0.001$ ). Taken together, these results confirm the essential role the cellular adhesive processes have in the regulation of cellular behaviour, directly affecting GC morphology and modulating the neuronal active state.

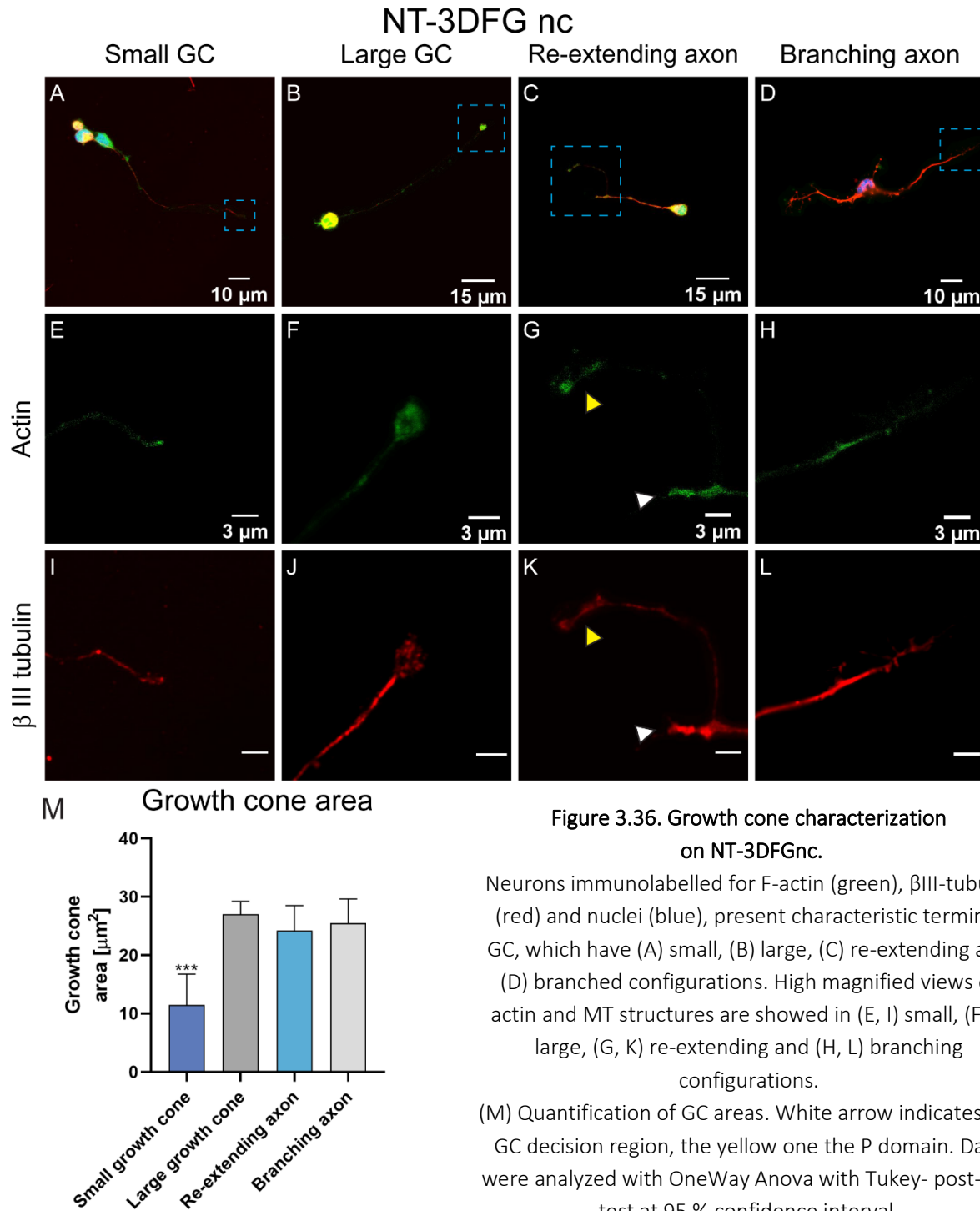


**Figure 3.36. Growth cone characterization on NT-3DFGnc.**

Neurons immunolabelled for F-actin (green),  $\beta$ III-tubulin (red) and nuclei (blue), present characteristic terminal GC, which have (A) small, (B) large, (C) re-extending and (D) branched configurations. High magnified views of actin and MT structures are showed in (E, I) small, (F, J) large, (G, K) re-extending and (H, L) branching configurations.

(M) Quantification of GC areas. White arrow indicates the GC decision region, the yellow one the P domain. Data were analyzed with OneWay Anova with Tukey- post-hoc test at 95 % confidence interval.

### 3.5.6 Actin and tubulin arrangement at the growth cone.

To further characterize the actin and MTs architecture and protein expression, confocal fluorescence micrographs have been further analyzed (**Materials and Methods 2.8.4** and **2.8.5**). In general, the actin-associated fluorescence signal is mainly punctuated, while MTs arrange in a fiber-like assembly. Moreover, actin and  $\beta$ III-tubulin mean fluorescence signals intensity were measured in correspondence of the GC region in planar and out-of-plane cultures (**Figure 3.37, Materials and Methods 2.8.4**)<sup>140</sup>.

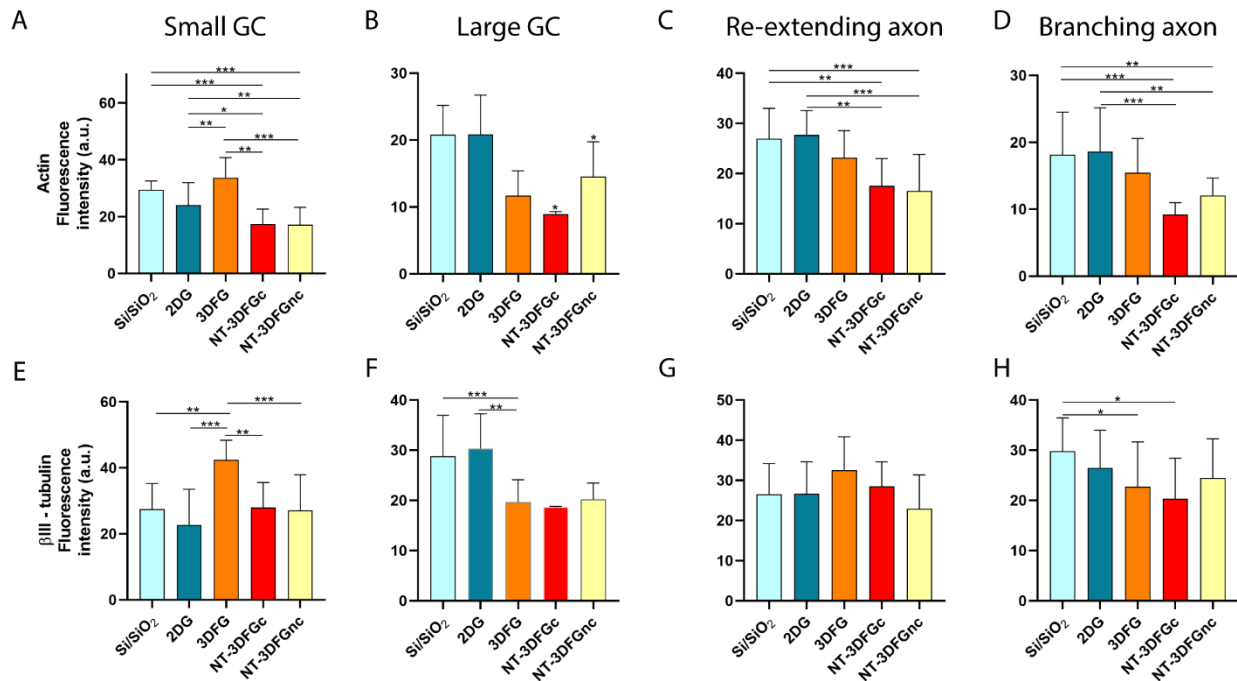


**Figure 3.37. Fluorescence intensity quantification of actin and  $\beta$ III-tubulin in neuronal cells.**

Comparison of actin and  $\beta$ III-tubulin fluorescence signals were performed between same GC morphologies across the different cultures. Actin fluorescence intensity analysis of small GCs, large GCs, re-extending and branching axons are depicted in (A), (B), (C) and (D), respectively. Similarly,  $\beta$ III-tubulin fluorescence intensity analysis of small GCs, large GCs, re-extending and branching axons are depicted in (E), (F), (G) and (H), respectively. Data were analyzed through OneWay Anova with Tukey- post-hoc test at 95 % confidence interval.

Here, the GCs actin-associated fluorescence intensity in planar cultures was generally higher than in out-of-plane conditions. However, small GCs developed in 3DFG cultures show an actin-associated fluorescence intensity significantly higher than planar and NWs-templated cultures (**Figure 3.37A**). Similarly,  $\beta$ III-tubulin-associated fluorescence intensity was significantly higher in 3DFG cultures (**Figure 3.37E**). In addition, on

planar cultures the ratio between actin and MTs fluorescence signals was found to be almost unitary, as actin and MT structures colocalize and interact together to perceive extracellular cues and facilitate axon routing. However, fluorescence ratios between the two signals from small GC over NWs cultures show a weaker actin contribution.

Large GCs highly populate planar and 3DFG cultures, but they were occasionally in contact with the protruding NWs on NT-3DFGc and nc materials, due to the reduced adhesion surface accessible to cells. As a matter of fact, larger GCs have a well-developed and complex MTs network with peculiar looped structures in the C domains towards the P domain. Thus, actin structures enrich the axonal appendage in T and P domains. Therefore, the large GCs developed in planar cultures show higher fluorescence intensities for both MTs and actin components. However, only actin fluorescence values collected from large GCs on planar cultures were statistically significant than the ones from out-of-plane graphene materials as shown in **Figure 3.37 B** (MTs associated fluorescence signals were not statistically different, **Figure 3.37 F**). In all culture conditions, actin and  $\beta$ III-tubulin fluorescence ratios show stronger  $\beta$ III-tubulin-associated signals than actin. For instance, in planar cultures GCs can largely spread and be supported by MTs developing from the axonal shaft to the P domain while actin structures are rather discontinuous (completely absent in the C domain). On the contrary, NWs-templated materials promote the formation of MTs in GCs which stabilize the axonal terminal appendage.

Although re-extending axons exhibit similar morphology of small GCs, the actin-associated fluorescence signal intensity was found to be different from the previous configuration. Indeed, the intensity was significantly higher in planar cultures. However, multiple comparison of actin values shows no significant difference by comparing them with GCs cultured on 3DFG (**Figure 3.37 C**). Oppositely, MTs-associated fluorescence intensities were comparable among all culture conditions (**Figure 3.37 G**). Fluorescence ratios between the mean values of actin and  $\beta$ III-tubulin intensity values show an equal contribution of these proteins to the appendage architecture when GC were developed in planar cultures while, increasing topography dimensionalities, MTs structures-associated fluorescence intensities are higher than actin-associated fluorescence intensities in out-of-plane cultures.

Finally, branching axons show comparable fluorescence intensity values associated to MTs structures among the graphene cultures (**Figure 3.37 H**). Similarly to the other GC morphologies, actin-related fluorescence intensity values were significantly lower in out-of-plane cultures than planar ones (**Figure 3.37 D**). However, no significant difference was estimated comparing the actin intensity values within branching axon terminal of planar and 3DFG cultures. In addition, ratios between the mean values gathered from the actin and  $\beta$ III-tubulin fluorescence signals show a prevalent contribution of MTs structures within the

branched GC among all cultures. These results further suggest that MTs stabilize and consolidate the extensions as new region of the axonal shaft.

During neuronal polarization, actin and MTs coordinate their activities through three different stages: protrusion formation with actin advancement, then stabilization of the axon direction and structures by MTs and ultimately consolidation of the new axonal branch with PM reinforcement around MT bundles and actin depolarization<sup>106,149–151</sup>.

Therefore, here, the predominant presence of MTs over actin in the P domain does not prevent axonal elongation or routing across the extracellular environment: in fact, GCs are stabilized by MTs bundles and, thereby, consolidated as a new axonal shaft section.

Indeed, the actin dynamics, which typically consists of assembly, retrograde flow and depolymerization processes require to be bias towards an increased polymerization phase to push the GC leading edge forward. However, one way to balance the higher level of actin polymerization and advancing protrusions involves a reduced retrograde flow or improved actin coupling with the growth substrate. When the coupling is strong, peripheral corridors devoid of actin will facilitate the gradual MTs occupancy into the P area<sup>106,161</sup>. Therefore, MTs might engorge filopodia into the P domain or invade lowered F—actin regions<sup>108,150,160</sup>.

Therefore, in this study, progressive MTs presence over the actin also in the P domains, as it typically occurs during the engorgement and consolidation phases<sup>151,161</sup>, might result from an enhanced coupling between the single neuron with the growth substrate.

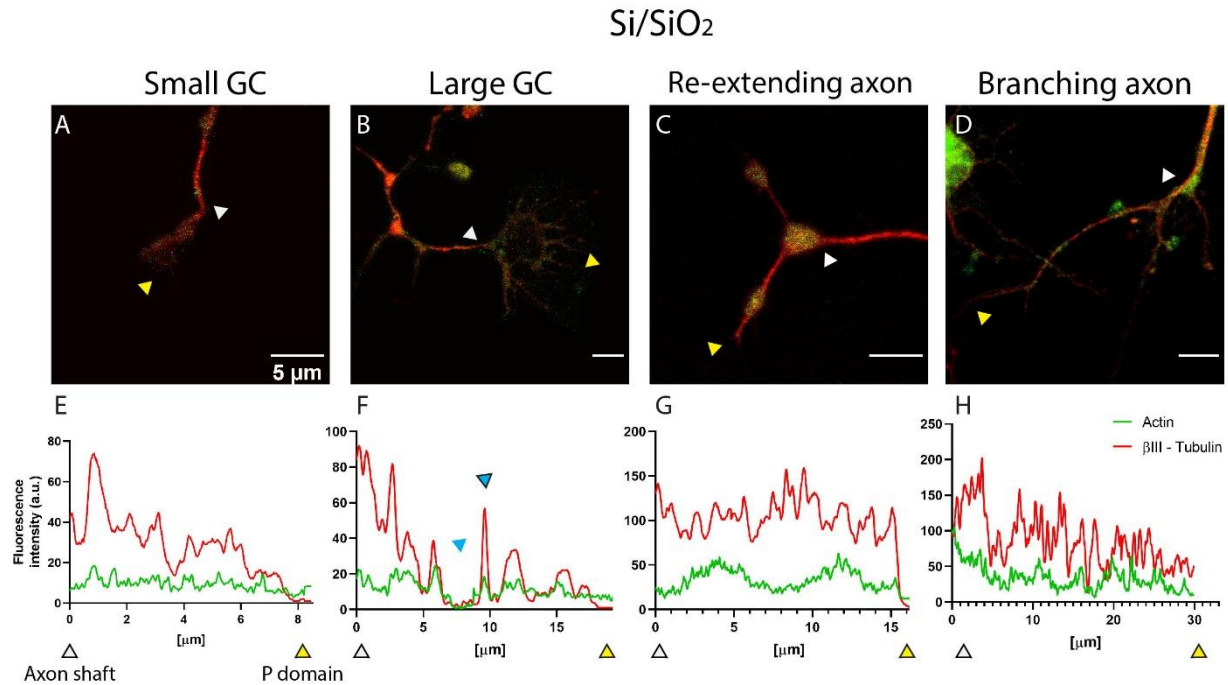


**Figure 3.38.** Fluorescence intensity quantification across GC domains on Si/SiO<sub>2</sub>.

Fluorescence signals of actin and  $\beta$ III-tubulin (in green and red, respectively) were quantified along a segment fixed from the axon shaft (indicated with a white triangle) to the P domain (indicated with a yellow triangle). Quantification was evaluated and plotted as a function of the segment length for small GC (A, E), large GC (B, F), re-extending axon (C, G) and branching axon (D, H). The green trace is associated to the actin fluorescence signal and the red trace to MTs. Light blue triangles, without and with black outline, point the C and T domains within the large GC (F), respectively. Scale bars 5  $\mu$ m.

A comprehensive assay which includes fluorescence intensity quantification (**Materials and methods 2.8.5**) across the specific GC domains (from the axon shaft to the P domain) was here provided for a better understanding of the cytoskeleton spatial organization within the various GC configurations across the different graphene-based cultures.

In the case of Si/SiO<sub>2</sub> planar cultures (**Figure 3.38**) all GCs configurations are supported by the presence of both actin and MTs structures. In particular, high values of tubulin intensity were always found at the axon shaft location, since MTs organize in thicker and composite bundles, as well as at “decision regions”, which are T domain in large GCs (dark blue triangle in **Figure 3.38 F**) or where MTs force new growing direction (white triangle in **Figure 3.38 C**). Here, the actin fluorescence signal is moderate, yet present within almost all GCs except the case of the large configuration which lacks actin structures in the C domain (light blue triangle in **Figure 3.38 F**). If the presence of the actin fluorescence signal almost in all GC domains still

indicates the continuous GC ability to collect information from the extracellular environment during its protrusive activity, instead, the presence of the tubulin fluorescence signal consolidates the neuron portion as new region of the axon shaft.

Similarly, in 2DG neuronal cultures (Figure 3.39), the axonal shafts and decision regions (dark blue and orange triangles in Figure 3.39 F and G, respectively) show higher tubulin fluorescence intensity. On the contrary, a less intense tubulin fluorescence signal was measured in the C domain in large GCs where MT loops are developed (light blue triangle in Figure 3.39 F). As active and motile structures, small GCs and re-extending axons show highly localized actin fluorescence signal at their P domains (Figure 3.39 E, G) as supportive structure to the protrusions and therefore axonal advancement. Colocalization of actin and tubulin within the GC domains in the branching configuration ensures the strong interactions of these two proteins to support axonal outgrowth, guidance and sensing (Figure 3.39 H).

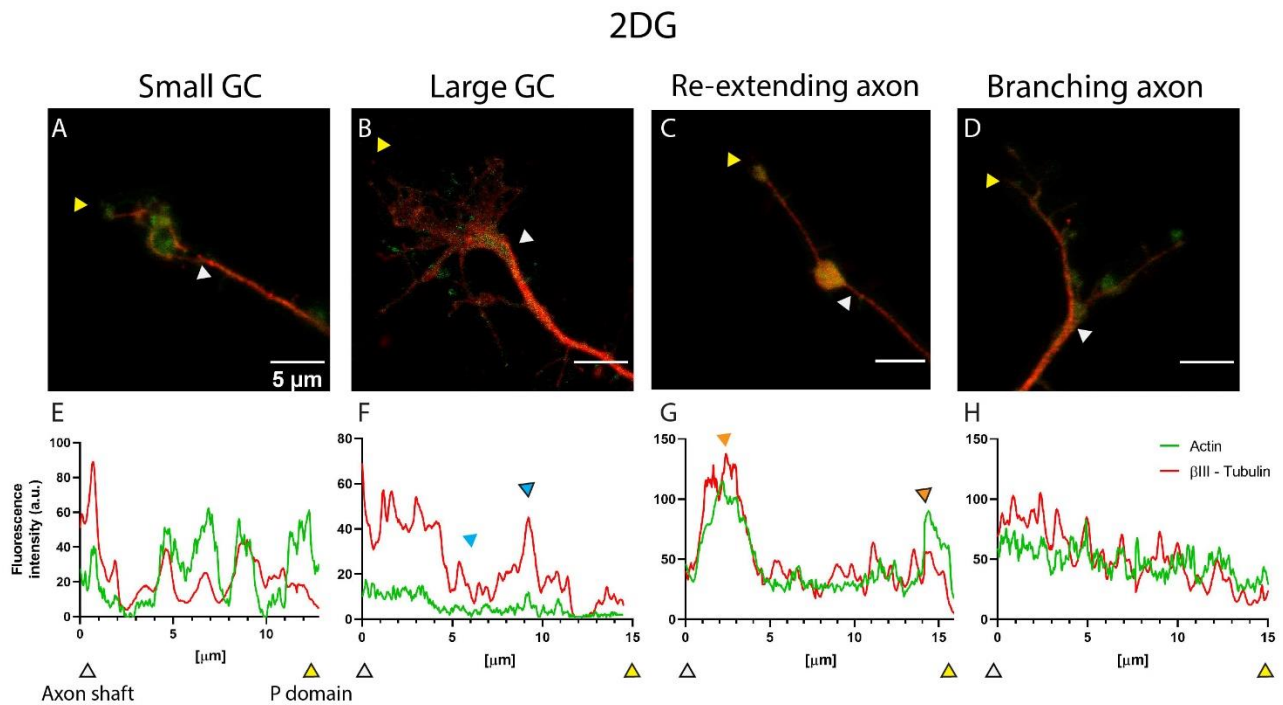


**Figure 3.39. Fluorescence intensity quantification across GC domains on 2DG.**

Fluorescence signals of actin and  $\beta$ III-tubulin (in green and red respectively) were quantified along a segment fixed from the axon shaft (indicated with a white triangle) to the P domain (indicated with a yellow triangle). Quantification was evaluated and plotted as a function of the segment length for small GC (A, E), large GC (B, F), re-extending axon (C, G) and branching axon (D, H). The green trace is associated to the actin fluorescence signal and the red trace to MTs. Light blue triangles, without and with black outline, point the C and T domains within the large GC (F), respectively. Instead, orange triangles, without and with black outline, point the first loop and the terminal end within the re-extending axon (G), respectively. Scale bars 5  $\mu$ m.

**Figure 3.40** shows the fluorescence intensity profiles within GC structures when cortical neurons were cultured on 3DFG. Here, the actin fluorescence signal was generally following the MTs-associated fluorescence signal within the GC elongation from the axon shaft to the P domain. Especially in the case of small and re-extending configurations, the actin-associated fluorescence signal increases in the P domain to reflect the active state in creating new protrusions (**Figure 3.40 E, G**)

Concurrently, MTs structures support GC bodies from the axon shaft to the more distal end of the GC.  $\beta$ III-tubulin fluorescence intensity values are higher than actin, beside the last few micrometres of the large, re-extending and branching axon configurations, where the actin fluorescence signal was predominant due to the protrusive process (**Figure 3.40 F, G, H**). Therefore, the higher fluorescence values associated to the actin emission within the terminal micrometres of the GC might be justified by the enhanced actin-mediated protrusive activity, which is propelled by the presence of topographic features at similar length scale of the adhesive protein structures in the GC.

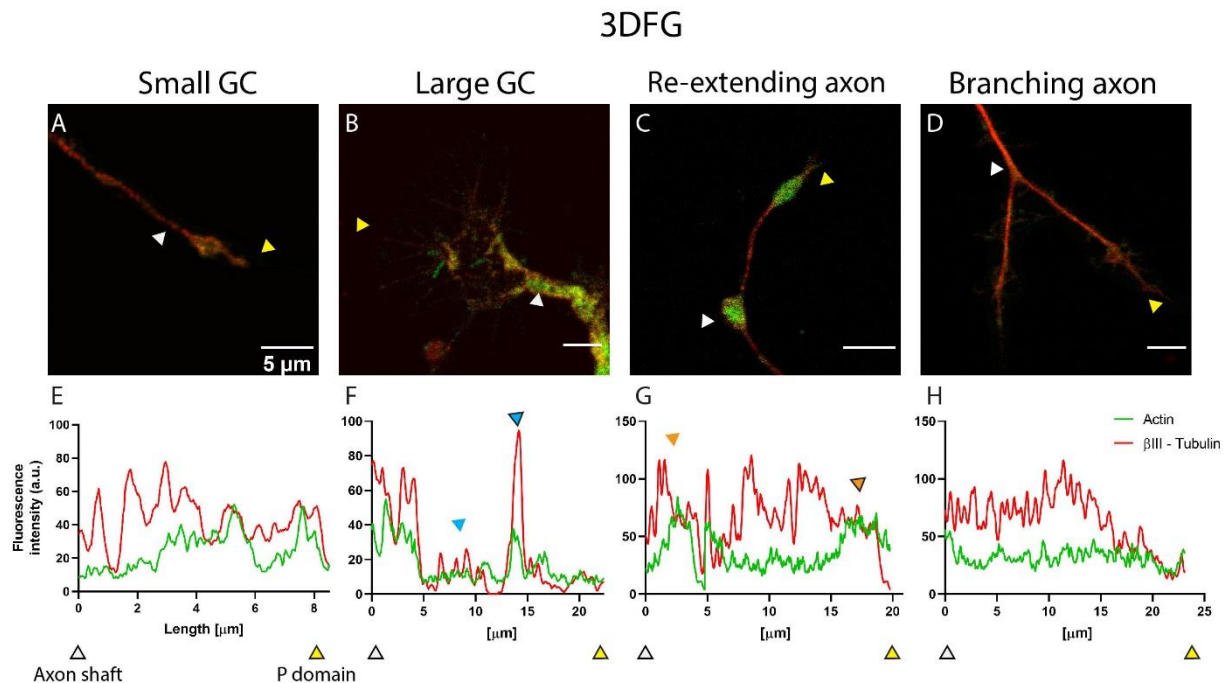


**Figure 3.40.** Fluorescence intensity quantification across GC domains on 3DFG.

Fluorescence signals of actin and  $\beta$ III-tubulin (in green and red respectively) were quantified along a segment fixed from the axon shaft (indicated with a white triangle) to the P domain (indicated with a yellow triangle). Quantification was evaluated and plotted as a function of the segment length for small GC (A, E), large GC (B, F), re-extending axon (C, G) and branching axon (D, H). The green trace is associated to the actin fluorescence signal and the red trace to MTs. Light blue triangles, without and with black outline, point the C and T domains

within the large GC (F), respectively. Instead, orange triangles, without and with black outline, point the first loop and the terminal end within the re-extending axon (G), respectively. Scale bars 5  $\mu\text{m}$ .

Cortical neurons are forced to assume slimmer shapes because of the reduced available growth area in NT-3DFG cultures. Hence, actin and MTs structures colocalized within the developed appendage (**Figure 3.41 A, E, C, G**), which consist of a single bullet-shaped terminal, in small GC configuration (pink triangle in **Figure 3.41 E**), instead in a double round-shaped appendages in the re-extending configuration (orange arrows with and without black border, respectively in **Figure 3.41 G**). Thereby, two fluorescence peaks are found only at the larger regions, which basically indicates the colocalization of actin and MTs. Similarly, in the branching configuration, both actin and tubulin fluorescence signals were found along the axonal extension, which terminates with actin accumulation (purple triangle in **Figure 3.41 H**). The few large GCs recognized across the NT-3DFGc cultures had similar behaviour of small GCs, which results in higher signals both for actin and MTs structures colocalized within the cytoplasmic region (light blue arrow in **Figure 3.41 F**).

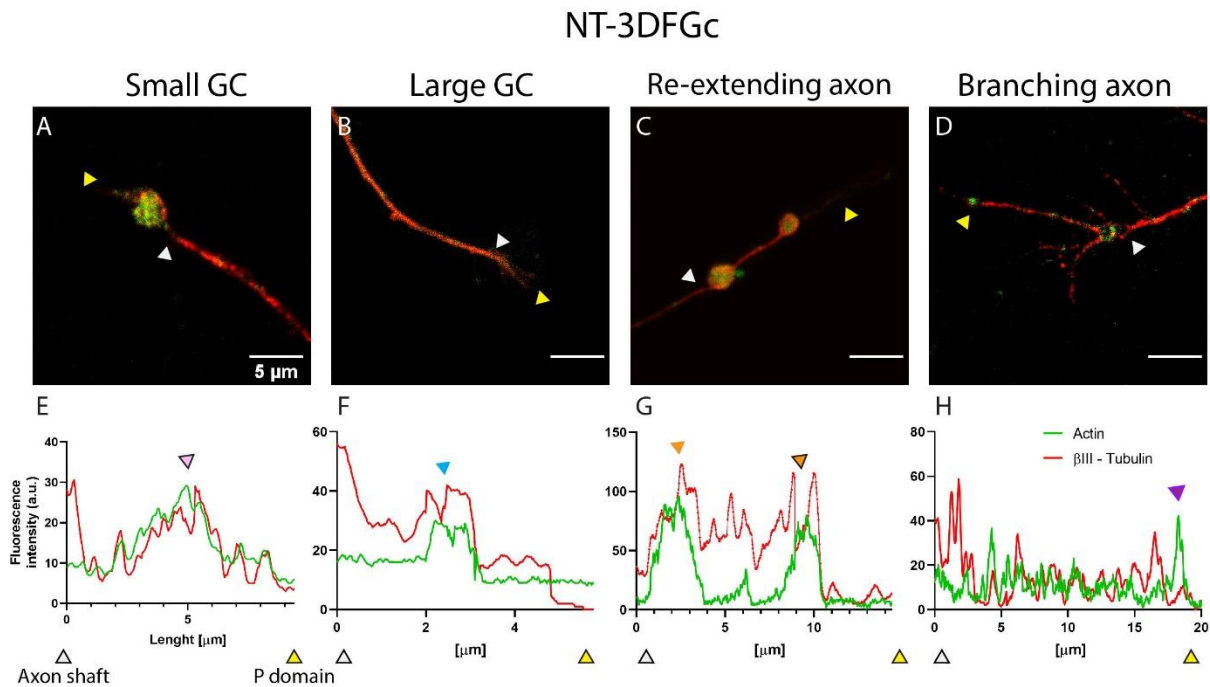


**Figure 3.41. Fluorescence intensity quantification across GC domains on NT-3DFGc.**

Fluorescence signals of actin and  $\beta$ III-tubulin (in green and red, respectively) were quantified along a segment fixed from the axon shaft (indicated with a white triangle) to the P domain (indicated with a yellow triangle). Quantification was evaluated and plotted as a function of the segment length for small GC (A, E), large GC (B, F), re-extending axon (C, G) and branching axon (D, H). The green trace is associated to the actin fluorescence

signal and the red trace to MTs. Pink arrow denotes the small GC body (E), instead the light blue one the large GC appendage. Orange triangles, without and with black outline, point the first loop and the terminal end within the re-extending axon (G), respectively. Purple triangle in panel H denote the filopodia contribution in the P domain. Scale bars 5  $\mu\text{m}$ .

Finally, **Figure 3.42** depicts the fluorescence intensity quantification across GCs domains in NT-3DFGnc cultures. As mentioned earlier, due to the physical properties of the topography (*i.e.*, discontinuous and reduced area faced at the junctional membrane of the neurons), neurons mostly built small GCs. As a consequence, extremely few large GCs were available across the cultures. The two classes were here differentiated considering the GCs width rather than the coverage area (no significant difference was found between the area values, **Figure 3.36 M**) where small GCs exhibit an aligned structure and small width while large GC had the typical fan-like and broadened architecture. Considering the reduced coverage area, the two configurations have similar fluorescence intensity profiles, with higher tubulin signal at the axonal shaft, and almost constant values for all the coverage area. In contrast, two evident actin peaks were found at the initial and terminal parts of the GC body (C and P domains).

In the re-extending configuration (**Figure 3.42 C, G**) MTs populate the whole GC body providing a higher fluorescence intensity at the axon shaft site, the initial loop and terminal end. Actin-associated fluorescence intensity is lower, thereby, figuring at the initial loop and bullet shape appendage.

The branching axon configuration, lastly, consists of MTs and actin which together mediate neurons pioneering activity in the surrounding extracellular environment (**Figure 3.42 D, H**).

Taken together, these results suggest how the synergistic organization of actin and MTs stabilizes the whole cellular structure, regulates the tension forces occurring at the interface with the growth substrate, necessary requirement during the neuritogenesis and, ultimately, determines the neural and GC shapes<sup>106,149,151</sup>.

As the presence of actin signal witnesses, the active state of neuron in protruding the leading edge of the GC, MT inclusion (together or separate from the actin activity) states the consolidation of the new axonal tract.

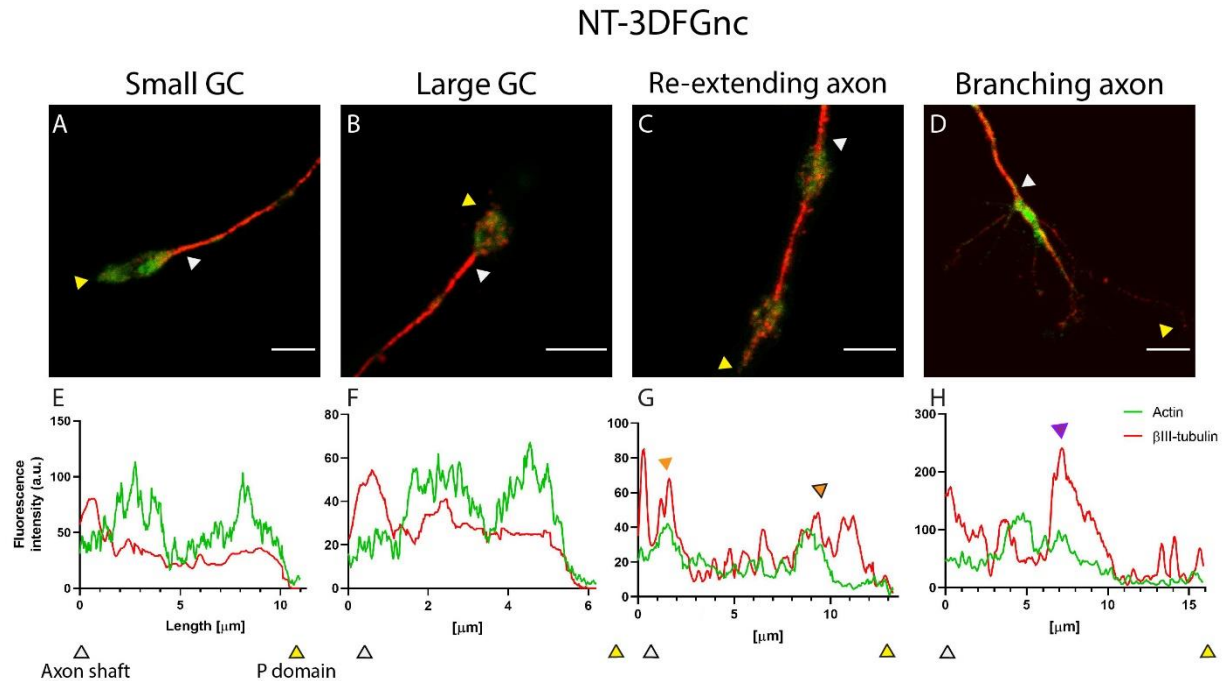


**Figure 3.42. Fluorescence intensity quantification across GC domains on NT-3DFGnc.**

Fluorescence signals of actin and  $\beta$ III-tubulin (in green and red, respectively) were quantified along a segment fixed from the axon shaft (indicated with a white triangle) to the P domain (indicated with a yellow triangle). Quantification was evaluated and plotted as a function of the segment length for small GC (A, E), large GC (B, F), re-extending axon (C, G) and branching axon (D, H). The green trace is associated to the actin fluorescence signal and the red trace to MTs. Orange triangles, without and with black outline, point the first loop and the terminal end within the re-extending axon (G), respectively. Scale bars 5  $\mu$ m.

### 3.5.7 Axon elongation, neuronal branching.

At the leading edge of a growing axon, the GC determines which path the axon will undertake to reach its target. During its outgrowth, an axon might alternate advancing phases to branching, turning, stopping, or even retracting states. Together with the intrinsic machinery which regulates the cell polarization, extracellular cues might provide relevant signals (*i.e.*, chemical, topographical) for addressing neurons towards a specific state regulating<sup>105,155,162,163</sup>, for instance, axonal motility and elongation also through the GC topography sensing<sup>105,155,163,164</sup>. As mentioned earlier, here different GC arrangements have been found depending on the substrate topography (**Figure 3.30**); however, as the out-of-plane features become more prominent with the presence of NWs meshes in the collapsed and non-collapsed arrangements, GC responsiveness to either the physical confinement or the reduced adhesive area leads axons to assume a small GC configuration.

Such differences in axonal morphology, which mimic the cytoskeleton organization underneath the plasma membrane, might trigger relevant changes in the neuronal dynamic outgrowth<sup>158,165</sup>.

Indeed, bullet-shaped GCs (small GCs), are associated to advancing axons while broad and rather flat GCs with emerging filopodia might pause for long time<sup>154,158,165</sup>. However, this stalling phase still includes the active movement of transient filopodia that can navigate nearby the GC location without an evident elongation<sup>155</sup>. In addition, neurons in the re-extending configuration resume the elongation and promote further navigation across the extracellular environment from the flattened region still persisting along the whole axon shaft. Finally, branching axons strive to maximize the sensory exploration of the environment and extend the advancing edge. Thereby, how neurons shaped their terminal ends has strong implications onto their activity state<sup>105,155,162,163</sup>.

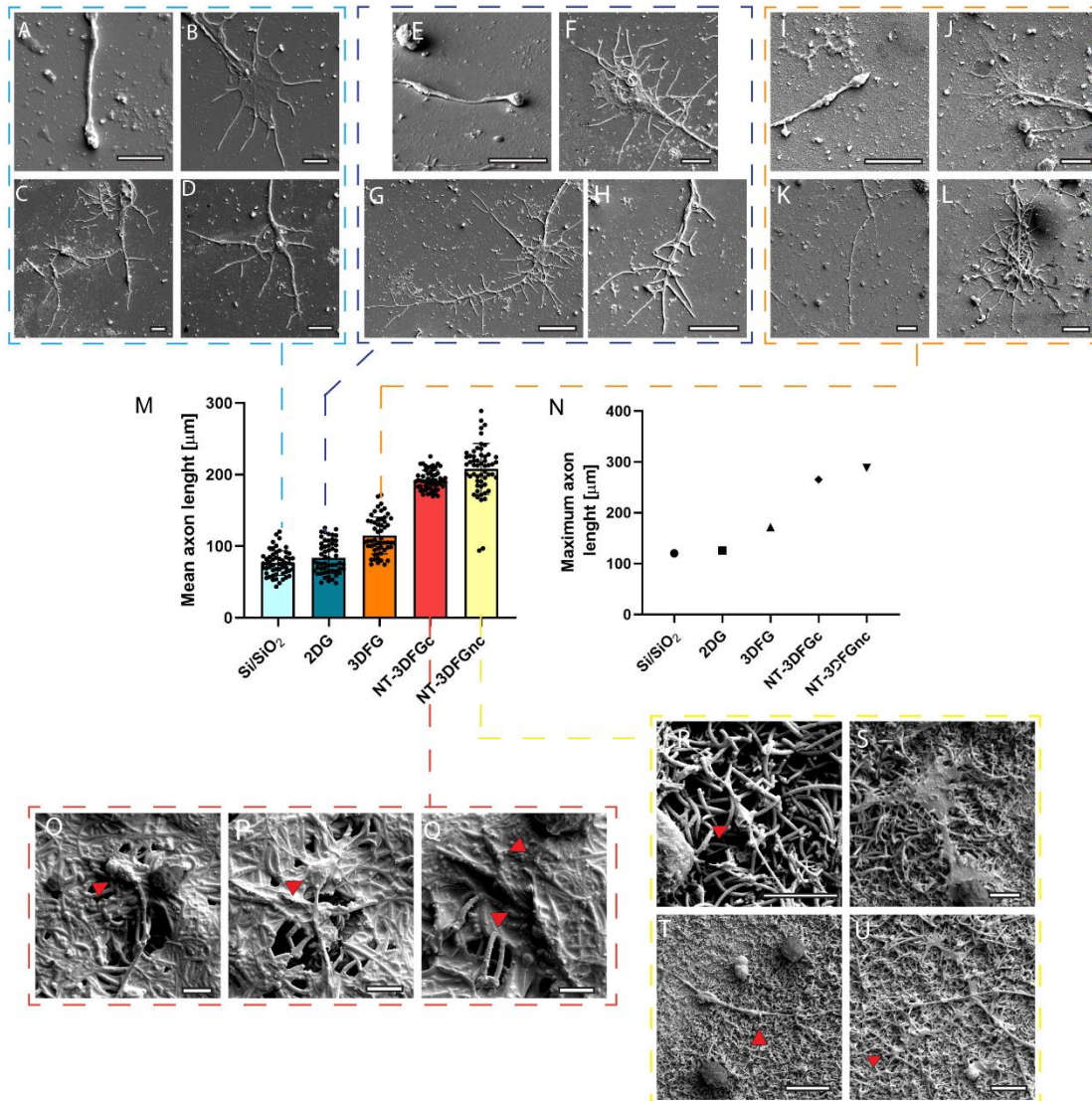


**Figure 3.43. Axon elongation through the graphene topographies.**

(A, B, C, D) SEM micrographs of small, large, re-extending and branching GCs, respectively, cultured on Si/SiO<sub>2</sub>. Scale bars 5  $\mu\text{m}$ . (E, F, G, H) SEM micrographs of small, large, re-extending and branching GCs, respectively, cultured on 2DG. Scale bars 5, (E, F), and 10  $\mu\text{m}$  (H, G), respectively. (I, J, K, L) SEM micrographs of small, large, re-extending and branching GCs, respectively, cultured on 3DFG. Scale bars 5  $\mu\text{m}$  (I - L), 10  $\mu\text{m}$  (J - K). (M) Quantification of the mean axon lengths attained by cortical neurons after 3 DIV on the different topographies. (N) Maximum extensions axons reached considering their saltatory growth. (O, P, Q) SEM micrographs of small, large and branching GCs, respectively, cultured on NT-3DFGc and indicated by red arrows. Scale bars 5  $\mu\text{m}$ . (R, S, T, U) SEM micrographs of small, large, re-extending and branching GCs, respectively, cultured on NT-3DFGnc. Scale bars 5  $\mu\text{m}$ .

Moreover, considering the preferential GC morphologies found over the different planar and out-of-plane materials, graphene substrates were employed as cell-instructive platforms to also modulate axonal elongation. **Figure 3.43 M** shows the mean axonal length measured after 3 DIV by using optical micrographs of neurons immunolabelled against MAP2 and Tau-1 proteins (dendrites and axon neuronal markers, respectively, **Materials and Methods 2.6.3**). The image analysis was carried out with ImageJ as described in **Materials and Methods 2.8.6**.

Here, all topographies promoted the axonal growth, resulting in neurons having longer axons pared to those on flat substrates. In particular, the large standard deviations on both planar and 3DFG materials highlight the presence of heterogeneous GC morphologies (**Figure 3.43 A – L**) which, in turn, might define diverse neuronal activity states. The longest axonal average length values were attained when cells adhered on top of the free-standing NWs and were confined by their side walls in NT-3DFGnc cultures. Similarly, in NT-3DFGc cultures, axons largely extend from the cell body. Although the reduced growth area offered by the limited area of NWs exposed to the cell attachment, these protruding structures and their spatial arrangement provide contact points from which cells might anchor the GC to pull forward advancement by means of actomyosin-driven traction forces<sup>153</sup>.

Indeed, considering the high affinity that GC morphologies have with the pattern of the underlying substrate, as well as the association between their morphological properties and functional behaviour, the external structural cues might consequently regulate axon movement and polarization<sup>158,165</sup>. Thus, the increased dimensionality of the topographies, from planar to pseudo 3D structures, allows neurons to stretch further and develop longer axons. **Table 3.9** shows the percentage increase of axonal length

compared to the growth across the planar graphene. On non-collapsed NWs the axonal elongation was more than doubled.

Axon increase length (%)	
3DFG	36.6
NT-3DFG c	79.4
NT-3DFG nc	129.5

**Table 3.9. Percentage increase of axonal length compared to planar graphene culture.**

Similar topographical guidance was obtained by Milos *et al.* using pillars as growth substrates<sup>164</sup>. Here, not only the median axon lengths were 40% longer when in contact with pillars in comparison to the flat substrates, but also the ordered protruding structures aligned neurites along the pillar distribution. In our case, no clear directionality was observed as the graphene materials exhibit randomly distributed topographical features. However, similar effects of local random micro and nanotopographies on the axon elongation has been previously reported<sup>166</sup>.

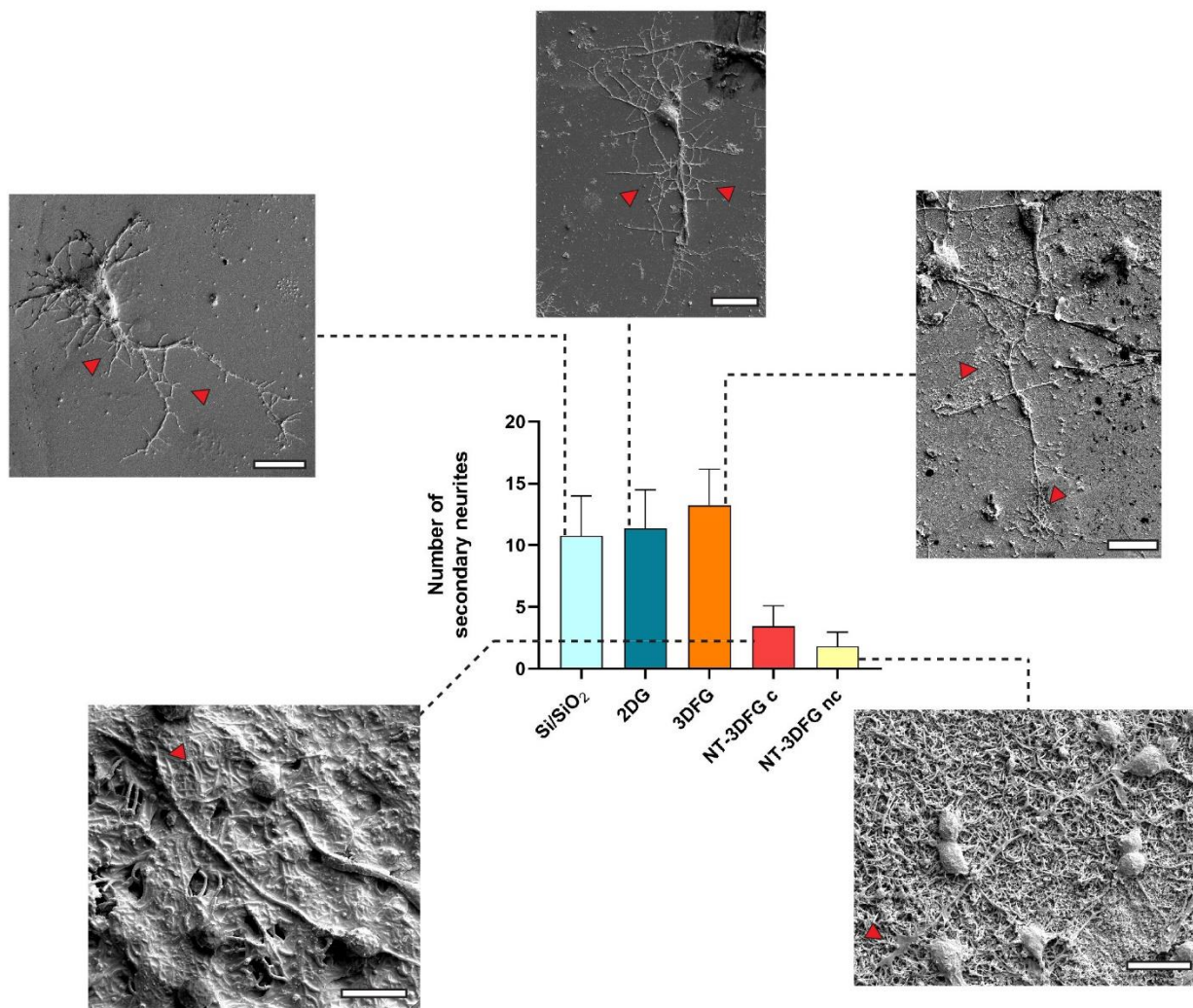


**Figure 3.44. Secondary neurites investigation along the axon shaft.**

The presence of secondary neurites was quantified from optical images of solitary neurons stained against Tau-1 axon-specific marker. For each substrate, an exemplary SEM micrograph of the neurons in contact with the pattern underneath has been provided. Scale bars 15  $\mu\text{m}$ .

Considering the neuronal growth process (stage 3, see **Figure 3.29**), the structural might affect the GC morphology and ultimately the neuronal functional activity. Therefore, restricted growth area, in NT-3DFGc and nc cell cultures, forced neurons to assume streamlined shape which proceeds through the path without minimal pausing, and ultimately results in higher values of the branches elongation. Moreover, as shown in **Figure 3.41 E, G** and **3.42 E**, the active state of small GCs is also supported by the presence of actin-based assemblies which play a key role in the initiation of the GC advancement<sup>151</sup>.

Instead, in the case of continuous material surfaces (*i.e.*, Si/SiO<sub>2</sub> and 2DFG) or out-of-plane features interdistance as equal as the contact adhesion size (*i.e.*, 3DFG material), neurons face only few physical boundaries to the GC establishment. This results in higher chance for neurons to build broad axonal terminals, which ultimately lead them to alternate advancing growth to pausing phases and minimal elongation.

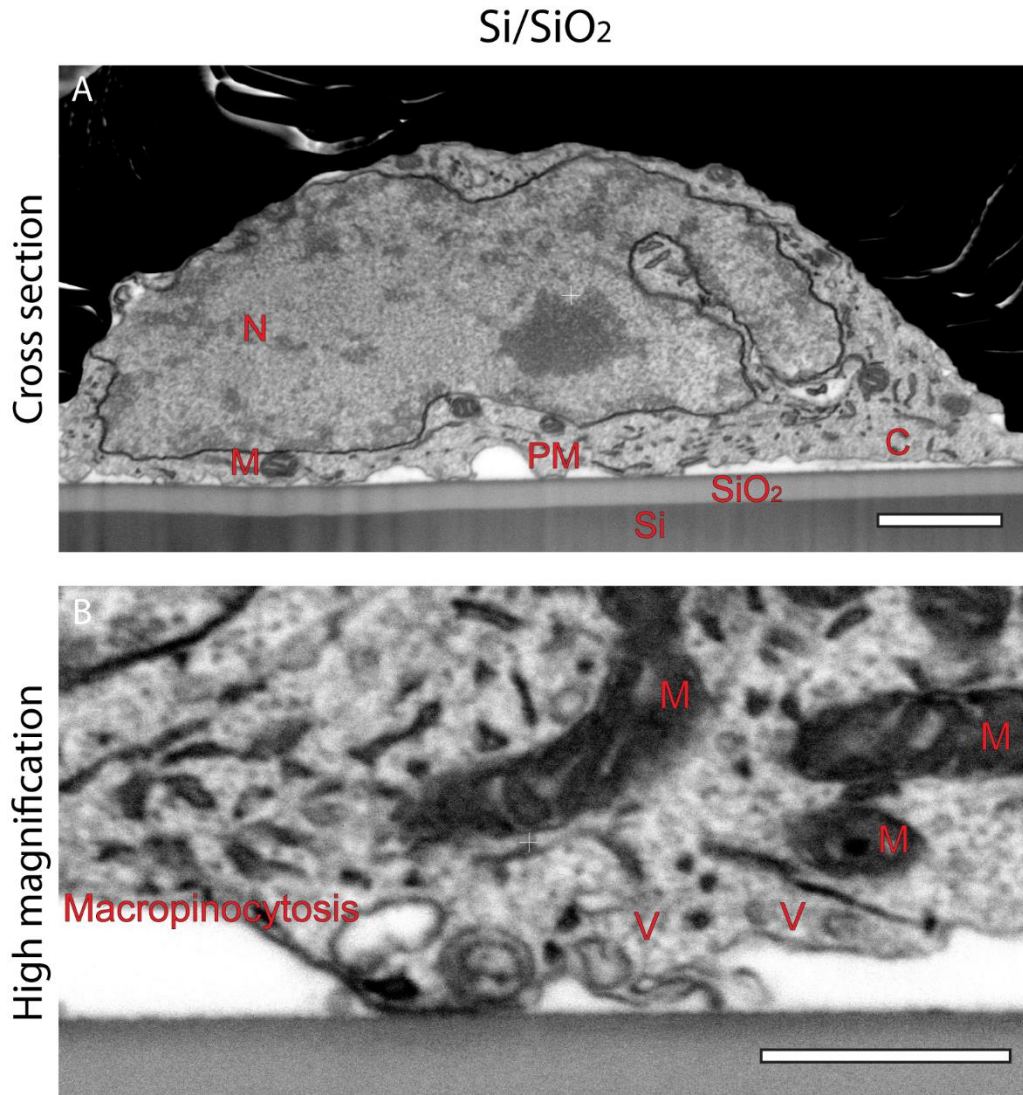
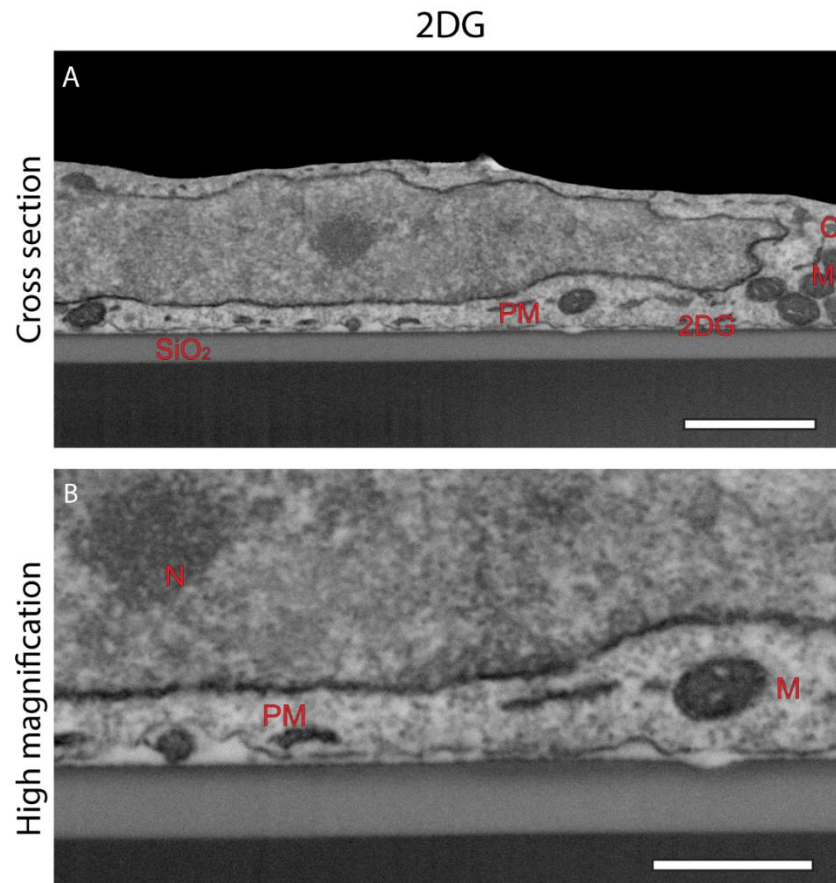


Figure 3.45. Neuron-Si/SiO<sub>2</sub> adhesion.

Cross-sections (A, B) acquired in backscattered electron mode show the intracellular environment which includes nucleus (N, in red), cytoplasm (C, in red), mitochondria (M, in red), as well as possible endocytic pathways (micropinocytosis and vesicles (V)). Cross-sections scale bar 1  $\mu$ m and 500 nm, for A and B micrographs, respectively.

Besides affecting the axonal elongation, the out-of-plane materials might also influence neurites' branching. **Figure 3.44** shows the statistical analysis of the average number of neurites developed on the different graphene substrates.

The presence of secondary neurites along the axonal shaft indicates not only the capability of cells to explore the neighbouring environment but also their capacity to create a well-developed cell network. Indeed, as the axon terminal crawls across the extracellular landscape to reach its targets, which might be another neuron, similarly secondary neurites might become new consolidated tracts of the axonal shaft, but also create contact points with adjacent cells<sup>151</sup>. However, the lack of physical confinements fosters the initiation of new emerging branches along the axonal shaft **Figure 3.44**. In particular, in line with the enhanced protrusive activity triggered by the nanoscale topography in 3DFG cultures, axons were enriched by a higher number of secondary processes. On the contrary, few protrusions emerging from the axon were found by analyzing NT-3DFG templates cultures. The analysis was performed on solitary or almost solitary neurons. However, by increasing the cells density, complex and well-formed neuronal networks developed even in presence of more prominent structures as in the NT-3DFGc and nc cases.



**Figure 3.46. Neuron-2DG adhesion.**

Cross-sections (A, B) acquired in backscattered electrode mode show the intracellular environment, as well as PM conformation to the flat material profile. Cross-sections scale bars 1  $\mu\text{m}$  and 500 nm, for A and B micrographs, respectively.

**3.5.8 Neuron-graphene material coupling investigated by SEM/FIB.**

As discussed earlier, the strong affinity that neuronal cells have with the topography of the underlying substrates also impacts GC migration across the external environment. In particular, the ability of neurons to migrate, which is considered at the basis of brain building and its functional outcome, simply arises with GC crawling and the polarization of the axon<sup>167,168</sup>. However, migration requires the establishment of forces that cells exchange with the substrate underneath. As a consequence, strict connections to the topographical features introduced by the substrate are necessary to activate the internal contractile machinery and finally produce a cellular response such as dynamic translocation<sup>30,31,153,167</sup>.

Similarly to the HL-1 case, the neuronal response to the topotaxis (*i.e.*, stimuli originating from the geometric structures of the substrate) involves complex mechanotransduction pathways which are located at both sides of the junctional PM or within internal compartments and drive cells during the adaptive process of attachment. In this scenario, the analysis of the adhesive coupling between cell and graphene materials is provided by means of SEM/FIB micrographs which depict the PM profile, its change in the curvature when in contact with out-of-plane features and, finally, the distance established between cell and material.

**Figure 3.45 A** shows a cross section of a neuronal cell cultured on Si/SiO<sub>2</sub>. Consistent with previous reports<sup>12,40,146</sup>, in planar cultures the distance between cell and material underneath hovers 100-150 nm, besides regions where PM is engaged in newly formed invaginations (**Figure 3.45 B**). A flatter neuronal body was found in the case of 2DG (**Figure 3.46 A**) where the PM still follows the plane material with sporadic invaginations (**Figure 3.46 B**).

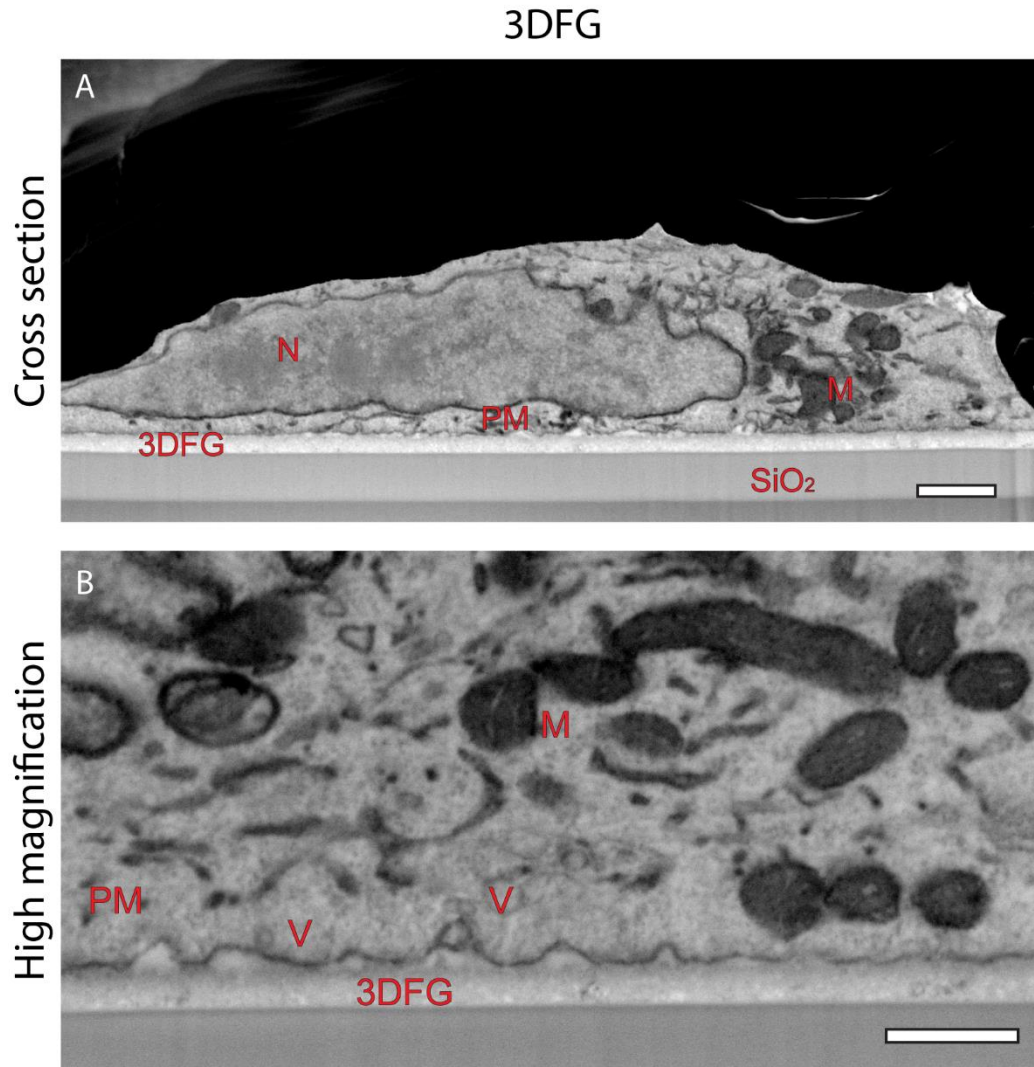


**Figure 3.47. Neuron-3DFG adhesion.**

Cross-sections (A - B) acquired in backscattered electron mode show the intracellular environment, as well as PM roughness due to graphene spikes protruding from the material. Cross-sections scale bars 1  $\mu\text{m}$  and 500 nm, for A and B micrographs, respectively.

In the case of 3DFG cultures, the nanoscale graphene spikes which protrude from the planar surface are mostly mirrored by the basal PM, which appears to be rough in **Figure 3.47 B**. This result supports the PM fluidity to conform to the external topographical stimuli. Moreover, the superficial fuzziness of the graphene material, which is in the dimension range of endocytic pathways<sup>40,46,142</sup>, might trigger curvature progression at the interface with the material, as indicated by the letter V in **Figure 3.47 B**.

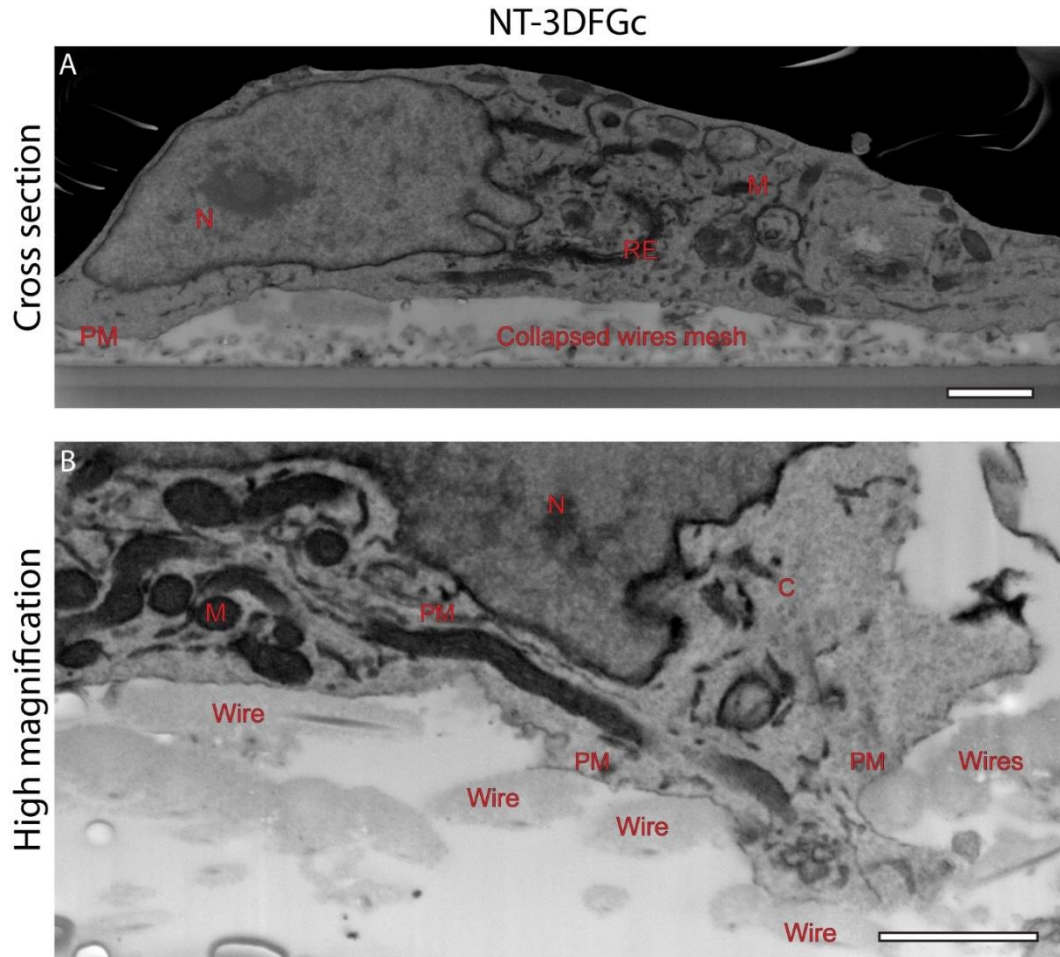


**Figure 3.48. Neuron-NT-3DFGc adhesion.**

Cross-sections (A-B) acquired in backscattered electron mode show the intracellular environment, as well as cell accommodation through NWs microcavities. Cross-sections scale bars 1  $\mu\text{m}$  and 500 nm, for A and B micrographs, respectively.

Cross sections of cells in NT-3DFGc cultures revealed that neuronal bodies closely follow the topography underneath also fitting portion of its body within the microcavities of the collapsed wire mesh (**Figure 3.48 A**). These findings demonstrate how flexible and fluid are both the cell itself and the PM. Indeed, during these processes of cellular adaptation, the PM assumes pronounced curvatures to accommodate through NWs microcavities which might foster the initiation of vesicle buds (**Figure 3.48 B**).

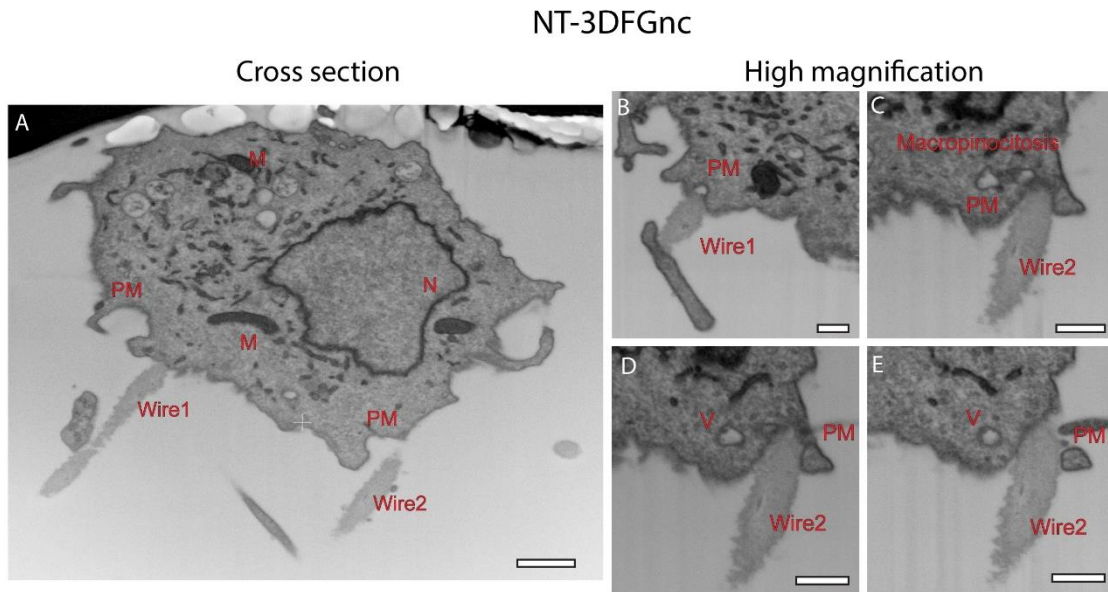


**Figure 3.49. Neuron-NT-3DFGnc adhesion.**

Cross-sections (A) acquired in backscattered electron mode show the intracellular environment and the interaction with free-standing wires. Scale bar 1  $\mu\text{m}$ . (B - E) High magnified views depict the invagination events which occurs at cell-wire contact points. Scale bar and 500 nm.

Finally, **Figure 3.49** illustrates the neuron-material interaction when cells were cultured on free-standing NWs. Comparing to the HL-1 cases shown in **Figure 3.26** where cells seem to be sink into the wire mesh and be far greater than the single structures, here the neuronal body appeared rather floating on the single NWs. This might also depend on the different cell size cardiomyocytes and neuronal cells have. Moreover, only few NWs underpin neuronal bodies, compared to the HL-1 case where packed NWs were found in direct contact with the cell body. Thus, the cell here appears to have contact only with occasional wires (**Figure 3.49 A**), which foster marked inwards PM curvature, typical of the engulfment phenomena<sup>40</sup>. However, from the serial milling, no internalization was detected, as depicted in **Figure 3.49 B, C, D, E**. Indeed, darker signal associated to the PM was easily detectable.

## Chapter 4: Conclusions.

The application of electronic devices in the study of human body has moved forward in the understanding of several biological dynamics and promises to lead additional advance in both biology and medicine science. However, the most enticing implications pledge to unlock new strategies for delivering personalized therapies.

Indeed, comprehensive study of the cellular electric state might further elucidate pathological conditions which comprises impaired electrical activity at cellular and/or cellular network level. However, detailed investigations require the adoption of “tissue-like” technologies capable of producing stable interface at the cellular to subcellular level when in contact with the biological system over extended periods of time. Concurrently, exploiting biomimicry mechanisms to encourage a stable coupling with the electronic devices enables to fulfil some bioelectronics requirements for an optimal analysis which, as mentioned already, include increasing exposed electronic surface area at the interface with the cells, lowering the electrode impedance and reducing cell-material cleft distance. For these purposes, flat electronics unlikely proves to be an ideal solution, due to reduced interface area, as well as their oversimplified architecture hardly recapitulates the complexity of the *in vivo* environment.

In this thesis, the development of three different out-of-plane carbon-based topographies were analyzed as promising candidate of electrode topographies. The non-planar nature of the materials enables to overcome some limits the current planar bioelectronics faced.

Such non-planar structures enable to leverage graphene outstanding surface-to-volume ratio by exposing both sides of graphene flakes to the basal membrane of the cells above them cultures. The physical characterization, here provided by means of scanning electron microscopy imaging, yet shows that the developed architectures are in the comparable scale of cellular processes (as filopodia or emerging neurites). As a consequence, direct activation of protein pathways occurs at the interface.

Significantly, from the interaction of HL-1 cardiomyocytes like-cells and abovementioned graphene materials, mature and adhesive processes in contact with nanoscale topographic feature (*i.e.*, 3DFG) enables cells to build stable long actin fibers-based cytoskeleton. As the feature height and interspacing start to increase (*i.e.*, as in the case of NT-3DFG templates), the distance between adjacent wires became relevant to stabilize focal adhesion maturation. Moreover, less organized cytoskeleton, with actin architectures similar to small spheres, develop at the interface with the upright features. The immediate consequence of this crosstalk causes cells to reshape their volumetric morphology accordingly. Flattened cells maximized the contact with the material, extending on xy-fashion in 3DFG, while on both nanowire

mesh templates cells show remarkable membrane deformations fitting their body between the microcavities left among the interwoven or free-standing nanowires, which enable them to adopt longer heights. Moreover, those peculiar membrane curvatures at the interaction sites with the nanostructures allow cells to be physically in contact with the upper regions of the graphene flakes, in 3DFG, and be completely sink into the micrometric topography on wires arrangements. In particular, wrapping event around the single wire developed in the fiber-like architecture of NT-3DFGc, as at the basal plasma membrane or with perimetral filopodia. Instead, the vertical arrangement of the wires in NT-3DFGnc, completely, perturb the junctional membrane profile, by promoting strong positive curvature and engulfment event of the single wire. The membrane ruffling occurring as consequence of the adaptive process of attachment to the structured graphene materials, results in enhanced activation of the endocytic pathways as the comprehensive analysis of clathrin-mediated vesicles and caveolae spatial distribution demonstrated.

Similarly, the interaction between cortical neurons and out-of-plane graphene was studied during the early phases of neural network development, when cellular processes (*i.e.*, neurons and dendrites) were distinguished. Here, rather than analyzing the cellular body, the focus was moved on growth cone terminals which are leading actuators of the brain wiring dynamics, and therefore, neuronal polarization. Thereby, growth cone morphologies were assessed with specific attention to the actin and microtubules cooperation, and then categorized in four different classes small, large, re-extending and branching. Growth cone classification has strong implications on neuronal cells behavior, influencing its active or pausing states. In particular, small bullet-shaped and re-extending configurations are associated to the advancing axons, broadened and flat morphologies to pausing phase in the advancing, and finally the branching topology to the sensory exploration. Resulting from the affinity with the graphene topographies, wires mesh templates encourage growth cone to assume a small bullet-shape and therefore, neurons to be active in the navigation which ultimately results in enhanced axon elongation. In parallel, the interaction with nanoscale graphene materials leads neuronal cells to preferentially develop branched structures. However, all the non-planar topographies foster longer axonal processes pared to those on flat substrates. These findings result from enhanced coupling cells have with vertical protruding structures.

In conclusion, this work demonstrates the advantages and versatility of using out-of-plane graphene structures as potential candidates for microelectrode fabrication. The required increase in exposed cell area to interface to the cells, in bioelectronics technologies, is completely fulfilled by leveraging out-of-plane structures which not only recapitulate topographical motifs already existing in *in vivo* context, but encourage a tight contact with cells, *via* membrane ruffling and engulfment events.

Although, the present study provides a comprehensive view of the interface between electrogenic cells and 3D micro and nano-structured materials by using fluorescence and electron microscopy for a biological readout, additional electrical recordings would add further information about the efficiency of the cell-material interaction as well as the functional state of the cells. Therefore, 3DFG, NT-3DFGc and/or NT-3DFGnc could be fabricated as sensing areas of MEAs by using a top-down patterning approach. Moreover, due to the sharp membrane engulfment events occurring at the interface with the single graphene features, the recording of electrical cell activity might be characterized on the basis of the detected action potential shapes as extra or intracellular. The exploited fine graphene structures might open up new possibilities to probe cells at the subcellular scale.

Further experiments might be addressed to use the graphene out-of-plane materials as cell-instructive platforms. Moreover, considering the endocytic processes triggered by the out-of-plane graphene materials, these structures might be used as tools to deliver cargoes in the cells as drug or gene (*i.e.*, in transfection approach). In this perspective, differential activation of endocytic pathways might be studied by incubating inhibitor drugs (for example of dynamin proteins).

Moreover, with specific reference to the neuronal culture, the different adhesion cues provided by the accessible surface area might be harnessed either to study calcium ions dynamics, involved into the neural polarization processes or to analyze the shaping of excitatory and inhibitory neurons circuitry, as several integrin families, at the forefront of cell adhesion, mediated intracellular calcium signalling and glutamatergic neurons activities.

## References

- (1) Precision electronic medicine in the brain | Nature Biotechnology <https://www.nature.com/articles/s41587-019-0234-8> (accessed 2021 -06 -09).
- (2) Ershad, F.; Sim, K.; Thukral, A.; Zhang, Y. S.; Yu, C. Invited Article: Emerging Soft Bioelectronics for Cardiac Health Diagnosis and Treatment. *APL Materials* **2019**, *7* (3), 031301. <https://doi.org/10.1063/1.5060270>.
- (3) The Physiology of Excitable Cells <https://www.cambridge.org/core/books/physiology-of-excitable-cells/0542F611C2AE1ECCF031D48F760C364B> (accessed 2021 -06 -09).
- (4) Reilly, R. B.; Lee, T. C. Electrograms (ECG, EEG, EMG, EOG). *Technol Health Care* **2010**, *18* (6), 443–458. <https://doi.org/10.3233/THC-2010-0604>.
- (5) *Modeling & Imaging of Bioelectrical Activity: Principles and Applications*; He, B., Ed.; Bioelectric Engineering; Springer US, 2005. <https://doi.org/10.1007/978-0-387-49963-5>.
- (6) Spira, M. E.; Hai, A. Multi-Electrode Array Technologies for Neuroscience and Cardiology. *Nature Nanotechnology* **2013**, *8* (2), 83–94. <https://doi.org/10.1038/nnano.2012.265>.
- (7) Shmoel, N.; Rabieh, N.; Ojovan, S. M.; Erez, H.; Maydan, E.; Spira, M. E. Multisite Electrophysiological Recordings by Self-Assembled Loose-Patch-like Junctions between Cultured Hippocampal Neurons and Mushroom-Shaped Microelectrodes. *Scientific Reports* **2016**, *6* (1), 1–11. <https://doi.org/10.1038/srep27110>.
- (8) Chen, K.-I.; Li, B.-R.; Chen, Y.-T. Silicon Nanowire Field-Effect Transistor-Based Biosensors for Biomedical Diagnosis and Cellular Recording Investigation. *Nano Today* **2011**, *6* (2), 131–154. <https://doi.org/10.1016/j.nantod.2011.02.001>.
- (9) Rastogi, S. K.; Kalmykov, A.; Johnson, N.; Cohen-Karni, T. Bioelectronics with Nanocarbons. *J. Mater. Chem. B* **2018**, *6* (44), 7159–7178. <https://doi.org/10.1039/C8TB01600C>.
- (10) Bruno, U.; Mariano, A.; Santoro, F. A Systems Theory Approach to Describe Dynamic Coupling at the Cell–Electrode Interface. *APL Materials* **2021**, *9* (1), 011103. <https://doi.org/10.1063/5.0025293>.
- (11) Santoro, F.; Zhao, W.; Joubert, L.-M.; Duan, L.; Schnitker, J.; van de Burgt, Y.; Lou, H.-Y.; Liu, B.; Salleo, A.; Cui, L.; Cui, Y.; Cui, B. Revealing the Cell–Material Interface with Nanometer Resolution by Focused Ion Beam/Scanning Electron Microscopy. *ACS Nano* **2017**, *11* (8), 8320–8328. <https://doi.org/10.1021/acsnano.7b03494>.
- (12) Toma, K.; Kano, H.; Offenhäusser, A. Label-Free Measurement of Cell–Electrode Cleft Gap Distance with High Spatial Resolution Surface Plasmon Microscopy. *ACS Nano* **2014**, *8* (12), 12612–12619. <https://doi.org/10.1021/nn505521e>.
- (13) Kreysing, E.; Hassani, H.; Hampe, N.; Offenhäusser, A. Nanometer-Resolved Mapping of Cell–Substrate Distances of Contracting Cardiomyocytes Using Surface Plasmon Resonance Microscopy. *ACS Nano* **2018**, *12* (9), 8934–8942. <https://doi.org/10.1021/acsnano.8b01396>.
- (14) Pennacchio, F. A.; Garma, L. D.; Matino, L.; Santoro, F. Bioelectronics Goes 3D: New Trends in Cell–Chip Interface Engineering. *J. Mater. Chem. B* **2018**. <https://doi.org/10.1039/C8TB01737A>.
- (15) Higgins, S. G.; Becce, M.; Belessiotis-Richards, A.; Seong, H.; Sero, J. E.; Stevens, M. M. High-Aspect-Ratio Nanostructured Surfaces as Biological Metamaterials. *Advanced Materials* **2020**, *32* (9), 1903862. <https://doi.org/10.1002/adma.201903862>.
- (16) Robinson, J. T.; Jorgolli, M.; Park, H. Nanowire Electrodes for High-Density Stimulation and Measurement of Neural Circuits. *Front Neural Circuits* **2013**, *7*, 38. <https://doi.org/10.3389/fncir.2013.00038>.

- (17) B Sakmann; Neher, and E. Patch Clamp Techniques for Studying Ionic Channels in Excitable Membranes. *Annual Review of Physiology* **1984**, *46* (1), 455–472. <https://doi.org/10.1146/annurev.ph.46.030184.002323>.
- (18) Abbott, J.; Ye, T.; Ham, D.; Park, H. Optimizing Nanoelectrode Arrays for Scalable Intracellular Electrophysiology. *Acc. Chem. Res.* **2018**, *51* (3), 600–608. <https://doi.org/10.1021/acs.accounts.7b00519>.
- (19) Dipalo, M.; McGuire, A. F.; Lou, H.-Y.; Caprettini, V.; Melle, G.; Bruno, G.; Lubrano, C.; Matino, L.; Li, X.; De Angelis, F.; Cui, B.; Santoro, F. Cells Adhering to 3D Vertical Nanostructures: Cell Membrane Reshaping without Stable Internalization. *Nano Lett.* **2018**, *18* (9), 6100–6105. <https://doi.org/10.1021/acs.nanolett.8b03163>.
- (20) Robinson, J. T.; Jorgolli, M.; Shalek, A. K.; Yoon, M.-H.; Gertner, R. S.; Park, H. Vertical Nanowire Electrode Arrays as a Scalable Platform for Intracellular Interfacing to Neuronal Circuits. *Nature Nanotechnology* **2012**, *7* (3), 180–184. <https://doi.org/10.1038/nnano.2011.249>.
- (21) Spira, M. E.; Kamber, D.; Dormann, A.; Cohen, A.; Bartic, C.; Borghs, G.; Langedijk, J. P. M.; Yitzchaik, S.; Shabthai, K.; Shappir, J. Improved Neuronal Adhesion to the Surface of Electronic Device by Engulfment of Protruding Micro-Nails Fabricated on the Chip Surface. In *TRANSDUCERS 2007 - 2007 International Solid-State Sensors, Actuators and Microsystems Conference*; 2007; pp 1247–1250. <https://doi.org/10.1109/SENSOR.2007.4300363>.
- (22) McGuire, A. F.; Santoro, F.; Cui, B. Interfacing Cells with Vertical Nanoscale Devices: Applications and Characterization. *Annual Rev. Anal. Chem.* **2018**. <https://doi.org/10.1146/annurev-anchem-061417-125705>.
- (23) Xie, C.; Lin, Z.; Hanson, L.; Cui, Y.; Cui, B. Intracellular Recording of Action Potentials by Nanopillar Electroporation. *Nature Nanotechnology* **2012**, *7* (3), 185–190. <https://doi.org/10.1038/nnano.2012.8>.
- (24) Patolsky, F.; Timko, B. P.; Yu, G.; Fang, Y.; Greytak, A. B.; Zheng, G.; Lieber, C. M. Detection, Stimulation, and Inhibition of Neuronal Signals with High-Density Nanowire Transistor Arrays. *Science* **2006**, *313* (5790), 1100–1104. <https://doi.org/10.1126/science.1128640>.
- (25) Yoo, J.; Kwak, H.; Kwon, J.; Ha, G. E.; Lee, E. H.; Song, S.; Na, J.; Lee, H.-J.; Lee, J.; Hwangbo, A.; Cha, E.; Chae, Y.; Cheong, E.; Choi, H.-J. Long-Term Intracellular Recording of Optogenetically-Induced Electrical Activities Using Vertical Nanowire Multi Electrode Array. *Sci Rep* **2020**, *10* (1), 4279. <https://doi.org/10.1038/s41598-020-61325-3>.
- (26) San Roman, D.; Garg, R.; Cohen-Karni, T. Bioelectronics with Graphene Nanostructures. *APL Materials* **2020**, *8* (10), 100906. <https://doi.org/10.1063/5.0020455>.
- (27) Zhang, W.; Yang, Y.; Cui, B. New Perspectives on the Roles of Nanoscale Surface Topography in Modulating Intracellular Signaling. *Current Opinion in Solid State and Materials Science* **2021**, *25* (1), 100873. <https://doi.org/10.1016/j.cossms.2020.100873>.
- (28) Lou, H.-Y.; Zhao, W.; Zeng, Y.; Cui, B. The Role of Membrane Curvature in Nanoscale Topography-Induced Intracellular Signaling. *Accounts of Chemical Research* **2018**, *51* (5), 1046–1053. <https://doi.org/10.1021/acs.accounts.7b00594>.
- (29) Biomechanical Cell Regulation by High Aspect Ratio Nanoimprinted Pillars - Viela - 2016 - Advanced Functional Materials - Wiley Online Library <https://onlinelibrary.wiley.com/doi/abs/10.1002/adfm.201601817> (accessed 2021 -06 -09).
- (30) Ventre, M.; Causa, F.; Netti, P. A. Determinants of Cell–Material Crosstalk at the Interface: Towards Engineering of Cell Instructive Materials. *Journal of The Royal Society Interface* **2012**, *9* (74), 2017–2032. <https://doi.org/10.1098/rsif.2012.0308>.
- (31) Ventre, M.; Netti, P. A. Engineering Cell Instructive Materials To Control Cell Fate and Functions through Material Cues and Surface Patterning. *ACS Appl. Mater. Interfaces* **2016**, *8* (24), 14896–14908. <https://doi.org/10.1021/acsami.5b08658>.

- (32) Wang, P.-Y.; Yu, H.-T.; Tsai, W.-B. Modulation of Alignment and Differentiation of Skeletal Myoblasts by Submicron Ridges/Grooves Surface Structure. *Biotechnology and Bioengineering* **2010**, *106* (2), 285–294. <https://doi.org/10.1002/bit.22697>.
- (33) Litowczenko, J.; Maciejewska, B. M.; Wychowaniec, J. K.; Kościński, M.; Jurga, S.; Warowicka, A. Groove-Patterned Surfaces Induce Morphological Changes in Cells of Neuronal Origin. *J Biomed Mater Res A* **2019**, *107* (10), 2244–2256. <https://doi.org/10.1002/jbm.a.36733>.
- (34) Driscoll, M. K.; Sun, X.; Guven, C.; Fourkas, J. T.; Losert, W. Cellular Contact Guidance through Dynamic Sensing of Nanotopography. *ACS Nano* **2014**, *8* (4), 3546–3555. <https://doi.org/10.1021/nn406637c>.
- (35) Ramirez-San Juan, G. R.; Oakes, P. W.; Gardel, M. L. Contact Guidance Requires Spatial Control of Leading-Edge Protrusion. *Mol Biol Cell* **2017**, *28* (8), 1043–1053. <https://doi.org/10.1091/mbc.E16-11-0769>.
- (36) Santoro, F.; Panaitov, G.; Offenhäusser, A. Defined Patterns of Neuronal Networks on 3D Thiol-Functionalized Microstructures. *Nano Lett.* **2014**, *14* (12), 6906–6909. <https://doi.org/10.1021/nl502922b>.
- (37) Dai, J.; Lu, Y.; He, X.-Y.; Zhong, C.; Lin, B.-L.; Ling, S.; Gong, J.; Yao, Y. Vertical Nanopillar Induces Deformation of Cancer Cell and Alteration of ATF3 Expression. *Applied Materials Today* **2020**, *20*, 100753. <https://doi.org/10.1016/j.apmt.2020.100753>.
- (38) Qi, S.; Yi, C.; Ji, S.; Fong, C.-C.; Yang, M. Cell Adhesion and Spreading Behavior on Vertically Aligned Silicon Nanowire Arrays. *ACS Appl Mater Interfaces* **2009**, *1* (1), 30–34. <https://doi.org/10.1021/am800027d>.
- (39) Gopal, S.; Chiappini, C.; Penders, J.; Leonardo, V.; Seong, H.; Rothery, S.; Korchev, Y.; Shevchuk, A.; Stevens, M. M. Porous Silicon Nanoneedles Modulate Endocytosis to Deliver Biological Payloads. *Advanced Materials* **2019**, *31* (12), 1806788. <https://doi.org/10.1002/adma.201806788>.
- (40) Li, X.; Matino, L.; Zhang, W.; Klausen, L.; McGuire, A. F.; Lubrano, C.; Zhao, W.; Santoro, F.; Cui, B. A Nanostructure Platform for Live-Cell Manipulation of Membrane Curvature. *Nature Protocols* **2019**. <https://doi.org/10.1038/s41596-019-0161-7>.
- (41) Bettinger, C. J.; Langer, R.; Borenstein, J. T. Engineering Substrate Topography at the Micro- and Nanoscale to Control Cell Function. *Angew. Chem. Int. Ed.* **2009**, *48* (30), 5406–5415. <https://doi.org/10.1002/anie.200805179>.
- (42) Hansel, C. S.; Crowder, S. W.; Cooper, S.; Gopal, S.; João Pardelha da Cruz, M.; de Oliveira Martins, L.; Keller, D.; Rothery, S.; Becce, M.; Cass, A. E. G.; Bakal, C.; Chiappini, C.; Stevens, M. M. Nanoneedle-Mediated Stimulation of Cell Mechanotransduction Machinery. *ACS Nano* **2019**, *13* (3), 2913–2926. <https://doi.org/10.1021/acsnano.8b06998>.
- (43) Lou, H.-Y.; Zhao, W.; Li, X.; Duan, L.; Powers, A.; Akamatsu, M.; Santoro, F.; McGuire, A. F.; Cui, Y.; Drubin, D. G.; Cui, B. Membrane Curvature Underlies Actin Reorganization in Response to Nanoscale Surface Topography. *Proc. Natl. Acad. Sci. U.S.A.* **2019**, *116* (46), 23143–23151. <https://doi.org/10.1073/pnas.1910166116>.
- (44) Persson, H.; Beech, J. P.; Samuelson, L.; Oredsson, S.; Prinz, C. N.; Tegenfeldt, J. O. Vertical Oxide Nanotubes Connected by Subsurface Microchannels. *Nano Res.* **2012**, *5* (3), 190–198. <https://doi.org/10.1007/s12274-012-0199-0>.
- (45) Yang, C.-Y.; Huang, L.-Y.; Shen, T.-L.; Yeh, J. A. Cell Adhesion, Morphology and Biochemistry on Nano-Topographic Oxidized Silicon Surfaces. *Eur Cell Mater* **2010**, *20*, 415–430. <https://doi.org/10.22203/ecm.v020a34>.
- (46) Zhao, W.; Hanson, L.; Lou, H.-Y.; Akamatsu, M.; Chowdary, P. D.; Santoro, F.; Marks, J. R.; Grassart, A.; Drubin, D. G.; Cui, Y.; Cui, B. Nanoscale Manipulation of Membrane Curvature for

- Probing Endocytosis in Live Cells. *Nat Nanotechnol* **2017**, *12* (8), 750–756.  
<https://doi.org/10.1038/nnano.2017.98>.
- (47) McMahon, H. T.; Gallop, J. L. Membrane Curvature and Mechanisms of Dynamic Cell Membrane Remodelling. *Nature* **2005**, *438* (7068), 590–596. <https://doi.org/10.1038/nature04396>.
- (48) Structure and Dynamics of the Acyl Chains in the Membrane Trafficking and Enzymatic Processing of Lipids | Accounts of Chemical Research  
<https://pubs.acs.org/doi/abs/10.1021/acs.accounts.9b00134> (accessed 2021 -06 -09).
- (49) Jones, T.; Liu, A.; Cui, B. Light-Inducible Generation of Membrane Curvature in Live Cells with Engineered BAR Domain Proteins. *ACS Synth. Biol.* **2020**, *9* (4), 893–901.  
<https://doi.org/10.1021/acssynbio.9b00516>.
- (50) Sun, M.; Duan, X. Recent Advances in Micro/Nanoscale Intracellular Delivery. *Nanotechnology and Precision Engineering* **2020**, *3* (1), 18–31. <https://doi.org/10.1016/j.npe.2019.12.003>.
- (51) Chiappini, C.; De Rosa, E.; Martinez, J. O.; Liu, X.; Steele, J.; Stevens, M. M.; Tasciotti, E. Biodegradable Silicon Nanoneedles Delivering Nucleic Acids Intracellularly Induce Localized in Vivo Neovascularization. *Nature Mater* **2015**, *14* (5), 532–539.  
<https://doi.org/10.1038/nmat4249>.
- (52) Jarsch, I. K.; Daste, F.; Gallop, J. L. Membrane Curvature in Cell Biology: An Integration of Molecular Mechanisms. *Journal of Cell Biology* **2016**, *214* (4), 375–387.  
<https://doi.org/10.1083/jcb.201604003>.
- (53) Teo, B. K. K.; Goh, S.-H.; Kustandi, T. S.; Loh, W. W.; Low, H. Y.; Yim, E. K. F. The Effect of Micro and Nanotopography on Endocytosis in Drug and Gene Delivery Systems. *Biomaterials* **2011**, *32* (36), 9866–9875. <https://doi.org/10.1016/j.biomaterials.2011.08.088>.
- (54) Pelkmans, L.; Helenius, A. Endocytosis via Caveolae. *Traffic* **2002**, *3* (5), 311–320.  
<https://doi.org/10.1034/j.1600-0854.2002.30501.x>.
- (55) Kiss, A. L. Caveolae and the Regulation of Endocytosis. *Adv Exp Med Biol* **2012**, *729*, 14–28.  
[https://doi.org/10.1007/978-1-4614-1222-9\\_2](https://doi.org/10.1007/978-1-4614-1222-9_2).
- (56) Lundmark, R.; Carlsson, S. R. Driving Membrane Curvature in Clathrin-Dependent and Clathrin-Independent Endocytosis. *Semin Cell Dev Biol* **2010**, *21* (4), 363–370.  
<https://doi.org/10.1016/j.semcdb.2009.11.014>.
- (57) Golani, G.; Ariotti, N.; Parton, R. G.; Kozlov, M. M. Membrane Curvature and Tension Control the Formation and Collapse of Caveolar Superstructures. *Developmental Cell* **2019**, *48* (4), 523-538.e4. <https://doi.org/10.1016/j.devcel.2018.12.005>.
- (58) Gittens, R. A.; McLachlan, T.; Olivares-Navarrete, R.; Cai, Y.; Berner, S.; Tannenbaum, R.; Schwartz, Z.; Sandhage, K. H.; Boyan, B. D. The Effects of Combined Micron-/Submicron-Scale Surface Roughness and Nanoscale Features on Cell Proliferation and Differentiation. *Biomaterials* **2011**, *32* (13), 3395–3403. <https://doi.org/10.1016/j.biomaterials.2011.01.029>.
- (59) Dolatshahi-Pirouz, A.; Jensen, T.; Kraft, D. C.; Foss, M.; Kingshott, P.; Hansen, J. L.; Larsen, A. N.; Chevallier, J.; Besenbacher, F. Fibronectin Adsorption, Cell Adhesion, and Proliferation on Nanostructured Tantalum Surfaces. *ACS Nano* **2010**, *4* (5), 2874–2882.  
<https://doi.org/10.1021/nn9017872>.
- (60) Teo, B. K. K.; Wong, S. T.; Lim, C. K.; Kung, T. Y. S.; Yap, C. H.; Ramagopal, Y.; Romer, L. H.; Yim, E. K. F. Nanotopography Modulates Mechanotransduction of Stem Cells and Induces Differentiation through Focal Adhesion Kinase. *ACS Nano* **2013**, *7* (6), 4785–4798.  
<https://doi.org/10.1021/nn304966z>.
- (61) Curtis, A. Tutorial on the Biology of Nanotopography. *IEEE Trans Nanobioscience* **2004**, *3* (4), 293–295. <https://doi.org/10.1109/tnb.2004.837898>.

- (62) Atlan, M.; Nuti, G.; Wang, H.; Decker, S.; Perry, T. Breast Implant Surface Texture Impacts Host Tissue Response. *J Mech Behav Biomed Mater* **2018**, *88*, 377–385. <https://doi.org/10.1016/j.jmbbm.2018.08.035>.
- (63) Huang, J.; Zhang, X.; Yan, W.; Chen, Z.; Shuai, X.; Wang, A.; Wang, Y. Nanotubular Topography Enhances the Bioactivity of Titanium Implants. *Nanomedicine: Nanotechnology, Biology and Medicine* **2017**, *13* (6), 1913–1923. <https://doi.org/10.1016/j.nano.2017.03.017>.
- (64) Woods, G. A.; Rommelfanger, N. J.; Hong, G. Bioinspired Materials for In Vivo Bioelectronic Neural Interfaces. *Matter* **2020**, *3* (4), 1087–1113. <https://doi.org/10.1016/j.matt.2020.08.002>.
- (65) Biggs, M. J. P.; Richards, R. G.; Dalby, M. J. Nanotopographical Modification: A Regulator of Cellular Function through Focal Adhesions. *Nanomedicine* **2010**, *6* (5), 619–633. <https://doi.org/10.1016/j.nano.2010.01.009>.
- (66) Surface Plasmon Resonance Microscopy: From Single-Molecule Sensing to Single-Cell Imaging - Zhou - 2020 - *Angewandte Chemie International Edition* - Wiley Online Library <https://onlinelibrary.wiley.com/doi/abs/10.1002/anie.201908806> (accessed 2021 -06 -09).
- (67) Giebel, K.-F.; Bechinger, C.; Herminghaus, S.; Riedel, M.; Leiderer, P.; Weiland, U.; Bastmeyer, M. Imaging of Cell/Substrate Contacts of Living Cells with Surface Plasmon Resonance Microscopy. *Biophysical Journal* **1999**, *76* (1), 509–516. [https://doi.org/10.1016/S0006-3495\(99\)77219-X](https://doi.org/10.1016/S0006-3495(99)77219-X).
- (68) Braun, D.; Fromherz, P. Fluorescence Interference-Contrast Microscopy of Cell Adhesion on Oxidized Silicon. *Appl Phys A* **1997**, *65* (4), 341–348. <https://doi.org/10.1007/s003390050589>.
- (69) Kiessling, V.; Tamm, L. K. Measuring Distances in Supported Bilayers by Fluorescence Interference-Contrast Microscopy: Polymer Supports and SNARE Proteins. *Biophys. J.* **2003**, *84* (1), 408–418. [https://doi.org/10.1016/S0006-3495\(03\)74861-9](https://doi.org/10.1016/S0006-3495(03)74861-9).
- (70) Mielanczyk, L.; Matysiak, N.; Michalski, M.; Buldak, R.; Wojnicz, R. Closer to the Native State. Critical Evaluation of Cryo-Techniques for Transmission Electron Microscopy: Preparation of Biological Samples. *Folia Histochem Cytobiol* **2014**, *52* (1), 1–17. <https://doi.org/10.5603/FHC.2014.0001>.
- (71) Wrobel, G.; Hoßler, M.; Ingebrandt, S.; Dieluweit, S.; Sommerhage, F.; Bochem, H. P.; Offenhausser, A. Transmission Electron Microscopy Study of the Cell–Sensor Interface. *Journal of the royal society interface* February 6, 2008.
- (72) Hanson, L.; Lin, Z. C.; Xie, C.; Cui, Y.; Cui, B. Characterization of the Cell–Nanopillar Interface by Transmission Electron Microscopy. *Nano Lett.* **2012**, *12* (11), 5815–5820. <https://doi.org/10.1021/nl303163y>.
- (73) Aslanoglou, S.; Chen, Y.; Oorschot, V.; Trifunovic, Z.; Hanssen, E.; Suu, K.; Voelcker, N. H.; Elnathan, R. Efficient Transmission Electron Microscopy Characterization of Cell–Nanostructure Interfacial Interactions. *J. Am. Chem. Soc.* **2020**, *142* (37), 15649–15653. <https://doi.org/10.1021/jacs.0c05919>.
- (74) A. Belu; J. Schnitker; S. Bertazzo; E. Neumann; D. Mayer; A. Offenhausser; Santoro, F. Ultra-Thin Resin Embedding Method for Scanning Electron Microscopy of Individual Cells on High and Low Aspect Ratio 3D Nanostructures. *Journal of Microscopy*. December 9, 2015.
- (75) Probing the Ultrastructure of Spheroids and Their Uptake of Magnetic Nanoparticles by FIB–SEM - Mollo - 2020 - *Advanced Materials Technologies* - Wiley Online Library <https://onlinelibrary.wiley.com/doi/abs/10.1002/admt.201900687> (accessed 2021 -06 -09).
- (76) Graphene: an emerging material for biological tissue engineering [http://www.kpubs.org/article/articleMain.kpubs?articleANo=HGTSB6\\_2013\\_v14n2\\_63](http://www.kpubs.org/article/articleMain.kpubs?articleANo=HGTSB6_2013_v14n2_63) (accessed 2021 -06 -09).
- (77) Goenka, S.; Sant, V.; Sant, S. Graphene-Based Nanomaterials for Drug Delivery and Tissue Engineering. *Journal of Controlled Release* **2014**, *173*, 75–88. <https://doi.org/10.1016/j.jconrel.2013.10.017>.

- (78) Lee, C.; Wei, X.; Kysar, J. W.; Hone, J. Measurement of the Elastic Properties and Intrinsic Strength of Monolayer Graphene. *Science* **2008**, *321* (5887), 385–388. <https://doi.org/10.1126/science.1157996>.
- (79) Mechanisms of mechanical reinforcement by graphene and carbon nanotubes in polymer nanocomposites - Nanoscale (RSC Publishing) <https://pubs.rsc.org/en/content/articlelanding/2020/nr/c9nr06952f#!divAbstract> (accessed 2021-06-09).
- (80) Balandin, A. A.; Ghosh, S.; Bao, W.; Calizo, I.; Teweldebrhan, D.; Miao, F.; Lau, C. N. Superior Thermal Conductivity of Single-Layer Graphene. *Nano Lett.* **2008**, *8* (3), 902–907. <https://doi.org/10.1021/nl0731872>.
- (81) Bolotin, K. I.; Sikes, K. J.; Jiang, Z.; Klima, M.; Fudenberg, G.; Hone, J.; Kim, P.; Stormer, H. L. Ultrahigh Electron Mobility in Suspended Graphene. *Solid State Communications* **2008**, *146* (9), 351–355. <https://doi.org/10.1016/j.ssc.2008.02.024>.
- (82) Guo, X.; Mei, N. Assessment of the Toxic Potential of Graphene Family Nanomaterials. *J Food Drug Anal* **2014**, *22* (1), 105–115. <https://doi.org/10.1016/j.jfda.2014.01.009>.
- (83) Rastogi, S. K.; Raghavan, G.; Yang, G.; Cohen-Karni, T. Effect of Graphene on Nonneuronal and Neuronal Cell Viability and Stress. *Nano Lett.* **2017**, *17* (5), 3297–3301. <https://doi.org/10.1021/acs.nanolett.7b01215>.
- (84) Li, N.; Zhang, Q.; Gao, S.; Song, Q.; Huang, R.; Wang, L.; Liu, L.; Dai, J.; Tang, M.; Cheng, G. Three-Dimensional Graphene Foam as a Biocompatible and Conductive Scaffold for Neural Stem Cells. *Scientific Reports* **2013**, *3* (1), 1604. <https://doi.org/10.1038/srep01604>.
- (85) Park, S. Y.; Park, J.; Sim, S. H.; Sung, M. G.; Kim, K. S.; Hong, B. H.; Hong, S. Enhanced Differentiation of Human Neural Stem Cells into Neurons on Graphene. *Advanced Materials* **2011**, *23* (36), H263–H267. <https://doi.org/10.1002/adma.201101503>.
- (86) Li, N.; Zhang, X.; Song, Q.; Su, R.; Zhang, Q.; Kong, T.; Liu, L.; Jin, G.; Tang, M.; Cheng, G. The Promotion of Neurite Sprouting and Outgrowth of Mouse Hippocampal Cells in Culture by Graphene Substrates. *Biomaterials* **2011**, *32* (35), 9374–9382. <https://doi.org/10.1016/j.biomaterials.2011.08.065>.
- (87) Zhang, Y.; Nayak, T. R.; Hong, H.; Cai, W. Graphene: A Versatile Nanoplatfor for Biomedical Applications. *Nanoscale* **2012**, *4* (13), 3833–3842. <https://doi.org/10.1039/c2nr31040f>.
- (88) Kireev, D.; Seyock, S.; Lewen, J.; Maybeck, V.; Wolfrum, B.; Offenhäusser, A. Graphene Multielectrode Arrays as a Versatile Tool for Extracellular Measurements. *Advanced Healthcare Materials* **2017**, *6* (12), 1601433. <https://doi.org/10.1002/adhm.201601433>.
- (89) Rastogi, S. K.; Bliley, J.; Shiowski, D. J.; Raghavan, G.; Feinberg, A. W.; Cohen-Karni, T. Graphene Microelectrode Arrays for Electrical and Optical Measurements of Human Stem Cell-Derived Cardiomyocytes. *Cell. Mol. Bioeng.* **2018**, *11* (5), 407.
- (90) Li, H.; Walsh, K. B.; Bayram, F.; Koley, G. Direct Measurement of K<sup>+</sup> Ion Efflux from Neuronal Cells Using a Graphene-Based Ion Sensitive Field Effect Transistor. *RSC Adv.* **2020**, *10* (62), 37728–37734. <https://doi.org/10.1039/D0RA05222A>.
- (91) Li, J.; Liu, X.; Crook, J. M.; Wallace, G. G. Development of a Porous 3D Graphene-PDMS Scaffold for Improved Osseointegration. *Colloids and Surfaces B: Biointerfaces* **2017**, *159*, 386–393. <https://doi.org/10.1016/j.colsurfb.2017.07.087>.
- (92) Nguyen, A. T.; Mattiassi, S.; Loeblein, M.; Chin, E.; Ma, D.; Coquet, P.; Viasnoff, V.; Teo, E. H. T.; Goh, E. L.; Yim, E. K. F. Human Rett-Derived Neuronal Progenitor Cells in 3D Graphene Scaffold as an in Vitro Platform to Study the Effect of Electrical Stimulation on Neuronal Differentiation. *Biomed Mater* **2018**, *13* (3), 034111. <https://doi.org/10.1088/1748-605X/aaaf2b>.
- (93) Lu, J.; He, Y.-S.; Cheng, C.; Wang, Y.; Qiu, L.; Li, D.; Zou, D. Self-Supporting Graphene Hydrogel Film as an Experimental Platform to Evaluate the Potential of Graphene for Bone Regeneration.

- Advanced Functional Materials* **2013**, *23* (28), 3494–3502.  
<https://doi.org/10.1002/adfm.201203637>.
- (94) Chen, L.; Guo, L.; Wu, Y.; Jia, Y.; Li, Z.; Chen, X. Fabrication of Vertically Aligned Graphene Sheets on SiC Substrates. *RSC Adv.* **2013**, *3* (33), 13926–13933. <https://doi.org/10.1039/C3RA40840J>.
- (95) Watanabe, H.; Kondo, H.; Okamoto, Y.; Hiramatsu, M.; Sekine, M.; Baba, Y.; Hori, M. Carbon Nanowall Scaffold to Control Culturing of Cervical Cancer Cells. *Appl. Phys. Lett.* **2014**, *105* (24), 244105. <https://doi.org/10.1063/1.4902054>.
- (96) Hejazi, M. A.; Tong, W.; Stacey, A.; Sun, S. H.; Yunzab, M.; Almasi, A.; Jung, Y. J.; Meffin, H.; Fox, K.; Edalati, K.; Nadarajah, A.; Praver, S.; Ibbotson, M. R.; Garrett, D. J. High Fidelity Bidirectional Neural Interfacing with Carbon Fiber Microelectrodes Coated with Boron-Doped Carbon Nanowalls: An Acute Study. *Advanced Functional Materials* **2020**, *30* (52), 2006101. <https://doi.org/10.1002/adfm.202006101>.
- (97) Garg, R.; Rastogi, S. K.; Lamparski, M.; de la Barrera, S. C.; Pace, G. T.; Nuhfer, N. T.; Hunt, B. M.; Meunier, V.; Cohen-Karni, T. Nanowire-Mesh-Templated Growth of Out-of-Plane Three-Dimensional Fuzzy Graphene. *ACS Nano* **2017**, *11* (6), 6301–6311. <https://doi.org/10.1021/acsnano.7b02612>.
- (98) Electron Transport in Multidimensional Fuzzy Graphene Nanostructures | Nano Letters <https://pubs.acs.org/doi/abs/10.1021/acs.nanolett.9b01790> (accessed 2021 -05 -31).
- (99) Vlasiouk, I.; Regmi, M.; Fulvio, P.; Dai, S.; Datskos, P.; Eres, G.; Smirnov, S. Role of Hydrogen in Chemical Vapor Deposition Growth of Large Single-Crystal Graphene. *ACS Nano* **2011**, *5* (7), 6069–6076. <https://doi.org/10.1021/nn201978y>.
- (100) Frantz, C.; Stewart, K. M.; Weaver, V. M. The Extracellular Matrix at a Glance. *J Cell Sci* **2010**, *123* (24), 4195–4200. <https://doi.org/10.1242/jcs.023820>.
- (101) Kular, J. K.; Basu, S.; Sharma, R. I. The Extracellular Matrix: Structure, Composition, Age-Related Differences, Tools for Analysis and Applications for Tissue Engineering. *Journal of Tissue Engineering* **2014**, *5*, 2041731414557112. <https://doi.org/10.1177/2041731414557112>.
- (102) Yue, B. Biology of the Extracellular Matrix: An Overview. *J Glaucoma* **2014**, S20–S23. <https://doi.org/10.1097/IJG.000000000000108>.
- (103) Claycomb, W. C.; Lanson, N. A.; Stallworth, B. S.; Egeland, D. B.; Delcarpio, J. B.; Bahinski, A.; Izzo, N. J. HL-1 Cells: A Cardiac Muscle Cell Line That Contracts and Retains Phenotypic Characteristics of the Adult Cardiomyocyte. *Proc. Natl. Acad. Sci. U.S.A.* **1998**, *95* (6), 2979–2984.
- (104) Watanabe, Y.; Yaginuma, H. Tangential Cell Migration during Layer Formation of Chick Optic Tectum. *Dev Growth Differ* **2015**, *57* (8), 539–543. <https://doi.org/10.1111/dgd.12238>.
- (105) Micholt, L.; Gärtner, A.; Prodanov, D.; Braeken, D.; Dotti, C. G.; Bartic, C. Substrate Topography Determines Neuronal Polarization and Growth In Vitro. *PLoS ONE* **2013**, *8* (6), e66170. <https://doi.org/10.1371/journal.pone.0066170>.
- (106) Flynn, K. C. The Cytoskeleton and Neurite Initiation. *Bioarchitecture* **2013**, *3* (4), 86–109. <https://doi.org/10.4161/bioa.26259>.
- (107) Importance of albumen during embryonic development in avian species, with emphasis on domestic chicken | World's Poultry Science Journal | Cambridge Core <https://www.cambridge.org/core/journals/world-s-poultry-science-journal/article/abs/importance-of-albumen-during-embryonic-development-in-avian-species-with-emphasis-on-domestic-chicken/FD52425EB84FED45D661B053E4A72F0F> (accessed 2021 -05 -31).
- (108) Kiernan, J. A. Formaldehyde, Formalin, Paraformaldehyde And Glutaraldehyde: What They Are And What They Do. *Microscopy Today* **2000**, *8* (1), 8–13. <https://doi.org/10.1017/S1551929500057060>.

- (109) Aguas, A. P. The Use of Osmium Tetroxide-Potassium Ferrocyanide as an Extracellular Tracer in Electron Microscopy. *Stain Technol* **1982**, *57* (2), 69–73. <https://doi.org/10.3109/10520298209066530>.
- (110) Santoro, F.; Neumann, E.; Panaitov, G.; Offenhäusser, A. FIB Section of Cell–Electrode Interface: An Approach for Reducing Curtaining Effects. *Microelectronic Engineering* **2014**, *124*, 17–21. <https://doi.org/10.1016/j.mee.2014.04.021>.
- (111) Ferrari, A. C.; Meyer, J. C.; Scardaci, V.; Casiraghi, C.; Lazzeri, M.; Mauri, F.; Piscanec, S.; Jiang, D.; Novoselov, K. S.; Roth, S.; Geim, A. K. Raman Spectrum of Graphene and Graphene Layers. *Phys. Rev. Lett.* **2006**, *97* (18), 187401. <https://doi.org/10.1103/PhysRevLett.97.187401>.
- (112) Ferrari, A. C. Raman Spectroscopy of Graphene and Graphite: Disorder, Electron–Phonon Coupling, Doping and Nonadiabatic Effects. *Solid State Communications* **2007**, *143* (1), 47–57. <https://doi.org/10.1016/j.ssc.2007.03.052>.
- (113) Ferrari, A. C.; Basko, D. M. Raman Spectroscopy as a Versatile Tool for Studying the Properties of Graphene. *Nature Nanotechnology* **2013**, *8* (4), 235–246. <https://doi.org/10.1038/nnano.2013.46>.
- (114) Cassie, A. B. D.; Baxter, S. Wettability of Porous Surfaces. *Trans. Faraday Soc.* **1944**, *40* (0), 546–551. <https://doi.org/10.1039/TF94444000546>.
- (115) Wenzel, R. N. RESISTANCE OF SOLID SURFACES TO WETTING BY WATER. *Ind. Eng. Chem.* **1936**, *28* (8), 988–994. <https://doi.org/10.1021/ie50320a024>.
- (116) Li, X.; Reinhoudt, D. N.; Crego-Calama, M. What Do We Need for a Superhydrophobic Surface? A Review on the Recent Progress in the Preparation of Superhydrophobic Surfaces; 2007. <https://doi.org/10.1002/chin.200744242>.
- (117) Marcon, L.; Boukherroub, R. Biocompatibility of Semiconducting Silicon Nanowires. In *Semiconducting Silicon Nanowires for Biomedical Applications*; 2014; pp 62–85. <https://doi.org/10.1533/9780857097712.1.62>.
- (118) Lagonegro, P.; Rossi, F.; Galli, C.; Smerieri, A.; Alinovi, R.; Pinelli, S.; Rimoldi, T.; Attolini, G.; Macaluso, G.; Macaluso, C.; Sadow, S. E.; Salviati, G. A Cytotoxicity Study of Silicon Oxycarbide Nanowires as Cell Scaffold for Biomedical Applications. *Materials Science and Engineering: C* **2017**, *73*, 465–471. <https://doi.org/10.1016/j.msec.2016.12.096>.
- (119) Wang, Y.; Wu, Y.; Quadri, F.; Prox, J. D.; Guo, L. Cytotoxicity of ZnO Nanowire Arrays on Excitable Cells. *Nanomaterials (Basel)* **2017**, *7* (4). <https://doi.org/10.3390/nano7040080>.
- (120) Gilbert, G.; Demydenko, K.; Dries, E.; Puertas, R. D.; Jin, X.; Sipido, K.; Roderick, H. L. Calcium Signaling in Cardiomyocyte Function. *Cold Spring Harb Perspect Biol* **2020**, *12* (3). <https://doi.org/10.1101/cshperspect.a035428>.
- (121) Czeschik, A.; Rinklin, P.; Derra, U.; Ullmann, S.; Holik, P.; Steltenkamp, S.; Offenhäusser, A.; Wolfrum, B. Nanostructured Cavity Devices for Extracellular Stimulation of HL-1 Cells. *Nanoscale* **2015**, *7* (20), 9275–9281. <https://doi.org/10.1039/C5NR01690H>.
- (122) Spencer, C. I.; Baba, S.; Nakamura, K.; Hua, E. A.; Sears, M. A. F.; Fu, C.; Zhang, J.; Balijepalli, S.; Tomoda, K.; Hayashi, Y.; Lizarraga, P.; Wojciak, J.; Scheinman, M. M.; Aalto-Setälä, K.; Makielski, J. C.; January, C. T.; Healy, K. E.; Kamp, T. J.; Yamanaka, S.; Conklin, B. R. Calcium Transients Closely Reflect Prolonged Action Potentials in iPSC Models of Inherited Cardiac Arrhythmia. *Stem Cell Reports* **2014**, *3* (2), 269–281. <https://doi.org/10.1016/j.stemcr.2014.06.003>.
- (123) Leybaert, L.; Sanderson, M. J. Intercellular Ca<sup>2+</sup> Waves: Mechanisms and Function. *Physiol Rev* **2012**, *92* (3), 1359–1392. <https://doi.org/10.1152/physrev.00029.2011>.
- (124) Cheng, H.; Lederer, M. R.; Lederer, W. J.; Cannell, M. B. Calcium Sparks and [Ca<sup>2+</sup>]<sub>i</sub> Waves in Cardiac Myocytes. *Am J Physiol* **1996**, *270* (1 Pt 1), C148-159. <https://doi.org/10.1152/ajpcell.1996.270.1.C148>.

- (125) Cardiac excitation–contraction coupling | Nature <https://www.nature.com/articles/415198a> (accessed 2021-05-27).
- (126) Rinklin, P.; Afanasenkau, D.; Wiegand, S.; Offenhäusser, A.; Wolfrum, B. Inducing Microscopic Thermal Lesions for the Dissection of Functional Cell Networks on a Chip. *Lab on a Chip* **2015**, *15* (1), 237–243. <https://doi.org/10.1039/C4LC00805G>.
- (127) Uchida, T.; Kitora, R.; Gohara, K. Temperature Dependence of Synchronized Beating of Cultured Neonatal Rat Heart-Cell Networks with Increasing Age Measured by Multi-Electrode Arrays. *Trends Med* **2018**, *18* (4). <https://doi.org/10.15761/TiM.1000145>.
- (128) Petersen, A. P.; Lyra-Leite, D. M.; Ariyasinghe, N. R.; Cho, N.; Goodwin, C. M.; Kim, J. Y.; McCain, M. L. Microenvironmental Modulation of Calcium Wave Propagation Velocity in Engineered Cardiac Tissues. *Cel. Mol. Bioeng.* **2018**, *11* (5), 337–352. <https://doi.org/10.1007/s12195-018-0522-2>.
- (129) Bursac, N.; Parker, K. k.; Iravanian, S.; Tung, L. Cardiomyocyte Cultures With Controlled Macroscopic Anisotropy. *Circulation Research* **2002**, *91* (12), e45–e54. <https://doi.org/10.1161/01.RES.0000047530.88338.EB>.
- (130) Spach, M. S.; Heidlage, J. F.; Barr, R. C.; Dolber, P. C. Cell Size and Communication: Role in Structural and Electrical Development and Remodeling of the Heart. *Heart Rhythm* **2004**, *1* (4), 500–515. <https://doi.org/10.1016/j.hrthm.2004.06.010>.
- (131) Nasrollahi, S.; Banerjee, S.; Qayum, B.; Banerjee, P.; Pathak, A. Nanoscale Matrix Topography Influences Microscale Cell Motility through Adhesions, Actin Organization, and Cell Shape. *ACS Biomater. Sci. Eng.* **2017**, *3* (11), 2980–2986. <https://doi.org/10.1021/acsbiomaterials.6b00554>.
- (132) Andersson, A.-S.; Brink, J.; Lidberg, U.; Sutherland, D. S. Influence of Systematically Varied Nanoscale Topography on the Morphology of Epithelial Cells. *IEEE Transactions on NanoBioscience* **2003**, *2* (2), 49–57. <https://doi.org/10.1109/TNB.2003.813934>.
- (133) Li, Z.; Persson, H.; Adolfsson, K.; Oredsson, S.; Prinz, C. N. Morphology of Living Cells Cultured on Nanowire Arrays with Varying Nanowire Densities and Diameters. *Sci China Life Sci* **2018**, *61* (4), 427–435. <https://doi.org/10.1007/s11427-017-9264-2>.
- (134) Pollard, T. D.; Cooper, J. A. Actin, a Central Player in Cell Shape and Movement. *Science* **2009**, *326* (5957), 1208–1212. <https://doi.org/10.1126/science.1175862>.
- (135) Schaller, M. D. Paxillin: A Focal Adhesion-Associated Adaptor Protein. *Oncogene* **2001**, *20* (44), 6459–6472. <https://doi.org/10.1038/sj.onc.1204786>.
- (136) Coyer, S. R.; Singh, A.; Dumbauld, D. W.; Calderwood, D. A.; Craig, S. W.; Delamarche, E.; García, A. J. Nanopatterning Reveals an ECM Area Threshold for Focal Adhesion Assembly and Force Transmission That Is Regulated by Integrin Activation and Cytoskeleton Tension. *J Cell Sci* **2012**, *125* (Pt 21), 5110–5123. <https://doi.org/10.1242/jcs.108035>.
- (137) Geiger, B.; Yamada, K. M. Molecular Architecture and Function of Matrix Adhesions. *Cold Spring Harb Perspect Biol* **2011**, *3* (5). <https://doi.org/10.1101/cshperspect.a005033>.
- (138) Aalipour, A.; Xu, A. M.; Leal-Ortiz, S.; Garner, C. C.; Melosh, N. A. Plasma Membrane and Actin Cytoskeleton as Synergistic Barriers to Nanowire Cell Penetration. *Langmuir* **2014**, *30* (41), 12362–12367. <https://doi.org/10.1021/la502273f>.
- (139) Mim, C.; Unger, V. M. Membrane Curvature and Its Generation by BAR Proteins. *Trends in Biochemical Sciences* **2012**, *37* (12), 526–533. <https://doi.org/10.1016/j.tibs.2012.09.001>.
- (140) Pennacchio, F. A.; Caliendo, F.; Iaccarino, G.; Langella, A.; Siciliano, V.; Santoro, F. Three-Dimensionally Patterned Scaffolds Modulate the Biointerface at the Nanoscale. *Nano Lett.* **2019**, *19* (8), 5118–5123. <https://doi.org/10.1021/acs.nanolett.9b01468>.
- (141) Formentín, P.; Catalán, Ú.; Alba, M.; Fernández-Castillejo, S.; Solà, R.; Pallarès, J.; Marsal, L. F. Effects of SiO<sub>2</sub> Micropillar Arrays on Endothelial Cells' Morphology. *New Biotechnology* **2016**, *33* (6), 781–789. <https://doi.org/10.1016/j.nbt.2016.07.002>.

- (142) Rennick, J. J.; Johnston, A. P. R.; Parton, R. G. Key Principles and Methods for Studying the Endocytosis of Biological and Nanoparticle Therapeutics. *Nat. Nanotechnol.* **2021**, *16* (3), 266–276. <https://doi.org/10.1038/s41565-021-00858-8>.
- (143) Murugan, K.; Choonara, Y. E.; Kumar, P.; Bijukumar, D.; du Toit, L. C.; Pillay, V. Parameters and Characteristics Governing Cellular Internalization and Trans-Barrier Trafficking of Nanostructures. *Int J Nanomedicine* **2015**, *10*, 2191–2206. <https://doi.org/10.2147/IJN.S75615>.
- (144) Mattila, P. K.; Lappalainen, P. Filopodia: Molecular Architecture and Cellular Functions. *Nat Rev Mol Cell Biol* **2008**, *9* (6), 446–454. <https://doi.org/10.1038/nrm2406>.
- (145) Gupton, S. L.; Gertler, F. B. Filopodia: The Fingers That Do the Walking. *Sci STKE* **2007**, *2007* (400), re5. <https://doi.org/10.1126/stke.4002007re5>.
- (146) Santoro, F.; Zhao, W.; Joubert, L.-M.; Duan, L.; Schnitker, J.; van de Burgt, Y.; Lou, H.-Y.; Liu, B.; Salleo, A.; Cui, L.; Cui, Y.; Cui, B. Revealing the Cell–Material Interface with Nanometer Resolution by Focused Ion Beam/Scanning Electron Microscopy. *ACS Nano* **2017**, *11* (8), 8320–8328. <https://doi.org/10.1021/acsnano.7b03494>.
- (147) Dotti, C. G.; Sullivan, C. A.; Banker, G. A. The Establishment of Polarity by Hippocampal Neurons in Culture. *J Neurosci* **1988**, *8* (4), 1454–1468.
- (148) Arimura, N.; Kaibuchi, K. Neuronal Polarity: From Extracellular Signals to Intracellular Mechanisms. *Nat Rev Neurosci* **2007**, *8* (3), 194–205. <https://doi.org/10.1038/nrn2056>.
- (149) Dent, E. W.; Tang, F.; Kalil, K. Axon Guidance by Growth Cones and Branches: Common Cytoskeletal and Signaling Mechanisms. *Neuroscientist* **2003**, *9* (5), 343–353. <https://doi.org/10.1177/1073858403252683>.
- (150) Axon Branching Requires Interactions between Dynamic Microtubules and Actin Filaments | Journal of Neuroscience <https://www.jneurosci.org/content/21/24/9757> (accessed 2021 -06 -09).
- (151) Lowery, L. A.; Vactor, D. V. The Trip of the Tip: Understanding the Growth Cone Machinery. *Nat Rev Mol Cell Biol* **2009**, *10* (5), 332–343. <https://doi.org/10.1038/nrm2679>.
- (152) Dunican, D. J.; Doherty, P. The Generation of Localized Calcium Rises Mediated by Cell Adhesion Molecules and Their Role in Neuronal Growth Cone Motility. *Mol Cell Biol Res Commun* **2000**, *3* (5), 255–263. <https://doi.org/10.1006/mcbr.2000.0225>.
- (153) Chighizola, M.; Dini, T.; Lenardi, C.; Milani, P.; Podestà, A.; Schulte, C. *Mechanotransduction in Neuronal Cell Development and Functioning*; preprint; LIFE SCIENCES, 2019. <https://doi.org/10.20944/preprints201909.0241.v1>.
- (154) Tang, F.; Dent, E. W.; Kalil, K. Spontaneous Calcium Transients in Developing Cortical Neurons Regulate Axon Outgrowth. *J Neurosci* **2003**, *23* (3), 927–936. <https://doi.org/10.1523/JNEUROSCI.23-03-00927.2003>.
- (155) Withers, G. S.; James, C. D.; Kingman, C. E.; Craighead, H. G.; Banker, G. A. Effects of Substrate Geometry on Growth Cone Behavior and Axon Branching. *J Neurobiol* **2006**, *66* (11), 1183–1194. <https://doi.org/10.1002/neu.20298>.
- (156) Messa, M.; Canale, C.; Marconi, E.; Cingolani, R.; Salerno, M.; Benfenati, F. Growth Cone 3-D Morphology Is Modified by Distinct Micropatterned Adhesion Substrates. *IEEE Trans Nanobioscience* **2009**, *8* (2), 161–168. <https://doi.org/10.1109/TNB.2009.2019109>.
- (157) Payne, H. R.; Burden, S. M.; Lemmon, V. Modulation of Growth Cone Morphology by Substrate-Bound Adhesion Molecules. *Cell Motil Cytoskeleton* **1992**, *21* (1), 65–73. <https://doi.org/10.1002/cm.970210108>.
- (158) Smirnov, M. S.; Cabral, K. A.; Geller, H. M.; Urbach, J. S. The Effects of Confinement on Neuronal Growth Cone Morphology and Velocity. *Biomaterials* **2014**, *35* (25), 6750–6757. <https://doi.org/10.1016/j.biomaterials.2014.04.097>.

- (159) Dent, E. W.; Gupton, S. L.; Gertler, F. B. The Growth Cone Cytoskeleton in Axon Outgrowth and Guidance. *Cold Spring Harb Perspect Biol* **2011**, *3* (3).  
<https://doi.org/10.1101/cshperspect.a001800>.
- (160) Gordon-Weeks, P. R. Microtubules and Growth Cone Function. *J Neurobiol* **2004**, *58* (1), 70–83.  
<https://doi.org/10.1002/neu.10266>.
- (161) Suter, D. M.; Forscher, P. Substrate-Cytoskeletal Coupling as a Mechanism for the Regulation of Growth Cone Motility and Guidance. *J Neurobiol* **2000**, *44* (2), 97–113.
- (162) Fabbro, A.; Prato, M.; Ballerini, L. Carbon Nanotubes in Neuroregeneration and Repair. *Adv Drug Deliv Rev* **2013**, *65* (15), 2034–2044. <https://doi.org/10.1016/j.addr.2013.07.002>.
- (163) Nanoscale Surface Topography Reshapes Neuronal Growth in Culture | *Langmuir*  
<https://pubs.acs.org/doi/10.1021/la5001683> (accessed 2021 -06 -10).
- (164) Milos, F.; Belu, A.; Mayer, D.; Maybeck, V.; Offenhäusser, A. Polymer Nanopillars Induce Increased Paxillin Adhesion Assembly and Promote Axon Growth in Primary Cortical Neurons. *Advanced Biology* **2021**, *5* (2), 2000248. <https://doi.org/10.1002/adbi.202000248>.
- (165) Mason, C. A.; Wang, L. C. Growth Cone Form Is Behavior-Specific and, Consequently, Position-Specific along the Retinal Axon Pathway. *J Neurosci* **1997**, *17* (3), 1086–1100.
- (166) Kang, K.; Choi, S.-E.; Jang, H. S.; Cho, W. K.; Nam, Y.; Choi, I. S.; Lee, J. S. In Vitro Developmental Acceleration of Hippocampal Neurons on Nanostructures of Self-Assembled Silica Beads in Filopodium-Size Ranges. *Angew. Chem. Int. Ed.* **2012**, *51* (12), 2855–2858.  
<https://doi.org/10.1002/anie.201106271>.
- (167) The principles of directed cell migration | *Nature Reviews Molecular Cell Biology*  
<https://www.nature.com/articles/s41580-021-00366-6> (accessed 2021 -05 -29).
- (168) Borrell, V. Recent Advances in Understanding Neocortical Development. *F1000Res* **2019**, *8*.  
<https://doi.org/10.12688/f1000research.20332.1>.
169. Dipalo, Amin, Lovato, Moia, Caprettini, Messina, Tantussi, Berdondini, De Angelis. Intracellular and extracellular recording of Spontaneous Action Potentials in Mammalian Neurons and Cardiac Cells with 3D Plasmonic Nanoelectrodes. *Nano Lett.* 2017, *17*, 6, 3932–3939  
<https://doi.org/10.1021/acs.nanolett.7b01523>
170. Petersen, Lyra-Leite, Ariyasinghe, Cho, Godwin, Young Kim, L McCain. Microenvironmental Modulation of Calcium Wave Propagation Velocity in Engineered Cardiac Tissues. *Cellular and Molecular Bioengineering* volume 11, pages337–352 (2018)
171. Spatch, Heidlage, C Barr, C Dobler. Cell size and communication: role in structural and electrical development and remodeling of the heart. <https://doi.org/10.1016/j.hrthm.2004.06.010>
172. Bursac, Parker, L Tung. Cardiomyocyte cultures with controlled macroscopic anisotropy: a model for functional electrophysiological studies of cardiac muscle. 10.1161/01.res.0000047530.88338.eb
173. Lee, Kang, Hicks, Chancellor Jr, Hwan Chu, Wang, G. Keselowsky, Ren, P Lele. The control of cell adhesion and viability by zinc oxide nanorods. <https://doi.org/10.1016/j.biomaterials.2008.05.029>
174. Formentin, Catalan, Alba, Fernandez-Castillejo, Solà, Pallarès, Marsal. Effects of SiO<sub>2</sub> micropillar arrays on endothelial cells' morphology. <https://doi.org/10.1016/j.nbt.2016.07.002>

## List of Publications

(\*relevant to this thesis)

- \* (1) Dipalo, M.; Rastogi, S. K.; Matino, L.; Garg, R.; Bliley, J.; Iachetta, G.; Melle, G.; Shrestha, R.; Shen, S.; Santoro, F.; Feinberg, A. W.; Barbaglia, A.; Cohen-Karni, T.; De Angelis, F. Intracellular Action Potential Recordings from Cardiomyocytes by Ultrafast Pulsed Laser Irradiation of Fuzzy Graphene Microelectrodes. *Sci. Adv.* 2021, 7 (15), eabd5175. <https://doi.org/10.1126/sciadv.abd5175>.
- (2) Rotenberg, M. Y.; Elbaz, B.; Nair, V.; Schaumann, E. N.; Yamamoto, N.; Sarma, N.; Matino, L.; Santoro, F.; Tian, B. Silicon Nanowires for Intracellular Optical Interrogation with Subcellular Resolution. *Nano Lett.* 2020, 20 (2), 1226–1232. <https://doi.org/10.1021/acs.nanolett.9b04624>.
- (3) Polino, G.; Lubrano, C.; Scognamiglio, P.; Mollo, V.; Martino, S. D.; Ciccone, G.; Matino, L.; Langella, A.; Netti, P.; Carlo, A. D.; Brunetti, F.; Santoro, F. Synthesis and Characterization of PEDOT-PEGDA Blends for Bioelectronic Applications: Surface Properties and Effects on Cell Morphology. *Flex. Print. Electron.* 2020, 5 (1), 014012. <https://doi.org/10.1088/2058-8585/ab71e1>.
- \* (4) Matino, L.; Rastogi, S. K.; Garma, L. D.; Cohen-Karni, T.; Santoro, F. Characterization of the Coupling between Out-of-Plane Graphene and Electrogenic Cells. *Adv. Mater. Interfaces* 2020, 7 (18), 2000699. <https://doi.org/10.1002/admi.202000699>.
- \* (5) Li, X.; Matino, L.; Zhang, W.; Klausen, L.; McGuire, A. F.; Lubrano, C.; Zhao, W.; Santoro, F.; Cui, B. A Nanostructure Platform for Live-Cell Manipulation of Membrane Curvature. *Nat. Protoc.* 2019, 14 (6), 1772–1802. <https://doi.org/10.1038/s41596-019-0161-7>.
- (7) Garma, L. D.; Matino, L.; Melle, G.; Moia, F.; Angelis, F. D.; Santoro, F.; Dipalo, M. Cost-Effective and Multifunctional Acquisition System for in Vitro Electrophysiological Investigations with Multi-Electrode Arrays. *PLOS ONE* 2019, 14 (3), e0214017. <https://doi.org/10.1371/journal.pone.0214017>.
- (7) Rotenberg, M. Y.; Yamamoto, N.; Schaumann, E. N.; Matino, L.; Santoro, F.; Tian, B. Living Myofibroblast–Silicon Composites for Probing Electrical Coupling in Cardiac Systems. *Proc. Natl. Acad. Sci.* 2019, 116 (45), 22531–22539. <https://doi.org/10.1073/pnas.1913651116>.
- (8) Pennacchio, F. A.; Garma, L. D.; Matino, L.; Santoro, F. Bioelectronics Goes 3D: New Trends in Cell–Chip Interface Engineering. *J. Mater. Chem. B* 2018, 6 (44), 7096–7101. <https://doi.org/10.1039/C8TB01737A>.
- \* (9) Dipalo, M.; McGuire, A. F.; Lou, H.-Y.; Caprettini, V.; Melle, G.; Bruno, G.; Lubrano, C.; Matino, L.; Li, X.; De Angelis, F.; Cui, B.; Santoro, F. Cells Adhering to 3D Vertical Nanostructures: Cell Membrane Reshaping without Stable Internalization. *Nano Lett.* 2018, 18 (9), 6100–6105. <https://doi.org/10.1021/acs.nanolett.8b03163>.

## Annex A

### 1. Optical cross section of HL-1 cytoskeleton

The optical cross sections (xz and yz views) reported in **Figure 3.21**, further confirms differences in cell height with the same cell volume. Here below, optical cross sections of the HL-1 cortical regions were provided.

In **Figure A.1**, the xz and yz views show HL-1 cells cultured on the planar graphene material, 2DG (the optical cross section has final thickness of  $5.56\ \mu\text{m}$ ). Cell cortical region basically consists of dense and actin fibres lattice and terminates with large paxillin patches. Indeed, if in the xz view the whole cell body is detectable, in yz view only the cell terminal region is visible.

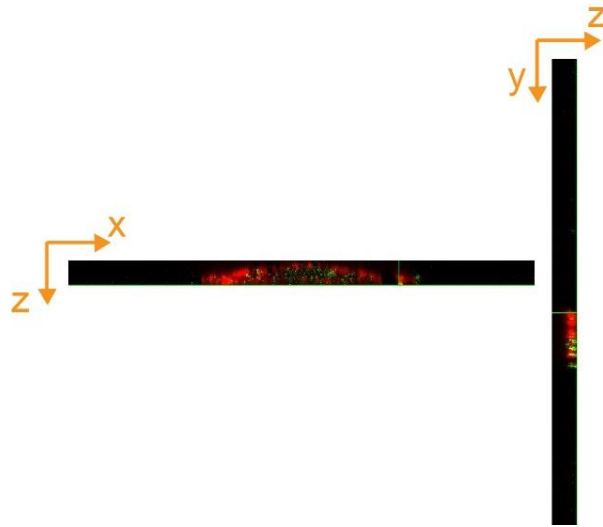


**Figure A1.1.** xz and yz views of HL-1 cells cultured on 2DG.

In **Figure A.2**, the xz and yz views show HL-1 cells cultured on the exposed graphene flakes present in 3DFG configuration, (optical cross section thickness equal to  $4.96\ \mu\text{m}$ ). Cell cortical region is a thin plasma membrane strip, consisted of dense and interlaced actin fibers. Thereby, if in yz view the whole cell body is detectable, in xz one we can pinpoint only the terminal region.

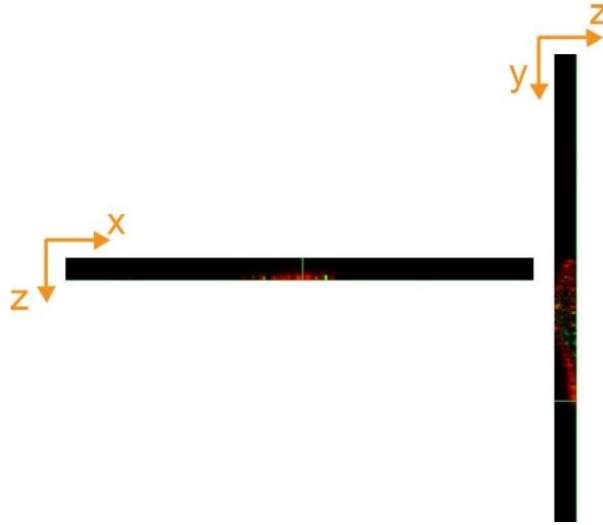


**Figure A1.2.** *xz* and *yz* vies of HL-1 cells cultured on 3DFG.

In **Figure A.3** the *xz* and *yz* views show HL-1 cells cultured on the interwoven texture formed by collapsed NWsin NT-3DFGc configuration (optical cross section thickens equal to  $7.02\ \mu\text{m}$ ). The focused cell region is a cortical area where actin accumulation is dominant due to the presence of out-of-plane micrometric features. Thereby, if in *yz* view the whole cell body is detectable, in *xz* one only the terminal region can be visible.

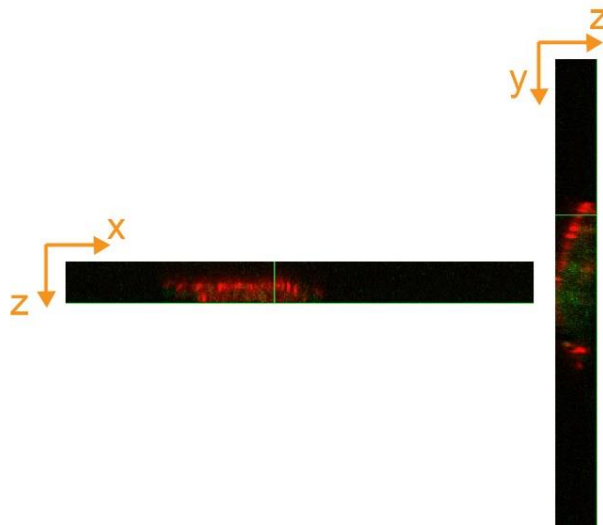


**Figure A1.3** *xz* and *yz* vies of HL-1 cells cultured on NT-3DFGc.

Finally, in **Figure A.4** below, the *xz* and *yz* views show HL-1 cells cultured on the freestanding graphene NWs of NT-3DFGnc configuration. Here, it is clearly visible the actin accumulation at the wire-cell points of contact.

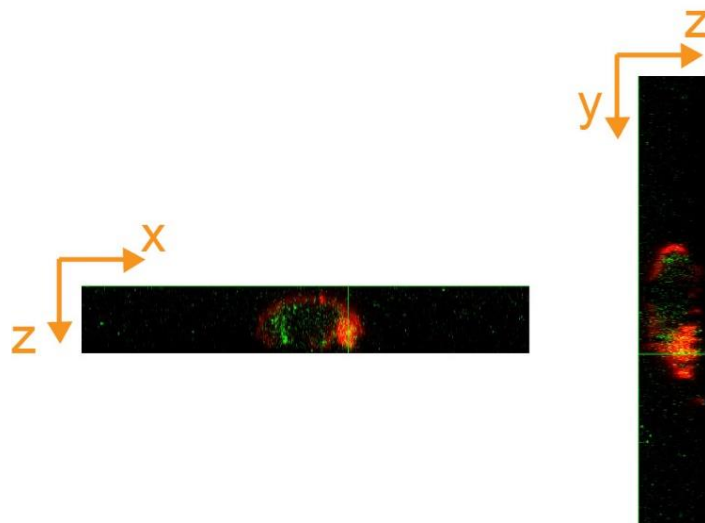


Figure A1.4. xz and yz vies of HL-1 cells cultured on NT-3DFGnc.

## 2. FIB/SEM cross sectioning parameters.

Revealing cell-material cross sections requires steps that should be executed sequentially: ROI identification, e-beam assisted deposition of Pt layer, i-beam assisted deposition of Pt layer, the physical milling of a cell, the polishing to remove the shallower exposed cross-section which might be affected by curtain effects. Here below possible milling parameters are provided (**Table A2.1**). Rough cutting/polishing reduce the overall processing time, however, might require additional fine step to clear out the exposed cross-section.

### Milling *via* FIB

	Coarse	Intermediate	Fine
Voltage [kV]	30.0	30.0	30.0
Current [A]	9.3 n	0.79 n	0.23 n
Nominal thickness [ $\mu\text{m}$ ]	5 $\mu$ (sample-specific)	5 $\mu$ (sample-specific)	5 $\mu$ (sample-specific)
Volume per dose [ $\mu\text{m}^3 \text{nC}^{-1}$ ]	1.500 e <sup>-1</sup>	1.500 e <sup>-1</sup>	1.500 e <sup>-1</sup>

Table A2.1. Milling operational setting.

### Polishing *via* FIB

	Coarse	Intermediate	Fine
Voltage [kV]	30.0	30.0	30.0
Current [A]	0.79 n	0.23 n	0.23 n
Nominal thickness [m]	200 n	200 n	200 n
Volume per dose [ $\mu\text{m}^3 \text{nC}^{-1}$ ]	3.000 e <sup>-1</sup>	1.500 e <sup>-1</sup>	1.500 e <sup>-1</sup>

Table A2.2. Polishing operational setting.

### 3. Optical cross section of CME pathways of HL-1 cells

The presence of out-of-plane features embedded onto the culture surfaces locally push PM inward. These pre-curved PM configurations promptly initiate the recruitment of endocytic proteins, in particular clathrin-mediated ones, at the contact site with the protruding structures (basically, at basal membrane). Here below, yz views of HL-1 fluorescently labelled with clathrin antibody extracted from confocal z-stack acquisition (fixing  $\Delta h = 0.2 \mu\text{m}$ ) clearly highlight protein accumulation at when PM adopts a high positive curvature, compared to the planar cultures which present quite homogeneous fluorescence signal distribution.

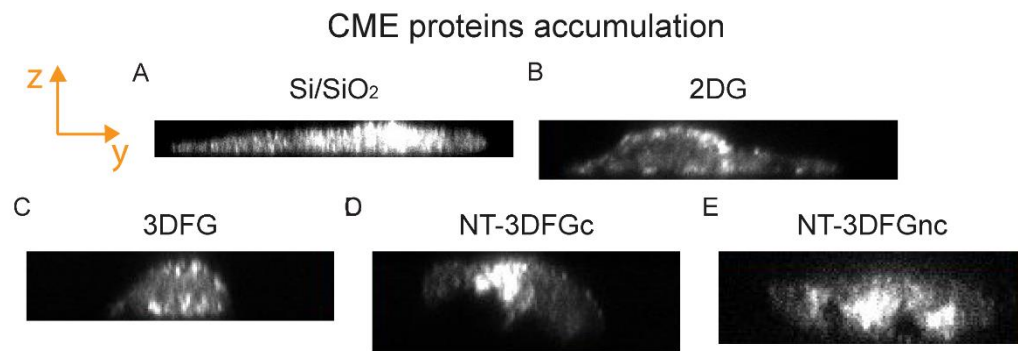


**Figure A3.1. Clathrin-mediated protein spatial distribution.** Yz views of clathrin fluorescent signal expressed by HL-1 cultured on (A) Si/SiO<sub>2</sub>, (B) 2DG, (C) 3DFG, (D) NT-3DFGc and (E) NT-3DFGnc.

#### 4. PM integrity through analysis of possible calcein internalization

For this analysis cells were prepared as described in **Materials and methods 2.6.6**.

Internalization events were detected when calcein fluorescence signal was observed in a non-punctuated pattern within the cell body, which generally occurs to calcein binding cellular debris and is characterized by bright fluorescence spots.

As depicted in **Figure A4.1**, calcein was not found to be concentrated within the cellular area. These results ultimately ensure HL-1 ability retain an intact PM, even when the interaction with protruding sharp NWs promotes marked invagination and engulfment. Therefore, any penetration occurs from the interaction of HL-1 and out-of-plane graphene materials.

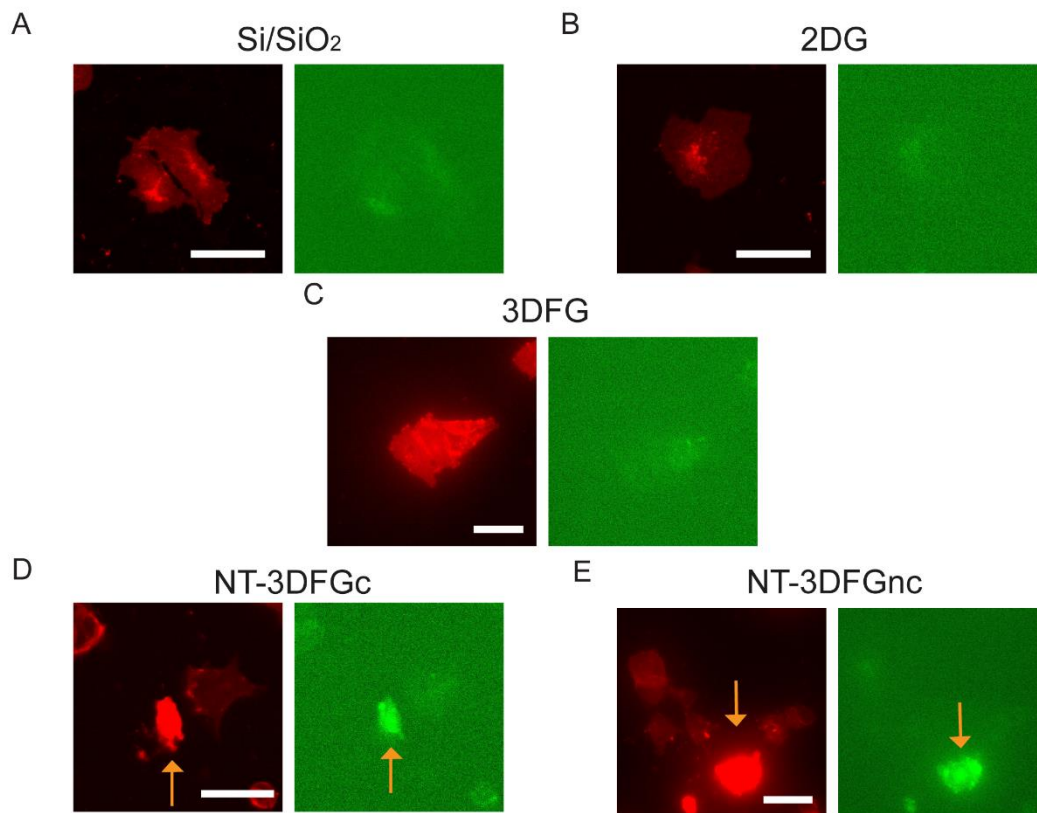


**Figure A4.1** HL-1 membrane integrity from interaction with out-of-plane structures.

HL-1 cells cultured on (A) Si/SiO<sub>2</sub>, (B) 2DG, (C) 3DFG, (D) NT-3DFGc and (E) NT-3DFGnc, were stained with cell mask (in red). Bright calcein signals (in green) point possible uptake of fluorescent dye, which occurs only with dead cells (in D and E). Scale bar 50  $\mu$ m.

## Annex B

Equipment			
Item	Specifications	Company	Catalog number
Countess™ II Automated Cell Counter		Thermo Fischer Scientific	A27977
Cu foil	99.8%	Alfa Aesar	
Dual beam microscope (SEM/FIB)	Helios NanoLab 600i and 650	Thermo Fischer Scientific	
Glass coverslips	12 mm diameter	Thermo Scientific	cat. Num. 11856933
Microtube		BioSigma	cat. num. CL20.002.0500
Polymethylmethacrylate	PMMA 950 A4	MicroChem	
Scanning electron microscopy (SEM)	ULTRAPLUSS ZEISS field emission gun (FEG)	ZEISS	
UV-ozone cleaner	PSD Pro series digital UV-Ozone	Novascan	
Video Contact Angle (VCA) optima		AST products	
Chemicals			
Item	Specifications	Company	Catalog number
Acid ascorbic		Sigma Aldrich	cat. num. A7506
Alexa Fluor 405	anti-chicken, 2 mg/mL	Abcam	cat. num. ab175674
Alexa Fluor 488	anti-rabbit, 2 mg/mL	Abcam	cat. num. ab150077
Alexa Fluor 488	anti-mouse, 2 mg/mL	Thermo Fischer Scientific	cat. num. A11029
Alexa Fluor 546	anti-mouse, 2 mg/mL	Thermo Fischer Scientific	cat. num. A11030
Anti - $\beta$ III-tubulin		Abcam	cat. num. Ab78078
Anti-Caveolin-1	0.1 mg/mL	Abcam	cat. Num. Ab17052
Anti-Clathrin heavy chain Ab I	1 mg/mL	Abcam	cat. num. Ab21679
Anti-MAP2		SYSY	cat. num. 188002
Anti-Paxillin Ab I	0.2 mg/mL	Thermo Fisher Scientific	cat. num. AHO0492
Anti-PSD95	1 mg/mL	SYSY	cat. num. 124011
Anti-Tau	anti-mouse, 0.5 mg/mL	Thermo Fisher Scientific	cat. num. 13-6400
Au Nanoparticles solution		Ted Pella	
B-27™ Supplement		Thermo Fisher Scientific	cat. num. 17504044
Bovine Serum Albumin BSA		Euroclone SPA	cat. num. CHB3057401
Brain-derived Neurotrophic Factor		Merck Life Science S.r.l.	B3795-SUG
Calcein		Sigma-Aldrich	cat. Num. C0875
Calcein-AM		Sigma Aldrich	17783
Cell mask™	1 mg/mL	Thermo Fisher Scientific	cat. num. C10046
CH <sub>4</sub>		Matheson Gas	
Claycomb medium		Sigma Aldrich	cat. num. 51800C
DRAQ5	5 mM	abcam	cat. num. ab108410
Dulbecco's Modified Eagle's Medium		Sigma-Aldrich	D6546
Ethidium Homodimer		Sigma Aldrich	cat. num. 46043
FeCl <sub>3</sub> ·6H <sub>2</sub> O		Sigma Aldrich	
Fertilized eggs		Charles rivers	
Fetal Bovin Serum for HL-1		Sigma Aldrich	cat. num. TMS-016-B
Fetal bovine serum		Sigma-Aldrich	cat. num. F7524
Fibronectine	0.1% solution	Sigma-Adrich	cat. num. F0895
Fluo-4 AM	1 mM	Thermo Fisher Scientific	cat. num. F14201
Glial fibrillary acidic protein GFAP		Abcam	ab4674
glutaraldehyde		Società Italiana Chimici	cat. num. 16220
Glycine	≥ 99 % (titration)	Sigma-Aldrich	cat.num. G7403
H <sub>2</sub>		Matheson Gas	
HCl acid	CMOS grade	J.T. Baker	
Hibernate™-A Medium		Thermo Fisher Scientific	cat. num. A1247501
HL-1			
HNO <sub>3</sub> solution	CMOS grade	J.T. Baker	
Hoechst	10 mg/mL	Thermo Fisher Scientific	cat. num. H3570
L-glutamine	200 mM	Sigma Aldrich	cat. num. G8541
MEM Non-essential Aminoacids 100x		EuroClone	cat. Num. ECB3054D
Neurobasal™ medium		Thermo Fisher Scientific	cat. num. 21103049
Norepinephrine powder		Sigma Aldrich	cat. num. A0937
Osmium tetroxide		Società Italiana Chimici	cat. num. 19190
Paraformaldehyde	16 % in aqueous solution	S.I.C. SOCIETA' ITALIANA CHIMICI	cat. Num. 15710
Penicillin-Streptomycin	10,000 units penicillin and 10 mg streptomycin/mL	Sigma Aldrich	cat. num. P4333
PH <sub>3</sub>		Matheson Gas	
Phalloidin-X 555 conjugated dyes		Abcam	cat. num. ab176756
Phosphate Buffer Saline		Sigma Aldrich	D8537
Poly-L-lysine	0.1% (w/v) H <sub>2</sub> O	Sigma-Adrich	cat. num. P8920
potassium ferrocyanide		Società Italiana Chimici	cat. num. 25102-20
Resin		Società Italiana Chimici	cat. num. 14300
SiH <sub>4</sub>	10% in H <sub>2</sub>	Matheson Gas	
silver conductive paste		RS Component	cat. num. 1863593
sodium cacodylate buffer		Società Italiana Chimici	cat. num. 11652
Tannic acid		Sigma-Aldrich	cat. num. 403040
Thiocarbohydrazide (TCH)		Società Italiana Chimici	cat. num. 21900
Triton-X 100		Sigma-Aldrich	cat. num. T9284-1L
Wheat Germ Agglutinin	5 mg/mL	Thermo Fisher Scientific	cat. num. W21404